

A METAMORPHIC HISTORY OF SUPRACRUSTAL ROCKS ON  
HARØYA AND FINNØYA, NORDØYANE, WESTERN GNEISS  
REGION, NORWAY

by

Holly M. Steenkamp

Submitted in partial fulfillment of the requirements  
for the degree of Master of Science

at

Dalhousie University  
Halifax, Nova Scotia  
November 2012

© Copyright by Holly M. Steenkamp, 2012

DALHOUSIE UNIVERSITY

DEPARTMENT OF EARTH SCIENCES

The undersigned hereby certify that they have read and recommend to the Faculty of Graduate Studies for acceptance a thesis entitled “A METAMORPHIC HISTORY OF SUPRACRUSTAL ROCKS ON HARØYA AND FINNØYA, NORDØYANE, WESTERN GNEISS REGION, NORWAY” by Holly M. Steenkamp in partial fulfillment of the requirements for the degree of Master of Science.

Dated: November 30, 2012

External Examiner:

---

Supervisor:

---

Readers:

---

---

---

---

# DALHOUSIE UNIVERSITY

DATE: November 30, 2012

AUTHOR: Holly M. Steenkamp

TITLE: A METAMORPHIC HISTORY OF SUPRACRUSTAL ROCKS ON  
HARØYA AND FINNØYA, NORDØYANE, WESTERN GNEISS  
REGION, NORWAY

DEPARTMENT OR SCHOOL: Department of Earth Sciences

DEGREE: M.Sc.

CONVOCATION: May

YEAR: 2013

Permission is herewith granted to Dalhousie University to circulate and to have copied for non-commercial purposes, at its discretion, the above title upon the request of individuals or institutions. I understand that my thesis will be electronically available to the public.

The author reserves other publication rights, and neither the thesis nor extensive extracts from it may be printed or otherwise reproduced without the author's written permission.

The author attests that permission has been obtained for the use of any copyrighted material appearing in the thesis (other than brief excerpts requiring only proper acknowledgement in scholarly writing), and that all such use is clearly acknowledged.

---

Signature of Author

# TABLE OF CONTENTS

<b>List of Tables</b> . . . . .	<b>vii</b>
<b>List of Figures</b> . . . . .	<b>viii</b>
<b>Abstract</b> . . . . .	<b>xii</b>
<b>List of Abbreviations Used</b> . . . . .	<b>xiii</b>
<b>Acknowledgements</b> . . . . .	<b>xiv</b>
<b>Chapter 1 Introduction</b> . . . . .	<b>1</b>
1.1 General Introduction . . . . .	1
1.1.1 The Scandinavian Caledonides . . . . .	2
1.1.2 Geology of the Western Gneiss Region . . . . .	2
1.1.3 Metamorphism in the WGR . . . . .	8
1.1.4 The Geology of the Nordøyane UHP Domain . . . . .	10
1.2 Problem and Objectives . . . . .	12
1.2.1 Statement of Problem . . . . .	12
1.2.2 Objectives . . . . .	13
<b>Chapter 2 Lithologies and Field Relationships</b> . . . . .	<b>15</b>
2.1 The Geology of Harøya and Finnøya . . . . .	15
2.2 Supracrustal Rocks of the Blåhø Nappe . . . . .	18
2.2.1 Dioritic Orthogneiss . . . . .	18
2.2.2 Garnet Amphibolite . . . . .	19
2.2.3 Migmatitic Aluminous Gneiss . . . . .	22
2.3 Deformation . . . . .	24
2.3.1 Deformation in the Blåhø Nappe . . . . .	24
2.3.2 Deformation in the Baltican Basement . . . . .	25
2.3.3 The Basement-Supracrustal Contact . . . . .	26
2.4 Summary . . . . .	28
<b>Chapter 3 Pressure and Temperature of Metamorphism</b> . . . . .	<b>30</b>
3.1 Background: Thermodynamics in Metamorphic Petrology . . . . .	30
3.2 Multi-Equilibria Thermobarometry . . . . .	32
3.2.1 Analytical Method . . . . .	33

3.2.2	AveragePT Summary . . . . .	53
3.3	Phase Equilibria Pseudosection Modelling . . . . .	61
3.3.1	The Model System and Bulk Composition . . . . .	62
3.3.2	Pseudosection Results . . . . .	65
3.3.3	Pseudosection Interpretations . . . . .	71
3.4	P-T Results Summary . . . . .	78
<b>Chapter 4</b>	<b>Geochronology: Microprobe Monazite and <math>^{40}\text{Ar}/^{39}\text{Ar}</math> Ages</b> . .	<b>81</b>
4.1	Microprobe Monazite Dating . . . . .	82
4.1.1	Background . . . . .	83
4.1.2	Sample Preparation . . . . .	85
4.1.3	EMPA Monazite Analysis . . . . .	86
4.1.4	EMPA Monazite Ages . . . . .	87
4.2	$^{40}\text{Ar}/^{39}\text{Ar}$ Geochronology . . . . .	93
4.2.1	Background . . . . .	93
4.2.2	Sample Preparation . . . . .	99
4.2.3	$^{40}\text{Ar}/^{39}\text{Ar}$ Analysis . . . . .	100
4.2.4	$^{40}\text{Ar}/^{39}\text{Ar}$ Ages . . . . .	103
4.3	Geochronology Summary . . . . .	113
<b>Chapter 5</b>	<b>Discussion and Conclusions</b> . . . . .	<b>119</b>
5.1	Metamorphic History of the Blåhø Nappe on Harøya and Finnøya . . . . .	120
5.1.1	PTt Path for the Blåhø Nappe . . . . .	123
5.2	Implications for the Tectonic History of the Study Area . . . . .	124
5.3	Regional Implications . . . . .	128
5.4	Recommendations for Further Work . . . . .	131
<b>Appendix A</b>	<b>Field Photograph Locations</b> . . . . .	<b>133</b>
<b>Appendix B</b>	<b>Geothermobarometry and Thermocalc Pseudosection Data</b> . .	<b>134</b>
B.1	SEM Scans and Initial Mineral Mode Outputs . . . . .	134
B.2	Pseudosection Isomodes and Isopleths . . . . .	139
<b>Appendix C</b>	<b>Monazite Petrography and Microprobe Data</b> . . . . .	<b>150</b>
C.1	Textural Context, Analysis Locations, and Trace Element Maps . . . . .	150
C.2	Quantitative Analyses of Monazite Major Elements . . . . .	159

C.3	Background Scans for U, Th, Pb, and Y Trace Elements in Monazite Domains . . . . .	171
C.4	Quantitative Analyses of Monazite Trace Elements and Calculated Ages .	176
C.5	Quantitative Analyses of Consistency Standards . . . . .	180
	<b>References . . . . .</b>	<b>185</b>

# LIST OF TABLES

Table 3.1	Peak and retrograde mineral analyses and calculated AveragePT results	57
Table 3.2	Representative mineral analyses for HS10-16	60
Table 3.3	Compared measured and modelled modes and compositions	75
Table 3.4	Compared <i>P-T</i> estimates from AvPT and pseudosection results	78
Table 4.1	EMPA average compositions of age domains in monazite and calculated ages	92
Table 4.2	Average mineral compositions for $^{40}\text{Ar}/^{39}\text{Ar}$ samples	101
Table 4.3	Northern Domain $^{40}\text{Ar}/^{39}\text{Ar}$ step-heating isotopic data	109
Table 4.4	Southern Domain $^{40}\text{Ar}/^{39}\text{Ar}$ step-heating isotopic data	115
Table A.1	Field photograph locations	133
Table B.1	SEM legend and data table	138
Table C.1	Core domain (D1) major element analyses for HS10-32 monazite grains	159
Table C.2	Inner rim domain (D2) major element analyses for HS10-32 monazite grains	162
Table C.3	Y-rim domain (D3) major element analyses for HS10-32 monazite grains	165
Table C.4	Core domain (D1) major element analyses for HS10-35 monazite grains	167
Table C.5	Y-rim domain (D3) major element analyses for HS10-35 monazite grains	169
Table C.6	Core domain minor elements and calculated ages	177
Table C.7	Inner rim domain minor elements and calculated ages	178
Table C.8	Outer rim domain minor elements and calculated ages	179

# LIST OF FIGURES

Figure 1.1	Tectonic framework in the Late Silurian to Early Devonian . . . . .	3
Figure 1.2	Geology of Norway and the Western Gneiss Region . . . . .	4
Figure 1.3	Geology of Nordøyane . . . . .	11
Figure 2.1	Geological map of Harøya and Finnøya . . . . .	16
Figure 2.2	Field observations of the Blåhø Nappe dioritic orthogneiss . . . . .	19
Figure 2.3	Field observations of the garnet amphibolite unit . . . . .	21
Figure 2.4	Field observations of the migmatitic aluminous gneiss unit . . . . .	23
Figure 2.5	Northern Domain cross-section through Finnøya . . . . .	26
Figure 2.6	Field observations of the supracrustal-basement contact . . . . .	27
Figure 3.1	HS10-02 textures and analysis locations . . . . .	37
Figure 3.2	HS10-02 garnet compositional maps and line traverse . . . . .	38
Figure 3.3	HS10-31 textures and analysis locations . . . . .	41
Figure 3.4	HS10-31 garnet compositional maps and line traverse . . . . .	42
Figure 3.5	HS10-32 textures and analysis locations . . . . .	44
Figure 3.6	HS10-32 Garnet compositional maps and line traverse . . . . .	45
Figure 3.7	HS10-35 textures and analysis locations . . . . .	46
Figure 3.8	HS10-35 garnet A compositional maps and line traverse . . . . .	47
Figure 3.9	HS10-35 garnet B compositional maps and line traverse . . . . .	48
Figure 3.10	HS10-16 textures and chemical garnet maps . . . . .	51
Figure 3.11	Chemistry of matrix biotite and biotite found as inclusions . . . . .	55
Figure 3.12	AveragePT estimates for peak and retrograde compositions from the four migmatitic aluminous gneiss samples . . . . .	56
Figure 3.13	SEM scan of HS10-32 and major mineral modes . . . . .	66
Figure 3.14	HS10-32 pseudosection . . . . .	68
Figure 3.15	HS10-32 pseudosection with M2 isomode intersections . . . . .	70



Figure 3.16	HS10-32 pseudosection with isopleth intersections . . . . .	71
Figure 3.17	HS10-32 pseudosection with estimated M1 isomodes . . . . .	74
Figure 3.18	HS10-32 pseudosection <i>P-T</i> paths . . . . .	76
Figure 3.19	Compared <i>P-T</i> estimates from AvPT and pseudosection results . .	79
Figure 4.1	Major element chemistry of monazite domains . . . . .	89
Figure 4.2	Paired Si + Ca and Th + U substitution in HS10-32 domains . . . .	91
Figure 4.3	Ratios of trace element concentrations in monazite domains . . . .	93
Figure 4.4	Probability distributions and monazite domain ages . . . . .	94
Figure 4.5	<sup>40</sup> Ar/ <sup>39</sup> Ar dating theory . . . . .	97
Figure 4.6	HS10-08 Biotite . . . . .	105
Figure 4.7	HS10-24 Hornblende . . . . .	106
Figure 4.8	HS10-34 Muscovite . . . . .	108
Figure 4.9	HS10-09 Phengite . . . . .	110
Figure 4.10	JB10-84 Phengite . . . . .	112
Figure 4.11	HS10-25 Phengite . . . . .	114
Figure 4.12	Northern Domain <sup>40</sup> Ar/ <sup>39</sup> Ar spectra . . . . .	116
Figure 4.13	Southern Domain <sup>40</sup> Ar/ <sup>39</sup> Ar spectra . . . . .	117
Figure 5.1	<i>PTt</i> path for the <i>Blåhø Nappe</i> . . . . .	125
Figure 5.2	Combined <i>PTt</i> path of the <i>Blåhø Nappe</i> and Baltican basement rocks on Harøya and Finnøya . . . . .	126
Figure 5.3	Conceptual model of the <i>Blåhø Nappe</i> and UHP Baltican basement relationships during the Scandian orogeny . . . . .	127
Figure B.1	SEM scan, BSE image, and photograph of HS10-02 polished thin section . . . . .	135
Figure B.2	SEM scan, BSE image, and photograph of HS10-31 polished thin section . . . . .	136
Figure B.3	SEM scan, BSE image, and photograph of HS10-32 polished thin section . . . . .	137
Figure B.4	Pseudosection calculated for the model bulk composition of HS10- 32 contoured for garnet proportions . . . . .	139

Figure B.5	Pseudosection calculated for the model bulk composition of HS10-32 contoured for $Al_2SiO_5$ proportions . . . . .	140
Figure B.6	Pseudosection calculated for the model bulk composition of HS10-32 contoured for biotite proportions . . . . .	141
Figure B.7	Pseudosection calculated for the model bulk composition of HS10-32 contoured for plagioclase proportions . . . . .	142
Figure B.8	Pseudosection calculated for the model bulk composition of HS10-32 contoured for quartz proportions . . . . .	143
Figure B.9	Pseudosection calculated for the model bulk composition of HS10-32 contoured for melt proportions . . . . .	144
Figure B.10	Pseudosection calculated for the model bulk composition of HS10-32 contoured for potassium feldspar proportions . . . . .	145
Figure B.11	Pseudosection calculated for the model bulk composition of HS10-32 contoured for muscovite proportions . . . . .	146
Figure B.12	Pseudosection calculated for the model bulk composition of HS10-32 contoured for $x(bi)$ . . . . .	147
Figure B.13	Pseudosection calculated for the model bulk composition of HS10-32 contoured for $x(g)$ . . . . .	148
Figure B.14	Pseudosection calculated for the model bulk composition of HS10-32 contoured for $z(g)$ . . . . .	149
Figure C.1	HS10-32 and HS10-35 polished thin section scans . . . . .	151
Figure C.2	Textural context, analysis locations, and chemical maps of HS10-32 monazites 1, 2, and 3 . . . . .	152
Figure C.3	Textural context, analysis locations, and chemical maps of HS10-32 monazites 4, 5, and 6 . . . . .	153
Figure C.4	HS10-32 Monazites 8, 9, and 11 . . . . .	154
Figure C.5	Textural context, analysis locations, and chemical maps of HS10-32 monazites 12, 13, and 14 . . . . .	155
Figure C.6	Textural context, analysis locations, and chemical maps of HS10-32 monazites 15, 17, and 19 . . . . .	156
Figure C.7	Textural context, analysis locations, and chemical maps of HS10-35 monazites 11, 37, and 38 . . . . .	157
Figure C.8	Textural context, analysis locations, and chemical maps of HS10-35 monazites 40, 45, and 48 . . . . .	158
Figure C.9	HS10-32 core domain background scans . . . . .	171

Figure C.10 HS10-32 low-Th rim domain background scans . . . . .	172
Figure C.11 HS10-32 high-Y rim domain background scans . . . . .	173
Figure C.12 HS10-35 core domain background scans . . . . .	174
Figure C.13 HS10-35 low-Th, high-Y rim domain background scans . . . . .	175

# ABSTRACT

The tectonometamorphic histories of allochthonous nappe units that were deeply buried and subsequently exhumed during the Scandian orogeny in the Western Gneiss Region (WGR) of Norway are poorly constrained and understood. One such unit is the *Blåhø Nappe* which underlies northern Harøya and Finnøya, two islands in the Nordøyane ultrahigh-pressure (UHP) metamorphic domain. The *Blåhø Nappe* contains a lower unit of garnet amphibolite gneiss with interlayered garnet-bearing quartzofeldspathic gneiss and marble, and an upper unit of migmatitic aluminous gneiss. Southern Harøya comprises orthogneisses attributed to the Baltican continental crust, and is separated from the *Blåhø Nappe* by the Finnøya migmatitic shear zone (FMSZ). Field and petrographic observations from these islands suggest that the *Blåhø Nappe* experienced peak metamorphism at high pressure amphibolite to granulite facies conditions before being overprinted by relatively lower pressure amphibolite facies conditions. In contrast, the adjacent Baltican basement gneiss contains coesite-eclogite pods, which attests to UHP conditions. However, the basement rocks are also overprinted by an amphibolite facies assemblage. To understand the implications of these observations, the metamorphic history of the *Blåhø Nappe* was investigated, and compared to that of the basement.

This thesis presents thermobarometric and geochronologic analyses used to define a metamorphic pressure-temperature-time (*PTt*) path for the *Blåhø Nappe* on Harøya and Finnøya. The results suggest prograde metamorphism between ca. 440 Ma and 415 Ma, peak temperature metamorphism at 860°C and 15 kbar at around 410 Ma, equilibration at amphibolite-facies conditions of 680°C and 9 kbar by 395 Ma, and cooling below Ar-closure *T* in muscovite by ca. 360 Ma. The *PTt* data from the *Blåhø Nappe* demonstrate that these rocks did not share the UHP history of the adjacent basement rocks, but that both experienced similar amphibolite facies metamorphism and deformation. These units were likely juxtaposed along the FMSZ during isothermal decompression from their respective maximum burial depths to ~30 km depth.

# LIST OF ABBREVIATIONS USED

## Mineral Abbreviations

Adr	andradite	Ksp	potassium feldspar
Alm	almandine	Liq	liquid (melt)
Amp	amphibole	Ky	kyanite
Ap	apatite	Ms	muscovite
An	anorthite	Phn	phengite
Bt	biotite	Pl	plagioclase
Cb	carbonate	Prp	pyrope
Cd	cordierite	Qz	quartz
Cpx	clinopyroxene	Rt	rutile
Di	diopside	Sil	sillimanite
Grs	grossular	Scp	scapolite
Gt	garnet	Sps	spessartine
Hbl	hornblende	Ttn	titanite
Hd	hedenbergite		

## Geological Terms

EMP	electron microprobe
EMPA	electron microprobe analysis
FMSZ	Finnøya migmatitic shear zone
HP	high pressure
<i>P</i>	pressure
<i>T</i>	temperature
UHP	ultra-high pressure
WGR	Western Gneiss Region
WMA	weighted mean age
WMPA	weighted mean plateau age

# ACKNOWLEDGEMENTS

I would first like to thank Becky Jamieson, for suggesting this project. She has been a great source of inspiration, and it has been a pleasure to have her as a supervisor. Living and working in Norway was a once-in-a-lifetime opportunity, and I am grateful to have been included in the adventure. This work could not have been done without the help and teachings of many faculty members and staff at Dalhousie: my thesis committee members (Nick Culshaw, Peter Reynolds, and Carl Guilmette), laboratory technicians (Dan McDonald, Keith Taylor, and Gordon Brown), and all those who make the Earth Sciences department a positive working and learning environment.

To all of the Dalhousie graduate students who have come and gone during my time here, and those who will remain when I leave, best of luck in your future endeavors! Since meeting all of you the world has become a lot smaller - I know that wherever I am, a friend is always nearby. I would especially like to acknowledge Alessandro for reminding me of the important things, and Annina, Louise, Joanna, Carl, Alan, and John for their friendship and relentless support. I would also like to thank Jared Butler for his friendship and teaching me how to drive standard in our Norwegian rental car.

Finally, I never would have made it this far without the love and support of my family, and my best friend, Casey, who called me one day in August 2009 and asked if I wanted to move to Halifax.

# CHAPTER 1

## INTRODUCTION

### 1.1 General Introduction

The Western Gneiss Region of Norway exposes Baltican basement and supracrustal nappe rocks that were subducted and subsequently exhumed during the Caledonian orogeny. On the Nordøyane islands, portions of the Baltican basement subducted to ultrahigh-pressure (UHP) conditions ( $\sim 100$ km depth), whereas infolded supracrustal rocks rarely preserve eclogite facies assemblages. This contrast raises the question of whether the basement and supracrustal rocks were subducted and exhumed as a coherent package. If not, then perhaps the supracrustal rocks detached from a down-going basement slab, and the two lithotectonic units were juxtaposed later during exhumation. The behavior of supracrustal lithologies relative to the basement is important for understanding the influences on subduction and exhumation processes, such as partial melt.

In this M.Sc. thesis, I have reconstructed the tectonometamorphic history of supracrustal rocks in northern Nordøyane, compared this history with adjacent UHP Baltican basement, and discussed the regional-scale implications of supracrustal rock metamorphism during the Scandian phase of the Caledonian orogeny. This chapter will introduce the continental collisional event involving Baltica and Laurentia, the geology of the WGR where Baltican basement and overthrust supracrustal nappe sequences are preserved, and what is known about the metamorphic and deformational histories of these lithotectonic units in the Nordøyane UHP domain.

### 1.1.1 *The Scandinavian Caledonides*

The Scandinavian Caledonide orogenic belt stretches approximately 1800 km from present day Finnmark (northern Norway) at 71°N latitude, southward across northwest Finland, western Sweden, and down to the Stavanger district of southern Norway at 59°N. Today, the mountain range is up to 300 km wide with glacial valleys exposing the deeper roots of the orogen (*Roberts and Gee* 1985).

The Caledonian orogeny includes all of the tectonic events related to and involved in the closure of the Iapetus Ocean between the Cambrian and Late Devonian (*McKerrow et al.* 2000). Prior to its closure, Iapetus was bordered by the Laurentian craton to the west, the Fennoscandian-Russian (Baltican) craton to the east, and various microcontinents to the south (*Ziegler* 1985). An arm of the Iapetus Ocean, the Tornquist Sea, extended E-W, bounded by Baltica's southern margin and the northern margins of Avalonia and Gondwana to the south.

Initiation of E-W convergence of Laurentia and Baltica resulted in subduction of the Iapetan margin below the Laurentian plate, and imbricate stacking of allochthonous nappe units. In the Scandinavian Caledonides, the highest structural levels preserve nappes derived from the Laurentian margin (Uppermost Allochthon) and lowest levels preserve nappes derived from Baltican sedimentary cover (Lower Allochthon). The thrust front propagated from west to east during the collision. The eventual closure of Iapetus was contemporaneous with the burial of the western Baltican margin (and overthrust sedimentary nappes) below Laurentia (*Roberts and Gee* 1985). This Late Silurian to Early Devonian collision is known as the Scandian phase of the Caledonian orogeny, postdating the Grampian and laterally equivalent Taconian phases of the Lower to Middle Ordovician. The Scandinavian Caledonides (Figure 1.2) specifically include rocks underlying present-day Norway, Sweden, and Finland that record Scandian metamorphism and/or deformation (*McKerrow et al.* 2000). The WGR of southern Norway is a tectonic window that exposes the deepest levels of the orogen where the highest grades of Scandian metamorphism and deformation are preserved.

### 1.1.2 *Geology of the Western Gneiss Region*

The WGR is dominated by Proterozoic crystalline orthogneisses of the Baltican basement (Figure 1.2). These polyorogenic 1700-950 Ma rocks range from granodioritic to dioritic compositions (*Corfu* 1980; *Tucker et al.* 1990), and typically contain mafic pods or



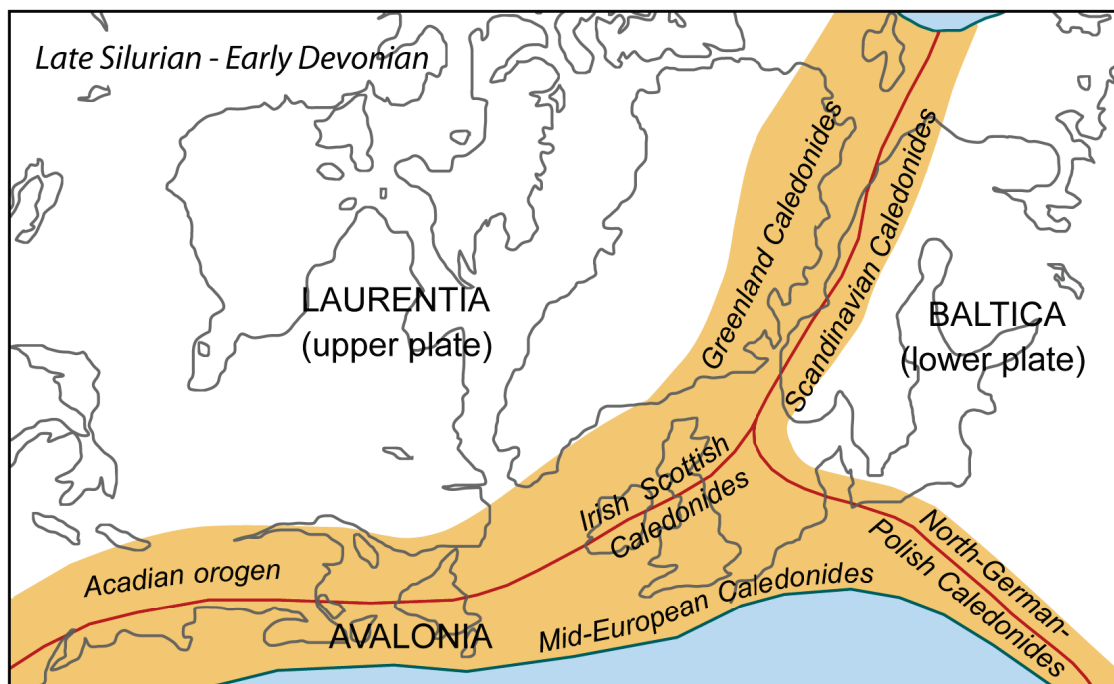
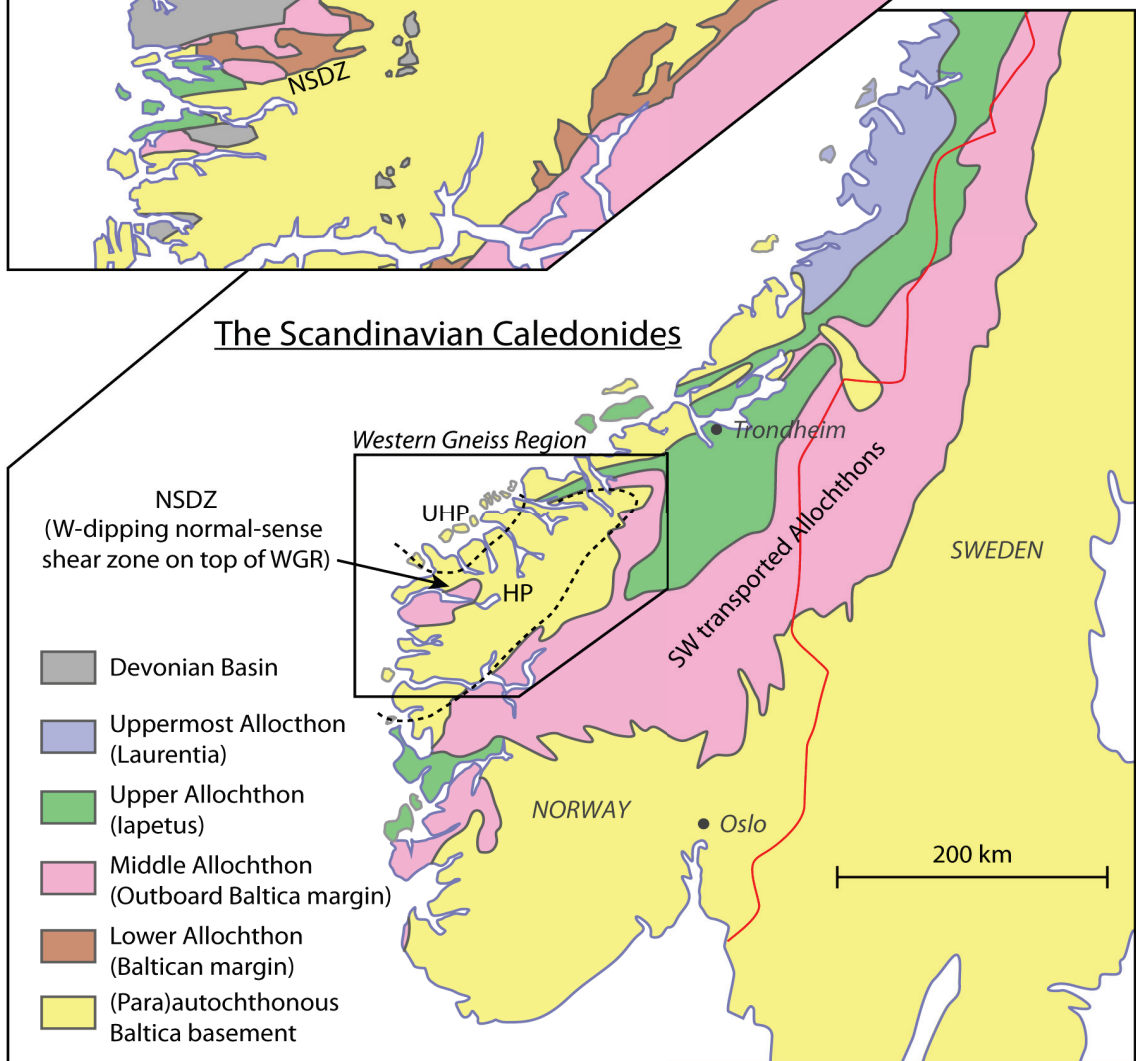
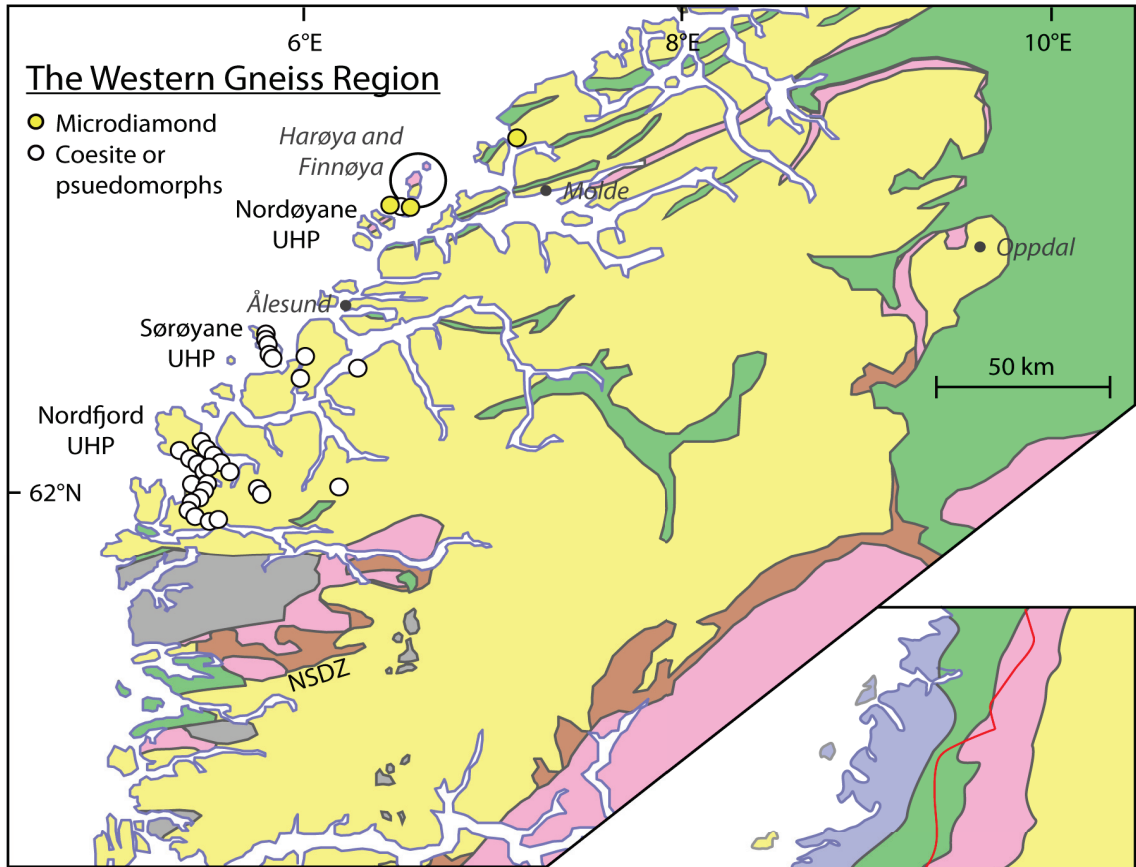


Figure 1.1: Tectonic framework in the Late Silurian to Early Devonian. This is around the time of peak Scandian deformation and metamorphism of the subducted Baltican margin below Laurentia. The coloured zones along the plate boundaries represent orogenic areas (Adapted from Ziegler 1985)

bodies that, within the HP and UHP zones, contain eclogite facies assemblages (Cuthbert *et al.* 2000). The presence of UHP indicator minerals (microdiamond, coesite, and polycrystalline quartz pseudomorphs after coesite) testifies to the burial of the Baltican margin to mantle depths (Smith 1984; Dobrzhinetskaya *et al.* 1995; Wain 1997; Terry *et al.* 2000b; Butler *et al.* doi: 10.1111/jmg.12004, in press, 2012).

The overlying allochthonous metasedimentary rocks in the WGR are tectonostratigraphically divided into four nappe sequences: the Lower Allochthon, Middle Allochthon, Upper Allochthon, and Uppermost Allochthon (Roberts and Gee 1985). The Proterozoic basement orthogneisses are overlain by thin parautochthonous metasedimentary cover including shale, greywacke, shallow marine sandstones, limestones, and fluvial sandstones. These sediments were deposited between the Late Neoproterozoic and Early Silurian, and record only weak Caledonian metamorphism (Bryhni and Sturt 1985; Hacker and Gans 2005; Gee *et al.* 2008).

Figure 1.2: *Following page.* Geology of Norway and the Western Gneiss Region. The geology of Norway (lower panel) is simplified to show the regional extent of allochthonous rocks overlying Baltican basement orthogneisses. Metamorphic pressures recorded in the WGR (outlined in the lower panel) increases from east to west. The WGR (upper panel) predominantly comprises basement orthogneisses overlain and infolded with thinned allochthonous nappe sequences. Three major UHP domains (Nordfjord, Sørøyane, Nordøyane) are recognized by concentrations of microdiamond- or coesite- (or coesite pseudomorph-) bearing sample localities (data based on: *Smith 1984; Dobrzhinetskaya et al. 1995; Wain 1997; Carswell et al. 2006; Vrijmoed et al. 2006; Butler et al. doi: 10.1111/jmg.12004, in press, 2012*). The islands of Harøya and Finnøya are the focus of this thesis. NSDZ = Nordfjord-Sogn Detachment Zone.



The Lower Allochthon is up to 350 m thick, and is dominated by internally thrust-imblicated psammitic and pelitic metasediments locally with detached basement slivers. In the WGR, the tectonostratigraphy of the Lower Allochthon is most complete in the east, where three units occur in sequence. At the base is the Lower Quartz Sandstone Nappe composed of dark grey sandstone (*Vengsås Formation*), shales, and limestones deposited from the Late Neoproterozoic (Ediacaran) to Lower Cambrian. A relatively flat thrust fault caps this unit, and similarly imbricated sediments of the same age make up the middle unit (*Dalselvi Formation*) of the Lower Allochthon (*Hossack* 1983). The uppermost unit (*Gausdal Formation*) is phyllitic, containing mostly Lower Cambrian turbidites (*Bryhni and Sturt* 1985). Caledonian metamorphism is weak throughout this unit, and the grade increases up-section (*Hacker and Gans* 2005). Slices of crystalline basement are incorporated at the base of some thrust sheets, and primary basement-cover contacts are locally preserved.

The Middle Allochthon of southern and western Norway comprises Upper Paleoproterozoic and Upper Mesoproterozoic metamorphic rocks with their low-grade metasedimentary cover units, both derived from the Baltican continental margin. The *Hardangervidda-Ryfylke Nappe Complex*, the *Jotun Nappe Complex*, and the *Bergen Anorthosite Complex* are the best documented Middle Allochthon sequences in eastern Norway (*Bryhni and Sturt* 1985). In the WGR, the Middle Allochthon is much thinner than it is further east. Two major units are described in the WGR, the tectonostratigraphically lower is the *Risberget Auger Gneiss Nappe* which comprises variably deformed rapakivi granites (with U/Pb ages of 1650 and 1185 Ma) (*Handke* 1985), gabbros, anorthosites, and other granitoid rocks. The upper unit is variably known as the *Sætra*, *Songa*, or *Leksdal Nappe*. This unit is dominantly Proterozoic feldspathic sandstones with interlayered amphibolite, derived from later Proterozoic diabase dikes (*Robinson et al.* 2003). In Sweden, this unit is correlated with the *Särv Nappe* which is up to 2 km thick in some areas. In contrast, the *Sætra Nappe* in the WGR is thinned to 1 to 10 m (*Terry* unpublished Ph.D. thesis, University of Massachusetts, Amherst, MA, 2000).

The *Blåhø Nappe* in the WGR, and its correlative eastern counterpart, the *Seve Nappe*, have been recently designated as the uppermost unit in the Middle Allochthon (*Gee et al.* 2008; *Gee et al.* 2010). Previously, this unit was placed at the base of the Upper Allochthon (*Gee et al.* 1985). The *Blåhø Nappe* is composed of migmatitic pelitic gneiss and garnet

amphibolite gneiss with thin, discontinuous intercalated crystalline marble. It has been suggested that these rocks are derived from the outboard Baltican margin, where volcano-sedimentary deposits from an exotic island-arc terrane gave rise to what is now garnet amphibolite gneiss (*Robinson et al.* 2003). In general, peak metamorphic grade decreases from high-pressure granulite facies in the westernmost *Blåhø Nappe* (the focus of this thesis) to low-temperature amphibolite-facies in the eastern *Seve Nappe* (*Hacker and Gans* 2005).

The Upper Allochthon is the most heterogeneous of the thrust nappe sequences, comprising various igneous, metasedimentary, and pre-Caledonian metamorphic rocks. It is dominated by the eastern *Köli Nappe* or its western correlative, the *Trondheim Nappe Complex*. This unit is generally composed of greenschist facies volcano-sedimentary rocks, locally with fossiliferous successions. The faunas range in age from the earliest Ordovician to Early Silurian, and their assemblages suggest an Iapetan to proximal Laurentian affinity. This upper unit also includes island-arc and basinal oceanic sequences, and ophiolite fragments transported from the Iapetan oceanic crust (*Slagstad* 2003).

The Uppermost Allochthon is exposed in north-central Norway, where it overlies rocks of the *Köli Nappe* with a thick mylonite zone marking the contact. The *Helgeland Nappe Complex* comprises dominantly locally migmatitic orthogneisses, lesser volumes of schists, psammites, conglomerates, dolomite and calcite marbles, sedimentary iron ore deposits, and variable amounts of amphibolites, greenstones and serpentinites (*Roberts and Gee*, 1985). There is growing evidence suggesting that the Uppermost Allochthon was derived from the continental margin of Laurentia. *Roberts* (2003) suggested the general easterly-thickening of carbonate successions implies deposition in a paleobasin that deepened to the east. Internal NW-vergent thrusts and folds, reminiscent of the Early Ordovician structures seen in the Appalachians of eastern Canada and the USA, suggest early accretion of these rocks along the margin of Laurentia before they were detached and transported over the Baltican margin during terminal collision between Baltica and Laurentia (*Roberts* 2003).

During and immediately following the Scandian orogeny, continental sandstones of Early and Middle Devonian age were deposited in intermontaine and extramontaine basins along the Scandinavian belt. These rocks structurally overlie Upper and Middle Allochthon rocks, and Baltican basement in some areas. The Hornelen Basin on the west

coast of the WGR is bounded to the north and south by high-angle normal faults, and contains up to 25 km of Devonian strata unconformably overlying rocks of the Lower and Middle Allochthons. Marginal alluvial fan conglomerates line the faulted boundaries, with sandstone and siltstone from stream-dominated fan systems making up the interior basin strata (Steel *et al.* 1985). Sedimentary deposition in the Hornelen Basin prograded eastward, evidence for coeval eastward shift of the basin depocenter. Below the basement-Lower Allochthon contact in this area, E-W trending ductile stretching lineations, amphibolite facies mylonites (<6 km thick) associated with top-W shear, and brittle normal structures are interpreted to mark a major normal-sense shear zone that was in part responsible for exhumation of basement and associated allochthonous rocks from lower crustal depths (Johnston *et al.* 2007b). This particular extensional feature is called the *Nordfjord-Sogn Detachment Zone* (NSDZ, Figure 1.2). Other ductile to brittle top-W extensional shear zones in the WGR are of a smaller scale and represent less extensional displacement (Andersen 1998).

### 1.1.3 Metamorphism in the WGR

In the Scandinavian Caledonides, the WGR hosts rocks that record the highest grades of Scandian metamorphism. Mafic pods and larger bodies hosted in felsic orthogneisses of the Baltican basement retain UHP mineral assemblages that include coesite or polycrystalline quartz pseudomorphs after coesite, indicating burial of this continental crust to mantle depths (>90 km) (Smith 1984; Wain 1997; Cuthbert *et al.* 2000; Terry *et al.* 2000b; Butler *et al.* doi: 10.1111/jmg.12004, in press, 2012). So far only one report of UHP metamorphism in supracrustal rocks exists: Dobrzhinetskaya *et al.* (1995) extracted microdiamonds from rocks correlated with the *Blåhø Nappe* of the Upper Allochthon by bulk sampling methods. There are three distinct zones along the western coast of the WGR where evidence of UHP metamorphism has been recognized: the southern Nordfjord/Stadlandet UHP domain, located just north of the NSDZ, the central Sørøyane UHP domain, and the northern Nordøyane UHP domain. Between each UHP domain only peak metamorphism at HP conditions has so far been documented. Considering this, it is debated whether the UHP domains originated as a single coherent body (Root *et al.* 2005; Young *et al.* 2007) or are distinct tectonic units with different metamorphic histories.

Peak metamorphic conditions of >2.5 GPa and 700-800 °C have been documented in eclogites across the UHP domains, based on thermobarometry and the presence of

UHP indicator minerals (*Hacker et al. 2010*, and references therein). The widespread distribution of ultramafic peridotites and pyroxenites with UHP mineral assemblages within the WGR suggests its burial to the sublithospheric mantle (*Brueckner et al. 2010*) of either the Laurentian or Baltican continent (this is still debated) at some point during their collision. UHP metamorphism in the WGR has been dated at 415-400 Ma, based on U/Pb zircon ages (*Krogh et al. 2011*; *Root et al. 2005*; *Carswell et al. 2003*), and is associated with top-SE thrusting (*Terry and Robinson 2004*), consistent with paleoreconstructions that suggest northwestwards subduction of Baltica below Laurentia (*Torsvik 1998*).

Following UHP metamorphism, much of the WGR experienced amphibolite facies overprinting related to the exhumation of deeply buried continental crust to middle crustal levels (*Krabbendam and Dewey 1998*; *Terry and Robinson 2003*). Crystallization of amphibole-bearing partial melt in boudin necks and pegmatite dykes took place at amphibolite facies conditions at around 395 Ma, based on U/Pb zircon (*Krogh et al., 2011*) and titanite (*Tucker et al. 2004*) ages. A pervasive NW-dipping amphibolite facies foliation and sinistral mylonitic fabrics are observed within the entire northern WGR, and have been linked with regional-scale transtension (*Krabbendam and Dewey 1998*). E-W stretching lineations and top-W extension are well documented near Nordfjord, providing more evidence for transtensional movement following UHP metamorphism.

Evidence for further exhumation of the WGR through upper crustal levels is based on  $^{40}\text{Ar}/^{39}\text{Ar}$  cooling ages from white mica (muscovite or phengite) and biotite, which have  $^{40}\text{Ar}^*$  closure temperatures of about 425-400°C (*Grove and Harrison 1996*) and 320°C (*Harrison et al. 2009*), respectively. *Walsh et al. (2007)* found that white mica ages young from east to west across the WGR from ~399 Ma to ~390 Ma, suggesting diachronous cooling. White mica ages of samples from UHP domains are even younger, with some recording  $^{40}\text{Ar}/^{39}\text{Ar}$  ages as young as ~375 Ma. The diachronous nature of these cooling ages indicates that while the eastern side of the WGR had cooled below 425°C, the western side was still at >500°C (*Walsh et al. 2007*; *Krogh et al. 2011*).

It is clear that UHP metamorphism of the Baltican continental crust was a product of continental collision involving burial to mantle depths, but the mechanisms responsible for the subsequent exhumation of these rocks remain controversial. Moreover, the metamorphic histories of allochthonous nappes in the WGR and their relationships with UHP Baltican crust during collision, deep burial, and exhumation have hardly been investigated.

One exception is the small outcrop of Ky-Grt-Gr migmatitic gneiss on Fjørtoft, Nordøyane, correlated with the *Blåhø Nappe* of the lower unit in the Upper Allochthon, as discussed in the following section (Terry *et al.* 2000b). Understanding and quantifying UHP metamorphism and exhumation of UHP rocks in continental collisional settings requires constraints on the metamorphic and structural histories of all the lithologies, including the thin nappe units that overlie the UHP basement rocks.

#### 1.1.4 *The Geology of the Nordøyane UHP Domain*

The focus of this thesis is the metamorphic history of the *Blåhø Nappe* on Harøya and Finnøya, the northernmost islands in the Nordøyane island chain and UHP domain (Figure 1.3). Previous studies in this domain include classical thermobarometry on Baltican basement eclogites (Butler *et al.* doi: 10.1111/jmg.12004, in press, 2012) and supracrustal rocks correlated with the *Blåhø Nappe* (Terry *et al.* 2000b), and ultramafic bodies (Carswell *et al.* 2006; van Roermund 2009), U/Pb isotopic (Krogh *et al.* 2011) and (U-Th)/Pb chemical (Terry *et al.* 2000b) geochronology, reports of microdiamond (Dobrzhinetskaya *et al.* 1995; Vrijmoed *et al.* 2008), and observations of *in situ* coesite (Butler *et al.* doi: 10.1111/jmg.12004, in press, 2012). The four southern islands in the chain are dominated by basement orthogneisses, with minor amounts of considerably thinned Upper Allochthon lithologies. The northern two islands, in contrast, are underlain by nearly equal proportions of basement orthogneisses and supracrustal lithologies, providing ample opportunity to study both lithotectonic units separately, and the contact that juxtaposes them.

Terry *et al.* (2000a) mapped the four southern islands at 1:10 000, and divided the geology into three crustal segments. The northern and southern segments comprise basement orthogneisses with abundant eclogite pods and larger-scale eclogite bodies. The central segment does not contain eclogite, but the granitoid gneiss hosts deformed mafic dykes. All three segments contain thinned *Sætra* and/or *Blåhø Nappe* units. Evidence of UHP metamorphism has so far been found only in the northern segment.

Microdiamond separates were reported from a 50 kg bulk sample of supracrustal Ky-Grt-Gr migmatitic gneiss, correlated with the *Blåhø Nappe* (Dobrzhinetskaya *et al.* 1995), on northern Fjørtoft. Peak metamorphism of the microdiamond-bearing Bardane garnet websterite body on western Fjørtoft is estimated at 875°C and 40 kbar (Carswell *et al.* 2006). Most recently, the first discovery of *in situ* coesite from an eclogite body in Nordøyane basement orthogneiss on Harøya was reported by Butler *et al.* (doi: 10.1111/jmg.12004,



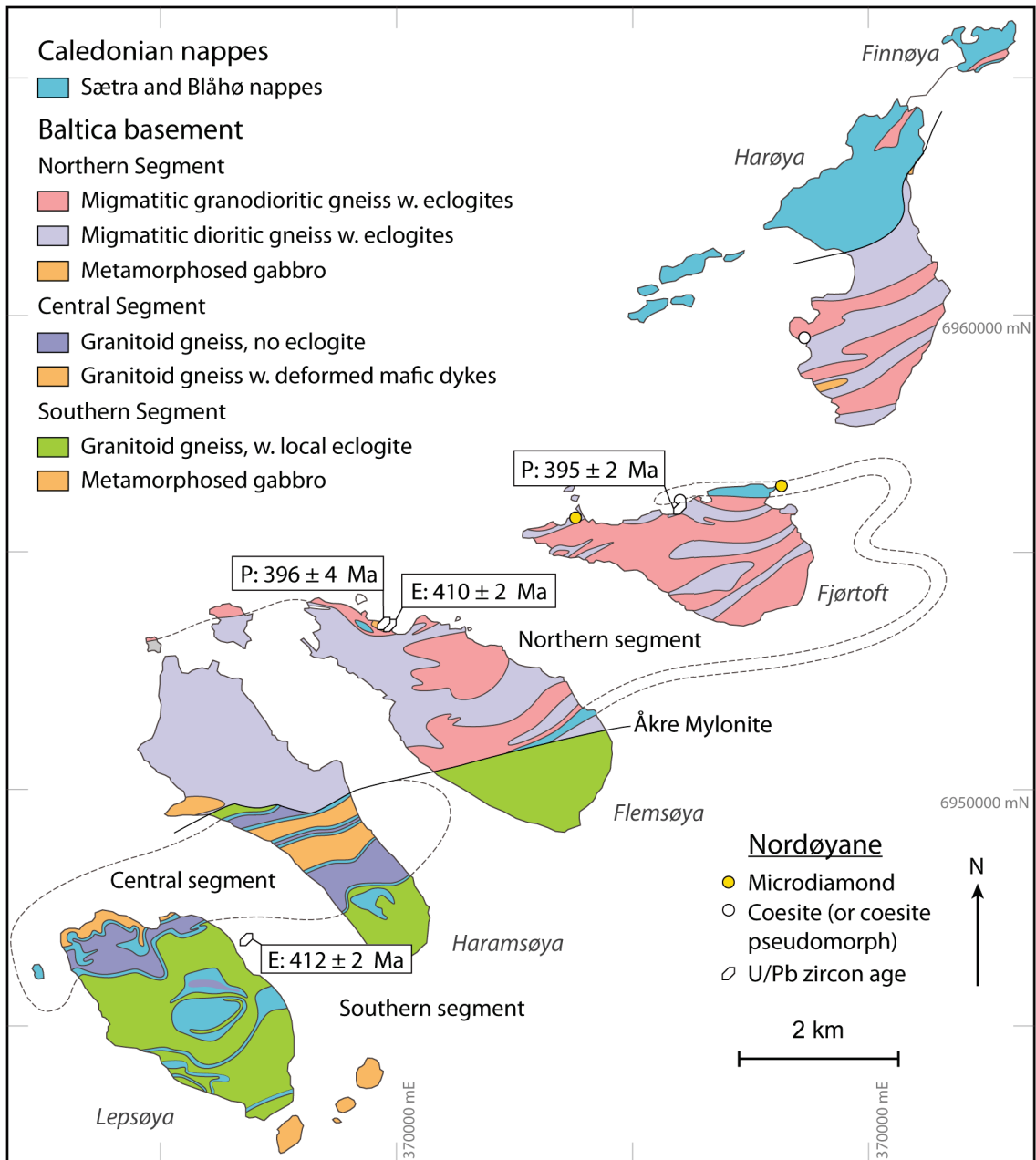


Figure 1.3: Geology of Nordøyane. This is based on mapping included in this thesis and previously reported by *Terry et al. 2000a*. The presence of UHP indicator minerals (microdiamond and coesite) confirms that the basement rocks underlying these islands were buried to mantle depths (*Dobrzhinetskaya et al. 1995; Terry et al. 2000b; Carswell et al. 2006; Butler et al. doi: 10.1111/jmg.12004, in press, 2012*). UHP metamorphism of the basement rocks in Nordøyane happened around 410 Ma (E), and crystallization of partial melting at amphibolite facies conditions took place around 395 Ma as pegmatitic granite (P) in the necks of boudinaged eclogite pods (*Krogh et al. 2011*).

in press, 2012). Amphibolite facies overprinting, common to all of the high-grade WGR, at 700°C and 11 kbar, with further decompression to 6-2.5 kbar has been estimated from the microdiamond-bearing Ky-Grt-Gr migmatitic gneiss and its mylonitic equivalent on Fjørtoft.

UHP metamorphism in this domain has been dated at 410-412 Ma, based on U/Pb zircon geochronology on UHP eclogite facies assemblages, with amphibolite facies overprinting in the basement at 395 Ma (*Krogh et al.* 2011). (U-Th)/Pb chemical dating of monazite by *Terry et al.* (2000b)) from the supracrustal rocks on Fjørtoft indicated 407 Ma as the timing of UHP metamorphism. Based on *P-T* estimates and metamorphic ages, the UHP basement is inferred to have exhumed at a rate of nearly 11 mm/yr to approximately 37 km depth by 395 Ma when it, and HP basement rocks currently underlying it, are inferred to have continued exhuming together at a much slower rate of 1-1.5 mm/yr (*Terry et al.* 2000b).

The limited data available point to the need for better constraints on the metamorphic structural and pressure-temperature-time *PTt* histories of supracrustal and basement rocks in the WGR. The metamorphic history of the *Blåhø Nappe* on Harøya and Finnøya, the two northern islands of Nordøyane that *Terry* (unpublished Ph.D. thesis, University of Massachusetts, Amherst, MA, 2000) did not map, are the focus of this study; a complementary study of the basement gneisses in this area was conducted by Jared Butler as part of his PhD research. These projects aim to quantify the metamorphic and structural histories of the rocks in this area, and to answer the following questions: Did the supracrustal and basement rocks share the same UHP history? If not, at what stage in their respective metamorphic histories were they juxtaposed? What is the nature of the contact between these units? Did partial melting of either lithotectonic unit occur? If so, when did this happen with respect to peak P and retrograde metamorphism?

## 1.2 Problem and Objectives

### 1.2.1 Statement of Problem

The metamorphic history of supracrustal nappe rocks, their behavior relative to Baltican basement orthogneisses, and their influence on subduction and exhumation processes during the Caledonian orogeny, are not fully understood in the Nordøyane UHP domain. Two opposing hypotheses currently stand regarding the metamorphic history of supracrustal

rocks with respect to the Baltican basement in this area: 1) these lithotectonic units were subducted and exhumed as a coherent body, and therefore share a common history, or 2) during subduction, the supracrustal rocks detached at mid-crustal levels from the down-going Baltican basement, which reached depths corresponding to UHP conditions, and later these lithotectonic units were juxtaposed during exhumation. In the second case, the timing and conditions of peak metamorphism recorded by these units would differ, but their retrograde history would be similar. To test these hypotheses, this study attempts to answer the following questions: Does the supracrustal *Blåhø Nappe* share a metamorphic history with underlying Baltican basement orthogneisses on Harøya and Finnøya? If not, what were the peak conditions experienced by the *Blåhø Nappe*, and when did peak metamorphism take place? Furthermore, when, and at what P-T conditions, did the supracrustal and basement rocks become juxtaposed in their current formation?

### 1.2.2 Objectives

1. Map the study area. Define the lithologic, structural, and metamorphic characteristics of the supracrustal rocks for comparison with the Baltican basement.
2. Document mineral assemblages in the supracrustal lithologies, and determine metamorphic *P-T* conditions from suitable assemblages.
3. Perform (U-Th)/Pb monazite microprobe dating to constrain the timing of high-grade metamorphism and amphibolite facies overprinting, and  $^{40}\text{Ar}/^{39}\text{Ar}$  dating to constrain the timing of subsequent cooling.
4. Compile a pressure-temperature-time (*PTt*) path describing the metamorphic history of the *Blåhø Nappe* based on field observations and analytical results.
5. Compare and contrast the *Blåhø Nappe PTt* path with the metamorphic and structural history of the adjacent Baltican basement.

These objectives were completed by conducting geologic mapping at 1:10 000 scale in June and July of 2010 and collecting samples for geochronology and thermobarometry analyses that were concluded by April, 2012. Chapter 2 documents the observed field relationships between supracrustal and basement lithologies, and presents the geological map of Harøya and Finnøya with labelled sample locations. Chapters 3 and 4 report the

methodologies and analytical results of the classical thermobarometry and pseudosection modelling, and (U-Th)/Pb monazite and  $^{40}\text{Ar}/^{39}\text{Ar}$  geochronology studies, respectively. By compiling these observations and analytical results, interpretations regarding the tectonometamorphic history of the *Blåhø Nappe* are presented and discussed in Chapter 5, along with recommendations for further work. Additional analytical and methodological documentation, and supporting data are catalogued in Appendices A, B and C.

## CHAPTER 2

# LITHOLOGIES AND FIELD RELATIONSHIPS

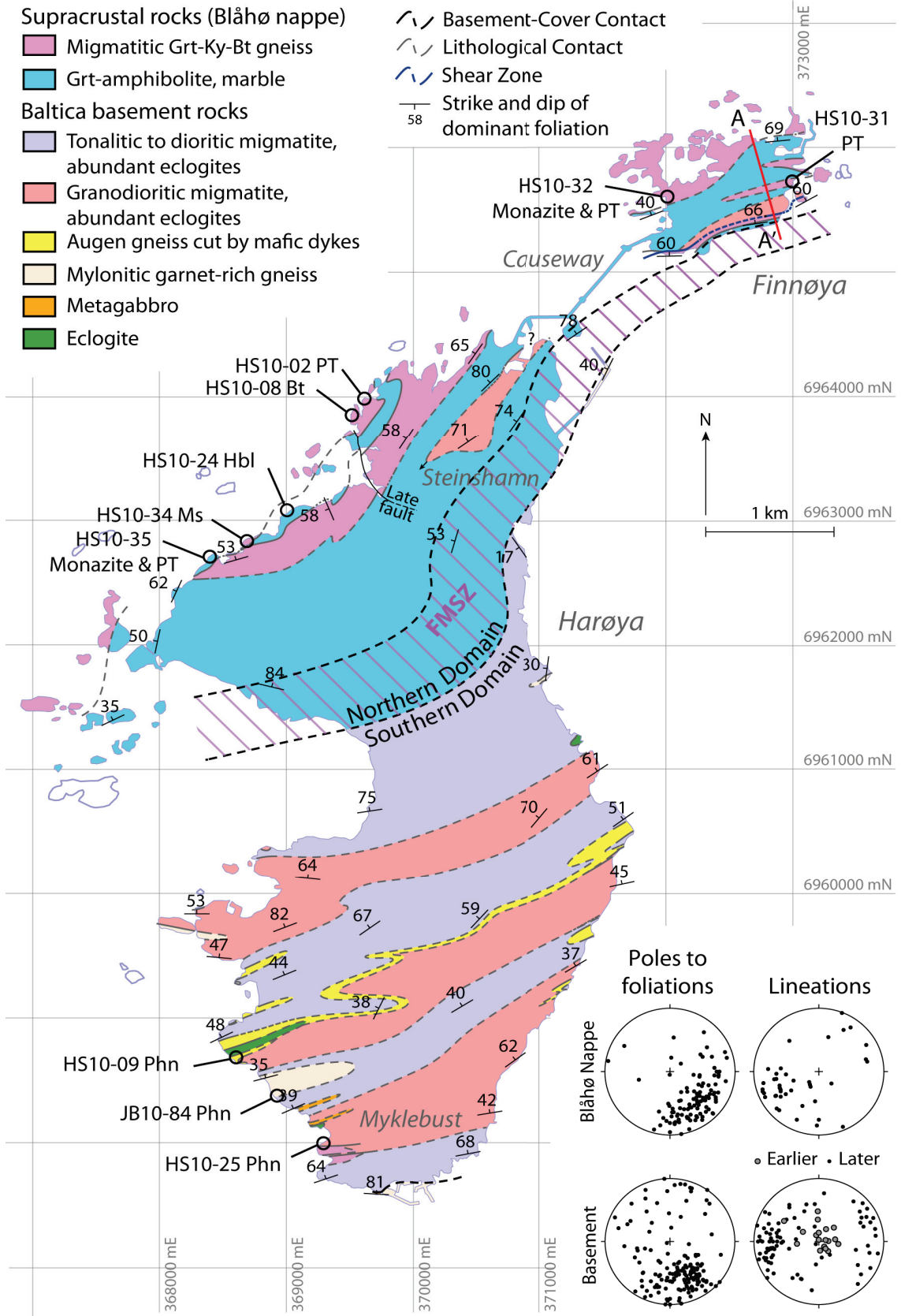
### 2.1 The Geology of Harøya and Finnøya

The islands of Harøya and Finnøya are located at the northern end of the Nordøyane UHP domain. These islands were previously mapped at 1:250 000 by the Norwegian Geological Survey as undifferentiated basement orthogneiss to the south, with overlying supracrustal garnet-amphibolite and mica- and garnet-gneiss to the north. The NE-SW trending contact between these lithotectonic units is poorly exposed, and therefore has not been well documented. It is believed that the supracrustal sequence on Harøya and Finnøya extends NE along strike to the islands of Ona, Orta, Sandøy, and Øtrøy, and is correlative with *Blåhø Nappe* sequences recognized elsewhere in the WGR.

This chapter documents the internal characteristics, variations, and relationships of the supracrustal units on Harøya and Finnøya as they were observed in the field. Metamorphic and structural features, and the nature and extent of the contact with the basement orthogneiss, are also described here. Features internal to the *Blåhø Nappe* bear witness to the metamorphic history of this unit, while its contact with the Baltican basement lithologies provides information on their juxtaposition. These observations are linked with the analytical thermobarometry and geochronology results, from Chapters 3 and 4, respectively, to produce ground-truthed interpretations of the data, which are discussed in Chapter 5.

For this study, Harøya and Finnøya were mapped at 1:10 000 (Figure 2.1), with field observations collected over a six week period from June to mid-July, 2010. Outcrops

Figure 2.1: *Following page.* Geological map of Harøya and Finnøya. The geology is interpreted in terms of two lithotectonic domains: the Northern Domain comprises rocks of the supracrustal Blåhø nappe, and the Southern Domain is dominated by Baltican basement orthogneisses. The tectonic contact between these units is characterized by a 50-60 m wide zone of felsic migmatite that hosts abundant boudins of garnet amphibolite, garnet-bearing quartzofeldspathic gneiss, and retrogressed eclogites, referred to as the Finnøya migmatitic shear zone (FMSZ). Both domains feature a pervasive NW-dipping foliation, consistent with regional deformation, that is interpreted to have developed under amphibolite-facies conditions. Two mineral lineations, an earlier and a later, were only observed in the basement rocks. Locations of samples used in thermobarometric and geochronologic analyses are labelled, and the cross-section in Figure 2.5 follows the red line from A to A' on Finnøya.



are best exposed along coastlines and in areas of high topographic relief. A prominent hill on southern Harøya slopes gently to sea level on its northeast side, but drops off dramatically on the southwest side. This cliff outcrop is quite weathered and dangerously steep in some areas, making mapping of its faces difficult. Areas with little to no topographic relief are either residential properties, fields for livestock and farm crops, or bogs with bunch grass and rare knobs of bedrock. Significant changes to the previous map resulting from this field work include major contact revisions, documentation and tracing of distinctive basement lithologies, and identification of numerous mylonite zones.

The geology can be divided into two distinct lithotectonic domains, both displaying a common NW-dipping foliation. Baltican basement lithologies make up the Southern Domain (SD), while supracrustal rocks correlative with the *Blåhø Nappe* are contained in the Northern Domain (ND). The *Blåhø Nappe* comprises two major lithologies, garnet amphibolite and migmatitic aluminous gneiss, and minor dioritic orthogneiss. A zone of eclogite to amphibolite facies mafic boudins wrapped in foliated felsic migmatitic gneiss is interpreted as the contact between the northern and southern domains. This contact is henceforth referred to as the Finnøya migmatitic shear zone (FMSZ). The remainder of this chapter describes ND lithologies, metamorphism, and structures, the FMSZ, and some contrasting characteristics of basement structures in the SD.

## 2.2 Supracrustal Rocks of the Blåhø Nappe

### 2.2.1 Dioritic Orthogneiss

The base of the *Blåhø Nappe* is interpreted to include local slivers of migmatitic dioritic orthogneiss. This lithology is best seen near the entrance to the causeway bridge on the southern coast of Finnøya, where it is in contact with overlying garnet amphibolite (Figure 2.2a). The contact here is sharp, and dips moderately to the NW. About 2 m below the contact, the orthogneiss becomes progressively more mylonitic before the outcrop disappears below the water. A late [Scp + Pl + Qz + Bt + Hbl + Ms ± Gt] pegmatite cuts N-S through the garnet amphibolites and then E-W through about half of the exposed contact here. Marble lenses and layers in the overlying garnet amphibolite are a possible source of carbonate for the 8-12 cm long scapolite crystals.

The migmatitic dioritic orthogneiss comprises [Pl + Qz + Hbl + Ksp ± Gt], with [Pl + Qz] concentrated in leucosome bands and [Pl + Hbl] in mesosome bands. In the 30-40 cm



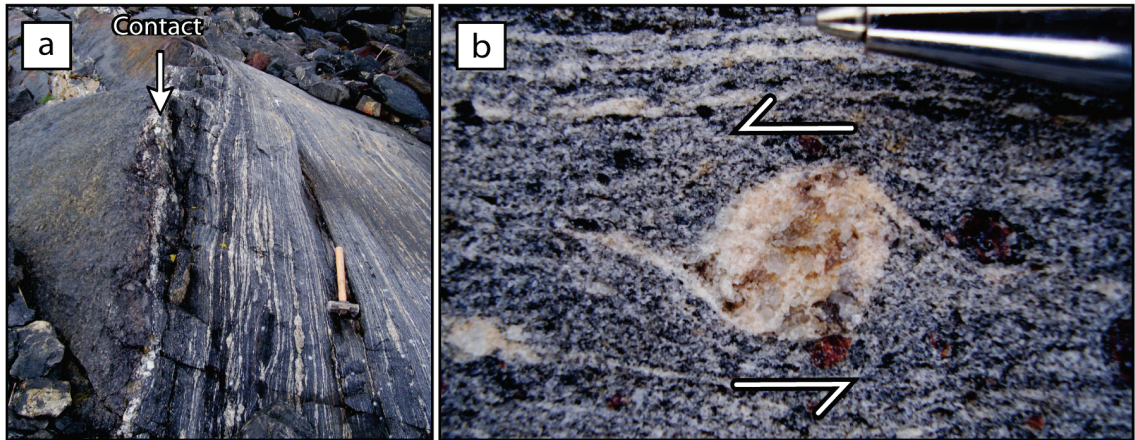


Figure 2.2: Field observations of the Blåhø Nappe dioritic orthogneiss. Late scapolite pegmatite marks the primary contact between the garnet amphibolite (left) and underlying orthogneiss (right) of the *Blåhø Nappe*. A polycrystalline delta clast (b) in the lower mylonitic zone of this orthogneiss indicates top-NW shear.

below the contact with the overlying garnet amphibolites, garnet decreases in abundance from approximately 10 to 3 modal %. All phases range in size from fine- to coarse-grained (1-8 mm) near the upper contact, and are xenoblastic. Closer to the shoreline, where the unit becomes more mylonitic, strain shadows around  $Pl \pm Qz$  delta porphyroclasts indicate a top-NW shear sense (Figure 2.2b). Porphyroclasts are typically <1 cm long, and the sheared matrix minerals are <0.5 mm wide. Mineralogically, this unit resembles the dioritic orthogneiss in the SD (Figure 2.1), but has a higher degree of strain.

### 2.2.2 Garnet Amphibolite

A generally coarse-grained, well-foliated garnet amphibolite unit makes up the base of the metasedimentary rocks in the *Blåhø Nappe*. This lithology underlies approximately 70% of the ND, and ranges in structural thickness from 30 m to 500 m. The base of this lithology was observed in contact with dioritic orthogneiss of the *Blåhø Nappe*, or with the NE-SW trending FMSZ (Figure 2.1), which is best preserved on southeastern Finnøya and western Harøya. The top of this unit is marked by a relatively sharp to gradational contact with the upper migmatitic aluminous gneiss unit of the *Blåhø Nappe*. This contact is folded, and therefore exposed in several coastal outcrops around Finnøya and on the northwest coast of Harøya.

The garnet amphibolite unit is characterized by 10-30 modal % xenoblastic garnet

porphyroblasts (0.5-4 cm wide, Figure 2.3a) in a coarse-grained (0.5-1 mm) hornblende-dominated matrix with lesser plagioclase and scapolite, and minor carbonate, quartz, and apatite. Garnet is typically rimmed by relatively fine-grained hornblende and plagioclase, and hornblende inclusions are visible in most large garnet grains. Compositional layering of [Hbl + Pl] or [Hbl + Scp] matrix (Figure 2.3b) is common. The proportion of garnet porphyroblasts to matrix remains relatively constant from one compositional layer to another, and presumably reflects the bulk composition.

Approximately 20% of the garnet amphibolite unit is made up of interlayered, compositionally variable lithologies. Laterally continuous garnet-bearing quartzofeldspathic gneiss, discontinuous lenses of marble, and rare lenses of hornblendite are found within the top of the garnet amphibolite unit, but there is no apparent pattern or repetition to their distribution. The quartzofeldspathic layers (Figure 2.3c) range in thickness from approximately 10 cm to <2 m with 0.2-2 cm wide xenoblastic garnets (Figure 2.3d). These layers can be traced laterally along most of northwestern Harøya and the low-lying intertidal islands of southwestern Finnøya.

Discontinuous layers of marble typically mark the top of the garnet amphibolite unit, just below the contact with the migmatitic aluminous gneiss. The thickness of this lithology swells to ~2 m, and laterally pinches down to ~5 mm, where the carbonate deflects around garnet porphyroblasts in the amphibole-rich matrix (Figure 2.3e). The marble contains 15-20% silicate phases, including [Cpx + Ms + Pl + Qz ± Scp ± Ksp ± Hbl].

A 50 cm wide layer of dark green hornblendite was found in one outcrop on northwestern Harøya between two layers of the garnet-bearing quartzofeldspathic gneiss. The 4-6 mm long hornblende crystals define a subhorizontal lineation parallel to the strike of the NW-dipping foliation. This evidence implies deformation associated with shallow lineations is linked to amphibolite facies conditions. A linear fabric likely developed in this lithology because garnet, a stronger phase that forces recrystallizing amphibole to deflect around it, is absent.

The lithological variability seen in the garnet amphibolite unit reflects compositional changes in the *Blåhø Nappe* protolith. The grain size, gneissic banding, and mineral assemblages in this unit suggest high-grade metamorphism up to high-pressure amphibolite-granulite facies conditions. Evidence of primary or prograde metamorphic features have likely been obliterated.

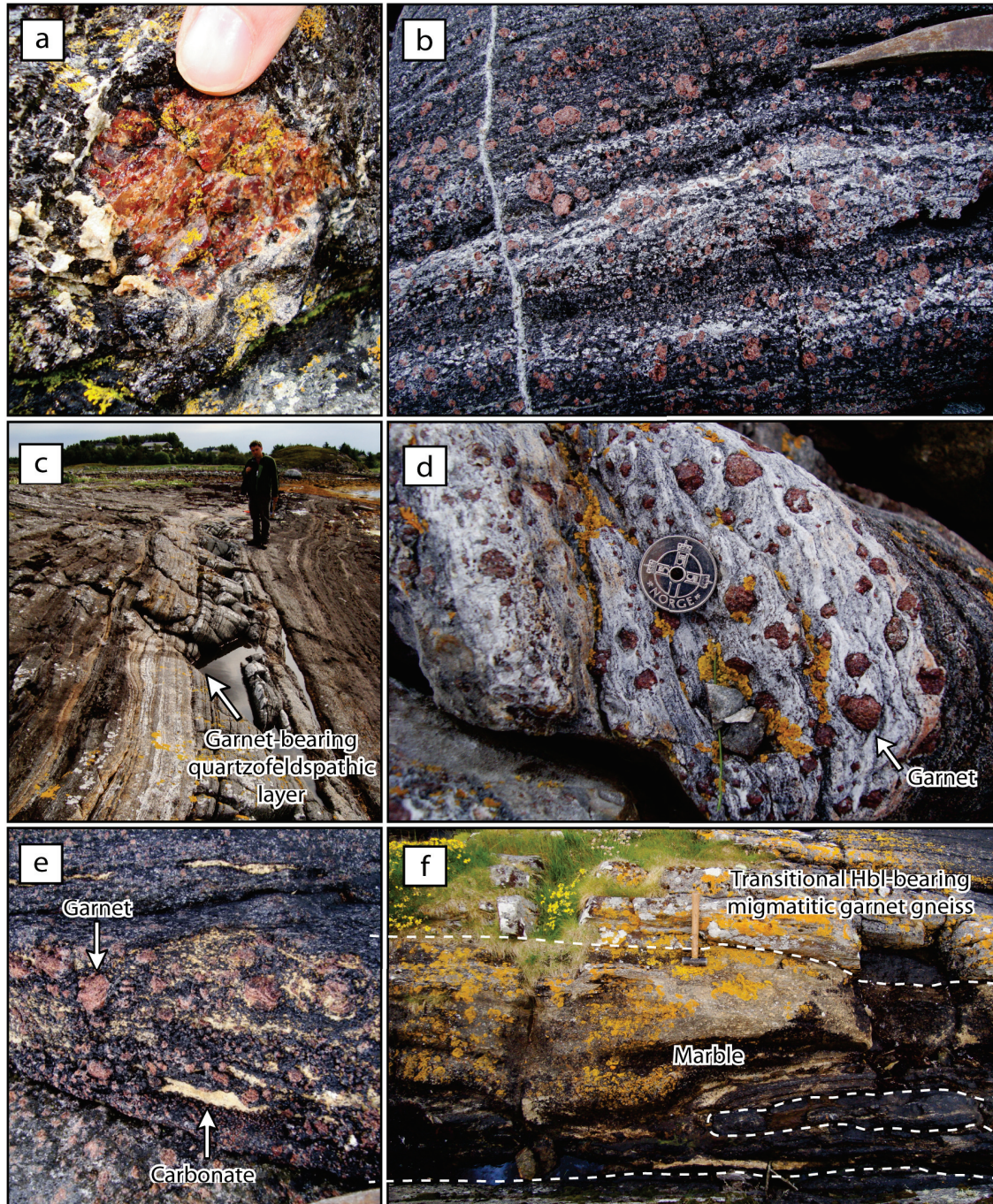


Figure 2.3: Field observations of the garnet amphibolite unit. a) 3 cm wide xenoblastic garnet near the top of the unit contains amphibole inclusions, similar to garnets from lower in the unit (b) where the foliation is defined by compositional layering of Amp + Pl (light layers) and Amp + Scp (dark layers). Laterally continuous garnet-bearing quartzofeldspathic gneiss (c, d), and minor lenses (e) to major discontinuous layers (f) of impure marble are common near the upper contact of this unit. See Appendix A for photo locations.

### 2.2.3 *Migmatitic Aluminous Gneiss*

The migmatitic aluminous gneiss unit of the *Blåhø Nappe* is characterized by 3-8 mm wide garnet and kyanite porphyroblasts, and dominantly planar gneissic banding oriented parallel to the pervasive NW-dipping foliation, as observed in the underlying garnet amphibolite unit. As mentioned previously, a relatively sharp to gradational contact marks the boundary between the garnet amphibolites and this migmatitic aluminous gneiss (Figure 2.4a). The minimum thickness of the aluminous unit is estimated as >25 m, but since an upper contact was not observed, the total thickness cannot be determined.

Gneissic banding in this lithology is defined by deformed leucosome and mesosome layers (Figure 2.4b), which make up approximately 25% and 75% of the rock, respectively. The mesosome contains the assemblage [Gt + Bt + Pl + Qz + Rt ± Ky/Sil] (Figure 2.4c). Medium- to coarse-grained biotite deflects and wraps around garnet porphyroblasts that commonly have biotite or oxide minerals in their cores. Where not deflected by garnet, biotite grains define a matrix foliation consistent with the regional NW-dipping foliation.

The foliation in this unit is better defined by 2-8 cm, discontinuous leucosome lenses and layers containing medium- to coarse-grained [Pl + Qz ± Ky/Sil ± Ms]. The presence of leucosome indicates partial melting of the *Blåhø Nappe*, and the colourless to blue kyanite in the leucosome (Figure 2.4d) suggests that crystallization of that partial melt occurred at relatively high pressures. Along the northwest coast of Harøya, rare crenulated leucosome (Figure 2.4e), and a second generation of leucosome that cuts the foliated fabric, were observed.

At the outcrop-scale, the migmatitic aluminous gneiss exhibits little to no compositional variation (Figure 2.4f), unlike the underlying garnet amphibolites. Absolutely no evidence of primary features remains in these rocks, and eclogite facies minerals expected in rocks with this bulk composition, such as clinopyroxene, are absent. Based on these observations, the mineral assemblages, and evidence of partial melting, this unit likely experienced HP amphibolite to granulite facies conditions along with the underlying garnet amphibolite unit. The similar peak metamorphic conditions for both units within the *Blåhø Nappe*, and the metamorphosed but structurally unaltered gradational contact between them, suggests that they formed a single package through the course of the Caledonian Orogeny. It is possible, however, that layer-parallel discontinuities exist between or within these layers, which can structurally thicken, thin, or repeat these lithologies.

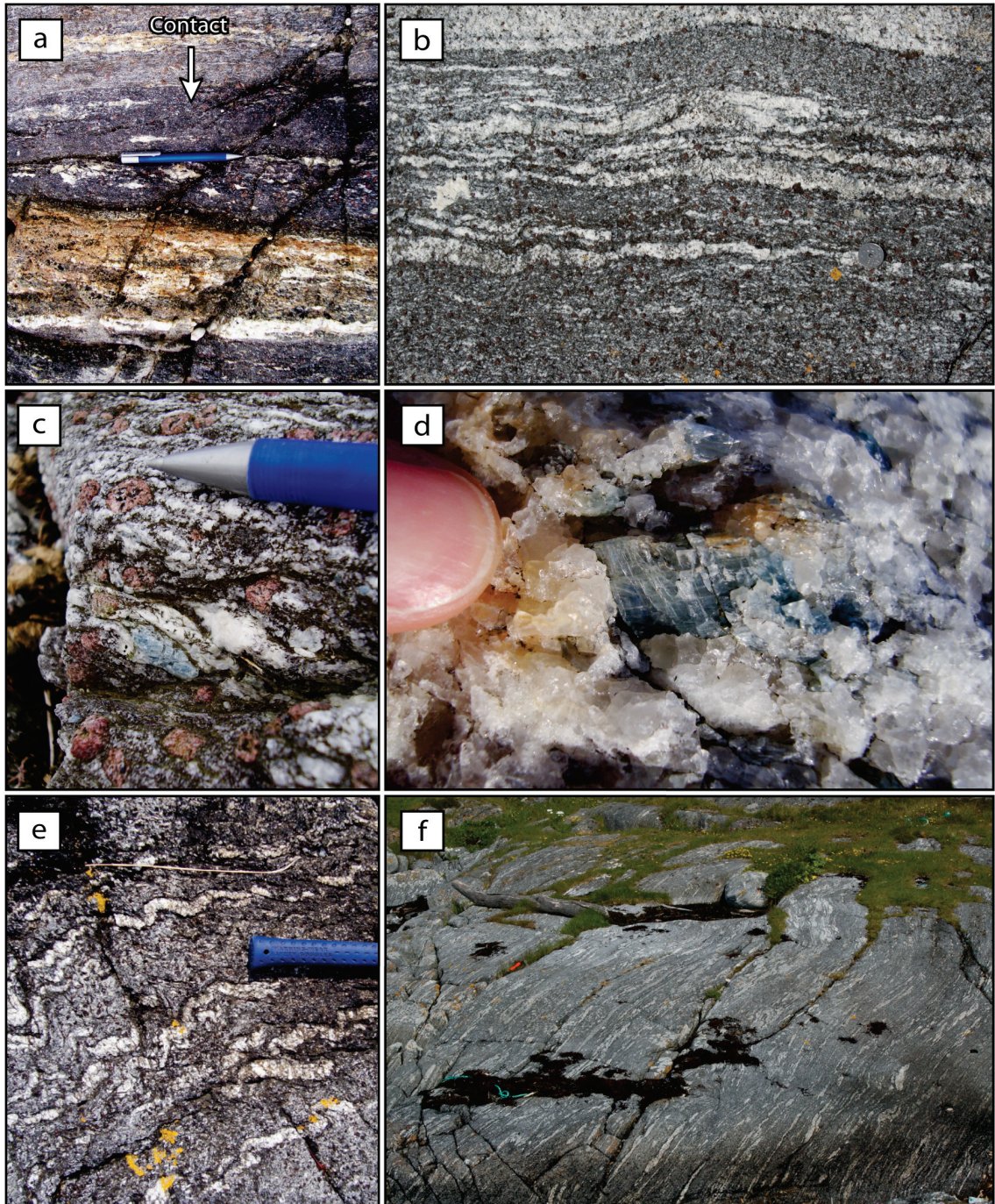


Figure 2.4: Field observations of the migmatitic aluminous gneiss unit. The lower contact with the garnet amphibolites is relatively sharp (a) in some areas, and gradational in others. Leucosome and mesosome layers (b) attest to high-grade metamorphism. The mesosomes contain  $Gt + Bt + Pl + Qz + Rt \pm Ky/Sil$  (c) and the leucosomes contain  $Pl + Qz \pm Ky/Sil \pm Ms$  (d). A rare crenulation was observed on Harøya, but this unit typically displays a planar gneissic foliation, and is broadly homogeneous at the outcrop-scale (f). See Appendix A for photo locations.

## 2.3 Deformation

Caledonian tectonic events are reflected in the *Blåhø Nappe* in the form of structural and deformational features, such as folds, fabrics, shear zones, and the lithotectonic contact with the Baltican basement. Documentation and interpretation of these features may contribute a fourth element, deformation (*d*), to the construction of a *PTt* path. The age and conditions for deformation events can be relatively (or less commonly, absolutely) linked with analytical thermobarometry and metamorphic ages, to produce a *PTtd* path. This would yield a complete metamorphic and structural history of the *Blåhø Nappe*, which can then be compared with what is known about the basement history.

### 2.3.1 Deformation in the *Blåhø Nappe*

The *Blåhø Nappe* in the study area displays a pervasive, moderately NW-dipping foliation, consistent with the regionally dominant metamorphic fabric. In the garnet amphibolites, this foliation is characterized by gneissic banding defined by [Hbl + Pl] or [Hbl + Scp]-rich layers. The major lithological variations (garnet-bearing quartzofeldspathic gneiss, marble, and hornblendite) seen at the top of the unit may reflect bulk composition changes in the protolith, metamorphic segregation effects, or a combination of both. The compositional layering is parallel to the dominant regional foliation. In the migmatitic aluminous gneiss, the foliation is primarily defined by interlayered leucosome and mesosome. Biotite within the mesosome deflects around garnet porphyroblasts, but is also aligned parallel with the regional foliation.

The foliation is folded about moderately- to steeply-dipping foliation-parallel fold axes. The hingelines of the folds generally plunge shallowly (10-20°) to the SW. The axial surfaces are sub-vertical, and the folds are isoclinal to slightly overturned, with amplitudes in the range of 30-80 m. Along a NW-SE transect on the northeast coast of Finnøya, the garnet amphibolite-migmatitic aluminous gneiss contact is repeated several times by folding (Figure 2.5).

Mineral lineations defined by stretched aggregates of quartz in the migmatitic aluminous gneiss are generally shallowly WSW-plunging. These are very rare, probably due to the coarse grain size and post-strain grain growth, and are consistent with late lineations in the SD and across the region. In contrast to the SD, discrete shear zones in the ND are rare. One 10-15 m wide mylonitic shear zone was found amongst the low-lying intertidal islands on the southwest coast of Finnøya. Positively-weathered kyanite, garnet, and [Pl +

Qz] porphyroclasts stand out from the very fine-grained grey matrix. The compositional layering common to this unit is nearly erased in this area; the [Pl + Qz] porphyroclasts are likely remnants of leucosome layers. A second shear zone, on the east coast of Finnøya (just south of the HS10-31 sample location, Figure 2.1), places dioritic orthogneiss of the *Blåhø Nappe* structurally above a repeated sequence of migmatitic aluminous gneiss and garnet amphibolite (Figure 2.6a). This shear zone can be traced from a small eastern island, accessible at low tide, westward onto Finnøya and up the coastal outcrop where it disappears below the vegetation. Porphyroclasts in the mylonitic aluminous gneiss (Figure 2.6b) are asymmetrical, but due to the angle of exposure, the shear sense is difficult to determine. Evidence of partial melting exists in both the dioritic orthogneiss and underlying sheared aluminous gneiss. A second generation of leucosome locally cross-cuts the contact, suggesting either shearing during prolonged melt-stable conditions, or two independent phases of partial melting, before and after shearing.

Late cross-cutting felsic pegmatite dykes are common across the ND, and range in width from 10 cm to 1 m. Most of these dykes are subvertical and concentrated in the garnet amphibolite unit.

All of these deformation features are linked with, or defined by, amphibolite facies mineral assemblages, implying formation at these conditions. There is no evidence in the *Blåhø Nappe* of earlier features associated with prograde metamorphism or eclogite facies conditions. If the *Blåhø Nappe* experienced conditions greater than HP amphibolite-granulite facies, the mineral assemblages and any associated fabrics have since been erased by the regional amphibolite facies overprint.

### 2.3.2 *Deformation in the Baltican Basement*

The SD displays several features common to the ND, such as the regionally pervasive amphibolite facies NW-dipping foliation, isoclinal folds, and late cross-cutting pegmatite dykes. In contrast to the ND, numerous mylonite zones mark lithological changes in basement, and two distinct mineral lineation directions were observed. In specific outcrops on both the east and west coasts of Harøya, an earlier steeply-plunging top-NW lineation is overprinted by the more regionally widespread shallowly- to moderately-plunging top-WSW lineation. These lineations are commonly defined by preferential growth of elongate minerals (such as hornblende) in a linear pattern, or stretched aggregates of pre-existing minerals (commonly quartz).

The basement orthogneisses commonly host boudinaged eclogite bodies elongated parallel to the dominant foliation, and ranging in size from a few centimeters to several meters long. These typically preserve eclogite facies mineral assemblages in their cores, and have retrograde amphibolite facies mineral assemblages at their rims. UHP metamorphism has been documented in the SD, based on the presence of coesite in a boudinaged eclogite pod (*Butler et al.* doi: 10.1111/jmg.12004, in press, 2012). In contrast, evidence of UHP metamorphism is absent in the supracrustal lithologies of the ND, implying that these lithotectonic units did not experience the same peak metamorphic pressure. The amphibolite facies overprint common to both units suggests that they deformed together at these conditions.

### 2.3.3 The Basement-Supracrustal Contact

The inferred NE-SW trending FMSZ between the *Blåhø Nappe* and the Baltican basement is poorly exposed on the west coast of Harøya, and covered by overburden across the interior and eastern coast. On Finnøya, however, the FMSZ is visible along the eastern coast. Here, the shore runs parallel to the regional foliation, and evidence of deformation

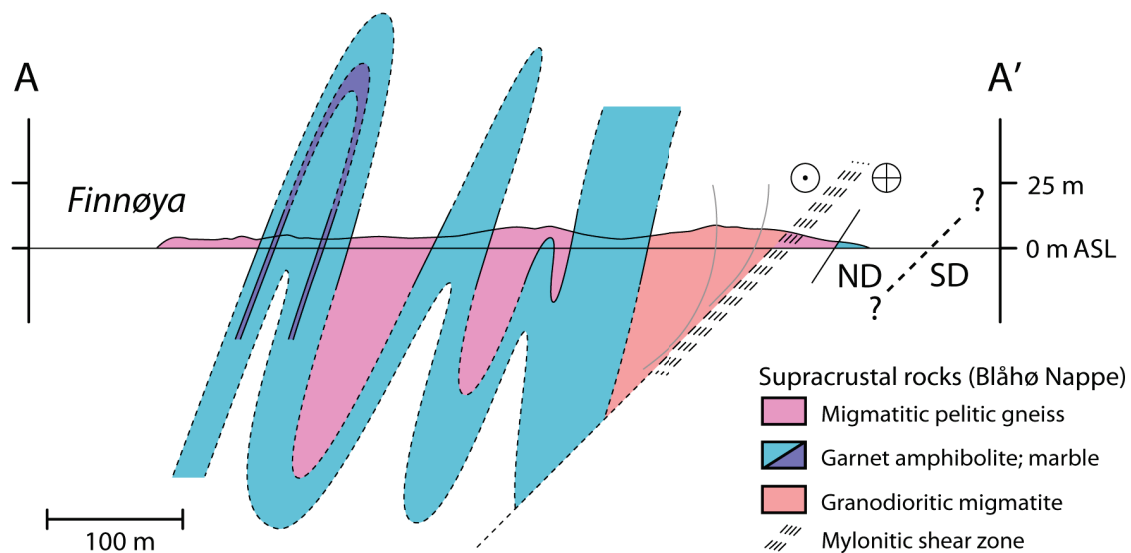


Figure 2.5: Northern Domain cross-section through Finnøya. The cross section is indicated by the red line (A to A') in Figure 2.1. Deformation in the *Blåhø Nappe* is characterized by subvertical isoclinal folds and a complementary NW-dipping foliation. Migmatitic orthogneisses on Finnøya are interpreted as a basal unit of the *Blåhø Nappe*. The contact between the ND (left) and SD (right) is inferred east of Finnøya. Vertical exaggeration is 2:1.



and partial melting is ubiquitous. The 10-20 m wide rocky coastline is relatively steep and reaches up to 20 m elevation in some areas, where grass and small trees cover the top of the outcrop.

Garnet amphibolite overlies the FMSZ along the water's edge of southeastern Finnøya (Figure 2.6a), and is very heterogeneous compared to the garnet amphibolite elsewhere on Finnøya and Harøya. The FMSZ is essentially a zone of boudinaged retrogressed eclogite (Figure 2.6b), garnet amphibolite, and garnet-bearing quartzofeldspathic gneiss wrapped in migmatitic, medium-grained felsic material (Figures 2.6c, d). Coarse-grained amphibole is present in these leucosomes, suggesting crystallization at amphibolite facies conditions.

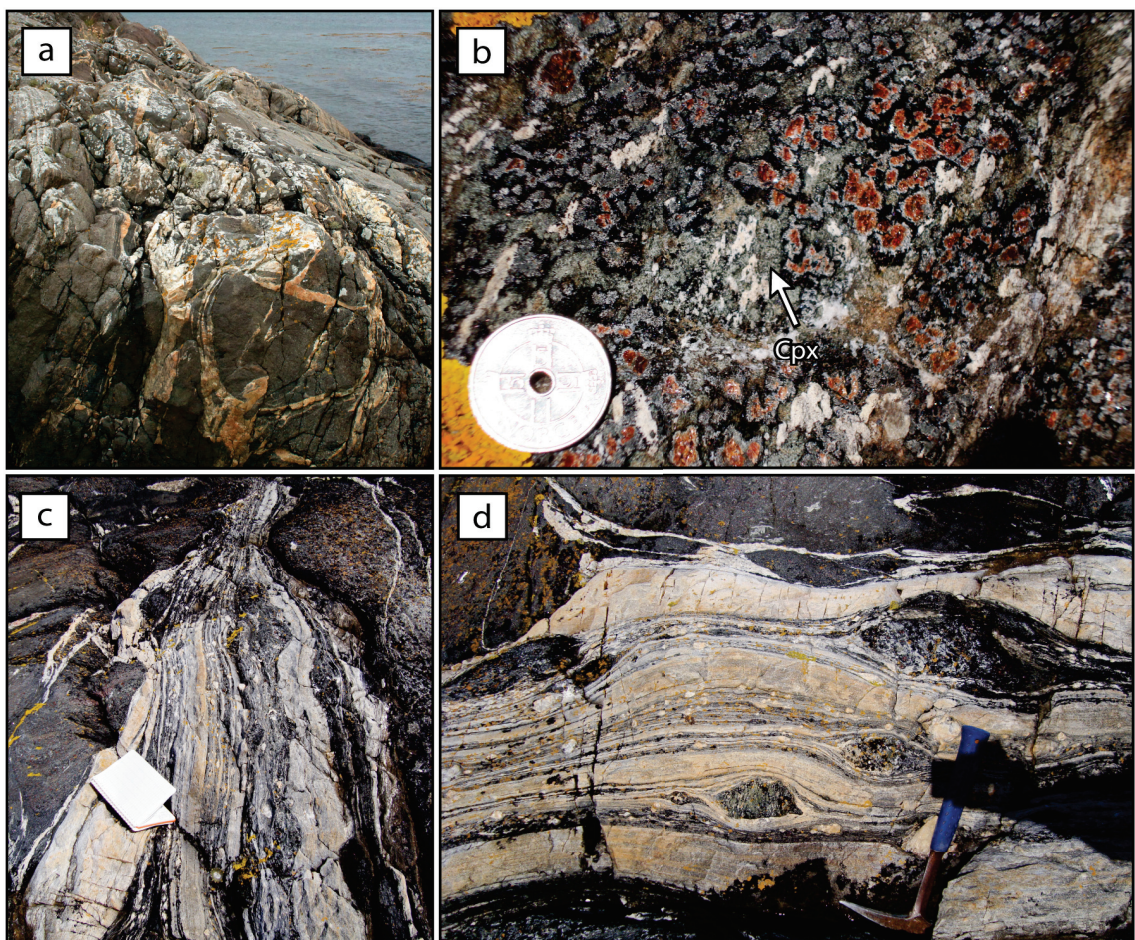


Figure 2.6: Field observations of the supracrustal-basement contact. Underlying the garnet amphibolite unit is the Finnøya migmatitic shear zone (FMSZ), which contains boudinaged garnet amphibolite (a), garnet-bearing quartzofeldspathic gneiss, and retrogressed eclogites (b). The volume of leucosome (c, d) increases to the SE (towards the shoreline), presumably reflecting proximity to underlying ND basement rocks.

The base of this highly migmatitic zone is below the water, but may represent the contact with the Baltican basement of the SD. If this is the case, then this leucosome-rich zone suggests that melt may have collected between the two domains during, or soon after, juxtaposition.

The western coast of Harøya exposes the FMSZ in a <2 m high, ~100 m wide discontinuous cross-section. The overlying garnet amphibolite is lithologically heterogeneous, similar to the Finnøya exposure, and the abundance of retrogressed eclogite bodies increases from NW to SE. Partial melt is ubiquitous here as well. The FMSZ appears to represent a 50-60 m wide tectonic contact between the garnet amphibolite of the *Blåhø Nappe* and the tonalitic to dioritic orthogneiss of the SD.

## 2.4 Summary

The supracrustal *Blåhø Nappe* of the ND comprises dioritic orthogneiss at its base, garnet amphibolite with discontinuous layers of marble, garnet-bearing quartzofeldspathic gneiss, and hornblendite, and migmatitic aluminous gneiss. It is unclear whether the dioritic orthogneiss is a slice of Baltican basement that detached with the overlying *Blåhø Nappe* sediments from a down-going basement slab during initial thrusting, or if the slice was juxtaposed with the garnet amphibolite later. The orthogneiss compositionally resembles rocks from the SD, but the sharp contact with the overlying garnet amphibolites, amphibolite-facies mylonitic zones, and late cross-cutting pegmatite dyke, suggest this association predates amphibolite facies overprinting.

The *Blåhø Nappe* protolith previously has been described to include island-arc and deep marine sediments (*Robinson et al.* 2003), likely derived from the outboard Baltican margin where exotic oceanic terranes influenced sedimentation (*Slagstad* 2003). The combination and proportions of mafic, felsic, and carbonate bulk compositions observed in the garnet amphibolite unit support an island-arc depositional environment. The protolith may have included volcanoclastic rocks, mafic flows, dykes, sills, and possibly oceanic crust with marine carbonate and siliciclastic components. The overlying migmatitic aluminous gneiss unit protolith would likely have been dominated by deep marine shales.

The *Blåhø Nappe* experienced HP amphibolite to granulite facies peak metamorphism, which obliterated protolith and prograde metamorphic features. If higher pressures or temperatures were experienced, the mineralogical or structural evidence no longer exists. The

peak metamorphic assemblages are overprinted by later amphibolite facies assemblages. The development of the dominant foliation observed across the island, shallowly-dipping lineations, isoclinal folding, and shearing in the *Blåhø Nappe* are also associated with this amphibolite facies overprint. Basement rocks in the SD contain evidence of UHP metamorphism, but share the amphibolite facies overprint with the ND.

The ND and SD are separated by the FMSZ, a zone of boudinaged garnet amphibolite, garnet-bearing quartzofeldspathic gneiss, and retrogressed mafic eclogite hosted in felsic migmatite. This contact likely developed at amphibolite facies conditions, as indicated by the NW-dipping foliation consistent with the regional amphibolite facies fabric, recrystallized hornblende in partial melt, and retrogressed eclogite assemblages in mafic boudins. The contrasting peak metamorphic conditions, and ubiquitous evidence for partial melt and deformation in the FMSZ, imply that the northern and southern domains followed independent prograde metamorphic paths, but were juxtaposed during amphibolite facies conditions. Following this, felsic pegmatitic dykes cut both lithotectonic units, which acted as a coherent unit through later exhumation and cooling.

## CHAPTER 3

# PRESSURE AND TEMPERATURE OF METAMORPHISM

Regional metamorphism is a dynamic process, with continuously changing external conditions through a cycle (or  $P$ - $T$  path). Numerous chemical reactions, a series of textural fabrics, and the production or consumption of fluids may develop in response to these changes. The interpretation of textural and chemical changes identified in a metamorphic rock can be combined with regional geology, structural geology, and geochronology data to constrain the tectonic evolution of a study area. The focus of this chapter is to identify, document, and estimate the changes in metamorphic conditions as recorded by rocks from the *Blåhø Nappe*.  $P$ - $T$  estimates have been generated using two different methods: multi-equilibria thermobarometry, and phase equilibria pseudosection modelling. These methods are described independently in sections 3.2 and 3.3, respectively. The results are presented in sections 3.2.2 and 3.3.2, and compared in section 3.4. The significance of these results, with respect to the metamorphic history of the *Blåhø Nappe*, and their geological implications are discussed in Chapter 5.

### 3.1 Background: Thermodynamics in Metamorphic Petrology

The word “metamorphism” is derived from the Greek “metamorphosis,” which means to alter or change form. As changes in external conditions influence the thermodynamic stability of a rock beyond a previously equilibrated state, the rock must react to the newly imposed environment by altering its mineralogy. The most common external factors that impart changes to the mineralogy or mineral chemistry of a rock body are temperature

( $T$ ) and pressure ( $P$ ). Deviatoric stress and fluid migration also affect the stability or bulk composition of a rock, but do not typically imply  $P$ - $T$  changes. The following discussion, based on *Spear* (1993), reviews the fundamentals of thermodynamics that drive chemical reactions and result in rock metamorphism.

In nature, chemical reactions proceed until the system has achieved a minimum energy state. This state is referred to as thermodynamic equilibrium in metamorphic petrology. If the system, such as a rock with a given bulk composition, is subjected to new  $P$ - $T$  conditions, metamorphic reactions will proceed to bring the system to a new, re-equilibrated state of minimum energy. This is typically done by consuming unstable phases (mineral species, melt, fluids) and/or generating new stable phases, and by chemical diffusion of components (elements) within and between phases that have solid solution series. Reversible chemical reactions (such as the example given on the following page) will proceed in the direction, towards either products or reactants, with the lower Gibbs free energy ( $G$ ). To determine the reaction direction, the difference in free energy between reactants and products at specific  $P$ - $T$  conditions can be calculated with the following equation:

$$\Delta G_{rxn}^{P,T} = \Delta H_{rxn}^{o,T} + P\Delta V_{rxn}^{P,T} - T\Delta S_{rxn}^T + RT \ln(K) = 0 \text{ (at equilibrium)} \quad (3.1)$$

where  $\Delta H_{rxn}^{o,T}$  is the change in enthalpy (heat released or absorbed) of the reaction at standard  $P$  (usually 1 bar) and  $T$  of interest;  $\Delta V_{rxn}^{P,T}$  is the change in volume induced by the reaction; and  $\Delta S_{rxn}^T$  is the change in entropy (degree of atomic disorganization) of the reaction at  $T$  of interest.

The changes in  $H$ ,  $V$ , and  $S$  are determined by calculating  $\sum x_{products} - \sum x_{reactants}$  for each variable, for all phases in the reaction.  $H$  and  $S$  have a strong dependence on  $T$ , and are calculated based on the heat capacity ( $C_p$ ) of the phases involved in the reaction. If the calculated  $\Delta G_{rxn}^{P,T}$  is negative, the reaction will proceed to the right to generate more products. The reaction will proceed to the left to generate more reactants if  $\Delta G_{rxn}^{P,T}$  is positive. When  $\Delta G_{rxn}^{P,T}$  is 0, the thermodynamic stability of products is equivalent to the reactants in a reaction, indicating thermodynamic equilibrium. Equation 3.1 can be rearranged to solve for  $T$  at a given  $P$ , and vice versa.

The final term,  $RT \ln(K)$ , is included in the equation for reactions involving solid solutions.  $K$  is the equilibrium constant, which represents the change in activity ( $a$ ); the

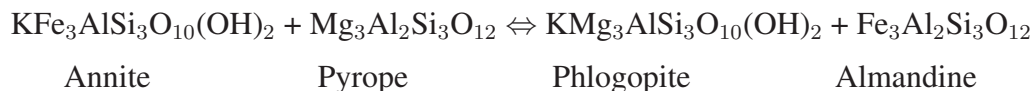
effective proportion of a component,  $i$ , in a phase that is able to react) of the components involved in the reaction. For the simplified reaction  $A + 2B \leftrightarrow C + 3D$ , where A, B, C, and D are phases with solid solution components,  $K$  is determined with the equation:

$$K = \frac{(a_i\text{C})(a_i\text{D})^3}{(a_i\text{A})(a_i\text{B})^2} \quad (3.2)$$

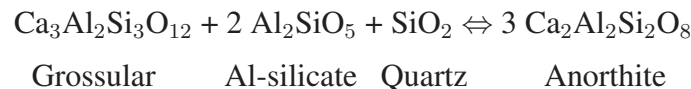
Determining the activities of components in many common silicate phases ( $a$ - $X$  relationships) is an active field of research. Non-linear  $a$ - $X$  relationships, and mixing between components within a single phase, complicate the formulation of activity expressions. Thermodynamic properties of minerals, melts, and fluids are empirically determined by experimentation, and added to thermodynamic datasets for easy integration with software programs designed to estimate  $P$ - $T$  conditions.

### 3.2 Multi-Equilibria Thermobarometry

In the past, empirical and calibrated single-reaction geothermometers and geobarometers were used to calculate independent temperature and pressure estimates, respectively (*Powell 1985; Powell and Holland 2008*). These equations require quantitative knowledge of the distribution of components (elements) between coexisting phases (minerals in equilibrium) with variation in  $P$  and/or  $T$ . For example, a commonly used geothermometer is the Fe-Mg cation exchange between biotite and garnet (*Ferry and Spear 1978*)



where, with increasing temperature, garnet becomes progressively more almandine-bearing and biotite becomes more phlogopite-bearing. The garnet-aluminosilicate-plagioclase (GASP) reaction is a common geobarometer (*Holdaway 2001; Koziol and Newton 1988*)



in which grossular is favoured at high pressure and anorthite at low pressure.

The independent nature of  $P$ - $T$  calculations for reactions that are, in fact, geochemically linked, and the limited experimental calibrations of reactions that involve increasing

numbers of end-members, has led to the development of sophisticated computer programs that use internally consistent thermodynamic datasets (*Holland and Powell* 1998, and upgrades; *Berman* 1988). The dataset of *Holland and Powell* (1998) is a compilation of experimentally determined phase equilibria, activity-composition ( $a$ - $X$ ) data, and the underlying thermodynamic properties (eg. enthalpy and entropy of formation) of mineral end-members and silicate fluids (*Powell and Holland* 2008). The data in these datasets have been adjusted or normalized, within experimental uncertainty, so the data mutually conform to all possible reactions.

To use these data for multi-equilibria thermobarometry, a program called **THERMOCALC** (*Powell and Holland* 1988) has been developed and continues to evolve with each addition of new thermodynamic data to the dataset. Compositions of phases are entered by the user into an input file, **THERMOCALC** identifies a set of *all* possible independent reactions involving the chosen phases, and calculates the associated  $P$  and  $T$  estimates for those reactions (using a more sophisticated version of Equation 3.1). **THERMOCALC** then averages the multiple estimates using a ‘least squares’ method to generate a single  $P$ - $T$  estimate. This is done in the AveragePT (or AvPT) mode.

The dataset also includes uncertainties related to thermodynamic properties and  $a$ - $X$  relationships. Empirical uncertainty values in the dataset are propagated through the pressure and temperature estimates of each independent reaction, and then through the ‘least squares’ averaging method in AvPT, resulting in a single  $P$ - $T$  uncertainty (*Powell and Holland* 1988). External to the **THERMOCALC** software and dataset, analytical uncertainty is also generated by microprobe analyses and compositional heterogeneity of the grains being analyzed. Depending on the bulk composition of the rock and the phases being considered, typical errors in  $T$  and  $P$  are about  $\pm 75$  °C and  $\pm 3$  kbar (*Spear* 1993). Uncertainties less than  $\pm 50$  °C and  $\pm 1$  kbar (at  $2\sigma$ ) should be treated with suspicion (*Powell and Holland* 2008). The largest assumption in metamorphic petrology is the inference that a mineral assemblage is in thermodynamic equilibrium. This assumption underlies the entire premise of thermobarometry, yet it is likely the greatest source of uncertainty.

### 3.2.1 Analytical Method

Estimating the  $P$  and  $T$  at a given time in a rock’s history using the multi-equilibria thermobarometry backward modelling approach of AvPT requires identification of a

group of metamorphic mineral phases that are inferred to have been in textural and/or thermodynamic equilibrium, called a mineral assemblage. This was done by petrographic assessment of textural characteristics in thin section, followed by electron microprobe (EMP) analysis, including spot analyses, chemical zoning profiles, and qualitative element distribution maps of solid solution phases, such as garnet and plagioclase.

Where chemically zoned porphyroblasts exist, the matrix assemblage is interpreted to include porphyroblast rims, plus all other mineral phases within the rock. Inclusions within a poikiloblast may be in equilibrium with the core composition, but commonly indicate the existence of a previously stable mineral assemblage. Textural equilibrium is more difficult to achieve, because it typically requires more time and energy to replace pre-existing igneous or metamorphic textures completely. However, textural equilibrium generally implies chemical equilibrium. Corona textures and incomplete replacement, or pseudomorphing of one mineral by another, indicate local disequilibrium.

Four migmatitic aluminous gneiss samples and one garnet amphibolite gneiss sample from the *Blåhø Nappe* were selected for petrographic and *P-T* investigation. They were all chosen based on clear textural evidence of high-pressure amphibolite facies to high-pressure/low-temperature granulite facies (peak) assemblages. In addition, both lithologies record overprinting of the peak assemblages by relatively lower-pressure amphibolite facies (retrograde) assemblages.

A second requirement of multi-equilibria thermobarometry is compositional data for each phase in the selected mineral assemblages. These data are used in the input file for AvPT. Because both peak and retrograde assemblages are present in each sample, minerals in both assemblages were analyzed from within a single polished section for each sample. Samples were analyzed using the JEOL 8200 electron microprobe at Dalhousie University, under standard operating conditions of 15 kV accelerating voltage and 20 nA beam current.

Petrographic descriptions, interpreted equilibrium assemblages, and mineral analysis choices for multi-equilibria thermobarometry estimates from each respective sample are presented below, along with AvPT results. Sample locations are shown in Figure 2.1 and AvPT results are compared between samples in section 3.2.2.

### **Migmatitic Aluminous Gneiss: HS10-02**

On the northwest coast of Harøya, this migmatitic aluminous gneiss unit is homogeneous at the outcrop-scale. Leucosome lenses (<8 cm thick) pinch and swell, and define



the foliation (228/52) with 20-30 cm spacings. Looking at a surface oblique to the foliation, leucosome also appears to cross-cut the foliation. Owing to the coarse-grained nature of this unit, it is difficult to determine whether there are two generations of leucosomes, or if a single generation of leucosome was deformed before the development of the regional foliation.

At the thin section-scale, HS10-02 (Figure 3.1a) has biotite-rich mesosomes with magenta garnet porphyroblasts, and coarse-grained pale green kyanite in leucosomes. Sillimanite is concentrated along leucosome-mesosome boundaries.

Garnet porphyroblasts average 5 mm in diameter, but reach up to 9 mm. Most are poikiloblastic, containing dominantly quartz inclusions with less abundant kyanite (Figure 3.1b), rutile, biotite, apatite, and zircon. These inclusions do not define an internal foliation. Exsolved rutile needles (up to 500  $\mu\text{m}$  long and 15  $\mu\text{m}$  in diameter) are oriented parallel to the host garnet faces. The garnets commonly have a nearly inclusion-free mantle and an idioblastic shape with an irregular, embayed grain boundary. Chemical maps and complementary line traverse analyses show slight zoning of major cations throughout the garnets interiors, with depletion of Grs and Prp, and enrichment of Sps and Alm at the rims (Figure 3.2). Ca in garnet diffuses at a relatively slower rate than Fe, Mg or Mn (*Carlson* 2006). Considering this, the flat Ca profile may reflect a garnet growth with a relatively constant Grs content during prograde metamorphic growth, or prolonged high temperature metamorphism. In either case, the core and mantle compositions are indistinguishable in this sample, and are collectively referred to as garnet *cores* from this point on.

Bladed kyanite porphyroblasts are inclusion-free with straight grain boundaries parallel to the c-axis, and rounded top and bottom edges. Kyanite is idioblastic in the leucosome, and typically xenoblastic, embayed, and partially pseudomorphed by sillimanite in the biotite-rich matrix (Figure 3.1c). Inclusions were observed in direct contact with garnet cores, suggesting that the two phases coexisted at an early stage of the garnet growth history.

The matrix is dominated by fine-grained biotite (<2 mm long) that defines the foliation. Also within the matrix are fine-grained sillimanite needles concentrated in groups or mats (Figure 3.1f) elongated with the biotite foliation, and fine-grained plagioclase and quartz. Rounded apatite grains, up to 1 mm long, are most commonly associated with this matrix assemblage. Matrix biotite and sillimanite deflect around the garnet porphyroblasts, while

quartz concentrates in the strain shadows.

Medium- to coarse-grained quartz and plagioclase leucosome defines the gneissic banding best observed at the outcrop scale. Where biotite in the mesosome is in contact with the leucosome, the grains are rounded and embayed. This texture suggests disequilibrium along the boundary, with biotite likely consumed in a [Gt + Liq]-producing reaction in the sillimanite field (Figure 3.1f, top left quadrant). Quartz shows substantial undulatory extinction, possibly due to leucosome recrystallization associated with later stages of amphibolite facies foliation development.

Based on textural relationships, the peak metamorphic assemblage is interpreted to include [Liq + Gt (cores) + Ky + Bt + Pl + Qz + Rt]. Garnet cores have inclusions of kyanite, biotite, quartz, and rutile indicating their co-existence prior to the late-stage porphyroblast-matrix relationships and textures. Because plagioclase was not identified as an inclusion, a plagioclase composition from the matrix had to be used in the peak metamorphic assemblage input file for AvPT calculations. With increasing metamorphic pressure, plagioclase commonly becomes more albitic in rocks with pelitic to aluminous bulk compositions, therefore the analysis with the lowest anorthite component ( $An_{32}$ ) was used. This composition still likely contains too much anorthite to represent the true plagioclase composition at the time of peak pressure, therefore AvPT results that use it are considered to represent *minimum pressure* estimates.

Likewise, because of the ease at which Fe and Mg cations exchange between biotite and garnet, biotite inclusions in contact with the host garnet have likely re-equilibrated since the peak metamorphic assemblage was established. Therefore, as a second option, a biotite composition with the highest Mg# (64) was selected for AvPT calculations of the peak assemblage (Figure 3.11). This analysis came from idioblastic, coarse-grained matrix biotite, and contributes to a *minimum* temperature estimate.

At high  $T$ , diffusion rates are high enough for relatively fast homogenization of pre-existing cation growth zoning in garnet. The homogenization of cation zoning lowers the entropy within a garnet while dampening the compositional signal of garnet that grew with prograde metamorphism, at the peak pressure, and/or the peak temperature conditions. Although Ca diffuses the slowest in garnet, relative to Mn, Mg, and Fe, the garnet core composition with the highest grossular content (14.4%) was used by the GASP geobarometer in the AvPT calculations.

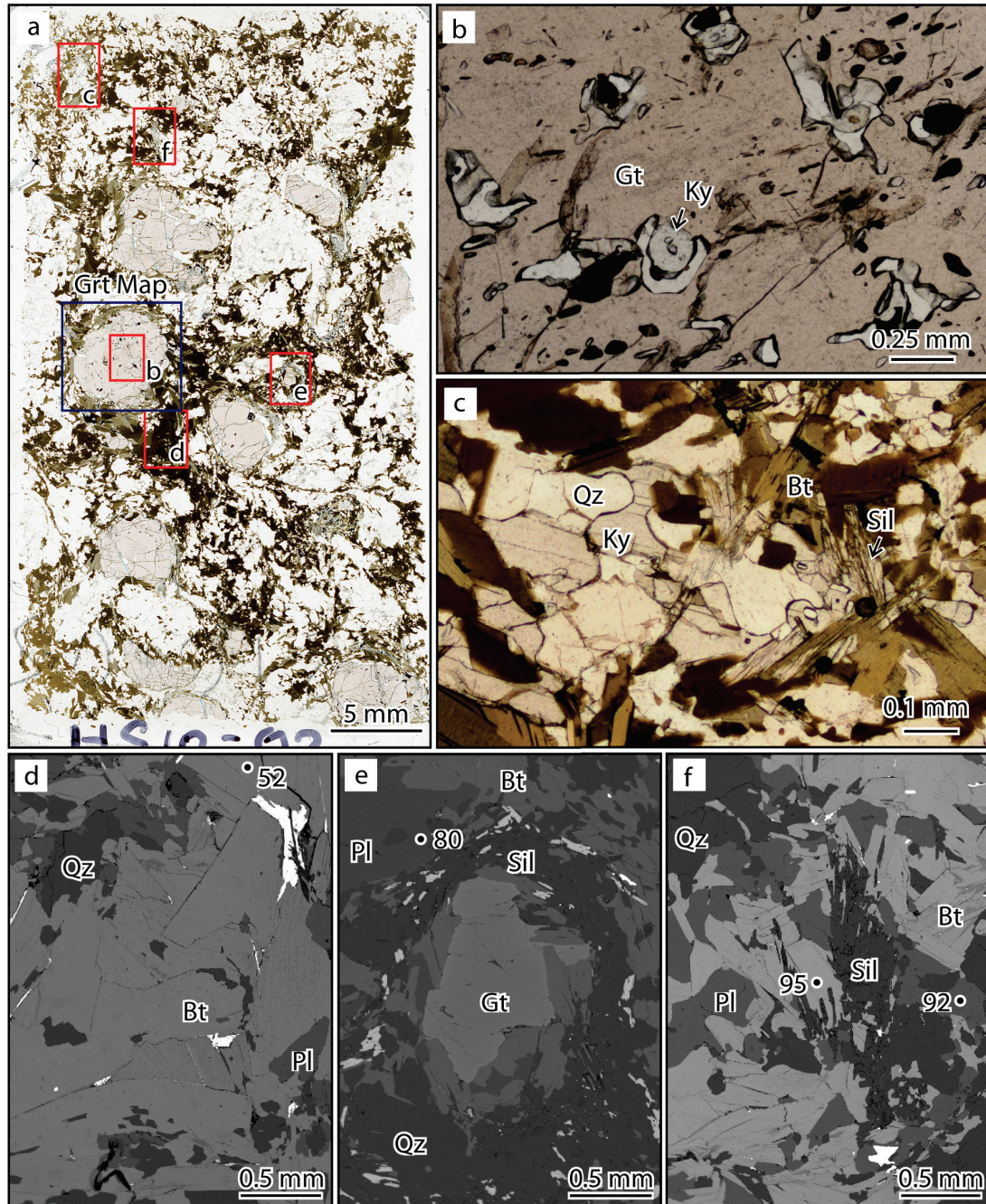


Figure 3.1: HS10-02 textures and analysis locations. Images of peak and retrograde assemblages are referenced to the polished section (a) with red boxes, while the compositional garnet map (Figure 3.2) is referenced with the blue box. Kyanite is stable in garnet cores (b, rotated 90° clockwise), and partially pseudomorphed by sillimanite in the matrix (c, rotated 90° clockwise). With re-equilibrated biotite inclusions and no plagioclase in garnet, matrix biotite (d) and plagioclase (e) compositions define minimum  $P$ - $T$  estimates for the peak assemblage. (f) The retrograde assemblage includes matrix biotite, plagioclase, and idioblastic sillimanite.

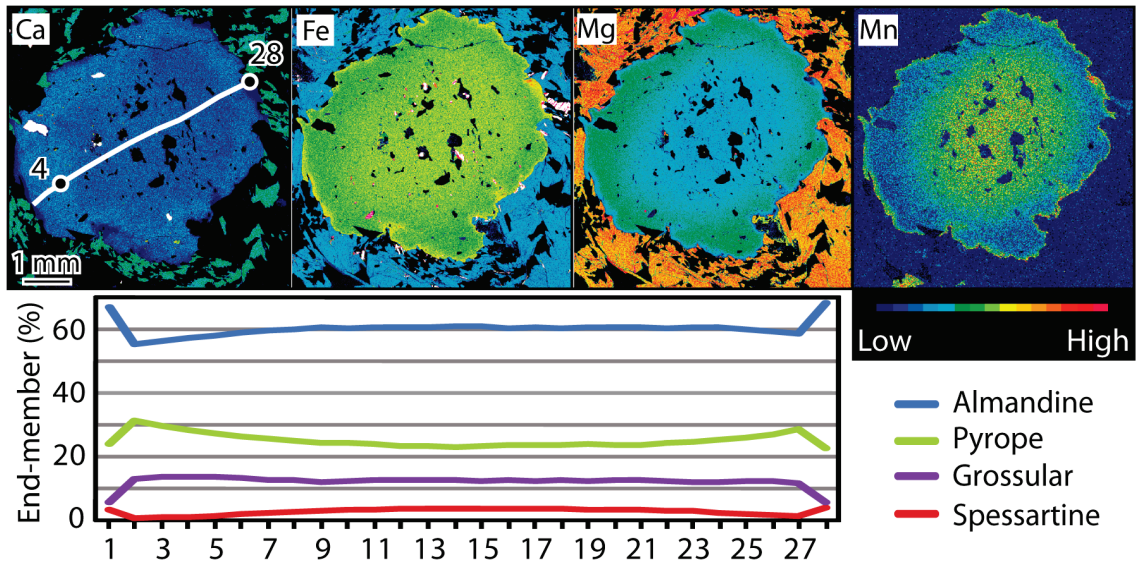


Figure 3.2: HS10-02 garnet compositional maps and line traverse. Maps are of Ca, Fe, Mg, and Mn in garnet (thin section location in Figure 3.1 a, blue box) and the x-axis of the composition plot shows analysis points spaced approximately equidistant across the 4.3 mm line traverse. Compositional zoning within the garnet core is weak, while at the garnet rim, retrograde reactions with the matrix have clearly altered the garnet chemistry. Peak and retrograde assemblage calculations used analyses 4 and 28, respectively, from the line traverse shown in the Ca map.

The interpreted retrograde assemblage that overprints the peak assemblage comprises [Gt (rims) + Sil + Bt + Pl + Qz + Rt]. Matrix plagioclase ( $An_{37}$ ) and biotite (62 Mg#, Figure 3.11) texturally associated with sillimanite were selected for retrograde AvPT estimates. A garnet rim composition with the lowest grossular content (5.7%) and highest Mg# (74) was also selected.

The chosen peak assemblage compositions yield a  $P$ - $T$  estimate (using AvPT) of  $895 \pm 176$  °C and  $15.2 \pm 3.6$  kbar. The peak estimates are poorly constrained since the chosen plagioclase and biotite compositions used in the calculations may have been affected by retrogression. In contrast, the chosen retrograde assemblage compositions yield an estimate of  $675 \pm 130$  °C and  $6.7 \pm 2.0$  kbar. These conditions likely represent the conditions of melt crystallization.

### Migmatitic Aluminous Gneiss: HS10-31

On eastern Finnøya, the the *Blåhø Nappe* has a slightly steeper foliation (265/68 to 270/75) defined by discontinuous leucosome layers, and relatively low-amplitude inclined

isoclinal folds. The fold wavelength varies from 30 to 70 m, and the contact to the underlying garnet amphibolite unit is exposed in the fold cores. HS10-31 was taken from the core of a synform with this gradational contact visible in the adjacent fold limbs. At the outcrop-scale, within the immediate sampling location, the lithology is fairly homogeneous. Similar to HS10-02, this sample contains coarse-grained garnet porphyroblasts in biotite-rich mesosome, and quartz-rich leucosome (Figure 3.3a). The discontinuous leucosome layers average <1 cm thick but swell up to 4 cm thick. Kyanite <2 mm wide is visible in the biotite-rich mesosome.

There are two garnet morphologies. The first is highly poikiloblastic, fractured, and xenomorphic. Inclusions are typically quartz, biotite, and less commonly rutile and plagioclase. Inclusions become less dense toward the rims of these garnets, and sometimes show a weak internal foliation. The second type has an atoll form with medium-grained idioblastic biotite, and xenoblastic plagioclase, quartz, and rare kyanite within the core (Figure 3.3b and d).

Garnet commonly has a thin plagioclase melt film pseudomorph between the interior grain boundary and the included phases. A melt film pseudomorph is recognised as a thin, commonly cusped, ribbon of material that separates two or more mineral grains. It represents the area in which melt had previously been present, and usually contains a felsic phase as a pseudomorph, such as plagioclase, K-feldspar, or quartz (Holness *Holness and Sawyer 2008*). Melt film pseudomorphs are observed around embayed and rounded biotite grains, suggesting biotite consumption during melting. In general, all garnets have irregular, xenomorphic grain boundaries, but a few have maintained the typical six-sided shape. Compositional zoning (Figure 3.4) is less clear in this sample than in HS10-02. Some inclusions in garnet have reacted with the host garnet, resulting in obvious compositional zoning changes similar to those at the garnet rim. Around some inclusions, the grossular content of the surrounding garnet increases, opposite to what is commonly observed at the garnet rim.

Kyanite porphyroblasts are present in the biotite-rich mesosome and as inclusions in the atoll garnets, but not in the leucosome. They are xenomorphic, and equant with some large embayments and quartz inclusions. Plagioclase melt film pseudomorphs around kyanite are typically associated with matrix quartz (Figure 3.3e).

Biotite in the matrix is fine-grained, idioblastic where concentrated, and xenoblastic

where associated with matrix plagioclase and quartz. Biotite also wraps around the garnet porphyroblasts, or exists as a thin layer directly in contact with the garnet, possibly as a product of garnet breakdown. Matrix plagioclase has polysynthetic twins, and is chemically zoned with An<sub>28</sub> in the cores and An<sub>32</sub> at the rims. Sillimanite is rare in the matrix, always in contact with kyanite (Figure 3.3c), and therefore is inferred to have formed at the expense of kyanite. Rutile is observed as <0.5 mm prismatic inclusions in garnet and as fine- to medium-grained xenoblastic crystals in the matrix, and is commonly associated with opaque minerals such as sulphides and ilmenite.

A 1 cm wide quartz vein runs through this particular hand sample parallel to the dominant foliation. Alteration of the host rock along the vein walls includes fracturing of garnet, crystallization of muscovite and calcite, and sericitization of plagioclase. The vein fluid has penetrated a few centimetres into the host rock via microfractures, altering the host mineralogy adjacent to the vein. Calcite, muscovite, and rare chlorite have replaced some garnet inclusions and matrix minerals. The textures and mineral phases associated with the vein are not part of the equilibrium assemblages, and therefore do not warrant further investigation with respect to AvPT estimates.

The interpreted peak mineral assemblage in this rock is the same as in the previously described sample: [Liq + Grt (cores) + Ky + Bt + Pl + Qz + Ru]. With this sample however, all matrix phases are also present as inclusions in garnet or within the cores of atoll garnets. Unfortunately, plagioclase inclusions were only observed in the *thin* section rather than the *polished* section, so an alternative, low-anorthite (An<sub>28</sub>) matrix composition was used to estimate the peak conditions. Biotite (73 Mg#; Figure 3.11) from an atoll garnet with kyanite inclusions was analyzed for the peak assemblage. The garnet with the highest grossular content (13%) from a line traverse (Figure 3.4) was also used.

The interpreted retrograde assemblage comprises [Grt (rims) + Sil + Bt + Qz + Pl (rims and thin films) + Ru]. A low-grossular (7%) garnet rim analysis from a line traverse was used in the estimate calculations. The biotite (67 Mg#; Figure 3.11) and plagioclase melt film pseudomorph (An<sub>39</sub>) compositions associated with embayed kyanite were also used in the calculations.

Estimates of  $902 \pm 163$  °C and  $16.1 \pm 3.6$  kbar were obtained from the chosen peak assemblage compositions. Because a *matrix* plagioclase core composition was used in the peak *P-T* estimate, it is possible that it does not represent the composition of plagioclase

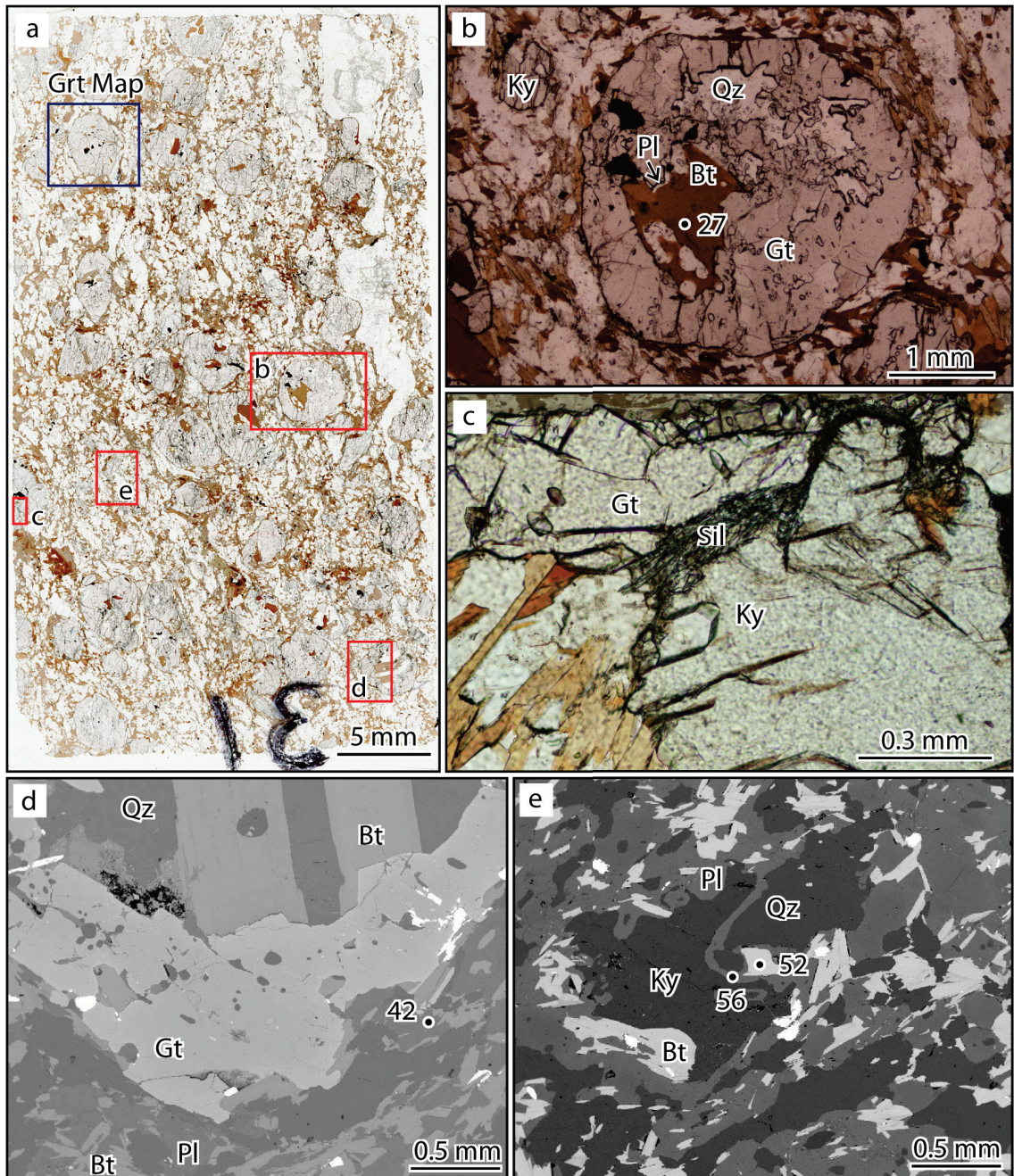


Figure 3.3: HS10-31 textures and analysis locations. Images of peak and retrograde assemblages from the polished section (a) are referenced with red boxes, while the compositional garnet map (Figure 3.4) is referenced with the blue box. Rounded, poikilblastic garnet preserves coarse biotite and plagioclase melt film pseudomorphs (b). Kyanite is associated with matrix sillimanite (c, rotated 90° clockwise). Matrix plagioclase was used in the peak assemblage (d, rotated 90° clockwise). Matrix biotite and associated plagioclase melt film pseudomorph compositions (e) are included in the retrograde assemblage.

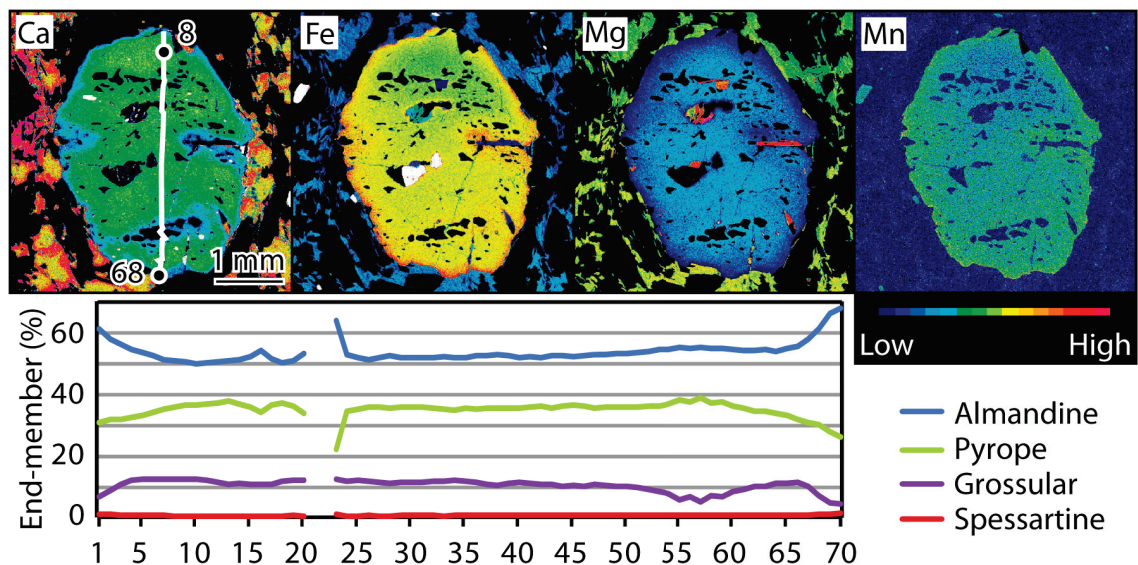


Figure 3.4: HS10-31 garnet compositional maps and line traverse. Maps are of Ca, Fe, Mg, and Mn in garnet (thin section location in Figure 3.1 a, blue box), and the x-axis of the composition plot shows analysis points spaced approximately equidistant across the 3.5 mm traverse. The garnet core does not have obvious compositional zoning, except near some inclusions, where alteration is similar to the retrograde rim pattern for almandine and pyrope components. Grossular behaves differently around different inclusions, sometimes increasing rather than decreasing as commonly observed at the garnet rim. Peak and retrograde assemblage calculations used analyses 8 and 68, respectively, from the line traverse shown in the Ca map.

at the peak conditions. Therefore, this  $P$ - $T$  estimate is poorly constrained. The chosen retrograde assemblage compositions yield a  $P$ - $T$  estimate of  $751 \pm 140$  °C and  $9.2 \pm 2.3$  kbar. The retrograde assemblage likely represents the conditions at or below melt phase crystallization, because plagioclase melt film pseudomorphs and associated matrix biotite compositions were used in the estimation. This temperature is certainly within the ‘normal range’ of partial melt crystallization conditions, albeit on the high-temperature side. This typically suggests some early melt has been lost from the system, leaving a slightly more refractory, residual bulk composition that melts (and crystallizes) at higher temperatures.

### Migmatitic Aluminous Gneiss: HS10-32

This aluminous gneiss is unique compared to the rest of the unit, because it is within a 10-15 m-wide shear zone. Coarse-grained garnet, kyanite, quartz, and feldspar porphyroclasts are set in a very fine-grained, homogeneous, biotite-rich matrix (Figure 3.5a). The foliation is congruent with the regional trend.



Magenta, poikiloblastic garnets are 1-5 mm in diameter, xenomorphic, and highly fractured (Figure 3.6). Most grains are rounded, but some are angular or are slightly elongate parallel to the shear foliation. Inclusions of quartz, biotite, plagioclase, and rutile do not clearly define an internal foliation. One garnet in thin section has the atoll morphology described in the previous sample, and several more can be seen in a cut surface on the hand sample. Biotite and plagioclase are visible within the atoll cores (Figure 3.5c).

Kyanite is elongate, up to 2 mm long with rounded ends. The grains are imbricated with the shear foliation. Some grains are poikiloblastic with quartz and biotite inclusions (Figure 3.5b).

In the matrix, biotite, plagioclase and quartz are equigranular (Figure 3.5f). The latter two phases are granoblastic with triple junction grain boundaries. Coarse quartz- and feldspar-bearing porphyroclasts, possibly formerly leucosome phases, also show granoblastic subgrain boundaries. This suggests high-temperature annealing of quartz and feldspar prior to or during shearing. The presence of matrix sillimanite aligned with the shear foliation corroborates the suggestion of high temperatures during shearing. Idioblastic biotite forms weak strain shadows around garnet and kyanite porphyroclasts, and is likely the product of garnet breakdown reactions (Figures 3.5d and e).

The interpreted peak metamorphic assemblage is the same as in the previously described samples: [Liq + Grt (cores) + Ky + Bt + Pl + Qz + Ru]. Garnet with the highest grossular (10%) component, biotite (73 Mg#; Figure 3.11) included in garnet but shielded by quartz, and plagioclase (An<sub>13</sub>) included in garnet were used in the *P-T* estimate calculations.

The interpreted retrograde assemblage is also the same as the previously described samples, comprising [Grt (rims) + Sil + Bt + Pl + Qz + Ru]. A garnet rim composition (Grs 7.5%), matrix plagioclase (An<sub>28</sub>) associated with sillimanite, and matrix biotite (62 Mg#; Figure 3.11) along the boundary of a garnet porphyroclast were used in the AvPT calculations.

The chosen peak assemblage compositions estimate condition of  $830 \pm 147$  °C and  $16.5 \pm 3.6$  kbar. It is possible that these estimates are minimum values. The retrograde assemblage compositions yield an estimate of  $658 \pm 99$  °C and  $9.1 \pm 2.3$  kbar. The retrograde estimate is interpreted as the conditions of melt-phase crystallization and

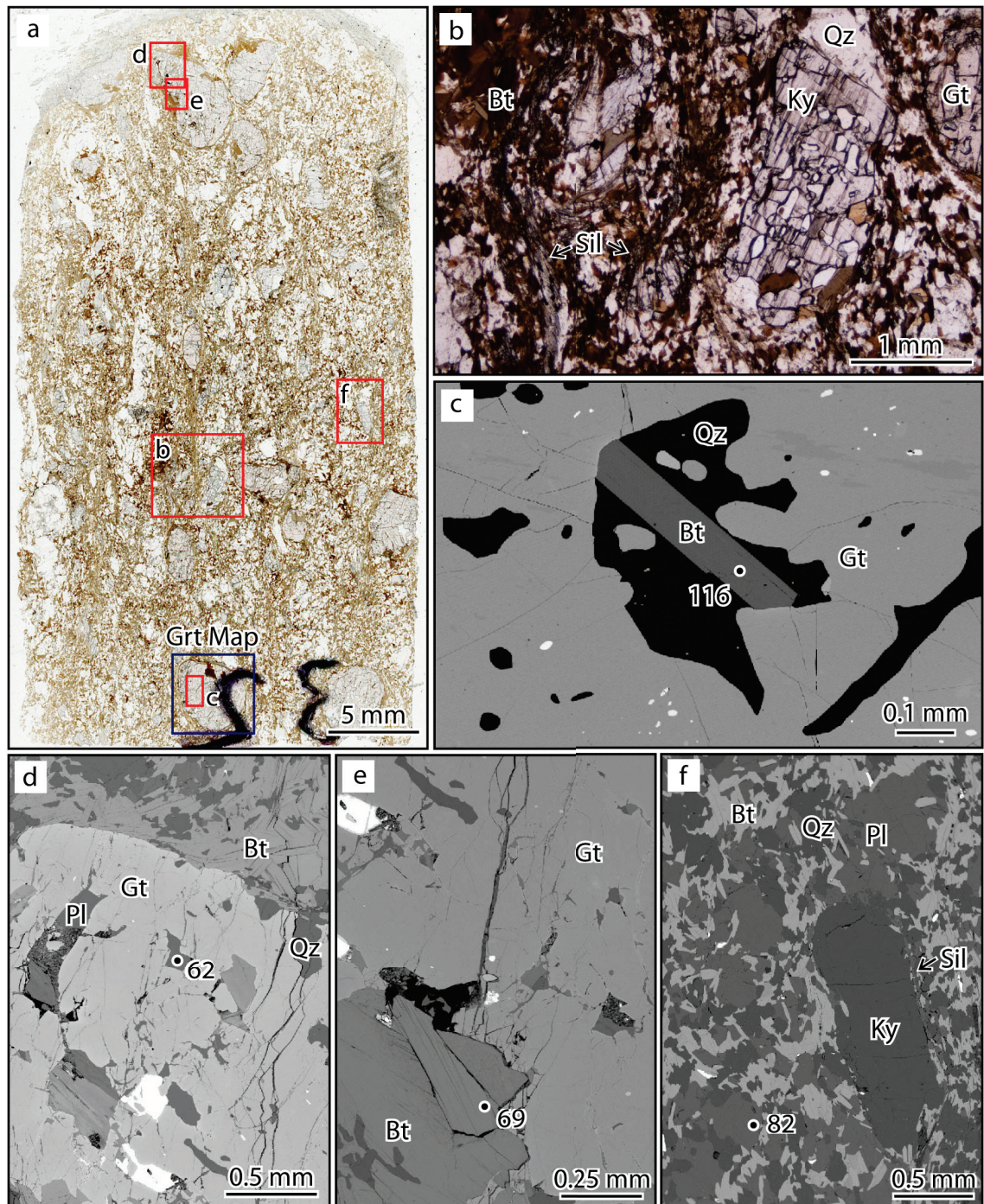


Figure 3.5: HS10-32 textures and analysis locations. Images of peak and retrograde assemblages from the polished section (a) are referenced with red boxes, while the compositional garnet map (Figure 3.6) is referenced with a blue box. Embayed kyanite in the matrix (b) is in disequilibrium with the retrograde assemblage that includes sillimanite, biotite (e) and plagioclase (f). Fractured garnet preserves included biotite (c, rotated 90° clockwise) and plagioclase (d) compositions of the peak assemblage.

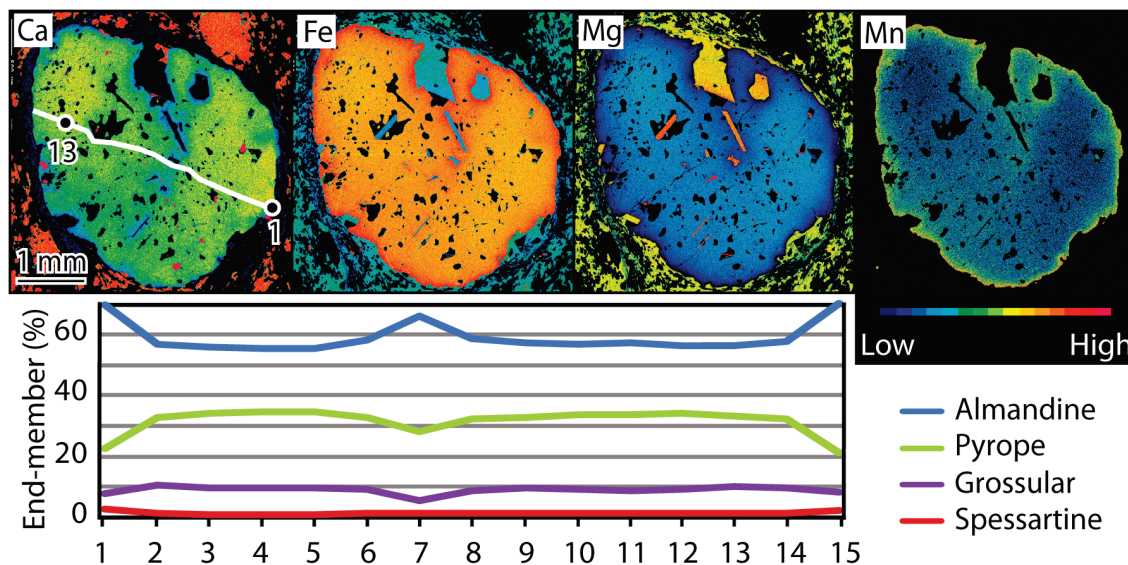


Figure 3.6: HS10-32 garnet compositional maps and line traverse. Maps are of Ca, Fe, Mg, and Mn in a xenomorphic garnet (thin section location in Figure 3.5 a, blue box), and the x-axis of the composition plot shows analysis points spaced approximately equidistant across the 4.3 mm transect. The core composition is only observed where minimal inclusions exist. Some inclusions have reacted with the host garnet resulting in a pattern similar to the retrograde rim. Peak and retrograde assemblage calculations used analyses 13 and 1, respectively, from the line traverse shown in the Ca map.

final recrystallization of matrix phases during or after shearing. The times of the peak metamorphism and amphibolite facies overprint in this sample have been constrained with monazite dating, discussed in Chapter 4.

### Migmatitic Aluminous Gneiss: HS10-35

This sample was collected from the southwestern limit of the migmatitic aluminous gneiss unit on Harøya. This unit is exposed in a 3 m wide synform that plunges  $55 \rightarrow 270^\circ$ , and is underlain by the garnet amphibolite unit which has a pervasive foliation of  $210/60$  and surrounds the outcrop on all accessible sides. In thin section (Figure 3.7a), this sample displays beautiful examples of all the previously described textures (except for shear fabrics). Garnet (Figures 3.8 and 3.9) and kyanite porphyroblasts are set in a fine- to medium-grained biotite matrix with a weak and irregularly banded gneissic foliation.

The 4-10 mm wide garnet porphyroblasts in this sample have spectacular atoll structures (Figure 3.7b) with peninsulas and islands at the cores. Included core phases are  $Qz \pm Pl \pm Bt \pm Ky \pm Ru \pm Ap$  (Figure 3.7d and e). In some grains, a thin plagioclase melt film

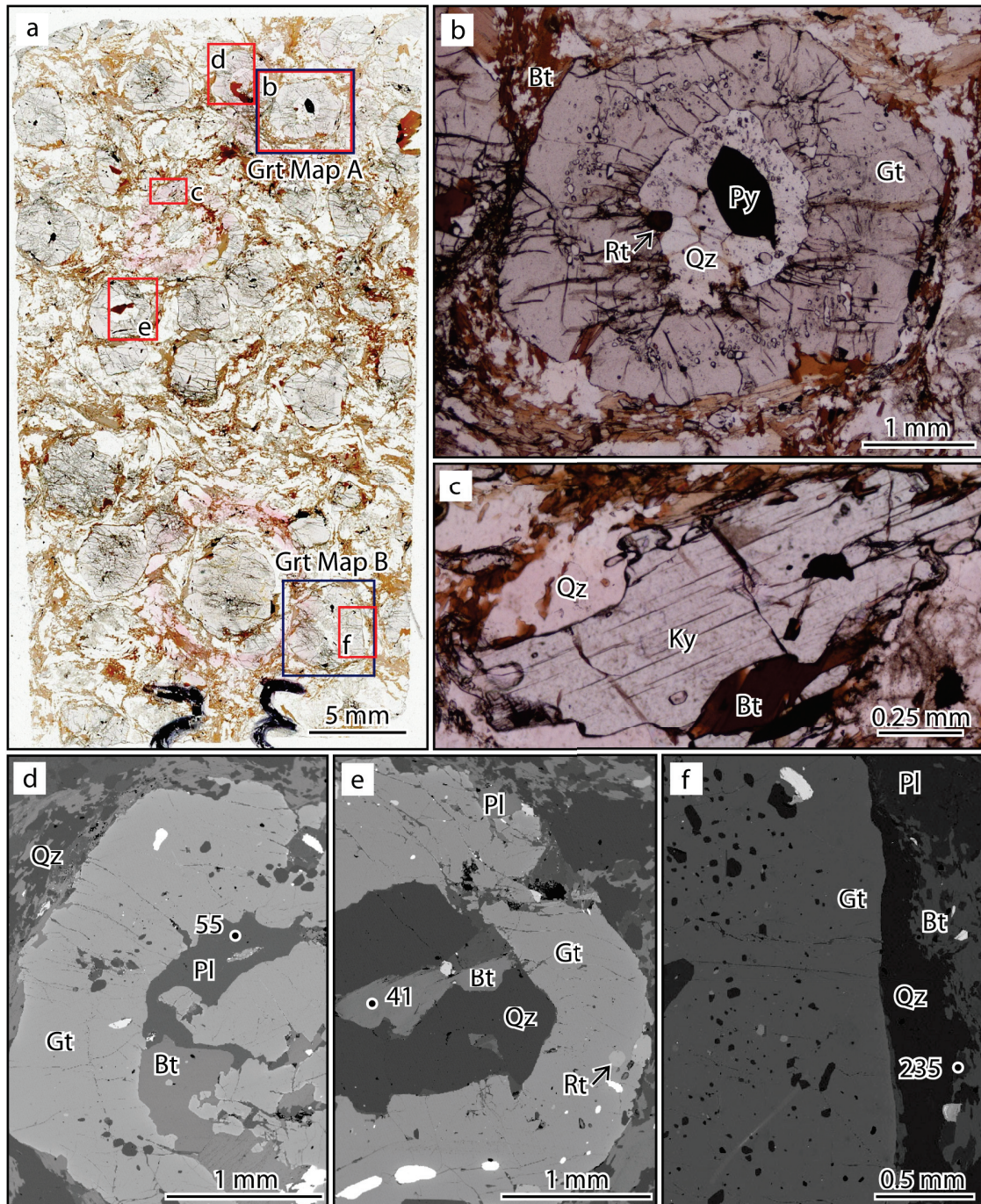


Figure 3.7: HS10-35 textures and analysis locations. Images of peak and retrograde assemblages from the polished section (a) are referenced with red boxes, while the compositional garnet maps (Figures 3.8 and 3.9) are referenced with blue boxes. Quartz in atoll garnets (b) has triple junction grain boundaries. The peak assemblage includes kyanite (c, embayed and in disequilibrium with the matrix), and plagioclase (d) and biotite (e) inclusions in garnet. A matrix plagioclase composition (f) is used in the retrograde assemblage  $P$ - $T$  estimate.

pseudomorph has crystallized between the included phases, but it is unclear whether the atoll garnets grew under melt-stable conditions (peritectic), or if the rock was subjected to melting after the garnets formed. A ring of primarily quartz inclusions is observed between the atoll core and a nearly inclusion-free rim. Most grains have retained the six-sided garnet shape, but have irregular grain boundaries, likely due to garnet breakdown reactions during decompression and cooling. Other grains are extremely xenomorphic, fractured, and poikiloblastic.

Remnants of fine-grained kyanite are embayed particularly in the matrix (Figure 3.7c). Grains shielded within atoll garnets are subidioblastic and up to 1 mm long, although only observed in *thin* section rather than *polished* section. The matrix foliation is defined in part by fine-grained sillimanite, suggesting relatively lower pressures during development of the pervasive matrix foliation.

Biotite in the matrix is fine-grained (<1 mm long), idioblastic, and wraps around garnet porphyroblasts (Figure 3.7f; Figure 3.8) with fine-grained matrix plagioclase and

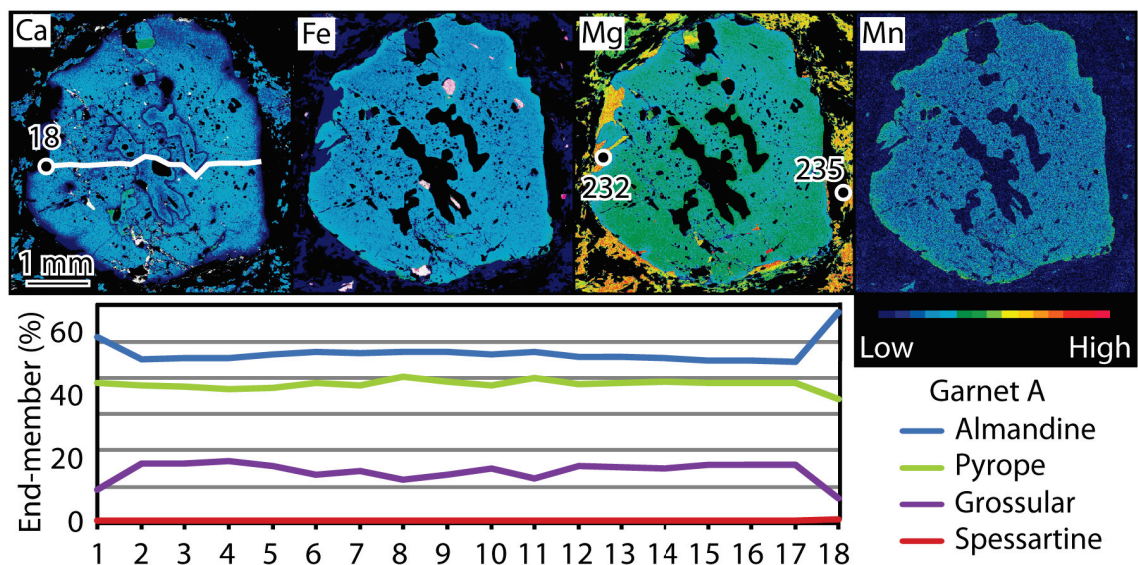


Figure 3.8: HS10-35 garnet A compositional maps and line traverse. Maps are for Ca, Fe, Mg, and Mn in garnet A (thin section location in Figure 3.7 a, blue box), and the x-axis of the compositional plot shows analysis points spaced approximately equidistant across the 3.2 mm traverse. Changes in the core compositions are influenced by plagioclase inclusions. The retrograde assemblage calculations used analysis 18 from the line traverse shown in the Ca map, and 232 and 235 for matrix biotite and plagioclase compositions, respectively.

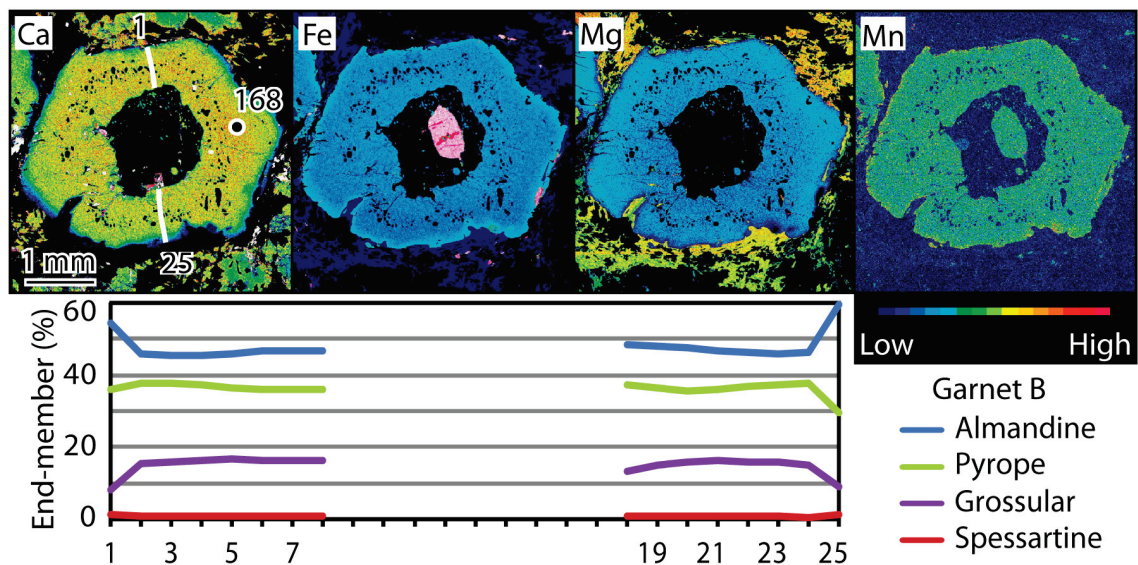


Figure 3.9: HS10-35 garnet B compositional maps and line traverse. Maps for Ca, Fe, Mg, and Mn in garnet B (thin section location in Figure 3.7 a, blue box), a remarkable atoll garnet, and the x-axis of the compositional plot shows analysis points spaced approximately equidistant across the 2.6 mm transect. There is minimal influence from the core phases (dominantly quartz, and pyrite, the pink coloured phase in the Fe map) on the interior garnet rim. Retrogression is observed at the garnet rim. The peak assemblage calculations used analysis 168 from the line traverse shown in the Ca map.

quartz in the pressure shadows. Since the biotite deflects around the coarse-grained garnet porphyroblasts, a matrix foliation is difficult to discern. Plagioclase and quartz have irregular but rounded boundaries and, in some cases, triple junctions.

The interpreted peak and retrograde mineral assemblages are the same as those described from the previous three samples: [Liq + Grt (cores) + Ky + Bt + Pl + Qz + Ru], and [Grt (rims) + Sil + Bt + Pl + Qz + Ru], respectively. Compositions used in AvPT modelling of the peak assemblage include a garnet core with 13% grossular component (Figure 3.9), plagioclase (An<sub>27</sub>) included in garnet, and biotite included in garnet (75 Mg#; Figure 3.11). The retrograde assemblage (Figure 3.8) used a garnet rim composition with 7% grossular component, an adjacent matrix biotite (78 Mg#; Figure 3.11), and matrix plagioclase (An<sub>29</sub>).

The peak mineral assemblage yielded a  $P$ - $T$  estimate of  $868 \pm 117$  °C and  $16.3 \pm 3.4$  kbar. It is possible that the peak assemblage has undergone post-peak re-equilibration

(such as homogenization of garnet zoning) with sustained high temperatures during decompression, making this a minimum estimate. The retrograde assemblage compositions yielded a  $P$ - $T$  estimate of  $661 \pm 99$  and  $8.9 \pm 2.0$  kbar. These conditions are interpreted to represent the final crystallization of melt in the system, and cessation of intergranular cation diffusion in the matrix and porphyroblast phases. Following this, a minor amount of fluid infiltrated the host rock, locally altering small areas in the matrix to muscovite and calcite.

### **Garnet Amphibolite Gneiss: HS10-16**

Since the migmatitic aluminous gneisses show post-peak re-equilibration that may have affected  $P$ - $T$  estimates, multi-equilibria thermobarometry was tested on one sample from the garnet amphibolite unit of the *Blåhø Nappe*. Sample HS10-16 (Figure 2.1) contains considerably less garnet (<10%) compared to other amphibolite samples from within this unit, but the presence of 15 modal % clinopyroxene in this mafic rock suggests possible high-pressure metamorphism. The sampled outcrop maintains the pervasive NW-dipping foliation (190/60). The sample comprises Cpx + Grt + Amp + Pl + Scp + Ttn with minor Ap + Cb + Ru + Qz + Bt  $\pm$  Mu (Figure 3.10a).

Clinopyroxene is fine-grained (0.5 mm), xenoblastic and typically partially altered to amphibole. It is also commonly associated with scapolite, plagioclase, and apatite, and is never observed in contact with garnet (Figure 3.10d). Based on microprobe analyses (Table 3.2), this is a calcic clinopyroxene with Di<sub>78</sub>Hd<sub>22</sub> end-member components, with minor substitution of Al, Fe<sup>3+</sup>, Mn, and Na.

Garnet is not in textural equilibrium with the surrounding matrix amphibole, plagioclase and scapolite. Fine-grained symplectite intergrowths of those three phases pseudomorph the pre-existing garnet up to its current grain boundary. Based on the symplectite area, greater than 50% of the garnet volume has reacted to form these symplectite phases. At the micron-scale, garnet edges are serrated, with concavities adjacent to reaction products (amphibole, scapolite, and plagioclase), and points adjacent to the intergranular boundaries of those reaction products (Figure 3.10c). What remains of the garnet is fine-grained (<0.8 mm in the analyzed section, but up to 1.5 mm in the hand sample) with few idioblastic rutile needles as inclusions. Some rutile inclusions display knee-shaped twins. Plagioclase inclusions are rare. Garnet chemical maps (Figure 3.10b) show <1% molar fraction change in end-member composition from core to rim, aside from the

<10  $\mu\text{m}$  wide rim adjacent to symplectite. These garnets have the average composition  $\text{Alm}_{39}\text{Prp}_{30}\text{Grs}_{29}\text{Sps}_{1.5}\text{Adr}_{<2}$ .

Recrystallized amphibole, 0.5-2 mm across, has remnant idioblastic boundaries and well developed 60/120° cleavage where it is not embayed or intergrown with plagioclase and scapolite. Amphibole is 0.01-0.1 mm wide where associated with clinopyroxene breakdown or in symplectites with plagioclase and/or scapolite after garnet (Figure 3.10c). Amphibole compositions (named according to Probe-AMPH; Tindle and Webb, 1994) are typically between ferropargasite  $[\text{NaCa}_2(\text{Mg},\text{Fe}^{2+})_4\text{Al}(\text{Si}_6\text{Al}_2)\text{O}_{22}(\text{OH})_2]$  and tschermakite  $[\text{Ca}_2(\text{Mg},\text{Fe}^{2+})_3\text{AlFe}^{3+}(\text{Si}_6\text{Al}_2)\text{O}_{22}(\text{OH})_2]$ . A more pargasitic composition dominates amphibole closely associated with the garnet symplectite intergrowths, while a composition closer to tschermakite is observed where amphibole is associated with matrix plagioclase and scapolite (Table 3.2). There is <0.6 a.p.f.u. Na in the analyzed grains.

Plagioclase is dominantly a matrix phase, although it is present as rare inclusions in garnet. Albite polysynthetic twinning is very common in the matrix plagioclase, which ranges in size from 0.1-0.5 mm. The plagioclase chemistry is quite variable, ranging from  $\text{An}_{33-43}$  in matrix grains, to  $\text{An}_{24}$  in one particular analysis from a 50  $\mu\text{m}$  wide plagioclase-filled crack in garnet. The single analyzed inclusion in garnet is  $\text{An}_{38}$ .

Scapolite is surprisingly coarse-grained (up to 1 cm across), and poikiloblastic with many amphibole, clinopyroxene, and titanite inclusions (Figure 3.10e). Some of these grains have a medium-grained feathery texture with zones of slight undulatory extinction between the subgrains. Fine-grained scapolite is associated with garnet breakdown and symplectite textures. The composition is  $\text{Mei}_{95-89}$   $[\text{Ca}_4\text{Al}_6\text{Si}_6\text{O}_{24}\text{CO}_3]$  end-member (with the remainder being  $\text{Mar}_{11-5}$   $[\text{Na}_4\text{Al}_3\text{Si}_9\text{O}_{24}\text{Cl}]$ ) in garnet symplectite associations, and  $\text{Mei}_{76-79}$  in the matrix when associated with pyroxene, hornblende, and plagioclase.

Titanite is xenoblastic, and up to 1 mm across. Quartz is observed in the matrix associated with plagioclase, but is quite rare. Apatite is up to 50  $\mu\text{m}$  across, and xenoblastic with small embayments. Muscovite and biotite form fine-grained, rare reaction products after plagioclase and hornblende, respectively, typically associated with minor amounts of carbonate.

At peak pressure and/or temperature conditions, the assemblage  $[\text{Cpx} + \text{Grt} + \text{Pl} + \text{Ru} + \text{Ttn}]$  was likely stable. This sample experienced high-temperature metamorphism, reducing any prograde growth zoning in garnet to a flat, homogeneous profile. Considering



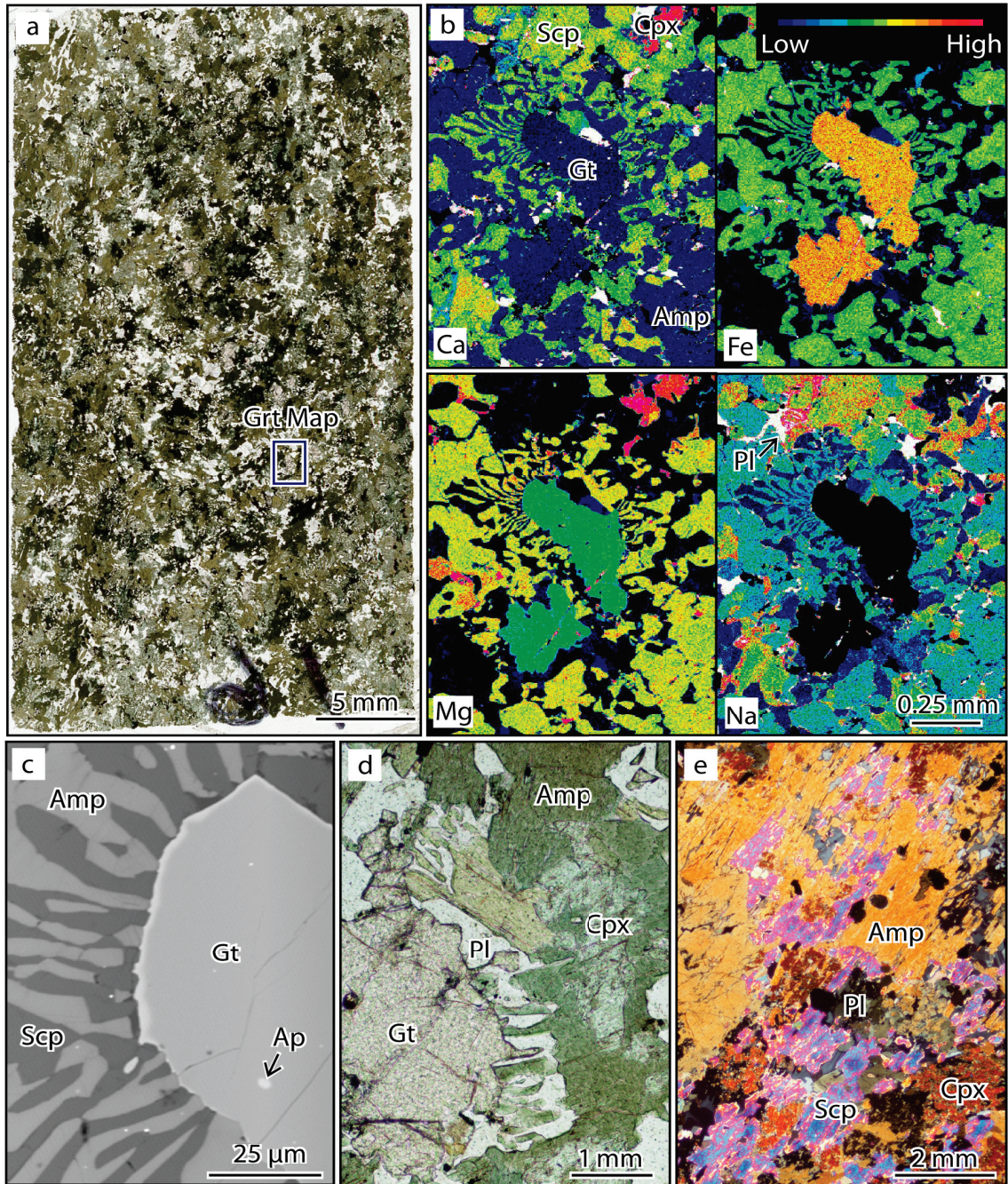


Figure 3.10: HS10-16 textures and chemical garnet maps. The garnet map (b) is referenced in the polished section (a) with the blue box. Garnets involved in symplectite reactions have a serrated grain boundary (c; northwest garnet grain boundary from maps in b); peaks are coincident with intergranular boundaries of the reaction products (amphibole and scapolite in this case). Garnet and clinopyroxene are never in contact (d, thin section), but always separated by amphibole, scapolite, or plagioclase. Scapolite (e, thin section cross polarized light) has high birefringence, suggesting a high meionite component, and has crystallized to envelope clinopyroxene, amphibole, and other minor phases.

the textural relationships of Scp + Cb throughout the unit, CO<sub>2</sub>-bearing fluids infiltrated the rock subsequent to peak metamorphism, contributing to the development of amphibolite-facies symplectites. The source of the fluid has not yet been determined, but may be related to late pegmatite dykes that cross cut most basement and supracrustal units on both Harøya and Finnøya.

This sample contains textural evidence of extensive disequilibrium, and is therefore unlikely to preserve peak assemblage compositions. Attempts to estimate peak metamorphic temperature and pressure conditions using AvPT gave illogical and unreasonable results. Garnet, clinopyroxene, plagioclase, and amphibole compositions were selected for the input file, with quartz and rutile as pure phases. Resulting temperature estimates ranged from 966 °C to 1211 °C, with and without textural context being considered when choosing mineral composition combinations for the input files. Pressures ranged from 15 to 18.6 kbar.

For example, mineral compositions that are inferred to have been in equilibrium at peak conditions yielded a peak *P-T* estimate of  $15 \pm 3.9$  kbar and  $1057 \pm 290$  °C. The input file included a diopside core, garnet core (Pyr<sub>29</sub>Alm<sub>40</sub>GrS<sub>30</sub>Spss<sub>1</sub>), plagioclase (An<sub>38</sub>) included in garnet, and idioblastic hornblende associated with pyroxene (rather than symplectite around garnet or matrix scapolite). Not only is the temperature estimate inconsistent with the estimates from the aluminous gneisses, but the errors are at least  $\pm 25\%$  of the calculated estimate. Additionally, this lithology is not migmatitic, nor was evidence of partial melting found at the outcrop or thin section scale. A mafic rock that had experienced metamorphism at  $>1000$  °C would most likely contain evidence of partial melting.

These results suggest that the peak temperature and pressure were likely high, but given the obvious evidence for compositional and textural disequilibrium, this garnet amphibolite sample does not provide a reliable constraint on the peak metamorphic conditions of the *Blåhø Nappe*. AvPT estimates from the previously discussed aluminous samples, and the following pseudosection description (section 3.3.2) further invalidate the results yielded from HS10-16. A mafic sample with little to no post-peak fluid infiltration would make a better thermobarometry candidate, however all the samples taken from this unit display evidence of at least minor textural disequilibrium.

### 3.2.2 Average *P-T* Summary

The four migmatitic aluminous gneiss samples have the same peak and retrograde assemblages. Using **THERMOCALC** in AvPT mode (*Powell and Holland 1988*), the chosen assemblage compositions yield peak and retrograde *P-T* estimates ranging from 830 °C to 900 °C and 15.2 kbar to 16.5 kbar, and 650 °C to 750 °C and 6.7 kbar to 9.2 kbar (Figure 3.12). A garnet amphibolite sample was also analyzed, but due to textural and compositional disequilibrium, it did not yield reliable *P-T* estimates.

In all of the aluminous samples, garnet core compositions with the highest grossular content (10-14.4%) were chosen for the AvPT calculations. With increasing pressure, garnet may grow with an increasing grossular component, depending on the *P-T* path trajectory. The anorthite component of plagioclase in equilibrium simultaneously decreases, according to the GASP reaction (*Holdaway 2001; Koziol and Newton 1988*). It is likely that garnet in these samples has undergone diffusion after experiencing peak pressures due to the relatively high temperatures sustained through peak temperature and retrograde conditions. However, Ca in garnet diffuses at a much slower rate than Fe, Mg, or Mn, so the M1 *P-T* estimates may represent a near-peak metamorphic pressure, in addition to peak metamorphic temperature. Plagioclase with a relatively low-anorthite composition, as would be expected at peak pressure conditions, is rare in three of the analyzed samples, and non-existent in HS10-02. This makes constraining the peak pressure conditions from the aluminous samples more difficult. A second lithology that is typically able to record and preserve high-pressure conditions (ie, the clinopyroxene-bearing garnet amphibolite sample) is commonly analyzed in a case like this. Unfortunately, the mafic samples taken from the study area have compromised peak assemblage compositions due to partial re-equilibration at amphibolite facies conditions.

The peak *P-T* estimates are more useful for constraining the peak temperature rather than pressure conditions experienced by the *Blåhø Nappe*. Peak assemblages from samples HS10-32 and HS10-35 include biotite from within atoll garnets that were almost completely shielded from direct contact with the interior garnet grain boundary. With increasing temperature, the Ti and Mg content increase in biotite (*Henry and Guidotti 2002*, and references therein). Therefore, compositions of biotite inclusions from other M1 phases (e.g. garnet core, kyanite) with a high Ti content and Mg# (~73-75) were selected for M1 *P-T* estimates (Figure 3.11). Compositions of matrix biotite associated with other

retrograde phases (e.g. sillimanite) typically had lower Ti contents and Mg# (~62-67). These compositional differences confirm that the biotite preserved and shielded within atoll garnets (HS10-31, HS10-32) is probably from an earlier, higher temperature assemblage than that of the matrix (e.g. *Kohn 2003; Ferry and Spear 1978*). The biotite included in garnet in HS10-35 has a relatively low Mg#, possibly due to late compositional diffusion. Despite the protection of this inclusion by surrounding quartz, infiltration of partial melt or late fluids can still penetrate and affect the biotite chemistry. It is important to remember that textures observed in thin section are only 2-D cuts through 3-D objects, and therefore, that some features, such as large cavities or embayments in porphyroblasts may not be well represented.

The retrograde assemblage compositions from the aluminous samples should theoretically represent the final conditions at which cation exchange and diffusional processes ceased during cooling. Retrograde rim analyses, from targeted Ca-poor areas identified on the qualitative element maps, represent the only garnet composition in equilibrium with the matrix phases and their compositions. Analyses of garnet rims have Grs<sub>5.7-7.5</sub> component, considerably lower than the peak assemblage core compositions.

The melt phase present in the peak assemblage is also assumed to have crystallized at, or before, the estimated retrograde conditions. Melt film pseudomorphs around remnant embayed kyanite porphyroblasts in the matrix suggest kyanite was partially consumed by the melt before the melt began to crystallize. Sillimanite appears texturally equilibrated with the matrix biotite, helping to define the foliation in most cases. However, the retrograde *P-T* estimates (except for HS10-02) plot in the kyanite field, while only the error bars overlap with the sillimanite field. This discrepancy suggests that the retrograde *P-T* paths for these samples crossed into sillimanite-stable conditions while decompressing, and then crossed back into kyanite-stable conditions with subsequent cooling. Alternatively, it is possible that the lowest-Ca garnet rim was not exactly pinpointed during microprobe analyses, since rim compositions are generally gradational, and a buffer of ~10 μm within grain boundaries was allowed. The *P-T* paths and potential influence on the mineralogy and mineral chemistry of these samples will be discussed further in section 3.3.2.

In general, using AveragePT multi-equilibria thermobarometry (*Powell and Holland 1988*) to constrain the peak pressure and temperature conditions experienced by the *Blåhø Nappe* is useful for making first-order estimates. Unfortunately, the associated uncertainties

are relatively large (up to  $\pm 20\%$  for  $P$  and/or  $T$  estimates), and higher than required to reconstruct a well-defined  $PTt$  path for the *Blåhø Nappe*. Such errors limit the ability to constrain interpretations on tectonic conditions and processes experienced by these samples. The nature of this study requires a more refined and informative estimate of peak and retrograde conditions for comparison with other lithotectonic units (such as the Baltican basement) and other studied examples of the *Blåhø Nappe*.

Despite the imprecise  $P$ - $T$  constraints offered by the multi-equilibria thermobarometry method for these samples, the results are useful as guides for initial construction of pseudosection models. Phase equilibria pseudosection modelling is more time consuming and requires more quantitative analytical input, but is the best way to get the most information out of a sample. This was the next application attempted on these rocks.

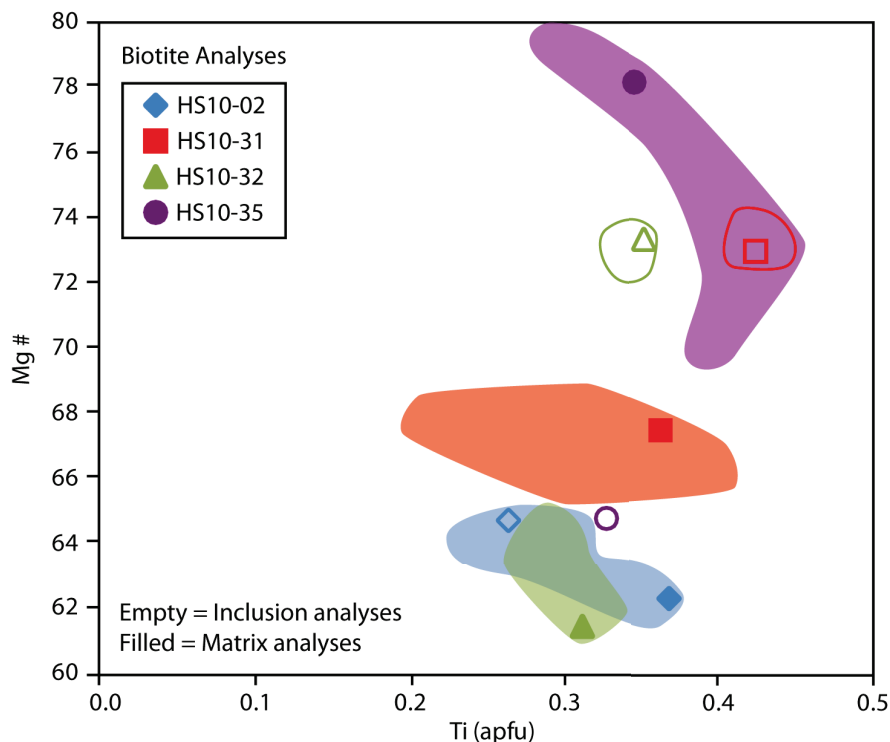


Figure 3.11: Chemistry of matrix biotite and biotite found as inclusions. Matrix biotite (filled symbols), and biotite found as inclusions in M1 phases (empty symbols), are overlain on areas defined by all matrix biotite analyses from each sample (filled areas) and by all analyses of biotite included in M1 phases (empty areas). Biotite was not found as an inclusion in HS10-02, so a composition with relatively high Ti and low Mg# was used in AvPT estimates of the M1 assemblage. Ti apfu is calculated according to 16 cations in biotite, and Mg# is  $Mg/(Mg + Fe)$ .

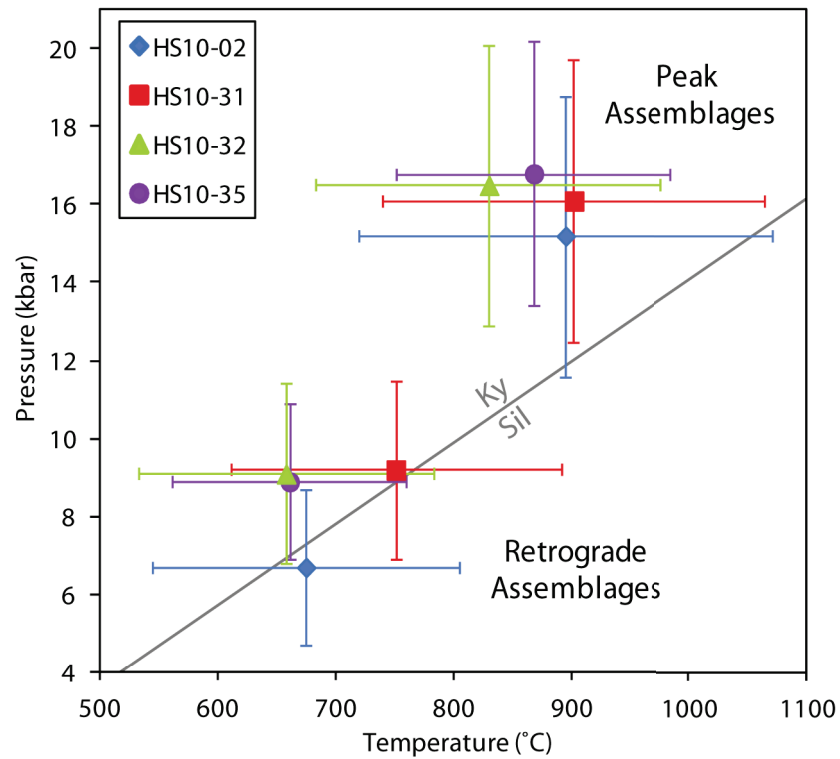


Figure 3.12: AveragePT estimates for peak and retrograde compositions from the four migmatitic aluminous gneiss samples. Large associated uncertainties limit the ability to interpret tectonic characteristics and the processes witnessed by these samples. For the most information, with possibly the smallest level of uncertainty, pseudosection modelling is required.

Table 3.1: (Continued on the following two pages) Peak and retrograde mineral analyses and calculated Average PT results. The analyses for each assemblage from the migmatitic aluminous gneiss samples were used in estimating the pressure and temperature of their thermodynamic equilibrium with AveragePT mode of tc. Analysis locations are shown in Figures 3.1, 3.3, 3.5, 3.8, and 3.7. Cations were calculated to the following oxygen atoms per formula unit: garnet = 12; biotite = 22; plagioclase = 8.

	HS10-02						HS10-31					
	4	52	80	28	95	92	8	27	42	68	52	56
Oxides (wt%)	Garnet	Biotite	Plag	Garnet	Biotite	Plag	Garnet	Biotite	Plag	Garnet	Biotite	Plag
SiO <sub>2</sub>	38.00	36.72	59.63	37.17	36.94	58.94	39.23	37.941	61.22	38.85	37.29	58.71
TiO <sub>2</sub>	0.01	2.21	0.00	0.00	3.25	0.00	0.03	3.907	0.00	0.02	3.44	0.00
Al <sub>2</sub> O <sub>3</sub>	21.48	18.84	25.76	21.24	18.70	26.66	22.34	18.062	24.38	21.93	18.07	26.06
Cr <sub>2</sub> O <sub>3</sub>	0.03	0.09	0.00	0.05	0.08	0.00	0.01	0.04	0.00	0.00	0.15	0.00
Fe <sub>2</sub> O <sub>3</sub>	2.73	0.00	0.00	1.98	0.00	0.00	2.14	0.00	0.00	0.79	0.15	0.00
FeO	24.89	14.14	0.00	29.71	14.67	0.03	22.94	10.473	0.09	28.26	12.57	0.00
MnO	0.46	0.03	0.00	1.73	0.01	0.00	0.27	0.017	0.00	0.51	0.04	0.00
MgO	7.61	14.15	0.00	5.87	13.59	0.00	9.83	15.947	0.00	8.03	14.33	0.00
CaO	5.10	0.00	6.74	1.97	0.00	7.95	4.84	0.004	5.74	2.64	0.00	8.04
Na <sub>2</sub> O	0.00	0.36	7.86	0.01	0.33	7.50	0.01	0.275	7.94	0.02	0.21	6.99
K <sub>2</sub> O	0.00	8.58	0.05	0.00	8.61	0.05	0.03	9.192	0.08	0.02	8.89	0.05
Total	100.31	95.12	100.03	99.72	96.17	101.13	101.67	95.86	99.45	101.06	95.12	99.85
Cations (p.f.u.)												
Si	2.940	5.423	2.655	2.947	5.408	2.607	2.948	5.476	2.728	2.984	5.482	2.625
Ti	0.001	0.246	0.000	0.000	0.359	0.000	0.002	0.425	0.000	0.001	0.381	0.000
Al	1.958	3.280	1.352	1.984	3.227	1.390	1.979	3.073	1.281	1.985	3.131	1.374
Cr	0.002	0.011	0.000	0.003	0.009	0.000	0.001	0.004	0.000	0.000	0.018	0.000
Fe <sup>3+</sup>	0.159	0.000	0.000	0.118	0.000	0.000	0.121	0.000	0.000	0.046	0.018	0.000
Fe <sup>2+</sup>	1.610	1.747	0.000	1.970	1.795	0.001	1.442	1.265	0.003	1.815	1.544	0.000
Mn	0.030	0.004	0.000	0.116	0.002	0.000	0.017	0.002	0.000	0.033	0.004	0.000
Mg	0.877	3.115	0.000	0.694	2.966	0.000	1.101	3.432	0.000	0.920	3.142	0.000
Ca	0.423	0.000	0.322	0.167	0.000	0.377	0.389	0.000	0.274	0.217	0.000	0.386
Na	0.000	0.103	0.678	0.001	0.095	0.643	0.001	0.077	0.686	0.004	0.059	0.606
K	0.000	1.617	0.002	0.000	1.608	0.002	0.004	1.692	0.005	0.002	1.668	0.002
Total	8.000	15.547	5.010	8.001	15.468	5.021	8.005	15.446	4.977	8.006	15.446	4.992
Temperature (°C)	895 ± 176						902 ± 163					
Pressure (kbar)	15.2 ± 3.6						16.1 ± 3.6					
	675 ± 130						751 ± 140					
	6.7 ± 2.0						9.2 ± 2.3					



	HS10-32						HS10-35					
	13	116	62	1	69	82	168	41	55	231	232	235
Oxides (wt%)	Garnet	Biotite	Plag	Garnet	Biotite	Plag	Garnet	Biotite	Plag	Garnet	Biotite	Plag
SiO <sub>2</sub>	38.42	38.24	65.84	37.68	37.64	61.82	38.48	37.67	62.42	38.61	38.99	59.40
TiO <sub>2</sub>	0.06	3.19	0.00	0.10	2.78	0.00	0.01	4.10	0.00	0.00	3.22	0.00
Al <sub>2</sub> O <sub>3</sub>	21.98	18.61	22.05	21.55	19.19	24.54	22.25	17.28	24.56	22.11	17.92	23.77
Cr <sub>2</sub> O <sub>3</sub>	0.12	0.06	0.00	0.15	0.00	0.00	0.01	0.14	0.00	0.08	0.07	0.00
Fe <sub>2</sub> O <sub>3</sub>	0.12	0.00	0.00	0.00	0.00	0.00	0.00	0.00	0.00	0.10	0.00	0.00
FeO	25.69	10.31	0.15	30.29	14.32	0.00	21.73	9.66	0.00	26.67	8.75	0.00
MnO	0.50	0.05	0.00	1.11	0.00	0.00	0.31	0.02	0.00	0.48	0.00	0.00
MgO	8.54	15.56	0.00	5.50	12.98	0.00	9.23	16.61	0.00	8.85	17.21	0.00
CaO	3.57	0.02	2.90	2.64	0.00	6.02	5.70	0.01	5.88	2.53	0.00	5.78
Na <sub>2</sub> O	0.02	0.27	10.64	0.04	0.23	8.59	0.00	0.18	8.67	0.01	0.18	8.25
K <sub>2</sub> O	0.05	9.20	0.05	0.05	9.14	0.12	0.03	9.35	0.10	0.03	9.11	0.10
Total	99.06	95.51	101.63	99.11	96.29	101.08	97.75	94.89	101.63	99.48	95.45	97.30
Cations (p.f.u.)												
Si	2.984	5.524	2.858	2.998	5.491	2.719	2.988	5.482	2.728	2.987	5.586	2.714
Ti	0.004	0.348	0.000	0.006	0.306	0.000	0.000	0.449	0.000	0.000	0.348	0.000
Al	2.011	3.170	1.128	2.021	3.302	1.272	2.036	2.966	1.264	2.016	3.027	1.280
Cr	0.007	0.007	0.000	0.010	0.000	0.000	0.001	0.015	0.000	0.005	0.007	0.000
Fe <sup>3+</sup>	0.007	0.000	0.000	0.000	0.000	0.000	0.000	0.000	0.000	0.006	0.000	0.000
Fe <sup>2+</sup>	1.669	1.245	0.006	2.015	1.749	0.000	1.411	1.175	0.000	1.725	1.047	0.000
Mn	0.033	0.007	0.000	0.074	0.000	0.000	0.020	0.002	0.000	0.031	0.000	0.000
Mg	0.989	3.353	0.000	0.652	2.823	0.000	1.068	3.604	0.000	1.021	3.676	0.000
Ca	0.297	0.002	0.135	0.225	0.000	0.283	0.474	0.002	0.272	0.209	0.000	0.283
Na	0.002	0.075	0.896	0.006	0.066	0.733	0.000	0.059	0.736	0.001	0.048	0.731
K	0.005	1.696	0.002	0.005	1.701	0.006	0.002	1.707	0.008	0.004	1.665	0.006
Total	8.007	15.426	5.026	8.011	15.437	5.014	8.002	15.462	5.008	8.005	15.404	5.014
Temperature (°C)	830 ± 147						661 ± 99					
Pressure (kbar)	16.5 ± 3.6						16.3 ± 3.4					

Analysis	HS10-16									
	4	130	120	87	103	128	99	151	155	159
Oxides (wt%)	Grt Core	Pl in Grt	Matrix Pl	Amp	Amp	Amp	Cpx	Cpx	Cpx	Cpx
SiO <sub>2</sub>	38.57	58.57	58.57	40.92	43.23	41.81	53.34	51.50	52.19	53.14
TiO <sub>2</sub>	0.04	0.00	0.00	1.06	1.35	1.03	0.02	0.32	0.32	0.07
Al <sub>2</sub> O <sub>3</sub>	21.70	26.54	26.20	15.33	12.55	15.38	0.92	3.23	2.49	1.19
Cr <sub>2</sub> O <sub>3</sub>	0.04	0.00	0.00	0.07	0.10	0.06	0.02	0.03	0.05	0.05
FeO	19.39	0.35	0.09	15.00	15.46	12.45	8.07	8.59	8.48	8.13
MnO	0.46	0.00	0.00	0.23	0.29	0.17	0.35	0.31	0.35	0.33
MgO	7.90	0.01	0.00	9.88	10.60	10.23	13.73	12.54	12.99	13.53
CaO	11.09	8.17	8.09	11.72	11.85	11.67	23.86	23.18	23.54	23.32
Na <sub>2</sub> O	0.04	7.39	7.23	2.08	1.81	2.04	0.42	0.63	0.50	0.46
K <sub>2</sub> O	0.02	0.03	0.03	0.26	0.26	0.28	0.00	0.00	0.00	0.00
Total	99.25	101.04	100.20	96.55	97.49	97.35	100.73	100.35	100.83	100.23
Cations (p.f.u.)										
Si	2.969	2.598	2.614	5.889	6.160	5.944	1.978	1.921	1.937	1.978
Ti	0.002	0.000	0.000	0.114	0.145	0.110	0.001	0.009	0.009	0.002
Al	1.968	1.388	1.378	2.603	2.108	2.576	0.040	0.142	0.109	0.052
Cr	0.002	0.000	0.000	0.009	0.011	0.007	0.001	0.001	0.001	0.002
Fe	1.248	0.000	0.000	1.806	1.841	1.745	0.250	0.268	0.261	0.253
Mn	0.030	0.000	0.000	0.029	0.035	0.020	0.011	0.010	0.011	0.011
Mg	0.906	0.001	0.000	2.129	2.251	2.167	0.759	0.697	0.718	0.751
Ca	0.914	0.388	0.387	1.808	1.811	1.778	0.948	0.926	0.936	0.930
Na	0.005	0.635	0.626	0.581	0.499	0.563	0.030	0.046	0.036	0.033
K	0.002	0.002	0.002	0.048	0.046	0.051	0.001	0.001	0.001	0.001
Total	8.047	5.025	5.011	15.008	14.907	14.962	4.018	4.021	4.019	4.012
				Prg	Hbl-Ts	Ts				

Table 3.2: Representative mineral analyses for HS10-16. These data were used in varying combinations by AvPT (*Powell and Holland* 1988) to constrain peak metamorphic pressure and/or temperature conditions the garnet amphibolite unit. Multi-equilibria thermobarometry resulted in dubious *P-T* estimates, likely due to fluid infiltration and pervasive chemical alteration of the original mineralogy. Amphibole species names were derived using Probe-AMPH (*Tindle and Webb* 1994). Cations were calculated to the following oxygen atoms per formula unit: garnet = 12; plagioclase = 8; amphibole = 22; pyroxene = 6.

### 3.3 Phase Equilibria Pseudosection Modelling

A pseudosection (or equilibrium phase diagram) is a forward modelling tool used to interpret a rock's metamorphic history given an in-depth knowledge of the petrography, bulk chemistry, and mineral chemistries of the sample. A  $P$ - $T$  pseudosection is a section through a total phase diagram where all of the compositional variables are fixed, and only  $P$  and  $T$  may vary. Within a given  $P$ - $T$  range, the stability fields of different equilibrium mineral assemblages are modelled based on information from an internally consistent thermodynamic database,  $a$ - $X$  relationships, and a well-defined, constant bulk-rock chemistry input by the user.

Pseudosections are different from standard  $P$ - $T$  diagrams or petrogenetic grids, because the latter show all the reactions that occur in a defined model system, with *all* possible bulk compositions, throughout  $P$ - $T$  space. Discontinuous reactions, such as those in  $P$ - $T$  diagrams, and continuous reactions between end-member phases are not explicitly predicted by pseudosections, but are inherent in their construction, and can be derived by looking at changes in phase assemblages within adjacent fields (see section 3.3.2).

Lines calculated and drawn on a  $P$ - $T$  pseudosection (called topology) represent the appearance or disappearance of a mineral phase with changes in temperature and/or pressure. The topology essentially outlines stability fields of equilibrium mineral assemblages. After the topology for a given bulk rock sample is modelled, a comparison is made between the observed and modelled assemblage(s) and the mineral compositions for that sample, to assess the fit of the model to real observations. The model may be refined by reassessing the bulk composition at this point.

Each field in a pseudosection has a variance, also known as degrees of freedom, according to the Phase Rule ( $F = C - P + 2$ , where  $F$  is the variance of the assemblage,  $C$  is the number of components in the system,  $P$  is the number of phases in the stable assemblage, and 2 refers to pressure and temperature as additional variables). The number of components, plus  $P$  and  $T$ , minus the stable phases defined by the user in a given field yields the variance of that field. Variance refers to the number of variables that do not require definition in order to calculate an equilibrium assemblage. Low variance assemblages have a higher number of phases, and thus reactions between phases in the model system become more abundant and complex. If the pseudosection is properly constructed, the Schreinemaker rules (*Zen* 1966) predict that the variance of adjacent fields

must differ by a value of 1 since the topology separating the fields represent the addition or subtraction of single phases. Where two lines intersect at a point, four fields meet. Of these four, two opposing fields must differ by a value of 2 since two phases have been either subtracted or added, and the other two opposing fields will have the same variance (one phase is added while the other is subtracted).

Commonly used programs with the ability to calculate pseudosections from an input bulk-rock composition include **THERMOCALC** (*Powell and Holland 1988*), **Perplex** (*Connolly 1990*), and **Theriak-Domino** (*de Capitani and Brown 1987; de Capitani and Petrakakis 2010*). **THERMOCALC** software uses non-linear equations to solve equilibrium calculations with each phase boundary being user-defined. Alternatively, **Perplex** automatically calculates the stable assemblage at each point in a pre-defined grid, and interpolates field boundaries between points with different stable assemblages. A disadvantage to this calculation method is the potential to miss narrow or small fields, depending on the grid spacing. **Theriak-Domino** calculates stable assemblages in the same manner as **Perplex**, but the calculations are based on minimization of Gibbs free energy rather than non-linear equations like **THERMOCALC**. Creating a pseudosection with either of the automated grid-style programs means the user does not need to have an understanding of the intricacies of modelled equilibria, which may be a disadvantage when trying to interpret textural and compositional observations in the actual sample. For these reasons, the following pseudosections for this study were built using **THERMOCALC**, which is the only program discussed in the remainder of this chapter.

### 3.3.1 *The Model System and Bulk Composition*

**THERMOCALC** (version 3.33) pseudosections have several requirements that define the system being modelled and contribute to phase boundary and equilibrium assemblage calculations. First, a model chemical system was established, based on all phases and respective components in the real sample. The four migmatitic aluminous gneiss samples described earlier contain the phases Als + Gt + Bt + Pl + Qz + Ru + Ap ± Sul ± Liq. Phosphate and sulphide minerals do not have well-constrained *a-X* relationships, so the observed apatite and sulphide phases cannot be modelled. Additionally, Mn-bearing end-members (e.g. spessartine) cannot be modelled with any precision if the oxidation state of the sample is unknown. Therefore, the minor phosphate, sulphide, and Mn-bearing phases were omitted from this study, and the equivalent components were subtracted from

the bulk composition. The 12-component system  $\text{NaO} + \text{CaO} + \text{K}_2\text{O} + \text{FeO} + \text{MgO} + \text{Al}_2\text{O}_3 + \text{SiO}_2 + \text{H}_2\text{O} + \text{TiO}_2 + \text{Fe}_2\text{O}_3 + P + T$  (NCKFMASHTO) was used to investigate equilibrium of the remaining observed pure phases and end-member solid solutions.

Second, the  $a$ - $X$  relationship models for end-member solid solutions of the observed phases, and phases commonly seen in metamorphosed pelitic to aluminous rocks, were written into the input file. Thermodynamic data for these models are referenced to the internally consistent dataset for phase and assemblage calculations. The following  $a$ - $X$  models were used in this study: clinopyroxene (Cpx; Green et al., 2007); orthopyroxene (Opx; White and Powell 2002); cordierite (Crd; Holland and Powell 1998); biotite, garnet, and melt (Bt, Gt, and Liq; White et al. 2007); muscovite (Mu; Coggon and Holland 2002); K-feldspar and plagioclase (Ksp and Pl; Powell and Holland 2008); and ilmenite (Ilm; White and Powell 2002). Pure phases ( $a = 1$ ) were also coded into the file: kyanite (Ky), sillimanite (Sil), quartz (Qz), rutile (Ru), and water ( $\text{H}_2\text{O}$ ).

Third, each sample bulk composition to be modelled is written into the input file as oxide mol% for the chosen system components (NCKFMASHTO). The bulk composition must be representative of the investigated polished section. Determining the bulk composition, however, is not a trivial exercise. A major consideration is the equilibration volume of the sample. This is the proportion of the bulk-rock composition that has participated in reactions, or the spatial range in which ions have freely diffused, throughout the metamorphic history of the rock (Powell and Holland 2008). Coarse-grained, heterogeneous, or compositionally banded rocks may vary in composition over short distances, suggesting the equilibration volume for the sample during a metamorphic event can be smaller than the width of the band or average grain size. If chemically zoned porphyroblast phases are observed, it is likely that the cores were shielded from reactions following further porphyroblast growth. Solutions to these problems include investigation of a banded rock as two separate domains, and removal of porphyroblast core compositions from the bulk composition, respectively, to constrain the effective bulk composition of the matrix. When partial melting and melt loss are interpreted from mineral assemblages and textural evidence, the pseudosection interpretations will only represent the metamorphic history of a rock after melt extraction took place.

For this study, the rock slabs corresponding to the polished section of each migmatitic aluminous gneiss sample were crushed, and the bulk-rock compositions measured by XRF

(X-ray fluorescence) with a Phillips PW2400 spectrometer at the Regional Geochemical Centre at St. Mary's University, Halifax. The bulk analysis was renormalized after removing MnO and converting the XRF  $\text{Fe}_2\text{O}_3$  output to FeO (Figure B.1). Since only minor oxide phases (primarily ilmenite, which implies a very low oxidation state) were observed in these samples, the  $\text{Fe}_2\text{O}_3$  content was assumed to be 0.01 mol%, the lowest allowable value for the input file. The XRF bulk analyses did not include  $\text{H}_2\text{O}$  concentrations, which are required in the pseudosection input file, since fluorescence photons from light elements (ie. H, C, N, O) do not have enough energy to reach the detectors. Fortunately, the amount of  $\text{H}_2\text{O}$  in a rock can be estimated using a mass-balance approach, given the modal proportions of the rock-forming phases in the sample and their typical compositions.

To determine modal mineral proportions of each sample, the polished sections were imaged with the Scanning Electron Microscope (SEM) at the MicroAnalysis Facility of Memorial University, St. John's, Newfoundland. Mineral Liberation Analysis (MLA) software was used to link mineral compositions from EMP analyses (previously collected for the multi-equilibria thermobarometry method) with the atomic number-based gray-scale of a full backscatter electron image of each thin section (Figure 3.13; Figures B.1, B.2, and B.3). Every pixel in each BSE image is tagged with the appropriate mineral composition colour code, allowing for quick, simple, and very precise quantitative mineral mode estimates with the MLA software.

The mass-balance calculation to determine the molar  $\text{H}_2\text{O}$  content of the bulk composition was done in 4 steps. First, the SEM modal proportion of each phase was converted to a molar proportion. This required the molar volume of each pure phase or end-member phase, and end-member proportions for phases with solid-solution series. The molar proportions were normalized to 100%.

Second, the normalized molar proportion of each pure phase and end-member was divided into component proportions, based on the mineral composition stoichiometry of the respective species. Here, the  $\text{Ti}^{4+}$  in biotite is assumed to be in the octahedral site, and is a result of "Ti-oxy" substitution,  $\text{R}^{2+} + 2(\text{OH})^{1-} = \text{Ti}^{4+} + 2\text{O}^{2-}$  (Cesare *et al.* 2003, and references therein). The molar  $\text{TiO}_2$  component in biotite is equivalent to the lost  $\text{H}_2\text{O}$  component due to substitution, and therefore the [total moles of biotite] = [moles of  $\text{H}_2\text{O}$ ] + [moles of  $\text{TiO}_2$ ] (e.g. White *et al.* 2007). Third, solving this equation for the moles of  $\text{H}_2\text{O}$  gives the  $\text{H}_2\text{O}$  component in biotite, the only hydrous phase in the analyzed samples.

Third, the molar proportions of common components from all phases were summed, and normalized to 100% (ex:  $\text{SiO}_2^{bt}$  mol% +  $\text{SiO}_2^{pl}$  mol% +  $\text{SiO}_2^{qz}$  mol% + ... etc.). The normalized molar  $\text{H}_2\text{O}$  proportion is considered the  $\text{H}_2\text{O}$  component of the bulk composition. Fourth, the XRF bulk analyses was converted to molar proportions, and these were normalized to [100% -  $\text{H}_2\text{O}$  mol%]. The normalized XRF molar proportions and mass-balanced  $\text{H}_2\text{O}$  molar porportion were used in the **THERMOCALC** input files for phase equilibrium pseudosection modeling of each sample. Each bulk composition is therefore derived from a combination of methods: XRF for molar proportions of major element oxides, and SEM mineral mode/mineral analyses mass-balance for molar proportions of  $\text{H}_2\text{O}$  in hydrous phases.

After calculating the  $\text{H}_2\text{O}$  content, the bulk composition was tested to ensure that it is chemically representative of the thin section, and that the thin section is smaller than the equilibration volume. The best way to do this is to calculate lines of constant mineral modes (isomodes) corresponding to the observed SEM modes, and check that they intersect. If there is no intersection (within  $\pm 1$  modal % for each mineral), then some phases are over- or under-represented by the bulk composition, and the pseudosection should not be used for quantitative analysis. The bulk compositions of all four migmatitic aluminous gneiss samples were tested in this way, and only one sample satisfied the criteria for quantitative analysis with phase equilibria pseudosection modelling. This sample is HS10-32.

The three samples that failed the isomode test may have been too heterogeneous (compositionally banded), and therefore had a differentiated equilibration volume. HS10-32 has a finer grain size due to shearing, and is relatively homogeneous compared to the other three samples. These textural characteristics likely increased the equilibration volume of the sample, resulting in a better fit of the modelled and observed mineral modes. The following pseudosection description and *P-T* estimates specifically refer to only this sample.

### 3.3.2 *Pseudosection Results*

The topology within the range 5-15 kbar and 50-1000 °C was built for HS10-32. If changes were made to the bulk chemistry of this sample during metamorphism, the pseudosection is now representative of the final bulk-rock composition (ie, after melt loss or fluid migration). The model includes stability fields with assemblages matching the interpreted

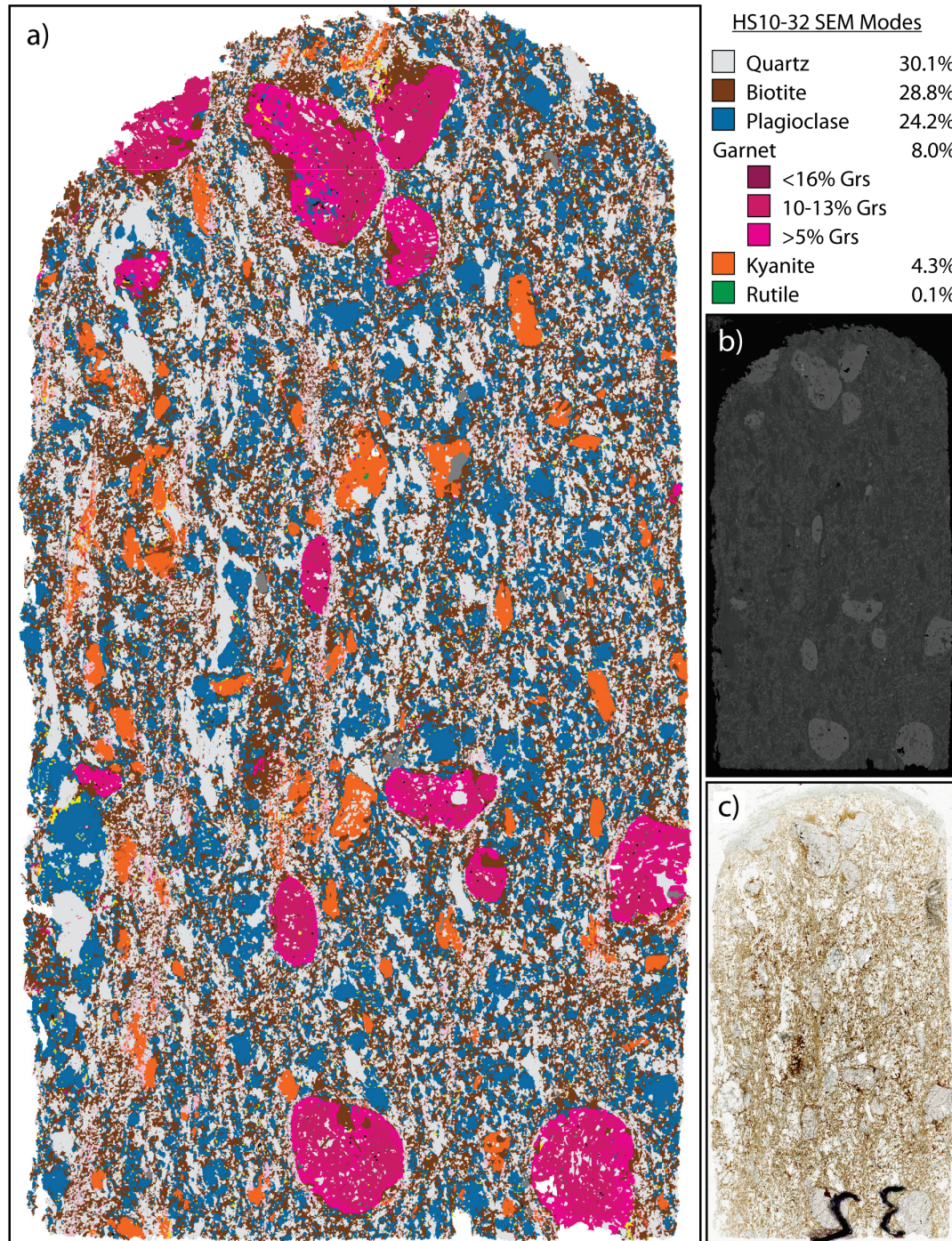


Figure 3.13: SEM scan of HS10-32 and major mineral modes. SEM (a), BSE (b), and the photomicrograph (c) of the polished thin section provide textural constraints on mineral assemblages and relationships. The colour legend defines only the major minerals required for pseudosection construction and  $P$ - $T$  estimates of this sample. A full legend, including initial SEM mineral modes, is available in Appendix B, Figure B.1.



peak temperature (M1) and retrograde (M2) assemblages in the real sample (Figure 3.14).  $P$ - $T$  estimates at the modelled M2 assemblage are considered particularly robust since the real bulk rock composition probably has not changed following metamorphism at these conditions.

### **Topology**

In Field I, at the lower left corner of this pseudosection, the modelled assemblage [Bt + Pl + Als (aluminosilicate) + Gt + Qz + Ru] corresponds to the observed M2 mineral assemblage. With increasing temperature to Field II, melt becomes stable, likely at the expense of biotite. With increasing pressure from Field I, biotite is also partially consumed to generate muscovite, which becomes stable in Field III.

Field II contains the modelled assemblage [Liq + Bt + Pl + Als + Gt + Qz + Ru], which is correlative with the observed M1 mineral assemblage. From Field II, plagioclase and biotite are partially consumed to generate K-feldspar at higher temperatures (Field IV) and muscovite at higher pressures (Field V). The model predicts complete biotite consumption and corresponding ilmenite growth at temperatures greater than 890 °C, and K-feldspar consumption at temperatures greater than 900 °C and pressures less than 9.5 kbar.

This pseudosection has a dominantly temperature-dependent solidus (Liq) between 7 and 12 kbar. The position and steep orientation of this line have been observed in modelled rocks with a similar bulk composition (*Indares et al.* 2008). At low pressures, stable assemblages include cordierite (Cd), while at high pressures stable assemblages include diopsidic clinopyroxene (Cpx). Neither of these phases was observed in thin section, therefore the fields in which they appear are not of concern.  $P$ - $T$  ranges for the M1 and M2 mineral assemblages can be interpreted from the boundaries of the corresponding modelled fields. However, the ranges can be further constrained using isomodes and isopleths.

### **Phase Isomodes**

Isomode values corresponding to the observed SEM modes were calculated to test how well the model bulk composition represents the real rock. In addition to topology, isomodes can also provide constraints on  $P$ - $T$  estimates. This did not involve additional analytical work since the modes in this sample were already estimated by the SEM imaging and MLA software to calculate the H<sub>2</sub>O component in the bulk. The SEM modes,  $\pm 1$

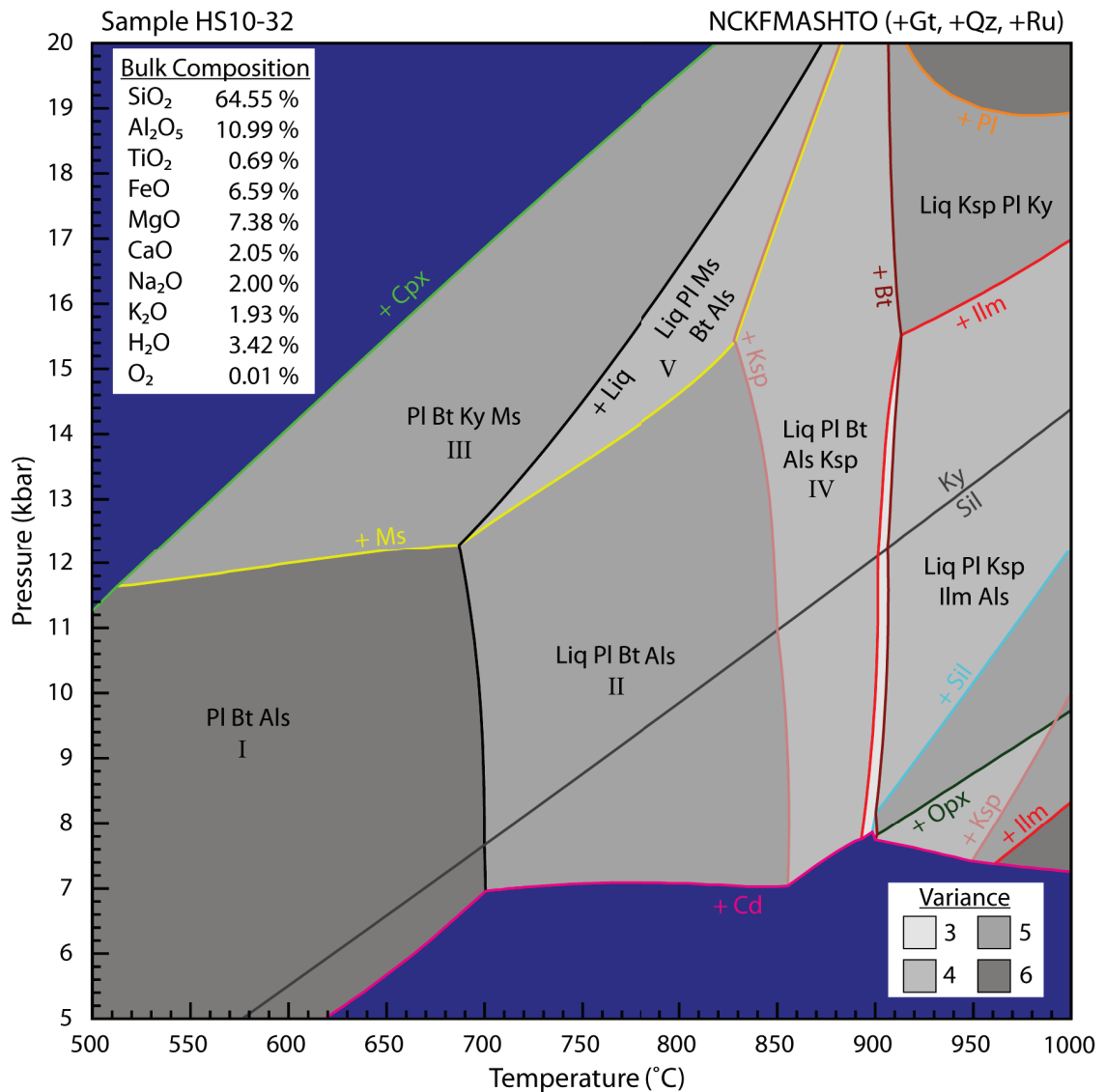


Figure 3.14: HS10-32 pseudosection. The interpreted peak temperature and retrograde assemblages are [Liq + Ky + Gt + Bt + Pl + Qz + Ru] in Field II, and [Sil + Gt + Bt + Pl + Qz + Ru] in Field I, respectively.

modal %, were calculated by **THERMOCALC** and plotted across the pseudosection. The isomodes define an area of intersection, centered on  $675\text{ °C} \pm 60\text{ °C}$  and  $9\text{ kbar} \pm 1.8\text{ kbar}$ , that overlaps the solidus (Figure 3.15). The overlap suggests that the modal mineralogy and texture of this sample have not changed since the crystallization of melt. Isomodes for each phase have been calculated across the entire pseudosection range, and are presented in Appendix B.2.

The only phase that does not overlap the solidus within  $\pm 1$  modal % is garnet.

The SEM analysis estimates garnet in the thin section to be 8.3 modal %, whereas the pseudosection predicts about 10 modal % garnet at the solidus. This is a minor difference, and likely reflects slightly less garnet in the polished section than was present in the corresponding crushed slab. These observations warrant further investigation into the compatibility of observed and modelled mineral compositions. Unlike the modes, mineral chemistries between the thin section and complementary slab are not expected to differ; therefore, isopleths have a stronger link to the modelled bulk composition.

### Compositional Isopleths

Isopleths are lines of constant composition that are calculated for solid solutions phases and compared with measured mineral chemistries. For this model,  $x(\text{bi})$  (Fe/Fe+Mg in biotite),  $x(\text{g})$  (Fe/Fe+Mg in garnet), and  $z(\text{g})$  (Ca/Ca+Fe+Mg in garnet) were calculated, with  $\pm 1\%$  uncertainties, and drawn over the topology based on EMP mineral chemistries from the M1 and M2 assemblages (Figure 3.16). The model isopleths of  $x(\text{bi}) = 37\%$ ,  $x(\text{g}) = 73\%$ , and  $z(\text{g}) = 4\%$  ( $\pm 1\%$ ), derived from EMP mineral analyses of the M2 assemblage, intersect to form an area that overlies the solidus. This area also overlies the M2 isomode intersection area, but constrains a narrower  $P$ - $T$  range centered on  $680\text{ }^{\circ}\text{C} \pm 40\text{ }^{\circ}\text{C}$  and  $9.1\text{ kbar} \pm 1.1\text{ kbar}$ . This is interpreted to be the equilibrium conditions for the observed M2 assemblage. The uncertainty in this estimate is simply assigned from the modelled  $P$ - $T$  minimum and maximum boundaries, and does not incorporate uncertainty from microprobe analysis, or thermodynamic properties and  $a$ - $X$  relationships from the internally consistent database.

The predicted isopleths of  $x(\text{bi}) = 27\%$ ,  $x(\text{g}) = 62\%$ , and  $z(\text{g}) = 11\%$  ( $\pm 1\%$ ), derived from EMP mineral analyses of the M1 assemblage, create an extremely well-constrained intersection area centered on  $860\text{ }^{\circ}\text{C} \pm 5\text{ }^{\circ}\text{C}$  and  $15.35\text{ kbar} \pm 0.25\text{ kbar}$ . This is interpreted as the equilibrium conditions for the observed M1 assemblage. This area is in Field IV, where K-feldspar is stable, but K-feldspar was not identified in thin section or by the SEM scan and MLA software. It is possible that K-feldspar existed in the peak assemblage, but was completely consumed in biotite-generating reactions during retrograde metamorphism, prior to final melt crystallization at M2 assemblage conditions.

The difference in intersection area between the M1 and M2 assemblages is due to the vectors of intersecting isopleths and their respective gradient magnitudes. For the M1 intersection,  $x(\text{g})$  and  $x(\text{bi})$  are subvertical and have higher gradients than the M2

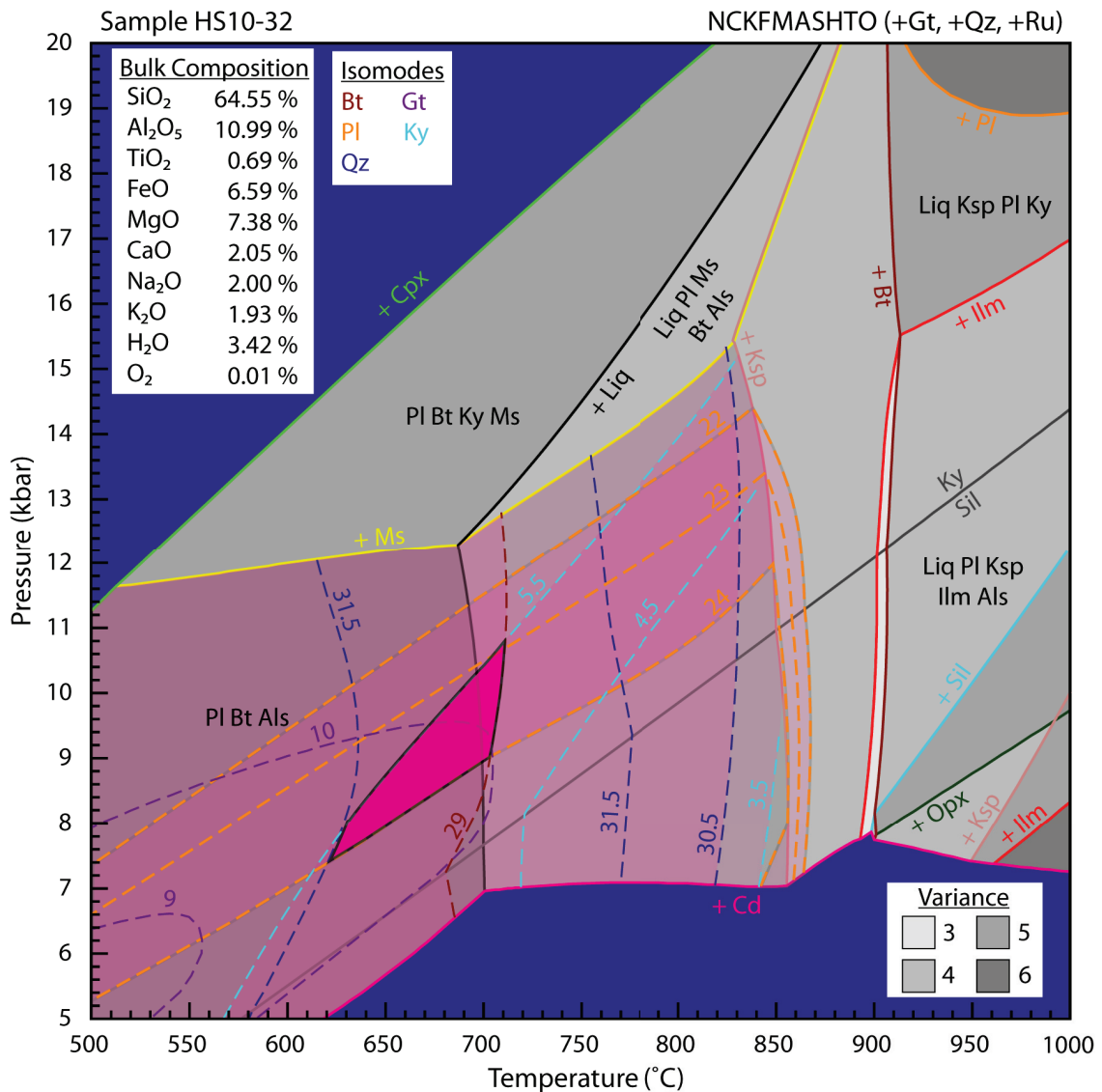


Figure 3.15: HS10-32 pseudosection with M2 isomode intersections. Calculated isomodes (in %) of Gt, Bt, Pl, Ru, Als intersect to produce an area that overlaps the solidus. This implies the modal, and therefore textural, characteristics of this sample have not changed since the time of final melt crystallization. This intersection is centered on  $675\text{ }^{\circ}\text{C} \pm 60\text{ }^{\circ}\text{C}$  and  $9\text{ kbar} \pm 1.8\text{ kbar}$ .

intersection. M2 is primarily constrained by  $x(g)$  and  $z(g)$  isopleths, but is also included within the calculated  $x(bi)$  range which has a considerably lower gradient than the other compositional ratios. The full suite of  $x(bi)$ ,  $x(g)$ , and  $z(g)$  isopleths calculated across the pseudosection  $P$ - $T$  range is presented in Appendix B.2.

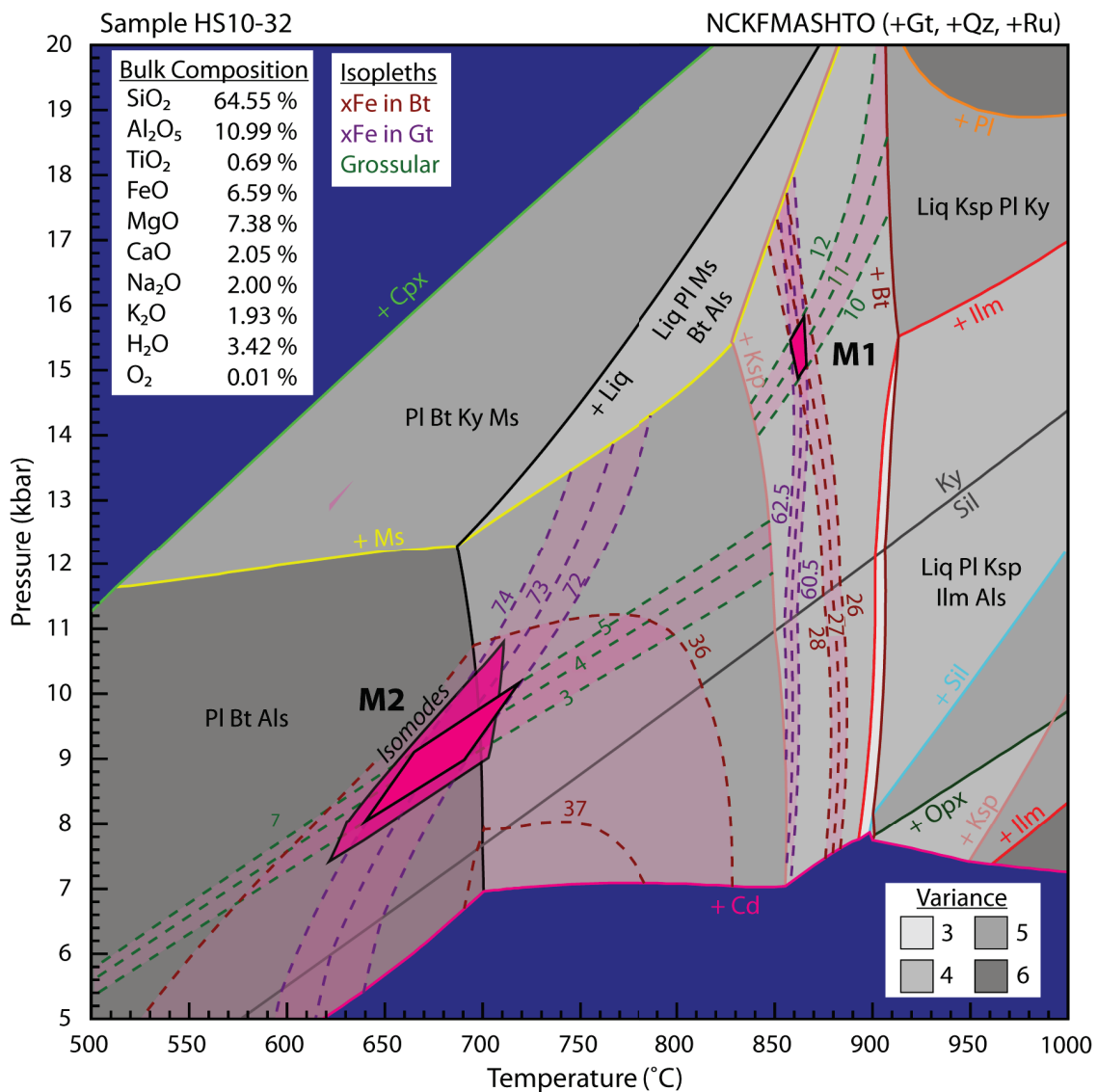


Figure 3.16: HS10-32 pseudosection with isopleth intersections. Calculated  $x(\text{bi})$ ,  $x(\text{g})$ , and  $z(\text{g})$  isopleths (in %) for the M1 and M2 assemblages are plotted with  $\pm 1\%$  uncertainties, and intersect to produce two distinct areas (pink polygons). These areas are the  $P$  and  $T$  extents at which the analyzed mineral compositions applied to the model are stable within uncertainty. The M1 and M2 intersections are centered on  $860\text{ }^\circ\text{C} \pm 5\text{ }^\circ\text{C}$  and  $15.35\text{ kbar} \pm 0.25\text{ kbar}$ , and  $680\text{ }^\circ\text{C} \pm 40\text{ }^\circ\text{C}$  and  $9.1\text{ kbar} \pm 1.1\text{ kbar}$ , respectively. The M2 assemblage area is underlain by the M2 isomode intersection area, for comparison.

### 3.3.3 Pseudosection Interpretations

This pseudosection was built with a well constrained bulk composition estimate from sample HS10-32: The modelled M2 isomodes and isopleths were calculated based on SEM and EMP analyses, respectively, and form individual intersection areas that directly

overlap with the solidus. Considering the ideal nature of this result, the M1 isomodes can be estimated by finding an area of intersection that overlaps with the modelled M1 isopleth intersection. Additionally, calculated gradients at which phases volumetrically increase or decrease, and mineral compositions change, between the modelled M1 and M2 assemblages can be related to modes and textural features in the real sample. This information can be used to interpret the melting history of the rock, and the retrograde *P-T* path from M1 to M2. These functions are what make pseudosections such powerful petrologic tools.

### **Melt Generation and Loss**

The abundance and pervasive presence of leucosome and plagioclase melt film pseudomorphs imply melt generation at some point during the metamorphic history of the *Blåhø Nappe*. What is unclear from field observations and petrography is if this lithology has lost melt during metamorphism and when it was lost. The outcrop and hand sample for HS10-32 do not particularly preserve these features because of the effects of later amphibolite-facies shearing, but the topology and Liq isomodes of this pseudosection provide evidence to support melt generation and loss prior to equilibration at M1 conditions.

Melt is initially generated in most metapelites by muscovite-dehydration reactions at upper- to mid-crustal levels and temperatures of 600-700 °C (*Thompson 1982*). During prograde metamorphism staurolite, biotite, garnet and/or K-feldspar may grow in response to muscovite breakdown. If melt was not lost from the system, these muscovite dehydration products would have been consumed by back-reactions to regenerate muscovite during the amphibolite facies overprinting of this unit. However, muscovite was not observed as a rock-forming phase in this lithology, and the pseudosection for sample HS10-32 predicts muscovite-stability only at high pressures. This suggests melt, including H<sub>2</sub>O from dehydrated muscovite, has been lost from the system prior to equilibration at M1 conditions. Similarly, peritectic garnet (garnet grown in the presence of melt) would have been consumed by retrograde reactions if the H<sub>2</sub>O content in the melt phase from which it grew remained constant (e.g. *Indares et al. 2008*; *Guilmette et al. 2011*). Instead, most migmatitic aluminous gneiss samples contain atoll peritectic garnets that preserve M1 assemblages within their cores. The presence of peritectic garnet and absence of muscovite suggests the current bulk chemistry of this sample is relatively refractory compared to the

protolith (e.g. *Indares et al.* 2008). This supports the relatively higher-temperature solidus (700 °C) predicted by the pseudosection for HS10-32 (e.g. *Guilmette et al.* 2011).

The amount of melt generated and lost during prograde metamorphism cannot be quantitatively determined based on field or petrographic observations, or pseudosection models. What can be said from the pseudosection isomodes, however, is that the melt fraction was equal to, or greater than, the melt-connectivity threshold (MCT) estimate of 7-8% (*Rosenberg and Handy* 2005) prior to equilibration at M1 conditions. The MCT corresponds to a change in the rock microstructure from a melt present in isolated intergranular pockets, to a network of interconnected melt channels between mineral grains. At melt fractions above this threshold, the rheology of the rock is drastically reduced irrespective of the metamorphic path trajectory (ie: melting or crystallizing) (*Rosenberg and Handy* 2005). Presumably, if modal melt exceeds the MCT, a melt loss event would take place until the modal melt proportion was reduced back down to the MCT. Considering the modal melt proportion at M1 conditions (discussed below) and the lack of retrograde muscovite, a melt loss event likely took place prior to M1 conditions, and the metamorphic history of the *Blåhø Nappe* can therefore be reliably estimated from these conditions through retrogression and cooling.

### **M1 Assemblage Modal Estimate**

Isomodes were plotted in 1% increments across the pseudosection *P-T* range (Appendix B.2). The isomodes that intersect and overlap with the M1 isopleth intersection are interpreted to represent the modal mineralogy of HS10-32 at M1 conditions. Based on the intersecting isomodes at these conditions, this sample is estimated to have equilibrated with 27.5% Qz, 21% Gt, 18% Bt, 18% Pl, 6% Liq, 5% Ksp, and 4.5% Ky. The radical difference between the predicted M1 modes and observed M2 SEM modes implies a dramatic textural change during retrograde metamorphism. These changes are integral in defining the trajectory of the retrograde path, which is discussed below.

### **P-T Paths**

Overlain on the topology and modal proportions in Figure 3.18 are a prograde and three retrograde path interpretations for the *Blåhø Nappe*. Since mineral inclusion compositions reflect the peak temperature assemblage, M1, an assemblage associated with peak pressure conditions is constrained to fields below the Cpx-in boundary based on the

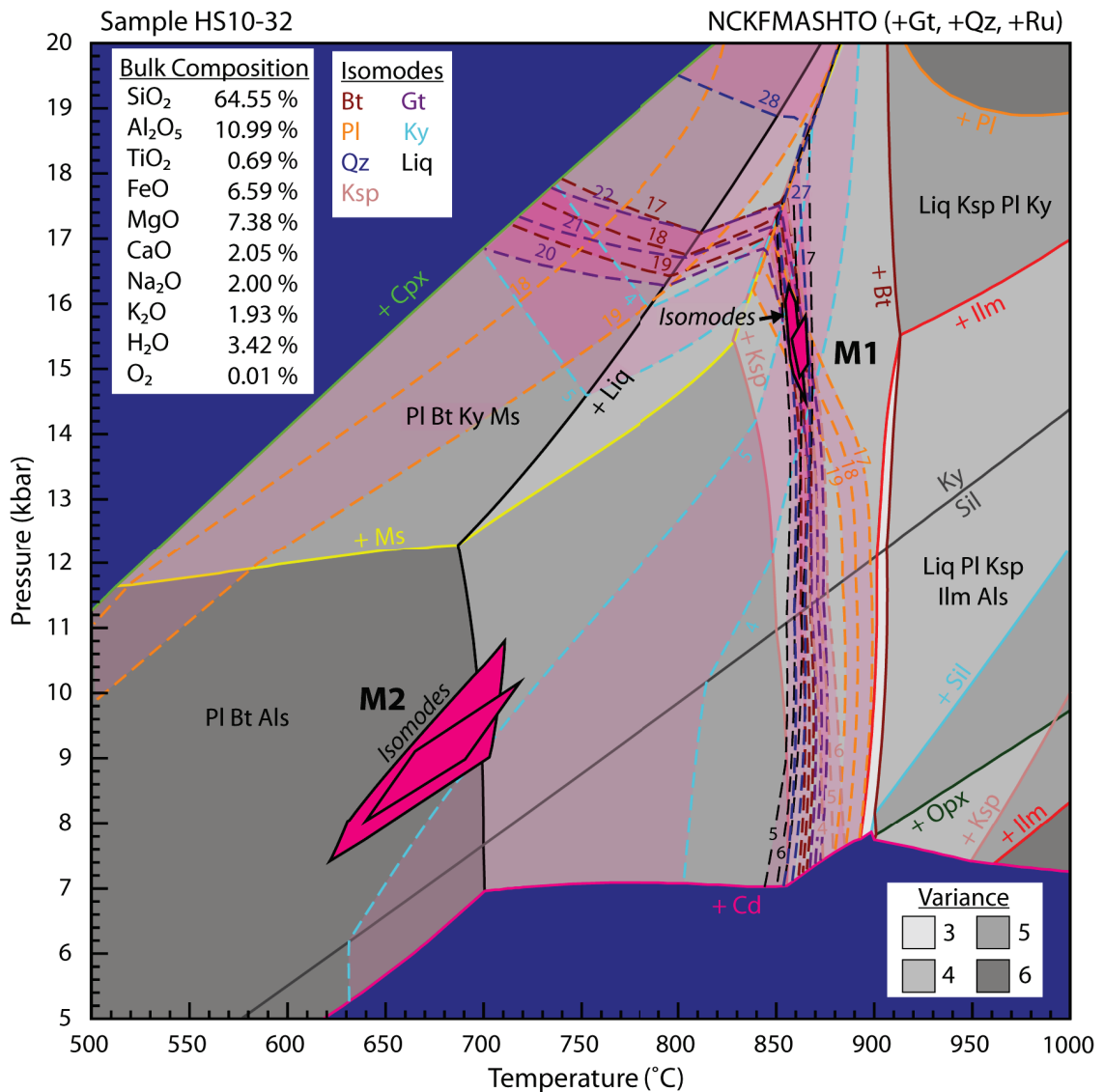


Figure 3.17: HS10-32 pseudosection with estimated M1 isomodes. Estimated isomodes (in modal %, with 1% uncertainties) for the M1 assemblage are based on the overlying M1 isopleth intersection area. The pseudosection predicts M1 modes of approximately 27.5% Qz, 21% Gt, 18% Bt, 18% Pl, 6% Liq, 5% Ksp, and 4.5% Ky.

absence of UHP phases in HS10-32. No other information pertaining to the prograde path was observed in this sample, therefore, the prograde path (grey medium-dashed line) is arbitrarily based on a broad, clockwise trajectory typical for collision zones.

The three possible retrograde paths interpreted from the M1 to M2 assemblages can be thought of as two end-member paths with a third path as a compromise between them. The first end-member, Path 1, is a straight vector through P-T space from M1 to M2. Along



	M1		M2	
	Measured	Modelled	Measured	Modelled
<i>Isomodes (vol %)</i>				
Qz	--	27.4	31.57	31.8
Bt	--	18.0	30.14	29.2
Gt	--	21.0	8.36	9.9
Pl	--	18.0	25.35	23.7
Als	--	4.5	4.48	5.3
Ru	--	0.1	0.10	0.1
Ksp	--	5.0	0.00	0.0
Liq	--	6.0	0.00	0.0
Total	--	100	100	100
<i>Isopleths (%)</i>				
x(bi)	27.2	27.0	37.4	36.3
x(g)	61.3	61.5	73.1	73.0
z(g)	10.6	11.0	4.4	4.0

Table 3.3: Compared measured and modelled mineral modes and compositions. The M1 modes are interpreted from intersecting isomodes that overlap with the modelled M1 isopleth intersection. These predictions provide insight into the textural history of this sample.

this trajectory only one mineral phase boundary is crossed (Ksp-out) before the liquid phase is consumed at the solidus. Ksp is lost from the M1 assemblage within the first 30 °C of cooling and 1 kbar of decompression.

Path 3, the second end-member, has two steps: first an isothermal decompression path, and then a sharp trajectory change to an isobaric cooling path. At approximately 11 kbar along the isothermal decompression path segment, the Ky-Sil stability boundary is crossed. With further decompression, the path crosses decreasing kyanite isomodes, so the modal proportion goes from about 5% to 3%. After the path turns sharply to the second segment, isobaric cooling, the Ksp-out boundary is crossed and sillimanite is grown since the path crosses increasing sillimanite isomodes. This path predicts the presence of both kyanite and sillimanite, which is observed in the modelled sample.

Path 2, being the compromise between the end-members, would initially experience more decompression than cooling, then progressively switch to more cooling than decompression. This path would likely only cross the Ksp-out boundary after 2.5 kbar of decompression and <20 °C of cooling, before the solidus and M2 assemblage are reached. Kyanite remains the stable aluminosilicate phase along this trajectory.

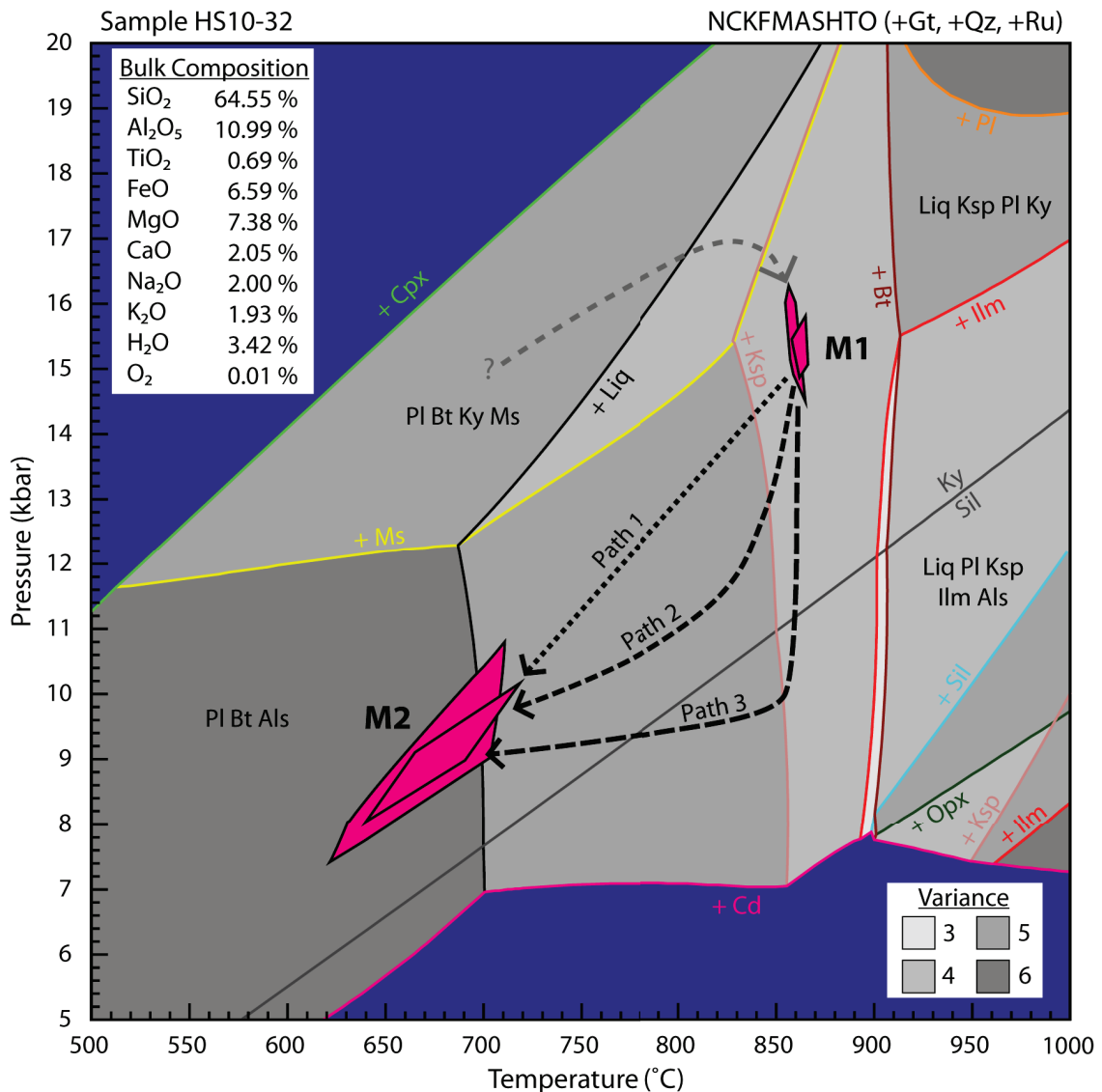
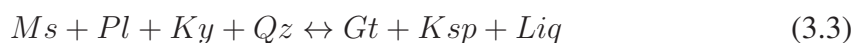


Figure 3.18: HS10-32 pseudosection  $P$ - $T$  paths. The retrograde  $P$ - $T$  path for HS10-32, from M1 to M2 equilibrium assemblages, can be interpreted in three different ways based on pseudosection interpretations: 1) a straight vector (short-dash black line), 2) a gently curved line with greater decompression over cooling close to M1, and greater cooling over decompression close to M2 (medium-dash black line), and 3) a sharply curved line with isothermal decompression from M1, followed by isobaric cooling to M2 (long-dash black line). Option 3 shares the most characteristics with the observed sample, and is therefore preferred as the retrograde path. The prograde path vector is only constrained by the observed absence of UHP mineral assemblages (ie, assemblages with Cpx) in the sample.

To choose which of the three modelled paths could produce features similar to those in the real sample, the modelled modes and phase boundaries must be linked to observed textures. The most obvious feature mentioned in the sample description (section 3.2.1), and only reflected by Path 3, is the presence of both kyanite and sillimanite in the rock. Kyanite is observed as inclusions in garnet, and as embayed porphyroblasts up to 3 mm long in the matrix. Sillimanite is seen in the biotite-rich matrix, helping to define the foliation, and partially pseudomorphing kyanite. Path 3 is the only path that reaches the sillimanite stability field. The path crosses decreasing Als, Gt, and Liq isomodes (ie, kyanite and garnet are partly consumed, and melt is progressively crystallized) during isothermal decompression, while increasing plagioclase and quartz isomodes are simultaneously crossed. Plagioclase and quartz are observed around embayed kyanite, but plagioclase is not typically associated with sillimanite. At the turning point of Path 3, plagioclase isomodes are at their highest while Als isomodes are at their lowest (Figures B.7 and B.5, respectively), therefore, the onset of sillimanite growth in the second segment of Path 3 is not matched by plagioclase growth. Biotite modes, however, increase dramatically along the second segment of Path 3, as garnet breaks down. Sillimanite and biotite modes increase together until M2, an association that is also observed in the real sample.

### **Pseudosection Summary**

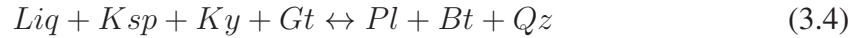
Modelled isomode and isopleth intersections, based on real analyses of the M2 assemblage, overlap on the solidus, proving that the pseudosection bulk composition is well constrained to that of the real sample (e.g. *Indares et al. 2008*; *Guilmette et al. 2011*). Due to the high metamorphic temperature experienced by this sample, it is unclear if the prograde garnet growth zoning patterns have homogenized or if garnet grew with a constant Grs component. This makes the prograde path and peak metamorphic pressure conditions difficult to constrain. However, prograde metamorphism likely involved muscovite dehydration to generate a melt phase and k-feldspar following the reaction:



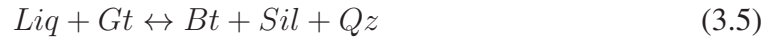
The topology, especially muscovite-in and solidus locations, suggests this sample lost melt prior to M1 assemblage equilibration (e.g. *Guilmette et al. 2011*). The M1 mineral assemblage, Liq + Gt + Bt + Pl + Ksp + Qz + Ky + Ru, has a modelled *P-T* intersection

estimate at  $860\text{ }^{\circ}\text{C} \pm 5\text{ }^{\circ}\text{C}$  and  $15.35\text{ kbar} \pm 0.25\text{ kbar}$ . The pseudosection  $P$ - $T$  estimates do not account for uncertainty in microprobe analyses, SEM imaging, or thermodynamic and  $a$ - $X$  relationship data from the internally consistent database.

Intersecting isomodes predict the modal proportions at the modelled M1 conditions, providing insight into textures and phases stable at those conditions. During isothermal decompression from the M1 conditions, this sample likely consumed K-feldspar and began melt crystallization following the reaction:



Isobaric cooling to the M2 assemblage  $Gt + Bt + Sil + Pl + Qz + Ru$  required complete melt crystallization and sillimanite growth following the reaction:



The textures relating to matrix phases and porphyroblast rims in the modelled sample correspond to final melt crystallization along the retrograde path, and yields a model  $P$ - $T$  intersection estimate at  $680\text{ }^{\circ}\text{C} \pm 40\text{ }^{\circ}\text{C}$  and  $9.1\text{ kbar} \pm 1.1\text{ kbar}$ .

### 3.4 P-T Results Summary

For the purpose of this study, estimating the  $P$ - $T$  conditions of peak temperature and retrograde assemblages is essential. Even more critical, however, is interpreting the retrograde path between the M1 and M2 assemblages. The forward-modelling approach of

<i>AvPT</i>	M1				M2			
	P (kbar)	$\pm$ (kbar)	T ( $^{\circ}$ C)	$\pm$ ( $^{\circ}$ C)	P (kbar)	$\pm$ (kbar)	T ( $^{\circ}$ C)	$\pm$ ( $^{\circ}$ C)
HS10-02	15.2	3.6	895	176	6.7	2.0	675	130
HS10-31	16.1	3.6	902	163	9.2	2.3	751	140
HS10-32	16.5	3.6	830	147	9.1	2.3	658	125
HS10-35	16.8	3.4	868	117	8.9	2.0	661	99
<i>Pseudosection</i>								
HS10-32	15.35	0.25	860	5	9.1	1.1	680	40

Table 3.4: Compared  $P$ - $T$  estimates from AvPT and pseudosection results. The AvPT results are useful as a first order estimate of the  $P$ - $T$  range, but the pseudosection provides unparalleled uncertainty constraints.

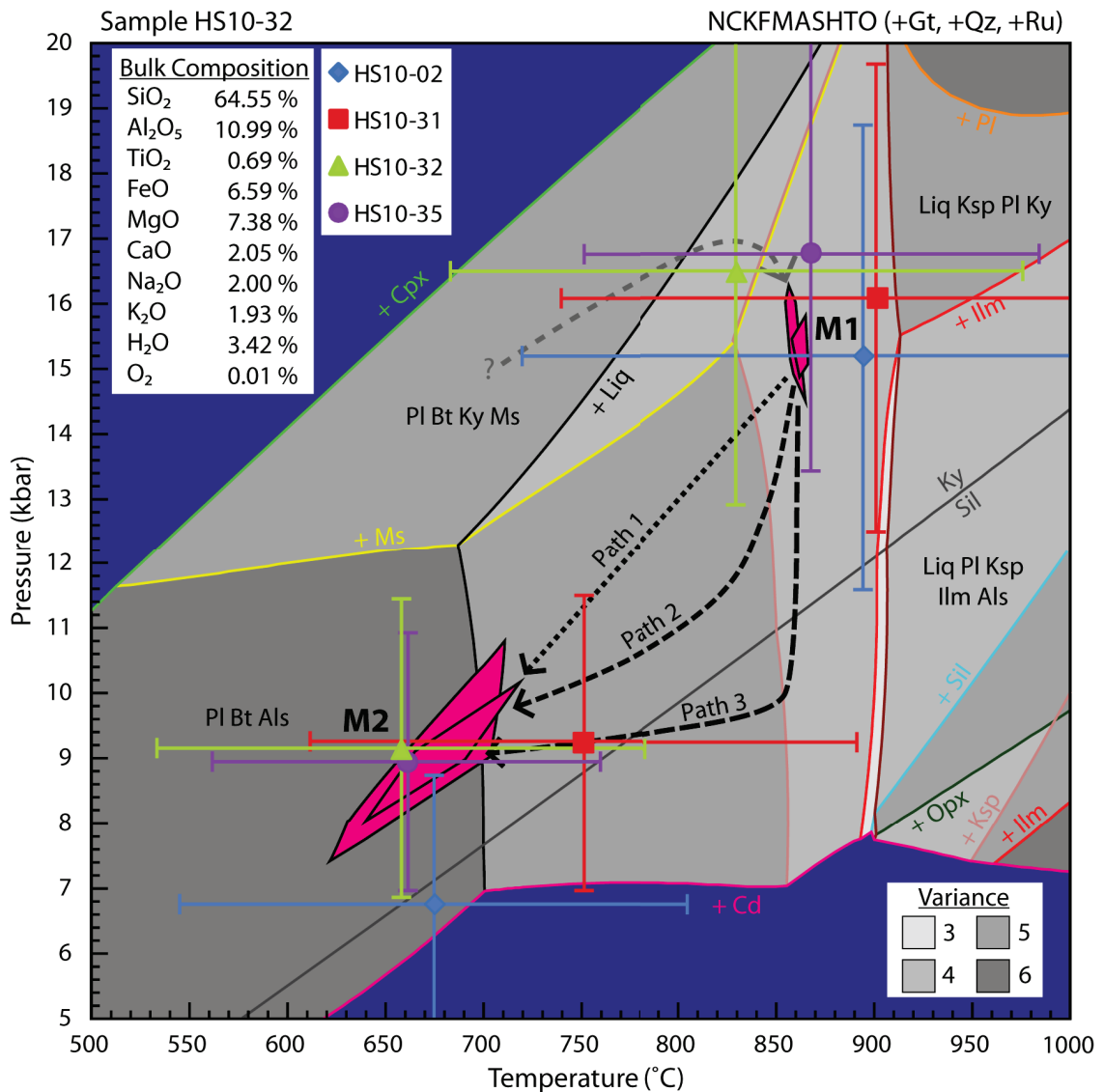


Figure 3.19: Compared  $P$ - $T$  estimates from AvPT and pseudosection results. The results from the AvPT multi-equilibrium phase modelling are overlain on the pseudosection for the model bulk composition of HS10-32 with unconstrained prograde path, M1 peak temperature assemblage, the three proposed retrograde paths, and the M2 retrograde assemblage. The magnitude of uncertainty in the AvPT calculations is several times greater in both axes than the M1 and M2 intersections. The AvPT peak temperature and retrograde assemblage results for HS10-32 overlie, within uncertainty, the modelled M1 and M2 assemblages of the pseudosection.

pseudosectioning yielded more precise results than the reverse-modelling multi-equilibria thermobarometry method (Table 3.4, Figure 3.19). Despite the additional time, analytical preparation, and costs, the pseudosection proved to be valuable by predicting peak

assemblage modes, and providing constraints on the M1 to M2 retrograde path.

The AvPT results were useful as first-order  $P$ - $T$  estimates since they overlap with the pseudosection estimates (Figure 3.19). However, the uncertainties were too large to constrain a  $PTt$  path. For the migmatitic aluminous gneiss samples, AvPT estimates ranged from  $15.2$ - $16.8 \pm 3.4$ - $3.6$  kbar and  $830$ - $902 \pm 117$ - $176$  °C for the M1 assemblage, and  $6.7$ - $9.2 \pm 2.0$ - $2.3$  kbar and  $658$ - $751 \pm 99$ - $140$  °C for the M2 assemblage. Pseudosection  $P$ - $T$  estimates, based on the modelled HS10-32 bulk composition, were  $15.35 \pm 0.25$  kbar and  $860 \pm 5$  °C for the M1 assemblage, and  $9.1 \pm 1.1$  kbar and  $680 \pm 40$  °C for the M2 assemblage (Table 3.4). The pseudosection results are compared to analyses on other *Blåhø Nappe* localities, and contrasted with basement lithologies in Chapter 5.

## CHAPTER 4

# GEOCHRONOLOGY: MICROPROBE MONAZITE AND $^{40}\text{Ar}/^{39}\text{Ar}$ AGES

The timing of metamorphic events as recorded by the *Blåhø Nappe* of the Nordøyane UHP domain is essential for derivation of the unit's metamorphic history, and for the interpretation of processes along a *PTt* path. By constraining the timing of growth of metamorphic mineral phases, and linking the age of specific new phases with observed geochemical, modal, or larger-scale physical changes in the unit, we can interpret the state of the tectonic environment at each age.

On Harøya and Finnøya, evidence of partial melting in the *Blåhø Nappe* is clear in outcrop. As discussed in Chapter 3, partial melting often begins at the temperature and pressure conditions required for dehydration melting of hydrous minerals, such as muscovite and biotite. The timing of crystallization of that melt phase and of new accessory phases or new rims on pre-existing accessory phases is constrained by dating the new accessory growths, commonly zircon and monazite. Electron microprobe analysis (EMPA) monazite dating was done to determine the minimum age of partial melt crystallization in the migmatitic pelitic gneiss of the *Blåhø Nappe* on Harøya. We expect the growth of this phase to be linked to the timing of peak temperature conditions experienced by the lithology (M1 conditions, Chapter 3).

To constrain the timing of cooling of both the Northern and Southern Domains,  $^{40}\text{Ar}/^{39}\text{Ar}$  dating of hornblende, biotite, and white mica samples was conducted. Cooling of the regionally metamorphosed WGR is generally associated with its exhumation through middle and shallow crustal levels (*Hacker et al.* 2010; *Walsh et al.* 2007). By comparing

$^{40}\text{Ar}/^{39}\text{Ar}$  ages from the Northern and Southern Domains, we can determine whether or not the two lithotectonic units cooled at the same time through upper crustal levels. Furthermore, comparing and contrasting the monazite crystallization ages with ages from the different  $^{40}\text{Ar}/^{39}\text{Ar}$  geochronometers will result in a crystallization and cooling history of the *Blåhø Nappe* migmatitic pelitic gneisses.

#### 4.1 Microprobe Monazite Dating

Monazite [La, Ce, LREE(PO<sub>4</sub>)] is a monoclinic accessory phase common in metaluminous to peraluminous granitoid rocks as well as high-grade pelitic metasedimentary rocks. It is a light rare earth element (LREE)-bearing phosphate that can contain significant amounts of U, Th, and heavy rare earth elements (HREEs), and minor amounts of Si, S, Ca, and Y (*Williams et al.* 2007). In the early 1990's, EMPA composition data from monazites were used to develop a new (U-Th)/Pb geochronometer (e.g. *Suzuki and Adachi* 1991). Since then the EMPA monazite method (*Montel et al.* 1996) has grown into an extremely useful and powerful tool to identify the age of crystallization for granitoid rocks and the timing of metamorphism in rocks of variable grade (*Williams and Jercinovic* 2002).

In metamorphic rocks, monazite generally grows from a crystallizing melt phase or during prograde metamorphism, commonly from xenotime [Y, HREE(PO<sub>4</sub>)] or allanite [(Ce, Ca, Y, La)<sub>2</sub>(Al, Fe<sup>+3</sup>)<sub>3</sub>(SiO<sub>4</sub>)<sub>3</sub>OH] breakdown. Throughout a rock's history, there may be several geologic events that promote monazite growth. With each growth stage new monazite may have a distinct major and trace element chemistry compared to previous generations. Each chemically distinct generation is called a domain, which may appear as chemical zoning on pre-existing grains, or as new individual grains. The chemistry of the monazite depends on the geologic environment, the changes in that environment (e.g., strain, heating versus cooling, burial versus decompression), the bulk rock chemistry, the stability of other mineral phases, and interaction with fluid or melt phases from outside the local system (*Spear and Pyle* 2010; *Kelsey et al.* 2008; *Williams et al.* 2007; *Pyle et al.* 2001).

The chemistry of each domain therefore records the geologic events that promote monazite growth. By comparing the chemistry of the domains with other mineral phases that contain the same major and trace elements, it is possible to link chemical changes in those phases with monazite growth. For example, after xenotime, garnet is a major



repository for HREE and Y. As a major phase in medium- to high-grade metamorphic rocks, garnet typically dictates the distribution and availability of HREE and Y in accessory phases. With the growth of garnet along a prograde path, the composition of synchronously growing monazite has relatively depleted HREE and Y concentrations. The opposite is true with garnet breakdown along a retrograde path. This relationship has been well documented in many case studies (*Pyle and Spear 2003; Pyle et al. 2001; and Terry et al. 2000a*) and is summarized by *Williams et al. (2007)*, and references therein. In addition to the geochemical links between monazite growth and compositions of other mineral phases, the EMPA method allows for *in situ* analysis. This is a major advantage compared to some isotopic geochronometers that use mineral separates, since the textural context of the dated grain is preserved throughout the analytical process.

#### 4.1.1 Background

##### Isotopic Decay and Monazite Chemistry

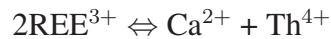
The EMPA (U-Th)/Pb monazite dating technique is based on the natural decay of both U and Th parent isotopes to their respective Pb\* daughter isotopes (\* denotes a radiogenic product). Through complex chains of intermediate daughter isotopes,  $^{232}\text{Th}$  decays to  $^{208}\text{Pb}$  with a half-life of 14.0 Ga,  $^{235}\text{U}$  decays to  $^{207}\text{Pb}$  with a half-life of 704 Ma, and  $^{238}\text{U}$  decays to  $^{206}\text{Pb}$  with a half-life of 4.47 Ga (*Dickin 2005*). The corresponding decay constants are  $0.494 \times 10^{10}$ ,  $9.85 \times 10^{10}$ , and  $1.55 \times 10^{10}$ , respectively. A microprobe cannot be used to measure individual isotopes of the same element, so the monazite age equation incorporates coefficients for the constant relative abundances of the parent and daughter isotopes in question. A single analysis age ( $\tau$ ) is determined by entering measured amounts of U, Th, and Pb into the Montel equation (*Montel et al. 1996*), and iteratively solving for  $\tau$ :

$$Pb = \frac{Th}{232} [exp(\lambda^{232}\tau) - 1] \cdot 208 + \frac{U}{238.04} 0.9928 [exp(\lambda^{238}\tau) - 1] \cdot 206 + \frac{U}{238.04} 0.0072 [exp(\lambda^{235}\tau) - 1] \cdot 207 \quad (4.1)$$

where Pb, Th, and U are concentrations in ppm, and  $\lambda^{232}$ ,  $\lambda^{235}$ , and  $\lambda^{238}$  are the radioactive decay constants of  $^{232}\text{Th}$ ,  $^{235}\text{U}$ , and  $^{238}\text{U}$ , respectively. This method assumes that the U/Th/Pb ratio has only changed with time due to radioactive decay, and that the decay

rates for each isotope are constant over geological time.

Compositional variation in monazite is commonly due to isomorphous chemical substitutions at either of two cation sites, or coupled substitutions at both sites. These are the A<sup>[9]</sup> and X<sup>[4]</sup> sites, with the latter typically the host of P<sup>4+</sup>. Isomorphous substitution may be simple, where REE<sup>3+</sup> ions (or Y<sup>3+</sup>) are replaced by other REE species, or more complex, where non-REE cations may replace REE cations in the A-site. One example of the latter is the common substitution:



referred to as the brabantite [Ca,Th(PO<sub>4</sub>)<sub>2</sub>] substitution. Compositions dominated by [Ca,Th(PO<sub>4</sub>)<sub>2</sub>] are called cheralite, one end-member of the ternary system that also includes monazite and huttonite [2ThSiO<sub>4</sub>]. A second, less common, cheralite-type substitution involves U<sup>4+</sup>, but there are no end-member U minerals that are isostructural or form solid-solutions with monazite. Typically, the Th/U ratio of monazite is >1.0 (*Williams et al.* 2007).

### U, Th, and Pb Retention and Diffusion in Monazite

The retention of a daughter isotope in any mineral is said to begin once the temperature experienced by that mineral cools below a temperature specific to the isotope and mineral combination in question. At this point the daughter product can no longer diffuse out of the mineral grain. This temperature is known as the ‘blocking temperature’ or ‘closure temperature’ ( $T_C$ ) and was defined by *Dodson* (1973) as:

$$\frac{E}{RT_C} = \ln \left( \frac{ART_C^2 D_o / a^2}{E \partial T / \partial t} \right) \quad (4.2)$$

where  $E$  is the activation energy of the diffusion process,  $R$  is the gas constant,  $A$  is defined by the geometry of diffusion (a sphere, cylinder, or plane sheet),  $D_o$  is the initial concentration of a diffusing element,  $a$  is the grain radius, and  $\partial T / \partial t$  is the cooling rate of the system. This theory assumes cooling from a high temperature so efficient diffusion allows daughter isotopes to escape the grain prior to reaching  $T_C$ .

The  $T_C$  for Pb in monazite is >900 °C (*Cherniak et al.* 2004), and the EMPA method assumes non-radiogenic Pb is negligible in monazite. However, a Pb end-member of cheralite [Pb,Th(PO<sub>4</sub>)<sub>2</sub>] has been successfully synthesized by *Montel et al.* (2006), so it

is incorrect to state that Pb is completely incompatible in natural monazite. Nevertheless, typical natural monazite compositions contain very little inherited Pb. Fortunately, monazite incorporates and retains radioactive elements and their daughter products exceptionally well, making this mineral ideal for geochronologic applications. Furthermore, the slow diffusion rates of many elements through the crystal lattice, the refinement of *in situ* analytical EMPA techniques, and the increasing understanding of crystallization and recrystallization conditions can link monazite growth with petrological assemblages and geochemical changes seen in the rest of the rock (*Williams et al.* 2007).

This method is primarily limited by the assumed age of the sample: young samples may have very low concentrations of Pb\*, making detection difficult and count times longer. Samples can be significantly burned by the high beam current, so application of heat-dispersing film coatings, such as double-carbon or gold, is important to reduce beam damage. Additionally, standard calibration and peak overlap corrections are complex tasks that can generate unnecessary error if improperly done. However, it is possible to run at least one hundred analyses within a single day using the EMPA technique. Analysis of five to ten points within the same chemical zone of a single grain can achieve an age error as low as 1% at the  $2\sigma$  level given adequate counting statistics and calibration (*Williams et al.* 2007). While other dating techniques, such as the isotopic U-Pb TIMS method, produce higher-precision ages, EMPA monazite dating is commonly performed when textural relevance is important to consider or when small spot sizes (down to 5  $\mu\text{m}$  diameter) are required.

#### 4.1.2 *Sample Preparation*

Field photographs and notes, including a GPS location, for each sample were collected at the time of sampling. Hand samples were typically less than 1 kg, depending on grain size and abundance of the targeted mineral. A thin and polished section were made from each sample, and petrographic analyses conducted to establish which samples are suitable for dating. Monazite was identified in several pelitic samples but dating was only carried out on samples HS10-32 and HS10-35. These samples in particular have abundant monazite grains that are large enough for multiple analyses. In both samples, monazite is only present in the matrix (Appendix C), while other accessory phases, such as zircon and apatite, exist in both the matrix and porphyroblastic garnet. Other REE-bearing minerals, such as allanite and xenotime, were not observed. Hand sample locations and petrographic

descriptions are in Figure 2.1, and sections 3.5 and 3.7, respectively.

Polished thin sections were cleaned and repolished with  $<25 \mu\text{m}$  diamond polishing paste. This was done to remove unwanted Pb from the lap used in the initial polishing routine from cracks and grain boundaries in the sections. Since Pb is one of the elements used in calculating monazite ages, Pb contamination on the thin section surface can produce major analytical problems, namely an overestimation of the calculated age. Aside from repolishing, the sample must also be handled with care, avoiding contact with instruments and tools that may contain Pb.

The repolished sections were double carbon-coated to a thickness of approximately 40 nm. This increases thermal and electrical conductivity across the section, therefore decreasing the likelihood of beam damage on the polished mineral surface. Damage to the thin section surface can occur after long periods of beam exposure at high current densities (Williams *et al.* 2007).

#### 4.1.3 EMPA Monazite Analysis

All major element analyses were conducted on the JEOL 8200 electron microprobe, with an accelerating voltage of 15 kV and a beam current of approximately 20 nA. Monazite X-ray mapping and trace element analyses required a beam current of 200 nA. Trace element analysis also required extended dwell times for peak and background measurements, as described by Gagnè (unpublished M.Sc. thesis, Dalhousie University, Halifax, N.S., 2004) and Gagné *et al.* (2009).

Analyses were focused on 16 grains in sample HS10-32 and the 6 largest grains in sample HS10-35. Grains from HS10-32 range in size from 50 to 150  $\mu\text{m}$ , while HS10-35 monazites are 20 to 80  $\mu\text{m}$ . BSE images and chemical maps of U, Th, Pb, and Y were made to define compositional zones within every grain. Initially, three domains were identified in both samples: high Th cores, low Th/high Y rims, and Y-rich rims. The Y-rich rims in HS10-35 are much too small and rare for reliable analysis.

Quantitative analyses for major (Appendix C.2) and trace (Appendix C.4) elements were collected following the protocol outlined by Gagnè (unpublished M.Sc. thesis, Dalhousie University, Halifax, N.S., 2004), and modifications by Warren (2007, personal communication). For each domain in each sample, major element oxide wt% values were converted to element wt% and entered as fixed weights (except for U, Th, Pb, and Y) into the trace element quantitative analysis conditions. Also, background scans for U,

Th, Pb, and Y (Appendix C.3) were generated to constrain the spectrometer positions of background noise on both sides of each peak. With these conditions fixed, trace elements were then analyzed. Unfortunately, problems with stage position reproducibility were encountered when age analyses were attempted on the thin Y-rich outermost rims. Therefore, trace element analyses in this domain were contaminated with adjacent mineral phases. The successful trace element analyses were used with the Montel equation (4.1) to determine a date from each analysis. Analytical errors were rigorously propagated through the age equation following *Gagnè* (unpublished M.Sc. thesis, Dalhousie University, Halifax, N.S., 2004), and subsequent statistical analyses of the age data, which follow the format and presentation suggested by *Williams et al.* (2006).

Monazite consistency standard GSC 8153 was analyzed before, during and after acquiring each round of major and minor element analyses in each domain of HS10-32 to monitor uncertainty in the accuracy of data collection. For HS10-35, Monazite 53 was analyzed as the consistency standard during major and minor element data collection. Because the minor element analyses are constrained by keeping major element concentrations constant, and the major elements are based on the monazite chemistry from each sample domain, the calculated ages of the GSC standard is not necessarily comparable to the accepted  $489 \pm 8$  Ma age (*Williams et al.* 2006). The major and minor element data, and calculated ages from the standard analyses are presented in Appendix C.5.

#### 4.1.4 EMPA Monazite Ages

After compiling the major and trace element data from each correlative domain, it became apparent that there are actually *four* chemical domains in HS10-32: high-Th core, moderate-Th and -Y inner rim, low-Th and high-Y outer rim, and Y-rich outermost discontinuous rim. The four chemical domains were not documented together in a single grain. In most cases the core and one of the rim domains were observed with the thin Y-rich outermost film, or the inner rim domain was observed as the center of a grain surrounded by the outer rim and a discontinuous Y-rich outermost film (Figure 4.4). Because the four domains were not recognised until after ages were calculated, results in the following section are described according to the initial three-domain interpretation.

Monazites in the two rock samples (Appendix C.4) were analyzed approximately four weeks apart, under different microprobe calibration conditions. Differences observed in the propagated errors from one sample to the other are likely due to this recalibration.

## Major Element Analyses

Monazite in both samples has the formula  $[\text{Ce}_{0.4}, \text{La}_{0.2}, \text{Nd}_{0.2}, \text{REE}_{0.2} \text{PO}_4]$ , where REE primarily refers to the elements filling the remaining A sites, including variable proportions of Pr, Sm, Gd, Eu, Dy, Th, U, Y, Si, and Ca. In general, the most obvious chemical differences between the two samples are in the REE (or A site) and S (which substitutes for P in the X site) concentrations. Considering all domains, HS10-32 has <0.6 wt% CaO, <2.5 wt%  $\text{Y}_2\text{O}_3$ , and 0.8-1.6 wt%  $\text{SO}_2$  (Figure 4.1). In contrast, HS10-35 monazite has a larger CaO component (0.8-1.5 wt%, plus two analyses with 2.5 wt%), and smaller components of  $\text{Y}_2\text{O}_3$  (<0.2 wt%) and  $\text{SO}_2$  (<0.1 wt%). These differences likely reflect the differences in bulk composition of the samples (see Chapter 3) and possibly compositions of melt phases from which the monazite may have crystallized.

The oxide concentrations that show the greatest variation between domains in sample HS10-32 are  $\text{ThO}_2$ ,  $\text{Y}_2\text{O}_3$ , and  $\text{Gd}_2\text{O}_3$ . From core to rim,  $\text{ThO}_2$  decreases from almost 8.0 wt% to 3.0 wt%.  $\text{Y}_2\text{O}_3$  is <0.4 wt% in the core and inner rim domain, but increases up to 2.5 wt% in the Y-rich rim domain.  $\text{Gd}_2\text{O}_3$  increases from 0.2 wt% in the core domain to almost 2.0 wt% in the Y-rich rim domain. Variation of other oxide species is less pronounced (<1.5 wt% change), but locally show increasing  $\text{Sm}_2\text{O}_3$ ,  $\text{Eu}_2\text{O}_3$ , and  $\text{UO}_2$  or decreasing  $\text{SO}_2$  from core to rim.

In sample HS10-35,  $\text{ThO}_2$  shows the greatest variation between domains, from almost 7.0 wt% in the core to 2.6 wt% in the moderate-Th, Low-Y rim domain. Interestingly, the two lowest  $\text{ThO}_2$  concentrations correspond to the high CaO values in the rim domain. The high CaO values may also be attributed to x-ray interference from adjacent mineral phases (e.g., plagioclase) if the probe beam was placed too close to the edge of the grain (grain 40, for example; Appendix C.1). This sample generally shows similar small scale variations and trends in concentrations to those in HS10-32.

## Trace Element Analyses and Ages

Excluding the high-Y rim domain because of the stage position reproducibility problems, four groups of trace element analyses were acquired based on the sample and the chemical signatures seen in monazite maps and major element analyses: high Th (denoted HT in analysis point names) and low Th (denoted LT or LTA in analysis point names) groups in both HS10-32 and HS10-35. This resulted in four datasets from which individual analysis ages were calculated. By compiling the ages and comparing the results with the

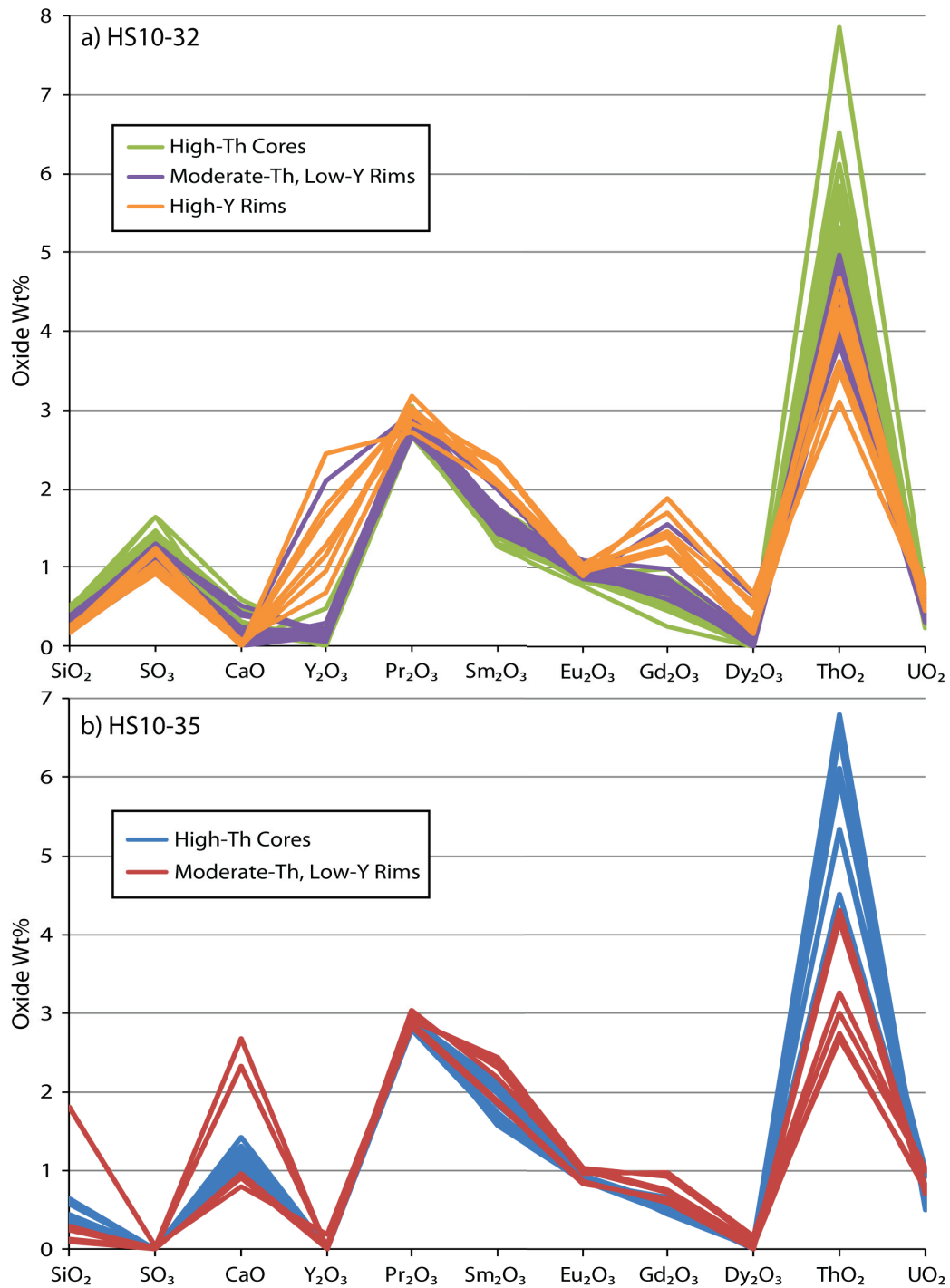


Figure 4.1: Major element chemistry of monazite domains. Domains in HS10-32 (a) and HS10-35 (b) were initially defined by chemical maps. Major differences are seen in the amounts of CaO, Y<sub>2</sub>O<sub>3</sub>, and SO<sub>2</sub> between the two samples. These differences may reflect the bulk chemistry of each sample, or the chemistry of fluids from which the monazite grew. Both samples show a decrease in ThO<sub>2</sub> and increases in Sm<sub>2</sub>O<sub>3</sub> and Eu<sub>2</sub>O<sub>3</sub> from core to rim. See Appendix C.2 for major element data sets.

major element trends and domain definitions seen in the chemical maps, four chemical domains in HS10-32 were distinguished, corresponding to three age domains, separated into two analytical groups (HT and LTA). Therefore, the individual spot analyses from HS10-32 had to be separated into three groups: core, inner rim, and outer rim domains. The spot analyses from HS10-35 with correlative major element results were combined with the appropriate newly defined HS10-32 age groups (Figure 4.4, Table 4.1, Appendix C.1).

The ages from each domain were plotted as Gaussian (normal) probability distributions (Figure 4.4). The standard deviation of the mean (SDOM, or width of the distribution) for each dataset is an indication of the short-term random error at the time of data acquisition, which comes from (but is not limited to) x-ray production variation, thermal effects during analysis such as burn damage, subtle compositional variations, and stage drift. It is important to remember, however, that these datasets were acquired at *different times*, and that the microprobe had been recalibrated between analysis of the two samples. This may have introduced short-term systematic error to the datasets, which is also reflected in the large SDOM. To minimize the effects of short-term systematic error, the weighted mean age (WMA) was calculated for each of the chemical domains. A weighted uncertainty ( $2\sigma_w$ ) was also calculated with the associated uncertainty of each measurement, as propagated through the age equation, as the weight (Figure 4.4; Taylor, 1997). Analyses of monazite standards (Appendix C.5) provide an estimate of the external analytical reproducibility. Based on the standard deviation of consistency standard ages the analytical reproducibility is  $\sim 2.5\%$  (ca.  $\pm 13$  Ma for these samples).

The core domain is characterized by relatively high Th/Y and low U/Th (Figure 4.3). It has a WMA of  $426.5 \pm 1.7$  Ma, calculated from 17 individual analyses from both samples. The relatively small  $2\sigma_w$  uncertainty (1.7 Ma) calculated for this domain cannot account for the wide range in ages (low accuracy) that contribute to the SDOM (14.1 Ma). This indicates that the ages and associated errors are independently precise, but their compilation as a dataset does not produce a typical Gaussian distribution. There is likely a geological, rather than statistical, explanation for this wide age range, as discussed further below and in Chapter 5.

The inner rim domain has relatively lower Th/Y compared to the core domain, yet slightly higher Th/U (Figure 4.3). The WMA for the inner rim domain is  $400.1 \pm 1.4$  Ma



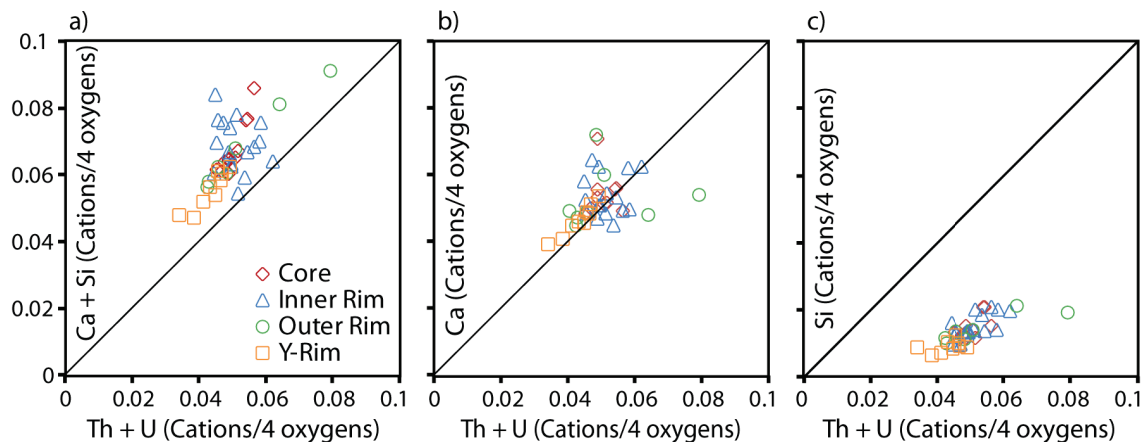


Figure 4.2: Paired Si + Ca and Th + U substitution in HS10-32 domains. The solid black line in each plot represents the hypothetical case of perfect substitution with a slope of 1. a) The higher relative abundance of Ca + Si compared to Th + U is likely due to the natural decay of the latter to Pb since crystallization. The plot of Ca in b) shows that brabantite is the dominant substitution for all monazite age domains given the fit of data close to the theoretical line. Huttonite substitution (c) is less significant in this sample.

based on 15 independent analyses from both samples. It also has a greater SDOM (7.5 Ma) compared to the  $2\sigma_w$  uncertainty (1.4 Ma).

The outer rim domain has the lowest Th/Y and highest U/Th, relative to the core and inner domains (Figure 4.3). The WMA for the outer rim domain is  $383.7 \pm 1.2$  Ma with 22 independent analyses from HS10-32. Again, the SDOM (5.7 Ma) is greater than the  $2\sigma_w$  uncertainty.

All three age domains are characterized by SDOM values that are larger than the  $2\sigma_w$  uncertainties. As mentioned above, the reason for this is likely geological. The core domain monazite is interpreted to have grown prior to high-grade metamorphism and melt generation in these rocks. Therefore, growth was strictly dependent on relatively slow intergranular diffusion processes, and limited by the availability of major (and minor) elements to those that are highly incompatible in most other mineral species. A slow monazite growth rate, and therefore variable core domain ages, suggests new monazite growth throughout a prolonged tectonic process. The core domain ages appear to have a bimodal distribution (Figure 4.4). This reflects two periods of favourable conditions for monazite growth, maybe due to changing  $P$ - $T$  conditions and partial breakdown of previously stable REE-bearing minerals (e.g., xenotime).

The probability distributions of the inner and outer rim domains have small shoulders

Sample	Domain	Y (ppm)	SD (ppm)	Th (ppm)	SD (ppm)	U (ppm)	SD (ppm)	Pb (ppm)	SD (ppm)	Age (Ma)	2 $\sigma$ (Ma)	n
HS10-32	HT	1983	232	41404	2140	3654	566	986	29	386.5	5.4	7
HS10-32	LT	1963	337	39086	2204	3789	500	879	48	383.8	5.7	15
<b>Weighted Mean Age <math>\pm 2\sigma</math></b>												
										<b>383.7</b>	<b>1.2</b>	
HS10-32	HT	1826	495	44254	7869	3305	865	1016	141	400.2	5.7	11
HS10-32	LT	1925	340	38080	1920	3515	724	885	29	399.4	6.2	4
HS10-35	HT	1325	1718	46895	19636	6585	1308	1275	311	407.1	15.6	2
HS10-35	LT	305	247	38605	4674	6395	1336	1110	49	405.9	12.0	2
<b>Weighted Mean Age <math>\pm 2\sigma</math></b>												
										<b>400.1</b>	<b>1.4</b>	
HS10-32	HT	1658	724	46256	8008	3297	754	1015	135	427.8	5.9	11
HS10-35	HT	460	274	48390	2986	6097	932	1243	32	422.3	16.6	3
HS10-35	LT	1356	474	33877	5155	6170	1051	977	61	420.8	19.8	3
<b>Weighted Mean Age <math>\pm 2\sigma</math></b>												
										<b>426.5</b>	<b>1.7</b>	

Note: SD = standard deviation; n = number of analyses; HT = high Th; LT = low Th

Table 4.1: EMPA average compositions of age domains in monazite and calculated ages

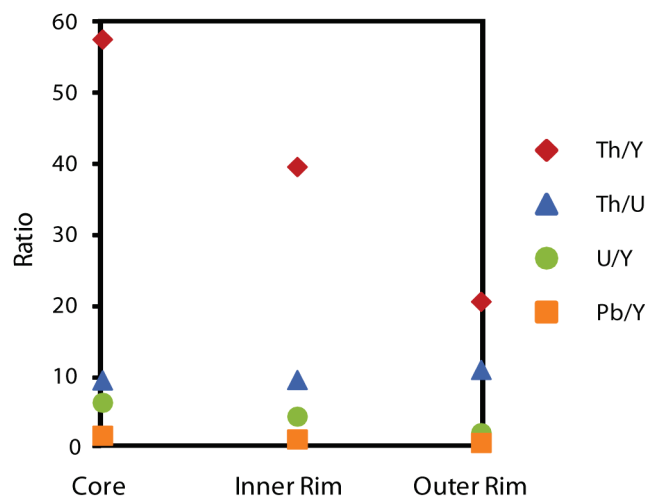


Figure 4.3: Ratios of trace element concentrations in monazite domains. These ratios are weighted mean averages of data found in Table 4.1. The negative slope of Th/Y indicates an increasing Y concentration and decreasing Th concentration from core to rim. The Th concentration also decreases relative to U, as shown by the slight positive slope of Th/U from core to rim.

around 410 Ma and 375 Ma, respectively (Figure 4.4). It is unclear if these small clusters of ages represent significant geologic events, or if they are a product of limited data sampling. Perhaps more age analyses within these chemical domains would fill out the distribution to create a more uniform peak. The overlap of all three age domains in Figure 4.4 implies monazite stability and growth, at varying rates, over most of the age range. The geochemical characteristics of each domain, however, reflect changes in the mineralogy due to metamorphism. The links between these monazite age domains and changing metamorphic conditions are discussed in detail in Chapter 5, along with the geological interpretation and regional significance of these ages.

## 4.2 $^{40}\text{Ar}/^{39}\text{Ar}$ Geochronology

### 4.2.1 Background

Potassium was shown to be a radioactive element through experiments done after the turn of the 20th century; however, it was not until the 1940's when the decay of parent  $^{40}\text{K}$  to its stable  $^{40}\text{Ar}^*$  daughter product was recognized as a reliable geochronometer (Aldrich and Nier 1948). Since this discovery, the K/Ar dating method has become an extremely versatile application. The original protocol requires the measurement of each isotope be

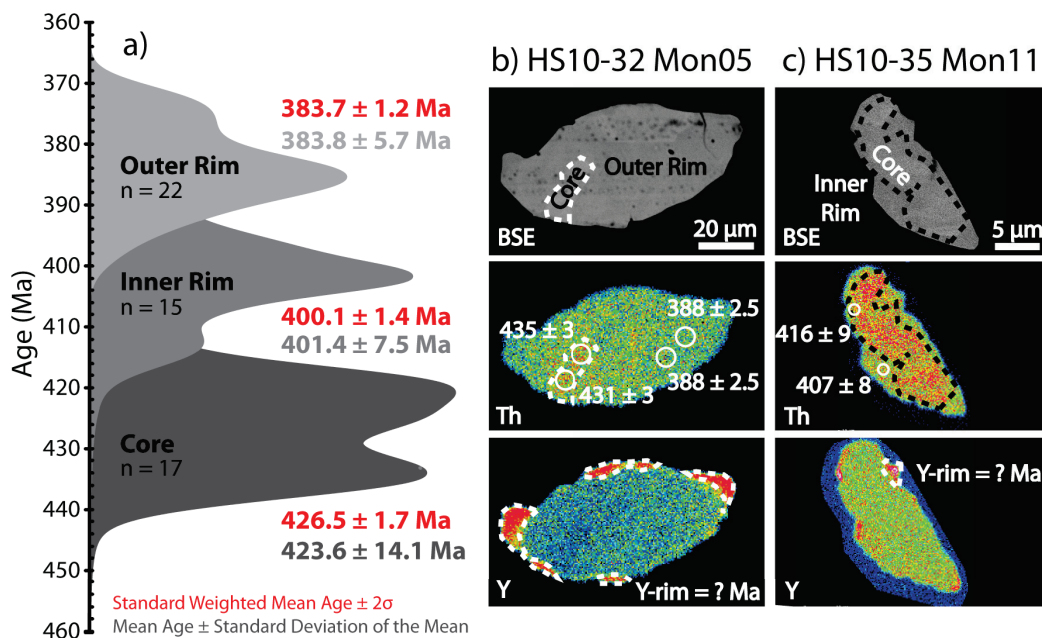


Figure 4.4: Probability distributions and monazite domain ages. a) Probability distributions (shaded grey) of all ages and normal distributions (red) of the weighted mean age with two standard deviations ( $2\sigma_e$ ) are for EMPA monazite minor element analyses of each chemical domain. b) and c) Backscatter electron images (BSE), and Th and Y chemical maps for monazite grains from sample HS10-32 and HS10-35, respectively, show three dated chemical domains with individual analysis locations and dates. The fourth, high-Y domain of unknown age is outlined by the white dashed lines in the Y maps.

done on separate portions of an individual sample. The total K can be measured from one sample portion by using flame photometry or atomic absorption spectroscopy, and the  $^{40}\text{K}$  concentration is calculated based on the known natural isotopic abundance ratios. The Ar concentration is determined by diluting the second sample portion with a known amount of  $^{38}\text{Ar}$  tracer gas, then heating the sample in a furnace under a vacuum with a gas extraction line. The total abundance of Ar gas is determined by mass spectrometry, and  $^{40}\text{Ar}^*$  is calculated using the known isotopic abundance ratios. Because the K-Ar method uses two portions of one sample, be it a single large mineral grain or several smaller grains, one must make the assumption that each portion is chemically identical (*McDougall and Harrison 1999*).

In the mid-1960's an entirely new approach to K/Ar dating was developed when production of  $^{39}\text{Ar}$  from applied neutron interactions on  $^{39}\text{K}$  was identified (*Merrihue*

1965; *Merrihue and Turner* 1966). This new geochronometer was called the  $^{40}\text{Ar}^*/^{39}\text{Ar}_K$  method (also denoted as  $^{40}\text{Ar}/^{39}\text{Ar}$ ), and proved to be a more precise adaptation of the K/Ar method. The  $^{40}\text{Ar}/^{39}\text{Ar}$  protocol requires only a single sample for analysis of both Ar isotopes, eliminating the assumption of chemical homogeneity and resulting in significantly reduced analytical uncertainties compared to the K/Ar method. Among the first  $^{40}\text{Ar}/^{39}\text{Ar}$  data to be published were cooling ages of lunar basalts recovered from the Apollo 11 mission (*Turner* 1970). Today, this geochronometer is widely used to provide cooling ages of minerals from metamorphic terranes, basalt flows, and igneous intrusions, for example.

### Isotopic Decay and Mineralogical Theory

To decipher the meaning behind each analytical age result, the concepts of radiogenic decay series, retention of isotopes in different mineral lattices, and the rates and effects of pressure and temperature on atomic diffusion must be understood. These processes all factor into the calculated analytical age, and therefore must be considered when interpreting the results.

Potassium (atomic number 19) exists naturally as three isotopes: stable  $^{41}\text{K}$  (6.7%), stable  $^{39}\text{K}$  (93.3%), and the radioisotope  $^{40}\text{K}$  (0.012%; *Garner et al.* 1975) which has a dual-decay sequence (4.5). It will decay to stable  $^{40}\text{Ar}^*$  10.48% of the time by electron capture (inverse  $\beta$ -decay) (*Kelley* 2002). This requires the capture of an inner atomic electron by a proton-rich nucleus, creating a new neutron and emitting an electron neutrino. The radiogenic decay of  $^{40}\text{K}$  to  $^{40}\text{Ar}^*$  has a half-life of  $1.248 \times 10^9$  years (*Kossert and Günther* 2004). Alternatively,  $^{40}\text{K}$  will decay to  $^{40}\text{Ca}^*$  89.52% of the time, but this is done by  $\beta$ -decay where a neutron is converted into a proton with the emission of an electron and an antineutrino (*Kelley* 2002). The decay of parent  $^{40}\text{K}$  to daughter  $^{40}\text{Ar}^*$  is represented by the equation:

$$t = \frac{1}{\lambda} \ln \left( \frac{^{40}\text{Ar}^*}{^{40}\text{K} \times 0.109} + 1 \right) \quad (4.3)$$

where  $\lambda$  is the decay constant for  $^{40}\text{K}$  ( $5.5 \times 10^{-10} \text{ yr}^{-1}$ ),  $^{40}\text{Ar}^*$  and  $^{40}\text{K}$  are the measured concentrations, and the constant 0.109 is the fraction of  $^{40}\text{K}$  that decays to argon.

Argon is an inert noble gas (atomic number 18) with 24 different isotopes, from  $^{30}\text{Ar}$  to  $^{53}\text{Ar}$ , and one isomer  $^{32m}\text{Ar}$ . Stable isotopes include  $^{36}\text{Ar}$ ,  $^{38}\text{Ar}$ , and  $^{40}\text{Ar}$  ( $^{40}\text{Ar}$  alone comprises 99.6% of all naturally occurring argon).  $^{39}\text{Ar}$  has the longest half-life, at 269

years, and undergoes  $\beta$ -decay to stable  $^{39}\text{K}^*$  (Figure 4.5).  $^{39}\text{Ar}$  is produced naturally by cosmic ray interaction with primarily atmospheric  $^{40}\text{Ar}$ , and by neutron capture within  $^{39}\text{K}$  or electron emission from Ca isotopes in the subsurface environment. In nature, the ratio of  $^{39}\text{Ar}$  to total argon is extremely low ( $8.0 \times 10^{-10} \mu\text{g/g}$  or ppm). This relationship underlies the development of the  $^{40}\text{Ar}/^{39}\text{Ar}$  dating method.

Bombardment of stable  $^{39}\text{K}$  with fast neutrons artificially creates  $^{39}\text{Ar}_K$  (subscript denotes artificial creation) by inverse  $\beta$ -decay. Since the relative abundance of naturally occurring  $^{39}\text{K}$  is known and the abundance of naturally occurring  $^{39}\text{Ar}$  is negligible, measurement of  $^{39}\text{Ar}_K$  can be used as a proxy for the amount of stable  $^{39}\text{K}$ , and in turn for the amount of parent  $^{40}\text{K}$ .  $^{40}\text{Ar}^*$  and  $^{39}\text{Ar}_K$  are analysed at the same time (*Merrihue and Turner* 1966), eliminating the need to split a sample for two different isotope measurement techniques. This is the basis of the  $^{40}\text{Ar}/^{39}\text{Ar}$  dating method, which is further described in section 4.2.3.  $^{40}\text{Ar}^*$  and  $^{39}\text{Ar}_K$  abundances are used to calculate a sample age with the decay equation:

$$t = \frac{1}{\lambda} \ln \left( 1 + J \frac{^{40}\text{Ar}^*}{^{39}\text{Ar}_K} \right) \quad (4.4)$$

where  $\lambda$  is the decay constant of  $^{40}\text{K}$  (approximately  $5.5 \times 10^{-10} \text{ yr}^{-1}$ ),  $J$  is a factor associated with the irradiation process ( $J$ -value), and  $^{40}\text{Ar}^*/^{39}\text{Ar}_K$  is the analysed ratio after  $t$  years of decay (*Merrihue and Turner* 1966).

### Argon Retention and Diffusion in Minerals

All minerals or whole rock samples that contain K can, in principle, be used for  $^{40}\text{Ar}/^{39}\text{Ar}$  dating. In practice, however, there are certain limitations that must be considered when attempting to date some samples. The sample must first contain detectable concentrations of potassium and radiogenic argon. For a meaningful result the radiogenic argon must be retained within the sample since it first started being produced, which is commonly dictated by the temperature history of its geological environment. The most useful minerals contain potassium as an essential cation in lattice sites. Minerals regularly used in  $^{40}\text{Ar}/^{39}\text{Ar}$  dating include potassium-feldspar, plagioclase, micas, and amphiboles. Whole rock samples and clays are less commonly used except in certain circumstances, such as provenance studies (*McDougall and Harrison* 1999).

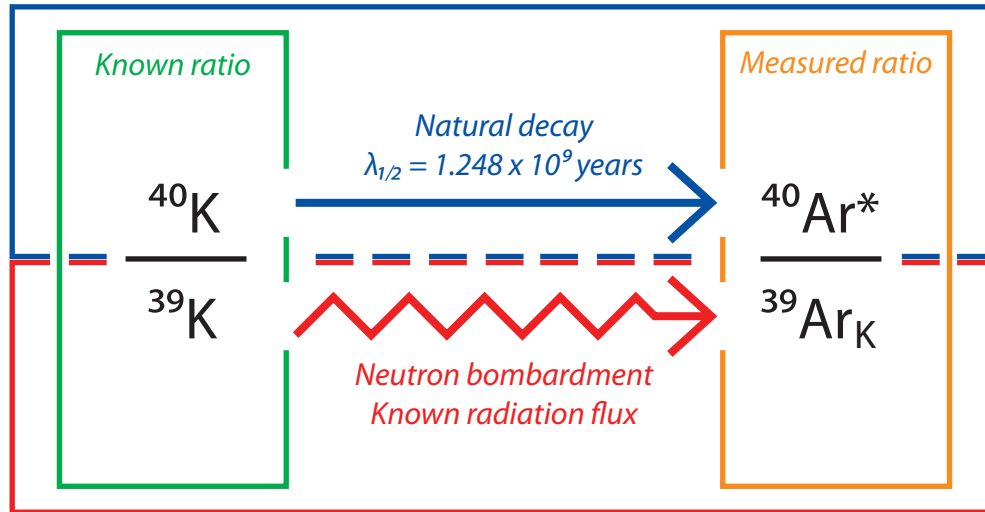


Figure 4.5:  $^{40}\text{Ar}/^{39}\text{Ar}$  dating theory. The initial concentration of parent  $^{40}\text{K}$  in a mineral or rock sample at the time of  $^{40}\text{Ar}^*$  closure must be determined to calculate the age of that sample. The  $^{40}\text{Ar}^*/^{39}\text{Ar}_K$  ratio (orange) is measured by mass spectrometry. Using the known neutron flux applied to the sample during irradiation to artificially create  $^{39}\text{Ar}_K$  from stable  $^{39}\text{K}$  (red),  $^{39}\text{Ar}_K$  becomes a proxy for the original  $^{39}\text{K}$  present in the sample. Because the ratio  $^{40}\text{K}/^{39}\text{K}$  is constant and known (green), the amount of parent  $^{40}\text{K}$  in the sample can be inferred. With this information,  $t$  is the only remaining unknown in the standard decay equation (4.3) for natural decay of  $^{40}\text{K}$  to  $^{40}\text{Ar}^*$  given a half-life of 1.248 billion years (blue).

A mineral's ability to retain argon depends upon its composition and chemical structure, thermal history and cooling rate, fluid flow interactions, and the grain's shape and size. Changes in argon concentration follow Fick's Law of Diffusion:

$$J = -D \frac{\partial \phi}{\partial x} \quad (4.5)$$

which states that the flux of an element ( $J$ ) will go from regions of high concentration to regions of low concentration with a magnitude proportional to the concentration gradient (the spatial derivative of volumetric concentration  $\phi$  by the distance of diffusion  $x$ ), and the diffusion coefficient of the medium ( $D$ ) (Fick 1855). Provided that the mineral has not cooled below  $T_C$  for given conditions, diffusion is possible within that mineral at a rate proportional to the temperature of the system, the element's concentration gradients inside and outside of the grain, and the crystal structure. For  $^{40}\text{Ar}^*$  the  $T_C$  is approximately 500 °C in hornblende (Harrison 1981), 400 °C in white mica (Harrison *et al.* 2009), and 325

°C in biotite (*Grove and Harrison 1996*). These estimates are based on  $\sim 80\mu\text{m}$  grains and  $5\text{ }^\circ\text{C}/\text{Myr}$  cooling rate. Faster cooling rates lead to higher  $T_C$  estimates.  $^{40}\text{Ar}^*$  diffusion in these minerals is commonly affected by intragrain exsolution and mineral impurities.

Diffusion (or retention) of argon in minerals that are subjected to metamorphism may be affected by changing pressure conditions. For instance, ultrahigh-pressure metamorphic terranes have reported extraneous, or excess, argon in dated minerals such as white mica or biotite (e.g., *Hacker and Wang 1995*; *Arnaud and Kelley 1995*). In these cases, 'parentless'  $^{40}\text{Ar}^*$  accumulates in the datable mineral if the external argon concentration is higher than that within the mineral. The result of extraneous  $^{40}\text{Ar}^*$  in a mineral sample is an age that is too old to be interpreted as a cooling age (e.g., *Warren et al. 2012*). This problem is usually only recognized after the samples have been dated, typically by the U-shape of the resulting age spectrum. Alternatively, old ages in (ultra)high-pressure metamorphic rocks may indicate that the experimentally-derived diffusion parameters  $E$  and  $D_o$  are invalid, possibly due to the higher pressure or differences in mineral compositions (*Warren et al. 2012*).

#### **$^{40}\text{Ar}/^{39}\text{Ar}$ Dating Methods and Age Interpretation**

A  $^{40}\text{Ar}/^{39}\text{Ar}$  date can be interpreted to represent the time of cooling after initial crystallization of the host mineral from an igneous melt. Metamorphism, with temperatures in excess of  $T_C$ , of K-bearing rocks or minerals can reset the  $^{40}\text{Ar}/^{39}\text{Ar}$  system by diffusing all  $^{40}\text{Ar}^*$  accumulated since initial crystallization. The age of the sample would then be interpreted to represent the time of cooling after the metamorphic event. When metamorphic conditions do not exceed  $T_C$ , partial diffusion of pre-existing  $^{40}\text{Ar}^*$  may occur. This can result in argon concentration zoning in a mineral grain (*Warren et al. 2012*), making interpretation of the age data more complicated.

To determine whether a mineral contains excess argon or has lost some of its accumulated  $^{40}\text{Ar}^*$ , the sample can be spot-dated with a UV laser, rather than step-heated in a furnace. Laser spot-dating requires a coarse enough grain size so that multiple spot analyses can be performed in a traverse across the grain. The spot size must be large enough to extract measurable quantities of Ar gas, but the analysis locations along the traverse must also be considered to optimize spot density without overlap or grain boundary effects. Each spot produces a date which can be plotted against the respective traverse location to create a diffusion profile across the mineral. If the ages young from rim to core,



it may indicate the presence of excess argon within the grain. Alternatively, if the ages young from core to rim, the sample may have experienced partial diffusive loss of  $^{40}\text{Ar}^*$ .

To determine whether the dated mineral will constrain the timing of crystallization or metamorphism (provided no excess argon is present or incomplete diffusion of argon has occurred), it is important to have an estimate for the timing and temperature of crystallization, the *P-T-t* path experienced since crystallization, and the expected cooling age the grain would have given an open system following crystallization (Warren *et al.* 2012). Warren *et al.* (2012) investigated the predicted Ar retention of white mica for specified pressure and temperature histories. Using numerical modelling, they predicted the *P-T* region where argon may be efficiently diffused out of white mica, and therefore the probable conditions at which a cooling age or crystallization age can be interpreted. Their models show that high temperature or pressure amphibolite and granulite facies conditions will likely allow for complete diffusion of  $^{40}\text{Ar}^*$  accumulated since initial crystallization from a white mica host, even with varying grain sizes (up to 1 mm), cooling rates, decompression rates, and residence times at peak conditions.

#### 4.2.2 *Sample Preparation*

A total of six samples were selected from both the Northern and Southern Domains (Figure 2.1) based on the quality, size, and abundance of the mineral grains to be dated. Hornblende, white mica, and biotite were targeted from the Northern Domain units. Samples were taken from the Southern Domain to compare full temperature-time histories between the two lithotectonic domains. Since white mica is sparse throughout the field area, it was sampled wherever it was found. Desired characteristics for  $^{40}\text{Ar}/^{39}\text{Ar}$  targets included a large grain size (>2 mm), clean grain boundaries with no visible inclusions in the grains, a recrystallized appearance, and minimal to no visible breakdown of the targeted mineral to retrograde products.

The mineralogy and textural relationships in each sample were evaluated to determine which of the  $^{40}\text{Ar}/^{39}\text{Ar}$  targets taken from the field would be most suitable for dating. Some samples were excluded based on the presence of microscopic retrograde reaction products, such as chlorite after biotite. GPS locations and chemical data for each of the following described samples are listed in Table 4.2.

Individual mineral grains were hand-picked from coarsely crushed portions of each hand sample. The grains were selected under a microscope based on grain size, clarity, and

form. Larger grains have a proportionally higher concentration of radiogenic argon, which can decrease the errors associated with its detection during analysis. Inclusions of other potassic mineral phases (e.g., biotite, K-feldspar) can generate  $^{39}\text{Ar}_K$  or other isotopes that interfere with detection when the sample is analysed. Therefore, inclusion-free grains were specifically chosen from each sample. The grain shape was also considered. Mineral grains that have been bent or broken can release argon gas through microfractures, dislocations, and physically altered cleavage planes (*Lee* 1995), a problem particularly associated with micas. Only mica grains with flat basal cleavage and straight grain boundaries, and hornblende grains with well defined 60/120 cleavage and smooth crystal faces were selected for analysis.

Since biotite and hornblende grains are fine- to medium-grained (<3 mm across), several grains were selected for samples HS10-08 and HS10-24, respectively (Figures 4.6d and 4.7d). The white micas, however, were typically coarse enough for single-grain samples, so three single grains from each rock were selected for analysis. The samples were carefully packed into an aluminum irradiation canister along with several aliquots of the Fish Canyon tuff sanidine standard (which has an apparent K/Ar age of  $28.205 \pm 0.046$  Ma), with both sample and standard positions in the canister recorded. The canister was irradiated (bombarded with a fast neutron flux) at the McMaster Nuclear Reactor in Hamilton, Ontario.

#### 4.2.3 $^{40}\text{Ar}/^{39}\text{Ar}$ Analysis

The irradiated samples were dated at the Dalhousie University Argon Laboratory in a double vacuum, internal tantalum resistance furnace using the step-heating method outlined by *McDougall and Harrison* (1999). The ratios of  $^{37}\text{Ar}/^{39}\text{Ar}$ ,  $^{36}\text{Ar}/^{40}\text{Ar}$ , and  $^{39}\text{Ar}/^{40}\text{Ar}$  were analysed by a VG3600 mass spectrometer with an electron multiplier collector as argon gas was released in each heating step. Following analysis of all sample grains and standard aliquots, the known apparent age of the Fish Canyon tuff sanidine standard was used to determine the *J*-value, or neutron flux parameter, for each standard aliquot using the equation:

$$J = \frac{e^{\lambda t} - 1}{^{40}\text{Ar}^*/^{39}\text{Ar}_K} \quad (4.6)$$

Table 4.2: *Following page.* Average mineral compositions for  $^{40}\text{Ar}/^{39}\text{Ar}$  Ar samples. Cations are corrected to 23 oxygen for hornblende, and 22 oxygens for phengite, muscovite, and biotite. \*UTM coordinates are zone 32; mE and mN are metres east and metres north, respectively.

Sample	HS10-24 Hornblende	HS10-34 Muscovite	HS10-09 Phengite	HS10-25 Phengite	JB10-84 Phengite	HS10-08 Biotite
UTM, <sup>a</sup> mE	369202	368688	368610	369271	368978	369543
UTM, mN	6963032	6962768	6958674	6957918	6958321	69663871
<i>Oxides</i>	Avg. $\sigma$ ; n=9	Avg. $\sigma$ ; n=8	Avg. $\sigma$ ; n=14	Avg. $\sigma$ ; n=8	Avg. $\sigma$ ; n=13	Avg. $\sigma$ ; n=8
SiO <sub>2</sub>	38.93 0.35	44.33 0.26	44.82 0.35	45.12 0.98	43.97 0.34	36.21 0.25
TiO <sub>2</sub>	1.67 0.09	0.02 0.02	0.86 0.29	0.47 0.06	0.48 0.17	2.61 0.35
Al <sub>2</sub> O <sub>3</sub>	16.88 0.29	36.02 0.79	30.13 0.44	31.25 0.58	29.31 0.18	17.20 0.21
Cr <sub>2</sub> O <sub>3</sub>	0.07 0.06	0.02 0.03	0.04 0.04	0.03 0.04	0.01 0.01	0.09 0.07
FeO	14.04 0.48	0.51 0.34	5.59 0.24	3.79 0.24	5.09 0.30	12.86 0.33
MnO	0.08 0.01	0.01 0.02	0.02 0.02	0.03 0.01	0.04 0.02	0.01 0.01
MgO	9.82 0.32	0.14 0.11	1.58 0.14	1.49 0.08	1.76 0.13	15.07 0.28
CaO	12.13 0.10	0.01 0.01	0.03 0.02	0.01 0.01	0.01 0.01	0.02 0.03
Na <sub>2</sub> O	2.67 0.07	0.42 0.10	0.27 0.03	0.42 0.06	0.30 0.02	0.42 0.02
K <sub>2</sub> O	1.55 0.06	10.86 0.10	10.37 0.15	10.49 0.13	10.41 0.09	8.82 0.18
BaO	0.07 0.02	0.00 0.00	0.45 0.08	0.17 0.06	1.11 0.10	0.10 0.03
Sum	97.89	92.34	94.16	93.55	92.49	93.41
<i>Cations</i>						
Si	5.840 0.03	6.081 0.05	6.225 0.04	6.249 0.04	6.250 0.02	5.449 0.02
Ti	0.188 0.01	0.002 0.00	0.090 0.03	0.049 0.01	0.051 0.01	0.295 0.04
Al	2.985 0.05	5.824 0.11	4.933 0.07	5.103 0.04	4.910 0.01	3.051 0.03
Cr	0.008 0.01	0.002 0.00	0.004 0.00	0.004 0.00	0.001 0.00	0.010 0.01
Fe	1.761 0.07	0.000 0.04	0.649 0.03	0.439 0.03	0.605 0.02	1.619 0.05
Mn	0.010 0.00	0.059 0.00	0.002 0.00	0.004 0.00	0.005 0.00	0.001 0.00
Mg	2.195 0.06	0.001 0.02	0.326 0.03	0.309 0.02	0.374 0.01	3.381 0.06
Ca	1.949 0.01	0.028 0.00	0.005 0.00	0.001 0.00	0.001 0.00	0.003 0.01
Na	0.777 0.02	0.001 0.03	0.072 0.01	0.112 0.02	0.083 0.00	0.122 0.01
K	0.296 0.01	0.111 0.02	1.837 0.03	1.855 0.05	1.887 0.01	1.694 0.04
Ba	0.008 0.00	1.901 0.00	0.025 0.00	0.010 0.00	0.123 0.01	0.006 0.00
Sum	16.017	14.010	14.169	14.135	14.291	15.631

where  $\lambda$  is the  $^{40}\text{K}$  decay constant,  $t$  is the known apparent age of the sanidine, and  $^{40}\text{Ar}^*/^{39}\text{Ar}_K$  is the analyzed argon ratio for each standard aliquot. The calculated  $J$ -values were plotted against the respective aliquot's position (or height) in the canister, and the line of best fit, known as the  $J$ -curve, was calculated. The slope of the  $J$ -curve represents the change in neutron flux through the canister. Given the position of each unknown sample in the canister and the  $J$ -curve equation, the appropriate  $J$ -value was applied to the  $^{40}\text{Ar}/^{39}\text{Ar}$  age equation (equation 4.4) for each sample. This corrects for differences in the neutron flux that a grain experiences at the top of the canister, for instance, to a grain packed at the bottom of the canister (see *McDougall and Harrison* 1999, for a full description of the  $J$ -value and its derivation).

#### 4.2.4 $^{40}\text{Ar}/^{39}\text{Ar}$ Ages

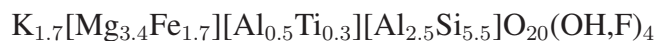
The results presented in this section are reported geographically from north to south. Unless otherwise stated, ages are reported with their  $2\sigma$  uncertainties, which includes uncertainty in the  $J$ -value, but not uncertainty in the assumed age of the Fish Canyon flux monitor. Four of the six samples analyzed gave well-constrained weighted mean plateau ages (WMPA) defined by at least three contiguous steps comprising  $>60\%$  of  $^{39}\text{Ar}$  released (*McDougall and Harrison* 1999, and references therein).

### Northern Domain

#### *HS10-08 Biotite*

This sample was taken from a coastal exposure of the kyanite-garnet-biotite gneiss on northwestern Harøya (Figure 2.1). The outcrop has little lithological variation laterally or vertically, other than lenses and discontinuous layers of leucosome defining the pervasive gneissic foliation (134/68; Figure 4.6a). The leucosome is locally crenulated (Figure 4.6b) and cuts the garnet- and biotite-rich mesosome, indicating two phases of partial melting.

In thin section and backscatter images the matrix biotite has very few inclusions and no evidence of retrogression (Figure 4.6e), but does have an opaque phase (likely ilmenite) along some grain boundaries and cleavage planes (Figure 4.6c). The biotite in this sample has a phlogopite-rich composition with an average chemical formula:



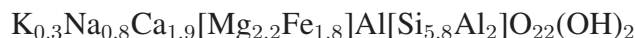
The dated group of black matrix biotite grains (up to 2 mm across; Figure 4.6d) yielded

a well-constrained WMPA of  $377.5 \pm 0.7$  Ma with 98.8% of  $^{40}\text{Ar}^*$  released (Table 4.3; Figure 4.12a).

#### *HS10-24 Hornblende*

This sample was taken from the garnet amphibolite unit on the northwest coast of Harøya (Figure 2.1), west of, and approximately 250 metres structurally below, the kyanite-garnet-biotite gneiss. The outcrop is strongly foliated (240/55), and includes a minor amount of interlayered carbonate-rich bands (<5 cm thick) and discontinuous lenses (<1 cm thick), and a laterally continuous 15-20 cm wide quartzofeldspathic layer containing fine-grained garnet. At the hand sample scale, abundant 5-10 mm garnet porphyroblasts comprise about 15% of the garnet amphibolite (Figure 4.7b).

In thin section, the medium-grained, green-brown amphibole has a granoblastic texture (indicating recrystallization at relatively high temperatures; Figure 4.7c, d) with few inclusions, and is not replaced by biotite or chlorite. This amphibole is a ferroan pargasite (*Deer et al.* 1992), with minor Ti (<0.2 a.p.f.u) and the chemical formula:



Amphibole is intergrown with either plagioclase or scapolite as very fine-grained symplectites around garnet porphyroblasts (Figure 4.7e), which was avoided when grains were being selected for dating. The dated group of amphibole grains yielded a well-constrained WMPA age of  $395.6 \pm 1.2$  Ma with 92.6% of the total  $^{40}\text{Ar}^*$  released (Table 4.3; Figure 4.12b). Additionally,  $\text{Ar}^{37}/\text{Ar}^{39}$  is consistent with the measured Ca/K.

#### *HS10-34 Muscovite*

This sample is from a 25-30 cm wide laterally discontinuous leucosome in kyanite-garnet-biotite gneiss approximately 500 m southwest of hornblende sample HS10-24 (Figure 2.1). The leucocratic layers define the foliation (252/63) between layers of coarse-grained pelitic mesosome (Figure 4.8a). Colourless to pale blue kyanite present in the leucosome at this location is very coarse-grained, with some crystals up to 2 cm long. Muscovite forms thin but clear grains, up to 4 mm wide (Figure 4.8c). In thin section, muscovite is primarily associated with very coarse-grained plagioclase (Figure 4.8b), which has sericite alteration and minor quartz exsolution parallel to cleavage planes. Minimal caledonite substitution (octahedral Al + Al = Fe + Si) indicates the white mica in this sample is muscovite (*Deer et al.* 1992) with an average chemical formula:

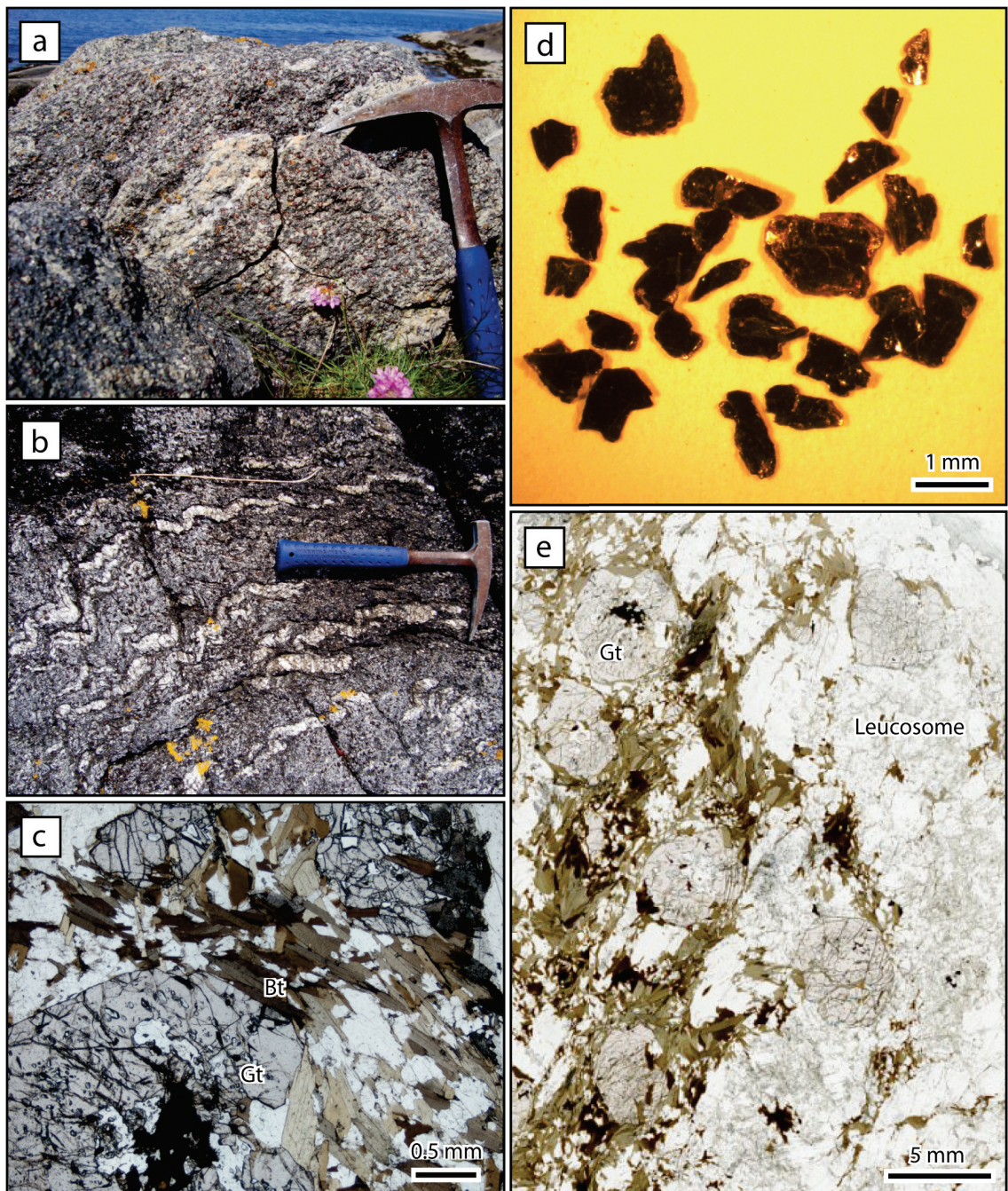


Figure 4.6: HS10-08 Biotite. Leucosome in the garnet-biotite gneiss of the Northern Domain defines the moderately dipping westward foliation (a) and is locally crenulated (b). In thin section (c) the biotite is medium- to coarse-grained, with a dark brown Mg-rich composition. This  $^{40}\text{Ar}/^{39}\text{Ar}$  sample (d) consisted of several flakes of biotite. Aside from biotite the sample also contains inclusion-rich garnet porphyroblasts (e) but lacks an aluminosilicate phase.

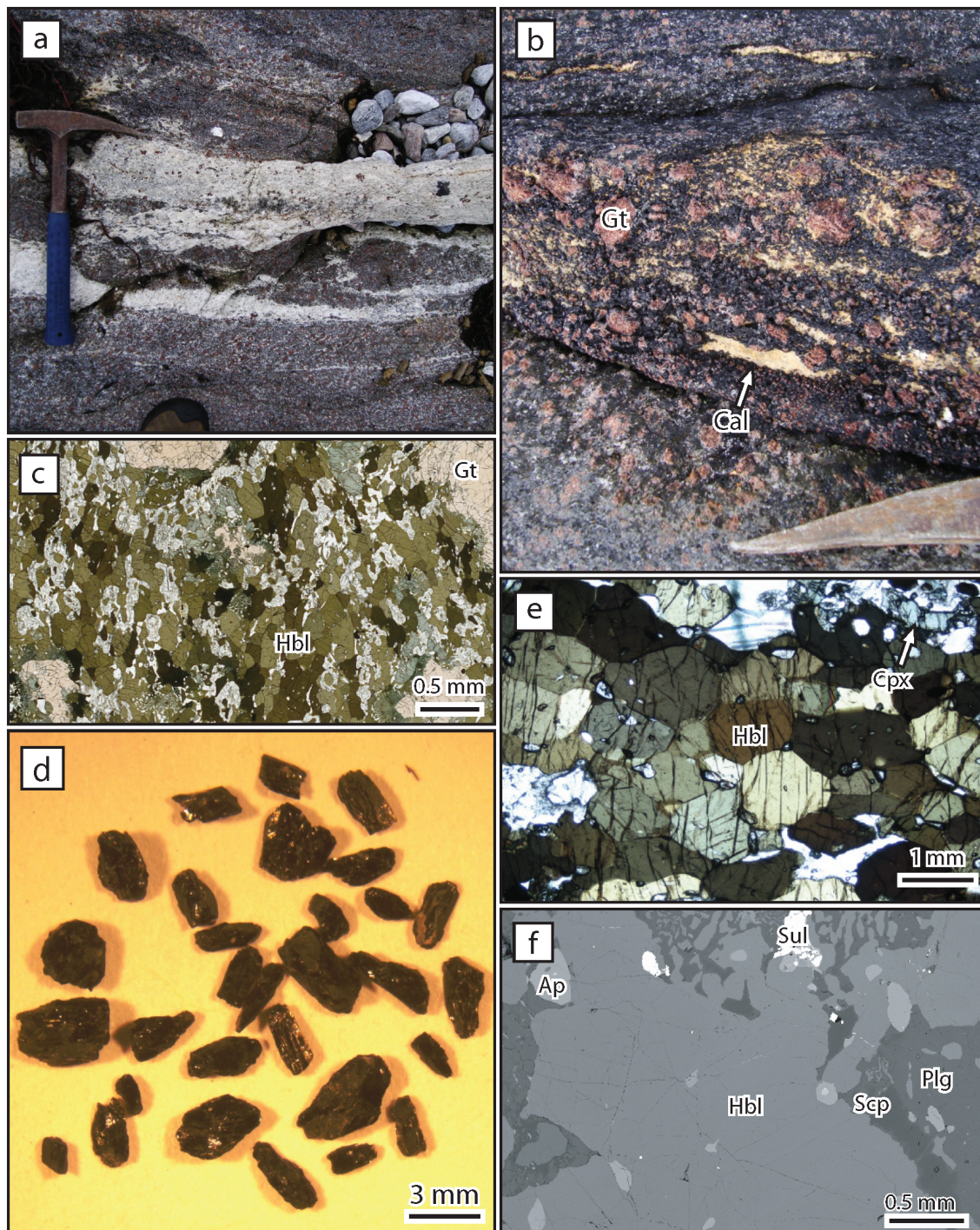
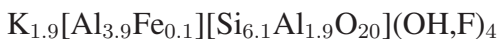


Figure 4.7: HS10-24 Hornblende. a) Felsic layer with thin melt seams cross-cutting the dominant foliation of the garnet amphibolite unit. b) Weathered orange carbonate lenses and coarse-grained garnets define the dominant foliation. HS10-24 thin section scan (c), picked grains for  $^{40}\text{Ar}/^{39}\text{Ar}$  dating (d), thin section photomicrograph (e), and backscatter electron image (f) confirm the absence of biotite intergrown with hornblende, and the recrystallized appearance of the pargasite hornblende.





The coarse-grained muscovite has few quartz inclusions, no apparent alteration (Figure 4.8d, e), and has yielded a poorly-constrained WMPA of  $362.4 \pm 1.2$  Ma with 5 contiguous heating steps comprising 74.6% of the total  $^{40}\text{Ar}^*$  released (Table 4.3; Figure 4.12c).

### Southern Domain

#### *HS10-09 Phengite*

Recrystallized leucosome that envelops boudinaged granodioritic basement gneiss (Figure 4.9a) and contains white mica was sampled (Figure 2.1) from boudin necks, where it had the coarsest grain size. Structurally above and below the raft are similarly strained interlayered granodioritic gneisses and felsic leucosome, garnet-bearing metagabbro, and coarse-grained augen gneiss. There is no noticeable repetitive pattern to the layering of these lithologies.

The white mica is up to 1.5 cm across (Figure 4.9b), arranged in small masses of 2-5 mm thick interlocking books (Figure 4.9c, d), and associated with coarse-grained pale pink plagioclase. Black tourmaline (up to 2 cm long), associated with minor calcite, is concentrated in the coarsest part of the sample area. Around and beyond the periphery of the sample area, where the grain size decreases, the leucosome contains up to 40% fine-grained epidote and chlorite along with plagioclase, white mica and rare quartz. In thin section and backscatter images the chlorite and phengite appear to be discrete phases. Some plagioclase grains exhibit undulatory extinction, suggesting these rocks were deformed after amphibolite-facies peak temperature conditions, initial cooling, and recrystallization. Average white mica compositions determined by microprobe analysis:



shows Fe and Mg in the octahedral site, and an Si:Al ratio  $>3$ , both characteristic of phengite (Deer *et al.* 1992). The dated phengite grain did not display a plateau age (more than 60% of total  $^{40}\text{Ar}^*$  released over at least 3 contiguous steps). A weighted mean age (WMA) of  $396 \pm 4$  Ma across 5 contiguous steps comprising 56% of the total  $^{40}\text{Ar}^*$  released (Table 4.4; Figure 4.13a) is instead reported as the age of this sample.

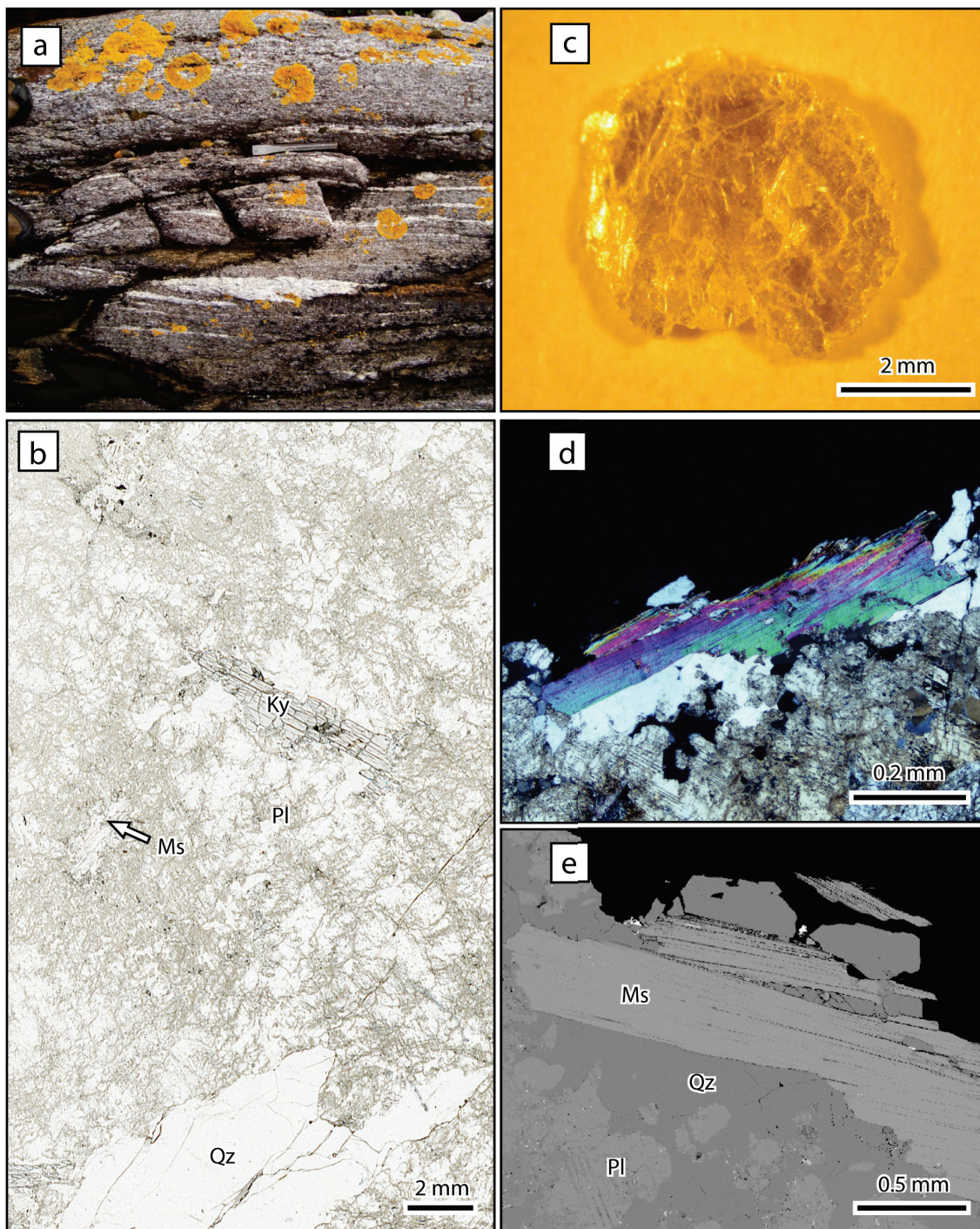


Figure 4.8: HS10-34 Muscovite. Leucosome from the pelitic kyanite-garnet-biotite gneiss of the Northern Domain hosts thin sheets of medium-grained muscovite (a). The presence of kyanite (b, thin section) in the leucosome indicates melting at relatively high pressures in this lithology. The grains picked for  $^{40}\text{Ar}/^{39}\text{Ar}$  dating were flat but thin books (c) with no inclusions (d, photomicrograph in XPL) and no signs of retrogression (e, BSE image).

## HS10-08 Biotite

T°C	<sup>39</sup> Ar (mV)	<sup>39</sup> Ar (%)	AGE (Ma)	1σ (Ma)	% ATM	<sup>37</sup> Ar/ <sup>39</sup> Ar	<sup>36</sup> Ar/ <sup>40</sup> Ar	<sup>39</sup> Ar/ <sup>40</sup> Ar	% IIC
650	26.0	1.1	301	22	49.7	0	0.001682	0.006683	0
700	50.4	2.2	378	5	37.5	0	0.001270	0.006477	0
750	120.6	5.2	378	2	2.2	0	0.000076	0.010112	0
800	186.4	8.1	377	2	1.0	0	0.000035	0.010282	0
825	134.5	5.8	376	2	0.6	0	0.000020	0.010355	0
850	123.9	5.4	385	4	0.4	0	0.000014	0.010108	0
875	144.7	6.3	374	2	0.8	0	0.000027	0.010394	0
900	136.9	5.9	374	2	0.2	0	0.000009	0.010445	0
925	183.0	8.0	375	2	0.7	0	0.000025	0.010370	0
950	222.3	9.7	377	2	0.7	0	0.000025	0.010316	0
1000	443.1	19.3	382	2	1.1	0	0.000037	0.010125	0
1050	354.1	15.4	380	2	1.8	0	0.000061	0.010101	0
1100	92.3	4.0	381	3	3.1	0	0.000105	0.009959	0
1200	60.0	2.6	378	2	7.9	0	0.000268	0.009525	0
1350	8.1	0.3	390	15	69.6	0	0.002355	0.003043	0

Mean Age (700°C - 1200°C) = 379 ± 4 Ma (2σ uncertainty, including error in *J*) = 0.002415 ± 0.0000242

## HS10-24 Hornblende

T°C	<sup>39</sup> Ar (mV)	<sup>39</sup> Ar (%)	AGE (Ma)	1σ (Ma)	% ATM	<sup>37</sup> Ar/ <sup>39</sup> Ar	<sup>36</sup> Ar/ <sup>40</sup> Ar	<sup>39</sup> Ar/ <sup>40</sup> Ar	% IIC
750	7.3	0.4	500	50	87.3	5.87	0.002954	0.000959	0.71
850	5.6	0.3	336	5	40.6	5.02	0.001377	0.006997	0.77
950	10.0	0.6	389	3	20.5	11.13	0.000695	0.008005	1.56
975	97.4	6.4	396	2	1.3	7.15	0.000045	0.009701	0.99
1000	170.3	11.3	405	4	0.4	7.45	0.000015	0.009534	1.02
1025	334.4	22.2	396	2	0.2	7.13	0.000009	0.009807	0.99
1050	696.5	46.3	395	2	0.5	7.20	0.000017	0.009814	1.00
1075	83.0	5.5	393	2	1.0	6.69	0.000035	0.009809	0.93
1100	17.7	1.1	382	2	6.6	7.67	0.000225	0.009558	1.08
1125	10.4	0.6	380	3	15.9	9.40	0.000538	0.008660	1.33
1150	13.8	0.9	386	6	9.7	10.86	0.000329	0.009132	1.53
1175	4.4	0.2	394	5	23.9	7.19	0.000811	0.007524	1.00
1200	6.7	0.4	370	5	33.3	10.76	0.001127	0.007067	1.55
1250	5.4	0.3	400	5	34.0	10.75	0.001152	0.006410	1.48
1300	30.9	2.0	389	4	14.5	9.9a7	0.000493	0.008569	1.40
1350	8.2	0.5	383	28	50.1	9.81	0.001696	0.005094	1.39

Mean Age (975°C - 1075°C) = 396 ± 4 Ma (2σ uncertainty, including error in *J*) = 0.002414 ± 0.0000242

## HS10-34 Muscovite

T°C	<sup>39</sup> Ar (mV)	<sup>39</sup> Ar (%)	AGE (Ma)	1σ (Ma)	% ATM	<sup>37</sup> Ar/ <sup>39</sup> Ar	<sup>36</sup> Ar/ <sup>40</sup> Ar	<sup>39</sup> Ar/ <sup>40</sup> Ar	% IIC
650	22.7	2.3	309	29	60.1	0	0.002036	0.005156	0
700	25.7	2.6	374	16	62.5	0	0.002116	0.003919	0
750	47.3	4.8	359	3	11.6	0	0.000394	0.009682	0
775	66.7	6.8	363	2	5.2	0	0.000178	0.010248	0
800	262.3	26.9	358	3	1.8	0	0.000061	0.010456	0
825	1284.1	33.0	365	2	1.4	0	0.000048	0.010579	0
850	1.2	0.2	374	4	8.1	0	0.000275	0.009635	0
875	3.2	0.3	315	4	18.6	0	0.000631	0.010273	0
900	8.4	0.8	359	3	2.2	0	0.000074	0.010711	0
950	173.1	17.8	364	2	5.6	0	0.000190	0.010198	0
1000	1.7	0.1	385	5	12.3	0	0.000416	0.008897	0
1050	16.5	1.7	362	2	4.3	0	0.000145	0.010384	0
1150	18.8	1.9	354	2	9.7	0	0.000330	0.010031	0
1200	1.0	0.1	317	28	81.9	0	0.002771	0.002274	0
1350	0.6	0.0	237	126	96.3	0	0.003259	0.000633	0

Mean Age (750°C - 825°C) = 366 ± 4 Ma (2σ uncertainty, including error in *J*) = 0.002414 ± 0.0000242

Table 4.3: Northern Domain <sup>40</sup>Ar/<sup>39</sup>Ar step-heating isotopic data. % IIC – interfering isotope correction.

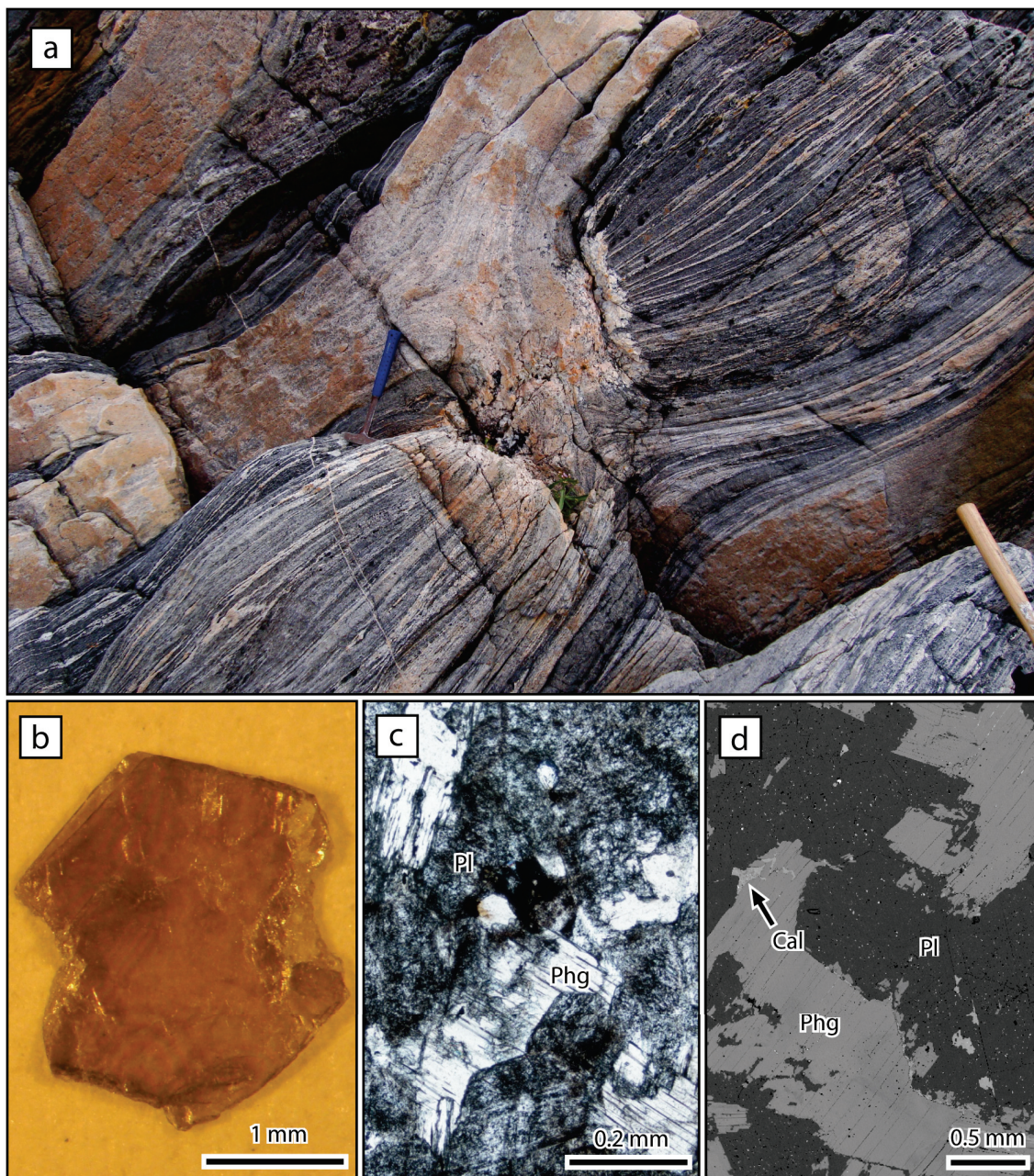


Figure 4.9: HS10-09 Phengite. Boudin necks developed from granitoid gneiss are filled with pegmatitic leucosome (a) in the Southern Domain. Euhedral phengite picked from this sample is transparent (b) and surrounded by sericitized plagioclase in thin section (c, XPL). The phengite in this sample is commonly associated with minor calcite (d, BSE image).

*JB10-84 Phengite*

Within a thin belt of garnet-hornblende gneiss (Figure 2.1), a 1.5 m wide late pegmatitic felsic dyke cuts across an eclogite body and the pervasive gneissic foliation (283/68) of the host rock. Further along the beach outcrop, the dyke eventually aligns with and follows that foliation. The dyke is compositionally layered from both the top and bottom contact to the core. Intergrown quartz, plagioclase and potassium feldspar dominate a 30 cm wide rim which grades into a 10 cm wide potassium feldspar-rich zone. Between the rims, the core of the dyke is almost pure quartz (Figure 4.10a). White mica has primarily grown at the interface between the K-feldspar-rich zone and the quartz core of the dyke.

The mica is coarse-grained and forms interlocking books up to 3 mm thick (Figure 4.10b). In thin section both the coarse-grained quartz and mica exhibit undulatory extinction with some of the mica visibly bent (Figure 4.10c), implying deformation after emplacement of the dyke. Backscatter images show that the white mica is inclusion-free, has clean grain boundaries, and does not appear to be altered (Figure 4.10d, e, f). The average chemical formula for white mica in this sample is:



The Si:Al ratio >3 and the presence of Fe and Mg in the octahedral site indicate that this white mica has a phengitic composition. The dated grain from this sample yielded a well-constrained WMPA of  $366.5 \pm 0.7$  Ma with 98.5% of total  $^{40}\text{Ar}^*$  released over 14 contiguous heating steps (Figure 4.13b).

*HS10-25 Phengite*

A strongly deformed, migmatitic section of garnet-biotite gneiss with abundant retrogressed eclogite pods and boudins was chosen as a site for detailed mapping and geochronology sampling (Figure 2.1). The  $^{40}\text{Ar}/^{39}\text{Ar}$  sample taken from this location is a coarse-grained white mica-bearing leucosome in the neck of a boudinaged eclogite body (Figure 4.11a). This felsic leucosome is locally discordant to the host rock fabric where cross-cutting relations were observed, yet typically concordant to eclogite boudin margins.

The mineralogy and general texture of this sample are very similar to HS10-09. White mica books are up to 2 cm across and approximately 3 mm thick (Figure 4.11c), and finer-grained white mica partially replaces medium- to coarse-grained plagioclase. Coarse

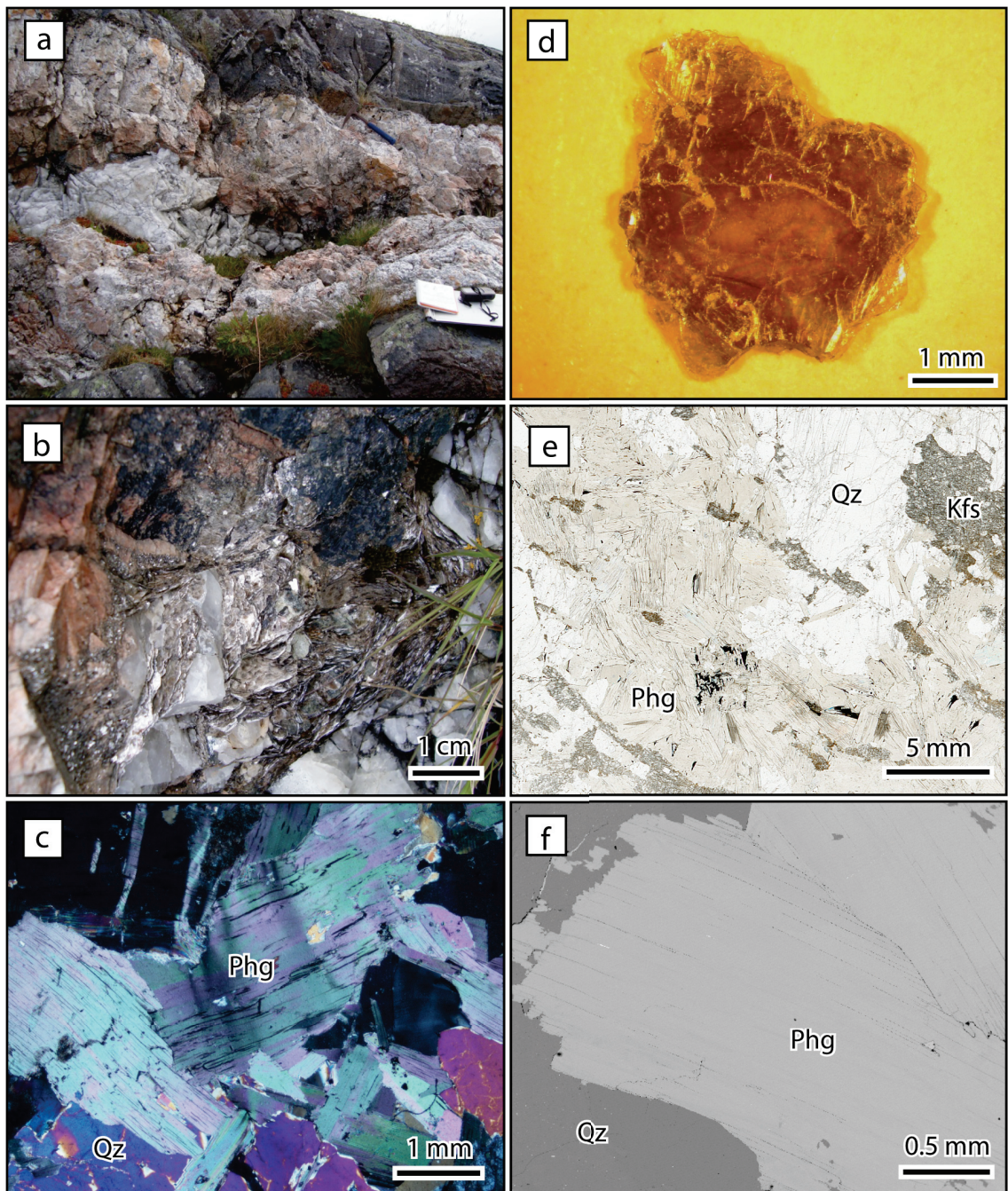


Figure 4.10: JB10-84 Phengite. A 1.5 to 2 metre wide dyke cuts the foliated host basement orthogneiss (a). Between the quartz-rich core and K-feldspar-rich rims of the dyke are coarse-grained mats of phengite mica (b and d). The phengite shows deformation with undulatory extinction in thin section (c, XPL), but shows no signs of retrogression, like the K-feldspar (e, photomicrograph). BSE imaging (f) shows the phengite is also free of inclusions.

masses of chlorite are visible in hand sample, typically associated with minor calcite. Tourmaline is not present in this sample.

In thin section and backscatter images (Figure 4.11b) the white mica appears inclusion-free and stable, and where coarser-grained, it is generally in contact with equal length masses of fine-grained radiating chlorite mats (Figure 4.11d, e). Minor calcite and quartz are present, and plagioclase has considerable sericite alteration. The average chemical formula for the white mica in this sample is:



which, similar to the other Southern Domain white mica samples, has a phengitic composition. The dated grain from this sample did not yield a well-constrained plateau age as the age of each heating step across the spectrum increases incrementally. A WMA of  $405 \pm 7$  Ma comprising 97% of the total  $^{40}\text{Ar}^*$  released in 9 contiguous heating steps (Figure 4.13c) is reported as the age of this sample.

### 4.3 Geochronology Summary

EMPA monazite dating was carried out on two migmatitic pelitic gneiss samples from the *Blåhø Nappe* to constrain the timing of metamorphic events. Four chemical domains were identified. The core domain is characterized by relatively high-Th and low-Y concentrations, and has an WMA of  $426.5 \pm 1.7$  Ma. The inner rim domain has a WMA of  $400.1 \pm 1.4$  Ma, with lower Th and higher Y concentrations relative to the core domain. The outer rim domain has the lowest Th and highest Y concentrations of these three domains, and a WMA of  $383.7 \text{ Ma} \pm 1.2$  Ma. The fourth chemical domain is a thin, discontinuous Y-rich outermost rim. Its small size and rarity, coupled with stage position reproducibility problems, made for unreliable analytical results of this domain.

$^{40}\text{Ar}/^{39}\text{Ar}$  step-heating produced six cooling ages from three Northern Domain and three Southern Domain samples. Biotite from the migmatitic pelitic gneiss of the *Blåhø Nappe* in the Northern Domain yielded a WMPA of  $379 \pm 4$  Ma, while muscovite from leucosome in the same unit has a poorly-constrained WMPA of  $362.4 \pm 1.2$  Ma.  $T_C$  estimates suggest that biotite cooling ages should be younger than white mica cooling ages, and therefore either the biotite age from this study is too old, or the white mica age is too young. The former is interpreted in this case, since biotite in HP metamorphic rocks is

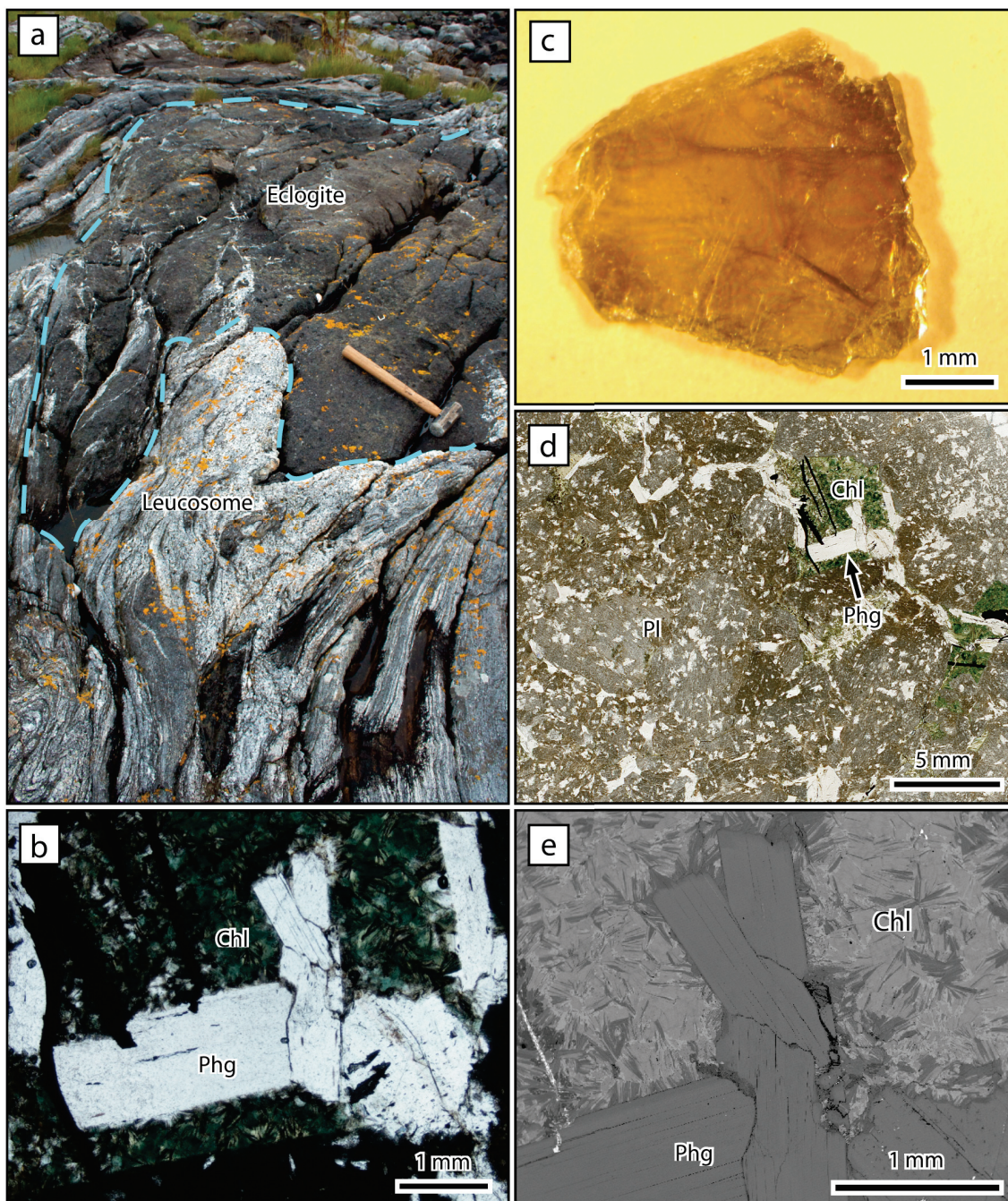


Figure 4.11: HS10-25 Phengite. An eclogite pod (a; outlined in blue) surround by leucosome and highly deformed host orthogneiss has a 'fish mouth' boudinaged neck in which coarser-grained leucosome crystallized (the hammer's wooden end points to the sample location). The phengite mica in this sample is typically surrounded by fine-grained, fibrous chlorite (b, d, and e), which appears to be a stable phase in equilibrium with the phengite. The grains chosen for  $^{40}\text{Ar}/^{39}\text{Ar}$  dating were coarse, transparent, and pale yellow (c).



## HS10-09 Phengite

T°C	<sup>39</sup> Ar (mV)	<sup>39</sup> Ar (%)	AGE (Ma)	1σ (Ma)	% ATM	<sup>37</sup> Ar/ <sup>39</sup> Ar	<sup>36</sup> Ar/ <sup>40</sup> Ar	<sup>39</sup> Ar/ <sup>40</sup> Ar	% IIC
650	4.4	0.3	1882	10	9.3	0	0.000316	0.001190	0
750	74.4	6.1	544	5	21.4	0	0.000724	0.005396	0
775	167.4	13.7	394	2	2.3	0	0.000079	0.009662	0
800	209.8	17.2	399	2	0.4	0	0.000014	0.009708	0
825	151.0	12.4	386	2	1.5	0	0.000053	0.009954	0
850	94.5	7.7	402	2	1.3	0	0.000045	0.009541	0
875	60.1	4.9	405	2	2.0	0	0.000069	0.009395	0
900	46.9	3.8	449	3	2.6	0	0.000088	0.008316	0
925	49.2	4.0	459	2	2.6	0	0.000088	0.008110	0
950	54.9	4.5	438	2	2.8	0	0.000095	0.008532	0
975	57.7	4.7	429	2	2.9	0	0.000101	0.008714	0
1000	61.6	5.0	439	2	3.3	0	0.000112	0.008478	0
1050	109.5	9.0	477	3	4.0	0	0.000136	0.007653	0
1100	54.9	4.5	732	5	4.8	0	0.000163	0.004594	0
1150	8.0	0.6	2192	8	10.9	0	0.000371	0.000907	0
1200	4.7	0.3	1727	13	32.6	0	0.001105	0.001013	0
1250	2.4	0.2	1314	42	69.1	0	0.002339	0.000695	0
1350	1.3	0.1	1298	195	90.0	0	0.003048	0.000227	0

Mean Age (775 °C - 875 °C) = 396 ± 4 Ma (2σ uncertainty, including error in J) J = 0.002416 ± 0.0000242

## JB10-84 Phengite

T°C	<sup>39</sup> Ar (mV)	<sup>39</sup> Ar (%)	AGE (Ma)	1σ (Ma)	% ATM	<sup>37</sup> Ar/ <sup>39</sup> Ar	<sup>36</sup> Ar/ <sup>40</sup> Ar	<sup>39</sup> Ar/ <sup>40</sup> Ar	% IIC
650	13.5	0.8	307	39	66.8	0	0.002260	0.004322	0
750	61.9	3.8	382	6	41.2	0	0.001395	0.006023	0
775	194.5	12.1	364	2	1.3	0	0.000044	0.010646	0
800	266.4	16.6	367	3	0.5	0	0.000018	0.010629	0
825	244.0	15.2	367	2	0.4	0	0.000016	0.010661	0
850	176.5	11.0	362	2	0.7	0	0.000024	0.010787	0
875	128.0	7.9	371	2	0.2	0	0.000008	0.010561	0
900	94.8	5.9	367	2	0.4	0	0.000014	0.010663	0
925	86.6	5.4	367	2	0.1	0	0.000006	0.010678	0
950	85.5	5.3	367	2	0.3	0	0.000010	0.010674	0
975	70.9	4.4	367	2	0.7	0	0.000026	0.010637	0
1000	48.8	3.0	366	2	1.0	0	0.000035	0.010617	0
1025	38.1	2.3	365	2	1.5	0	0.000051	0.010596	0
1050	33.1	2.0	367	2	0.8	0	0.000027	0.010615	0
1100	30.6	1.9	366	2	3.3	0	0.000113	0.010386	0
1150	15.5	0.9	360	4	14.4	0	0.000488	0.009365	0
1250	9.1	0.5	344	4	29.5	0	0.001000	0.008084	0
1350	1.7	0.1	293	35	86.8	0	0.002939	0.001797	0

Mean Age (775 °C - 1150 °C) = 366 ± 4 Ma (2σ uncertainty, including error in J) J = 0.002414 ± 0.0000242

## HS10-25 Phengite

T°C	<sup>39</sup> Ar (mV)	<sup>39</sup> Ar (%)	AGE (Ma)	1σ (Ma)	% ATM	<sup>37</sup> Ar/ <sup>39</sup> Ar	<sup>36</sup> Ar/ <sup>40</sup> Ar	<sup>39</sup> Ar/ <sup>40</sup> Ar	% IIC
650	22.4	2.0	320	28	51.8	0	0.001753	0.005992	0
750	99.2	9.0	377	8	2.0	0	0.000068	0.010184	0
775	54.8	5.0	371	2	3.0	0	0.000103	0.010268	0
800	94.5	8.6	379	2	1.2	0	0.000042	0.010195	0
825	169.5	15.4	396	2	1.5	0	0.000053	0.009674	0
850	86.6	7.9	397	2	1.3	0	0.000045	0.009665	0
875	164.0	14.9	402	2	2.0	0	0.000069	0.009479	0
900	93.5	8.5	435	2	2.7	0	0.000092	0.008607	0
925	67.5	6.1	434	2	2.7	0	0.000094	0.008627	0
950	71.3	6.5	431	2	2.8	0	0.000095	0.008694	0
975	57.9	5.2	427	2	2.9	0	0.000101	0.008775	0
1000	88.4	8.0	435	2	3.3	0	0.000112	0.008563	0
1025	15.9	1.4	368	4	6.0	0	0.000205	0.010014	0
1075	2.2	0.2	375	6	37.5	0	0.001269	0.006538	0
1100	1.5	0.1	404	15	50.2	0	0.001700	0.004786	0
1150	1.9	0.1	366	14	66.1	0	0.002238	0.003635	0
1250	2.1	0.1	416	27	79.9	0	0.002705	0.001851	0
1350	0.8	0.0	494	201	95.3	0	0.003227	0.000354	0

Mean Age (750°C - 1000 °C) = 405 ± 7 Ma (2σ uncertainty, including error in J) J = 0.002416 ± 0.0000242

Table 4.4: Southern Domain <sup>40</sup>Ar/<sup>39</sup>Ar step-heating isotopic data. % IIC – interfering isotope correction.

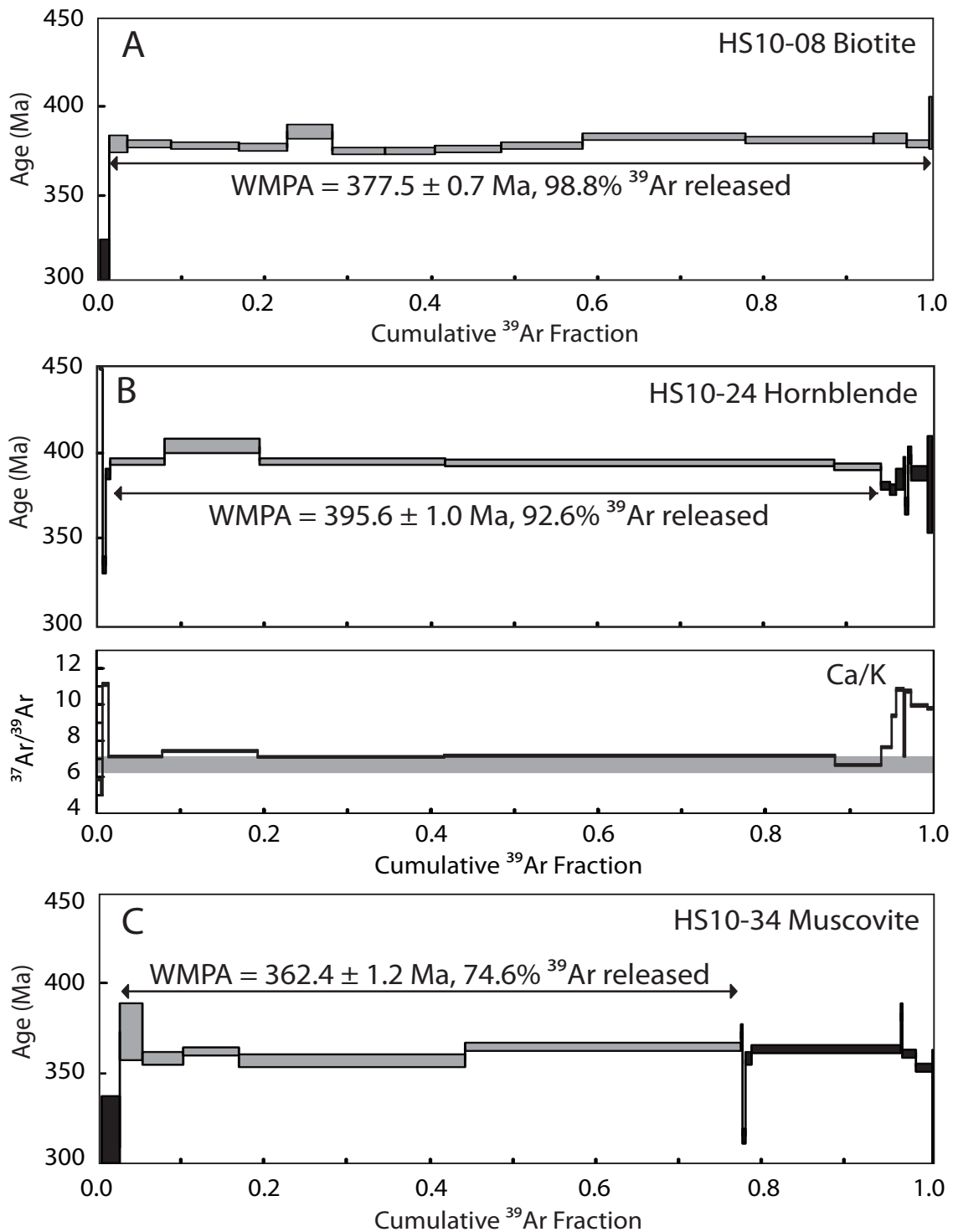


Figure 4.12: Northern Domain  $^{40}\text{Ar}/^{39}\text{Ar}$  spectra. The range of Ca/K ratios from microprobe analyses of hornblende is shaded gray in the  $^{37}\text{Ar}/^{39}\text{Ar}$  spectrum. Ages are weighted mean plateau ages (WMPA) with  $2\sigma$  uncertainties that incorporate internal laboratory and  $J$ -parameter errors.

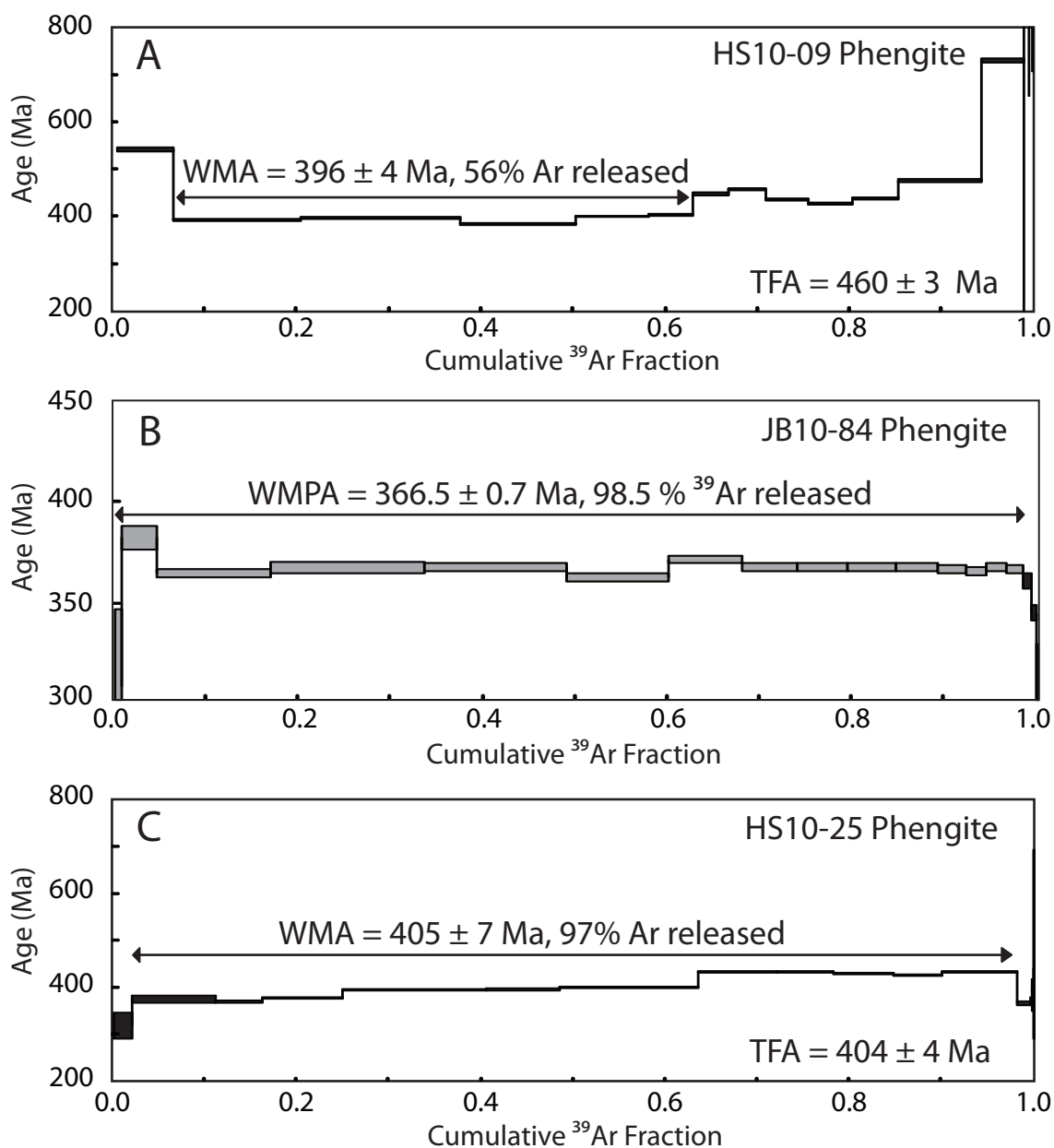


Figure 4.13: Southern Domain  $^{40}\text{Ar}/^{39}\text{Ar}$  spectra. Weighted mean ages (WMA) and total fusion ages (TFA) have  $2\sigma$  uncertainties that incorporate internal laboratory and  $J$ -parameter errors.

commonly affected by excess  $^{40}\text{Ar}^*$ . Furthermore, *Root et al.* (2005) described a 380 Ma biotite cooling age from the *Blåhø Nappe* on Fjørtoft, which was also suspected of being effected by excess  $^{40}\text{Ar}^*$ . From the garnet amphibolite unit, hornblende yielded a well-constrained WMPA of  $395.6 \pm 1.2$  Ma. The  $\text{Ar}^{37}/\text{Ar}^{39}$  ratio along most of the hornblende spectra is consistent with measured Ca/K from microprobe analyses of hornblende. The slight increases in  $\text{Ar}^{37}/\text{Ar}^{39}$  at the beginning and end of the spectra likely indicates compositional variation in the step heated grain, or minor inclusions, however the latter were not observed during microprobe analysis.

Phengite samples from leucosome enveloping granodioritic gneiss, a cross-cutting pegmatite dyke, and a pegmatitic leucosome in a boudin neck in the Southern Domain yielded a WMA of  $396 \pm 4$  Ma, a WMPA of  $366.5 \pm 0.7$  Ma, and a WMA of  $405 \pm 7$  Ma, respectively. The two leucosome cooling ages have likely been effected by excess  $^{40}\text{Ar}^*$  since the white mica is associated with rocks that experienced UHP metamorphic conditions. The cooling age of the cross-cutting pegmatite dyke, however, is interpreted as robust since the dyke is a late feature, likely emplaced during or after retrogression and associated exhumation of the SD basement rocks.

The link between these age results and the P-T estimates from Chapter 3, as well as the geological implications and regional significance of such linkages are discussed in Chapter 5. These ages are one of the key requirements for constructing a *PTt* path to constrain the metamorphic history of the *Blåhø Nappe*. With this information, the influence of supracrustal metasedimentary rocks in the burial and exhumation processes of the Scandinavian Caledonides can be better understood.

## CHAPTER 5

# DISCUSSION AND CONCLUSIONS

Supracrustal rocks correlative with the *Blåhø Nappe*, on the islands of Harøya and Finnøya in the Nordøyane UHP domain, are lithostratigraphically juxtaposed with UHP Baltican basement orthogneiss (*Butler et al.* doi: 10.1111/jmg.12004, in press, 2012). Both units were buried and metamorphosed during the Scandian orogeny in the Late Silurian and Early Devonian, but so far only the basement contains evidence for UHP metamorphism on Harøya and Finnøya. To explain the juxtaposition of these units, two opposing hypotheses have been suggested: 1) both units were buried and exhumed as a coherent body, or 2) the supracrustal rocks were buried up to lower-crustal levels during subduction, while portions of the Baltican basement reached depths corresponding to UHP conditions, and during later exhumation the two lithotectonic units were juxtaposed. In the first case, the two units should share a common metamorphic history. In the second case, the timing and conditions of peak metamorphism recorded by the two units should differ, but their retrograde histories should be similar. A series of questions was posed in Chapter 1 to test these contrasting hypotheses: Did the *Blåhø Nappe* and Baltican basement share a common metamorphic history? If not, what peak conditions did the *Blåhø Nappe* experience, and at what time? Finally, when, and at what conditions, did the two units become juxtaposed?

The field mapping, thermobarometry, and geochronology studies documented in this thesis have been focused on answering the above questions. Here, the various results are compiled as a *PTt* path summarizing the metamorphic history of the *Blåhø Nappe* (section 5.1.1), and the tectonic evolution of this unit is compared with that of the adjacent Baltican basement through the course of the Scandian orogeny. The local and regional significance of the final results is discussed in section 5.3, and considerations for future

work are offered in section 5.4.

## 5.1 Metamorphic History of the Blåhø Nappe on Harøya and Finnøya

### Protolith

The *Blåhø Nappe* metasedimentary protoliths are thought to have been deposited during the Neoproterozoic and Cambrian (*Hacker and Gans* 2005) along the outboard Baltican margin in deep ocean and volcano-sedimentary settings related to formation of an island-arc terrane (*Robinson et al.* 2003). In the northern-central WGR, minimally-deformed >525 Ma pillow lavas with MORB chemistry and eclogite facies assemblages have been documented in the uppermost unit of the *Seve Nappe* (*Kullerud et al.* 1990). Furthermore, psammitic schists, quartzofeldspathic schists, and minor carbonate-rich rocks are associated with these eclogitized pillow lavas. These lithological associations are very similar to those in the observed garnet amphibolite unit, which also contains quartzofeldspathic gneiss layers and minor marble, on Harøya and Finnøya. It is clear that the *Seve/Blåhø Nappe* protolith locally includes igneous rocks from a rift or island arc setting, but this remains to be determined for the area of *Blåhø Nappe* considered in this study.

### Prograde Metamorphism

The core domains from EMPA monazite analyses (section 4.1.4) yielded a WMA of  $426.5 \pm 1.7$  Ma. This age is derived statistically from 17 independent core domain analyses that range from about 440 Ma to 416 Ma. Monazite domain ages are interpreted to represent conditions conducive to monazite growth, which do not necessarily correspond to specific geologic or tectonic events (*Williams et al.* 2007). The core domain ages in this study are interpreted to represent the first appearance of monazite and its continued growth during prograde metamorphism of the *Blåhø Nappe*, possibly from reactions involving the breakdown of xenotime.

Prograde metamorphic assemblages or structures were not observed in the field or in thin section. These were presumably obliterated by later high-pressure amphibolite to granulite facies metamorphism of the *Blåhø Nappe*. However, the relatively low

Y concentration in the monazite core domain suggests stability of another Y-bearing phase, most likely garnet (*Williams et al.* 2007). Pseudosection modelling by *Spear and Pyle* (2010) of an average pelitic bulk composition predicted low Y concentrations in prograde metamorphic monazite formed by xenotime breakdown in the presence of garnet. The models showed xenotime breakdown and monazite generation by 6 kbar within the modelled range of temperatures. This is consistent with core domain monazite growth during prograde metamorphism at medium pressure and temperature amphibolite facies conditions. The monazite core domain provides a minimum age of Middle Allochthon burial below the Upper Allochthon during Scandian convergence and thrusting.

### **Peak P Metamorphism**

With further prograde metamorphism of the *Blåhø Nappe*, white mica likely became unstable, and began to break down via dehydration melting reactions (*Thompson* 1982; *Spear et al.* 1999). Pseudosection models of average pelitic compositions predict no monazite growth during melt-generating reactions, and consumption of monazite by the melt phase with increasing temperature (*Kelsey et al.* 2008). Considering the scarcity of monazite grains containing a core domain, it is possible that early monazite was largely consumed by melt-generating reactions, probably by 416 Ma (the youngest core domain monazite).

The time of peak pressure metamorphism is interpreted to correspond to a hiatus in monazite growth during melting, from 416 Ma to 414 Ma, when there is a lack of monazite core and inner rim domain dates (Figure 4.4). In general, with increasing P and T conditions, garnet remains stable even in the presence of melt. Petrographic analyses of the migmatitic pelitic gneiss unit reveal atoll garnets containing polymineralic inclusions of kyanite, biotite, quartz, rutile, and rare plagioclase melt film pseudomorphs along interior garnet faces, suggesting peritectic garnet growth. Yttrium released from consumed monazite might have been taken up by this generation of garnet. Monazite was not observed as an included phase in any generation of garnet.

No evidence of UHP metamorphism has been identified so far in the *Blåhø Nappe* within this study area. In the migmatitic pelitic gneiss unit, the presence of clinopyroxene would indicate elevated metamorphic pressures, given an appropriate bulk composition. In the underlying garnet amphibolite unit, preservation of omphacite + garnet would suggest

at least eclogite facies metamorphism. Minor pyroxene was identified in the M1 mineral assemblage in this unit, but the compositions were Na-poor, suggesting equilibria at lower pressures than the omphacite stability field. If (U)HP metamorphism affected the *Blåhø Nappe*, all evidence must have been completely overprinted during peak *T* metamorphism. The observed early assemblages and mineral compositions suggest upper amphibolite to granulite facies peak *P* metamorphism by about 415 Ma.

### **Peak *P* to Peak *T* Metamorphism**

Following peak *P* metamorphism, the migmatitic aluminous gneiss of the *Blåhø Nappe* likely experienced melt loss. This interpretation is based on a pseudosection model for a single sample, and therefore it is unclear whether melt loss was local or widespread within the unit. The small shoulder of monazite inner rim domain dates on the probability distribution plot at about 414 Ma (Figure 4.4), may record minor melt crystallization after a melt extraction event.

### **Peak *T* Metamorphism**

Equilibration of the M1 mineral assemblage [Liq + Ky + Gt + Bt + Pl + Ksp + Qz + Ru], is interpreted to represent peak metamorphic temperature conditions experienced by the *Blåhø Nappe* after melt extraction at about 15.3 kbar and 860 °C . By this time, garnet had increased to approximately 21 modal %.

### **Amphibolite Facies Retrogression and Later Cooling**

The *Blåhø Nappe* likely experienced isothermal decompression followed by isobaric cooling from the M1 to M2 assemblage conditions. All the remaining melt crystallized, K-feldspar was completely consumed, garnet was reduced to approximately 11 modal %, and the abundance of biotite and plagioclase increased. The M2 assemblage [Sil + Gt + Bt + Pl + Qz + Ru] equilibrated at around 9 kbar and 675 °C .

The monazite inner rim domain WMA of  $400.1 \pm 1.4$  Ma is interpreted to represent this melt crystallization event (Figure 4.4). Inner rim domain analyses have a slightly lower Th/Y ratio than the core domain (Figure 4.3). This suggests that relatively more Y was available for growth of the inner rim domain than during core domain growth. Breakdown of garnet along the retrograde path likely released Y and HREEs to the crystallizing melt



for consumption by growing inner rim monazite. Melt crystallization took place between about 408 Ma and 394 Ma, the range of inner rim monazite dates around the peak. Final melt crystallization and equilibration of the M2 assemblage is interpreted to correspond to the end of this range of dates. The modal and textural characteristics of the *Blåhø Nappe* reflect the  $P$ - $T$  conditions during this stage.

Hornblende from the garnet amphibolite unit (HS10-24) on Harøya has an  $^{40}\text{Ar}/^{39}\text{Ar}$  cooling age of  $396 \pm 4$  Ma. The *Blåhø Nappe* is interpreted to have cooled to  $^{40}\text{Ar}^*$  closure in hornblende, around  $500\text{ }^\circ\text{C}$  (Harrison 1981), at this time. This age may be affected by excess  $\text{Ar}^{40}$ , since it overlaps with the age range of inner rim monazite ages constraining the time of final melt crystallization at  $660\text{ }^\circ\text{C}$ . Alternatively, the garnet amphibolite may have cooled more quickly than the aluminous gneiss.

Of the two rock samples analysed for monazite ages, only the sheared sample contained monazite with an outer rim domain. This domain has a WMA of  $383.7 \pm 1.2$  Ma based on analyses ranging from about 394 Ma to 370 Ma, and is interpreted to correspond to fluid infiltration and percolation. This constrains the minimum age of amphibolite facies shearing in sample HS10-32 from Finnøya. The Y/Th ratio in this domain is higher than in the core and inner rim domains, implying a Y-enriched fluid. Based on muscovite in HS10-34 leucosome, the *Blåhø Nappe* is interpreted to have cooled through  $^{40}\text{Ar}^*$  closure in white mica, about  $400\text{ }^\circ\text{C}$  (Harrison *et al.* 2009), by  $362 \pm 1.2$  Ma.

### 5.1.1 $PTt$ Path for the *Blåhø Nappe*

A  $PTt$  path is a graphical representation of the metamorphic history of a region, unit, or sample from initial burial, through exhumation and unroofing. To construct a  $PTt$  path for the *Blåhø Nappe*, the analytically-derived  $P$ - $T$  estimates from Chapter 3 were integrated with geochronology results from Chapter 4 to define segments of the path (prograde, retrograde) and maximum  $P$  or  $T$ . Field, petrographic, and geochemical relationships link the  $P$ - $T$  estimates and ages, as described above.

The *Blåhø Nappe* followed a clockwise  $PTt$  path (Figure 5.1), typical of continental collisional settings. The metamorphic pressure at peak the  $T$  condition translates to burial at approximately 50 km depth. Melt was generated, with some likely lost from the system, before equilibration of the M1 assemblage around 410 Ma. The *Blåhø Nappe* experienced melt crystallization during retrogression along the two-phase isothermal decompression and isobaric cooling path from the M1 to M2 assemblage between 408 Ma and 394 Ma.

The M2 assemblage equilibrated at approximately 25 km depth. Late fluid infiltration (394 Ma to 370 Ma) took place during regional cooling based on  $^{40}\text{Ar}^*$  closure in hornblende at around 396 Ma, and white mica around 362 Ma. The tectonic implications are discussed below.

## 5.2 Implications for the Tectonic History of the Study Area

Based on 1:10000 mapping of the study area, the *Blåhø Nappe* of the ND lithotectonically overlies Baltican basement orthogneiss of the SD. The ND and SD are separated by the FMSZ, comprising boudinaged amphibolite, garnet-bearing quartzofeldspathic gneiss, and retrogressed eclogite wrapped in highly migmatitic and foliated felsic gneiss. *Butler et al.* (doi: 10.1111/jmg.12004, in press, 2012) discovered coesite in an eclogite pod from the SD, and estimated equilibration conditions for the UHP assemblage including this phase at 30 kbar and 760 °C between 415 Ma and 410 Ma (Figure 5.3a). They also documented an amphibolite facies assemblage overprinting the UHP assemblage which equilibrated at 10 kbar and 813 °C. Exhumation of the SD basement rocks involved an early phase of top-NW shearing and later subhorizontal sinistral shearing along the regionally pervasive NW-dipping foliation (*Butler et al.* doi: 10.1111/jmg.12004, in press, 2012).

UHP metamorphism in the SD contrasts with the lack of documented eclogite facies evidence in the adjacent ND *Blåhø Nappe*, implying that these two lithotectonic units did not follow the same prograde *PTt* path during the Scandian orogeny. The shared amphibolite facies structures, overprinted higher pressure mineral assemblages, and FMSZ suggest the basement became juxtaposed with the *Blåhø Nappe* while both units experienced isothermal decompression from peak pressure conditions (Figure 5.2, 5.3b). For the *Blåhø Nappe*, isothermal decompression happened between 408 Ma and 394 Ma.

$^{40}\text{Ar}/^{39}\text{Ar}$  dating on white mica from a cross-cutting pegmatitic dyke in the SD basement rocks (JB10-84) constrains cooling through white mica closure *T* at  $366 \pm 4$  Ma. This cooling age is similar to the 362 Ma age from leucosome in the migmatitic aluminous gneiss of the ND. A shared cooling history confirms that the Baltican basement and *Blåhø Nappe* units were juxtaposed and experiencing regional cooling together by this time.

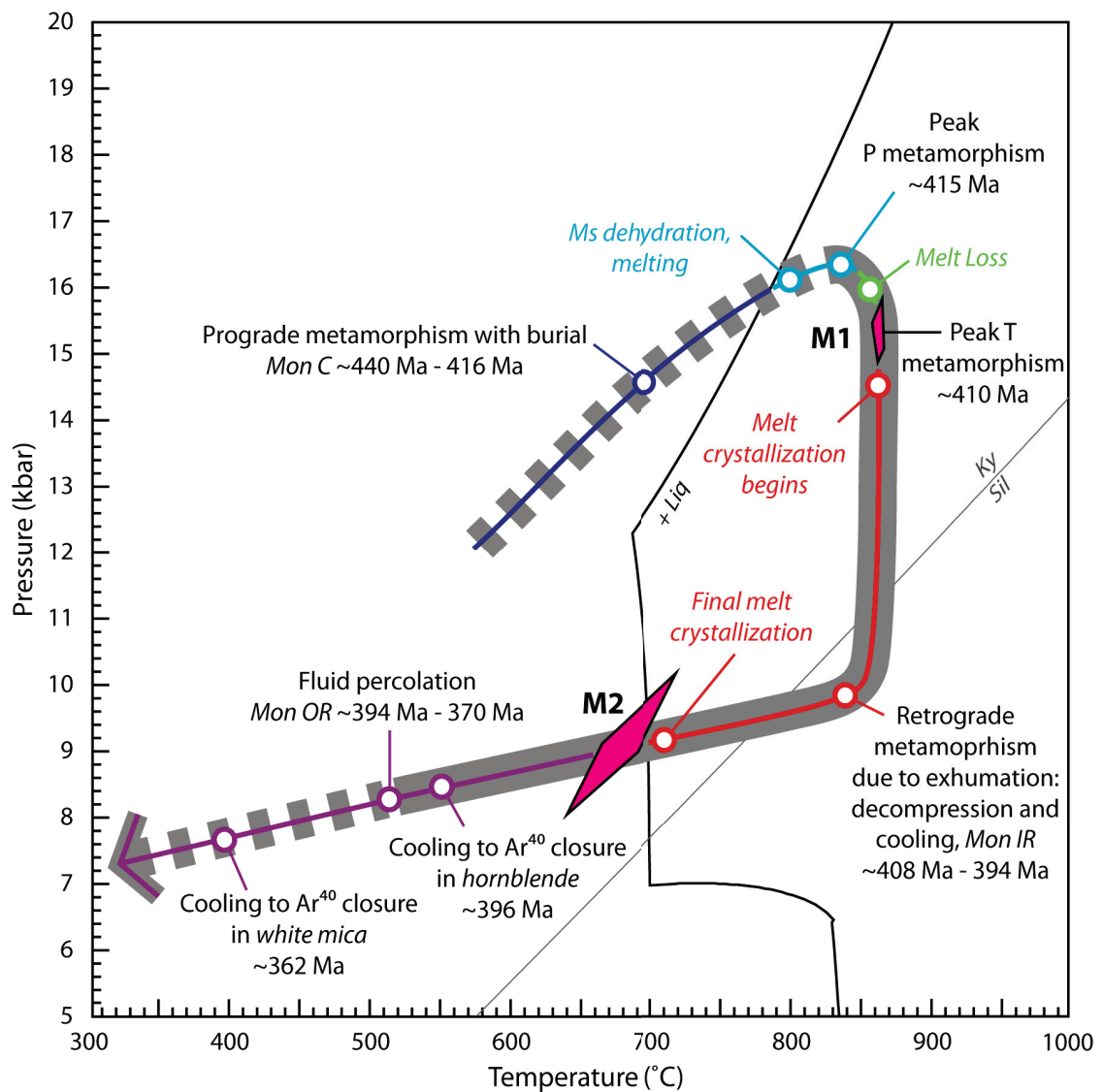


Figure 5.1:  $P$ - $T$ - $t$  path for the Blåhø Nappe. Burial and prograde metamorphism (dark blue path) culminated with melt generation and peak  $P$  metamorphism (light blue path) around 415 Ma. Local melt loss preceded peak  $T$  metamorphism (green path) at 410 Ma. Retrogression (red path) of the *Blåhø Nappe*, including partial melt crystallization, followed a two-phase isothermal decompression and isobaric cooling path. Further regional cooling (purple path) to  $^{40}Ar^*$  closure in hornblende and white mica was synchronous with local fluid infiltration.

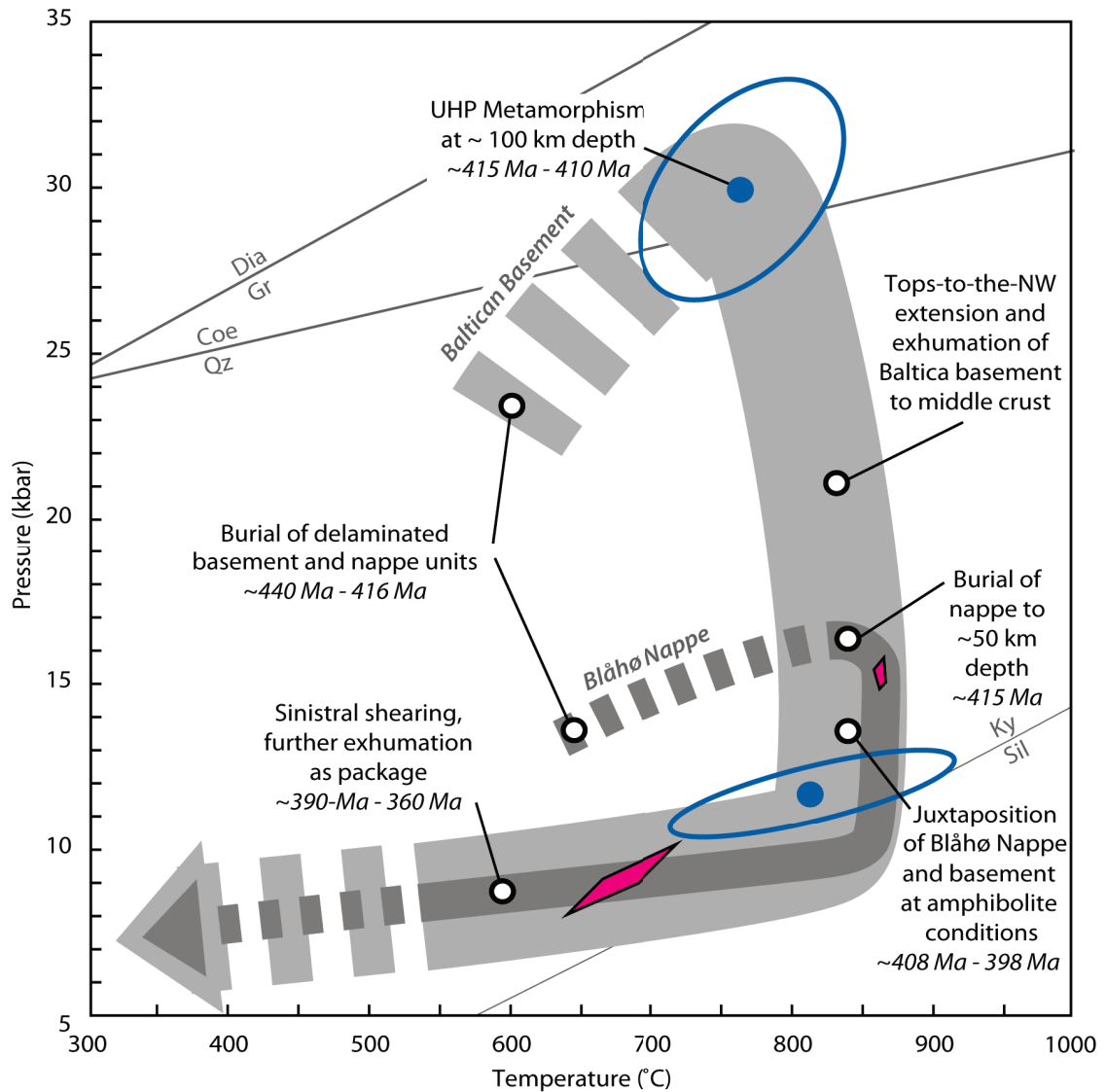


Figure 5.2: Combined *PTt* path of the *Blåhø Nappe* and Baltican basement rocks on Harøya and Finnøya. The basement *PTt* path is based on the metamorphic history of a coesite-eclogite pod (Butler *et al.* doi: 10.1111/jmg.12004, in press, 2012) from the SD. The basement rocks in this study area were buried to ~100 km depth, while the *Blåhø Nappe* reached ~50 km depth. These two lithotectonic units followed different burial paths, but were ultimately juxtaposed at amphibolite facies conditions during isothermal decompression between 408 Ma and 394 Ma. The basement and *Blåhø Nappe* experienced further exhumation and cooling together, as a package.

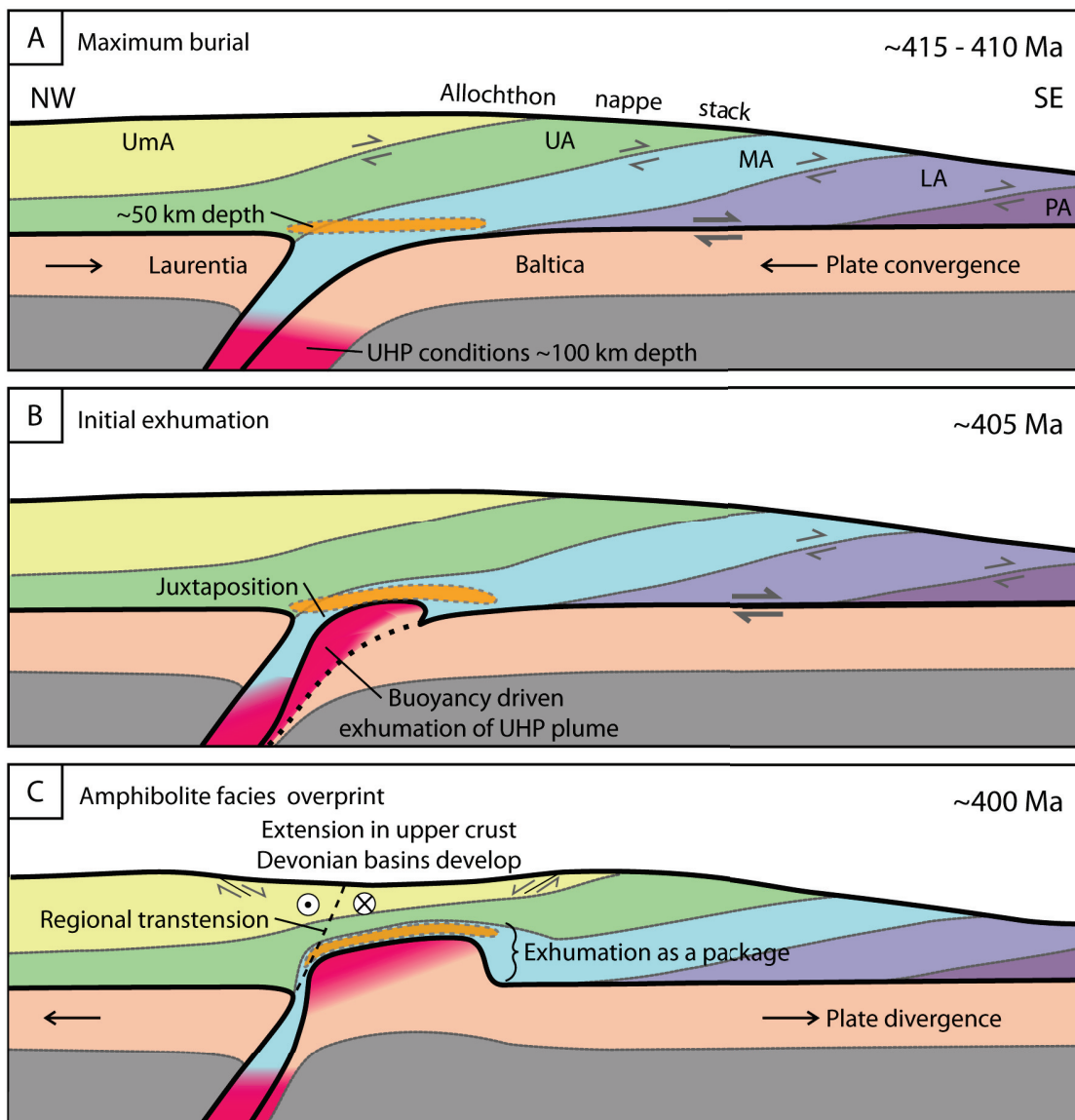


Figure 5.3: Conceptual model of the *Blåhø Nappe* and UHP Baltican basement relationships during the Scandian orogeny. This model shows the relative positions of deeply buried allochthonous sediments (orange area) and Baltican basement. a) Around 415 Ma, the *Blåhø Nappe* and basement rocks that underlie Harøya and Finnøya experienced peak *P* conditions, at approximately 50 km and 100 km depth, respectively. Abbreviations are UmA = Uppermost Allochthon; UA = Upper Allochthon; MA = Middle Allochthon; LA = Lower Allochthon; PA = Parautochthon. b) Following maximum burial, exhumation involving isothermal decompression of the *Blåhø Nappe* and buoyancy-driven exhumation of the basement, began by 410 Ma and brought the two units to similar crustal depths. c) The *Blåhø Nappe* and basement were juxtaposed at amphibolite facies conditions and exhumed to approximately 30 km depth by 394 Ma. Exhumation probably involved regional transtension, and extension in the upper crust where Devonian basins began to develop.

### 5.3 Regional Implications

The results of this study not only contribute to understanding the metamorphism in the *Blåhø Nappe* on Harøya and Finnøya, but also have implications outside the study area. These are listed below and discussed in terms of local-, regional-, and orogen-scale.

#### Nordøyane

Detailed mapping of the field area has led to identification of the FMSZ, which may be regarded as a marker unit since it is characteristically different from the units that it separates. Provided that the FMSZ represents the contact zone between the UHP basement and HP *Blåhø Nappe*, as interpreted in Chapter 2, there is potential to trace this contact zone to the northeast, to the mainland. Abundant leucosome, characteristic of the FMSZ, is likely related to decompression melting of the UHP basement orthogneisses during exhumation. With further mapping to delimit the FMSZ, the extent of HP *Blåhø Nappe* involved in burial and later juxtaposition with rapidly exhuming basement gneiss could be identified. These data would provide constraints on numerical models of UHP rock exhumation in continental collisional settings.

The structural evolution and present-day geometry within the Nordoyane UHP domain is undoubtedly complex, yet only partly understood since most of the region is hidden from view below the Norwegian Sea. On the island of Fjortøft, rocks interpreted as part of the *Blåhø Nappe* experienced UHP metamorphic conditions during the Scandian orogeny based on the presence of microdiamond (*Dobrzhinetskaya et al. 1995*) and *in situ* polycrystalline quartz pseudomorphs after coesite (*Terry et al. 2000b*). In contrast, evidence for UHP metamorphism in the *Blåhø Nappe* on Harøya and Finnøya has not yet been identified. The contrasting peak metamorphic histories of these supposedly correlative rocks suggest that either the rocks on Fjortøft are not part of the *Blåhø Nappe*, all evidence of UHP metamorphism in the *Blåhø Nappe* on Harøya and Finnøya has been completely obliterated, or that major structural breaks lie between Harøya and Fjortøft. The third theory is supported by the amphibolite facies mylonite zone underlying the southern tip of Harøya at Myklebust. It is at least 10 m thick on shore, and extends further south toward Fjortøft under water. In any case, this study has identified a metamorphic discontinuity between rocks on these islands.

Cooling and decompression rates can be estimated based on the *PTt* path for the *Blåhø*

*Nappe*. The rocks are interpreted to have decompressed from 15 kbar to 9 kbar between about 410 Ma and 405 to 400 Ma. This suggests a decompression rate of 0.6-1.2 kbar/Ma along the isothermal decompression path. This translates into an exhumation rate of 2-4 mm/yr from about 50 km to 30 km depth. Exhumation of HP rocks on the island of Fjortøft was interpreted at a rate of 3.7 mm/yr following juxtaposition with underlying UHP rocks (Terry *et al.* 2000a). On Harøya and Finnøya, isobaric cooling began at approximately 850 °C between about 405 Ma and 400 Ma, and continued through  $^{40}\text{Ar}^* T_C$  in hornblende ( $\sim 550$  °C) by about 395 Ma. This indicates a cooling rate of 30-60 °C /Ma along the isobaric cooling segment of the *Blåhø Nappe PTt* path. From this time, the cooling rate is interpreted to have slowed to about 5 °C /Ma by 365 Ma, when the rocks cooled through  $^{40}\text{Ar}^* T_C$  in white mica.

### **The Western Gneiss Region**

Much of the work in the WGR has been focused on the discovery of UHP metamorphic rocks (Smith 1984; Dobrzhinetskaya *et al.* 1995; Wain 1997; Cuthbert *et al.* 2000; Butler *et al.* doi: 10.1111/jmg.12004, in press, 2012), constraints on the timing and conditions of peak pressure metamorphism in UHP domains (Terry *et al.* 2000b; Terry unpublished Ph.D. thesis, University of Massachusetts, Amherst, MA, 2000; Walsh *et al.* 2007; Krogh *et al.* 2011; Butler *et al.* doi: 10.1111/jmg.12004, in press, 2012), and the tectonic processes required to exhume UHP rocks (Krabbendam and Dewey 1998; Johnston *et al.* 2007a; Kylander-Clark *et al.* 2012). Few studies, however, have considered how the burial and subsequent exhumation of allochthonous rocks during the Scandian orogeny relate to that of UHP rocks in the WGR. This study clearly indicates that some nappe rocks experienced relatively deep burial ( $\sim 50$  km depth) and probable detachment from the down-going Baltican basement. Partial melt generation and loss in nappes containing hydrous minerals, as described in this study, may have contributed to weakening of the surrounding subducted material, and possibly influenced processes related to UHP rock exhumation (Labrousse *et al.* 2002; Warren *et al.* 2008; Beaumont *et al.* 2009).

Constraining *P-T* estimates for mineral assemblages in gneissic and migmatitic rocks is complicated by segregation of phases into compositional bands. This increases the equilibration volume in a rock, which decreases the likelihood of full participation of the bulk-rock composition in metamorphic reactions. For this reason the typical migmatitic aluminous gneiss in the *Blåhø Nappe* did not qualify for pseudosection analysis. However,

the sheared sample from Finnøya used in this study had a small enough equilibration volume to estimate a model bulk composition precisely, from which a well-constrained pseudosection model was generated. This implies shearing at amphibolite facies conditions, probably synchronous with development of gneissic and migmatitic textures seen elsewhere in the unit. Despite partial melting and melt loss in the *Blåhø Nappe*, this study has shown that by using a combination of multi-equilibrium thermobarometry and phase equilibria pseudosections, the metamorphic history of migmatitic gneiss can be constrained from the melt loss event through retrogression and partial melt crystallization. Therefore, these methods may be useful for constraining *P-T* estimates for similarly migmatitic allochthonous rocks elsewhere in the WGR, if applied appropriately.

A westward decrease in  $^{40}\text{Ar}/^{39}\text{Ar}$  white mica cooling ages across the WGR, from  $\sim 399$  Ma to  $\sim 390$  Ma, was described by *Walsh et al.* (2007), but even younger cooling ages, down to 369 Ma, have been reported in the UHP domains (e.g. *Root et al.* 2005). Robust  $^{40}\text{Ar}/^{39}\text{Ar}$  ages from this study suggest cooling of the *Blåhø Nappe* and underlying Baltica basement as a package between 366 Ma and 362 Ma. These are northernmost and youngest  $^{40}\text{Ar}/^{39}\text{Ar}$  white mica ages reported from the WGR so far.

### **The Scandinavian Caledonides**

The timing of prograde metamorphism of allochthonous nappes during Scandian thrusting and stacking has been mostly based on paleontologic constraints (e.g. *Bruton and Harper* 1988). Recently, monazite dating of nappe units has narrowed the timing of prograde metamorphism in the respective allochthonous nappes, since monazite grows particularly well after xenotime breakdown in peraluminous sedimentary rocks. This metamorphic reaction has been predicted to take place at around 6 kbar by pseudosection models of an average pelitic bulk composition, equivalent to lower amphibolite facies conditions (*Spear and Pyle* 2010). The core domain monazite ages from this study support previous findings of an early monazite growth event, from approximately 440 Ma to 425 Ma, that has been interpreted to correspond to prograde metamorphism in the *Blåhø Nappe* or its equivalents (*Gromet et al.* 1996; *Hacker and Gans* 2005; *Walsh et al.* 2007). *Gromet et al.* (1996) reported similar prograde metamorphic ages in the eastern equivalent of the *Blåhø Nappe*, the *Seve Nappe*. Their results were interpreted to suggest that the *Seve Nappe* was at amphibolite facies conditions between 437 Ma and 427 Ma, when the units were imbricated during Scandian convergence.



## 5.4 Recommendations for Further Work

There are many additional projects and undertakings that would add to this study or complement its results. Some recommendations are suggested below.

### Mapping

Many small bedrock knobs and islands surround the northern and western coasts of Harøya and Finnøya. These should be mapped to extend and constrain lithological and lithotectonic contacts established in this study. This could better link the island and mainland *Blåhø Nappe* exposures, or alternatively, identify structures that separate or offset these exposures.

### P-T Estimates

Estimating the peak metamorphic pressure experienced by the *Blåhø Nappe* was not achieved during in this study. The garnet amphibolite sample chosen for this task had been altered by late fluid infiltration, resulting in unreliable peak *P-T* estimates. Further work on garnet-rich amphibolite samples might reveal included phases that record the prograde or peak *P-T* conditions. Using multi-equilibria thermobarometry and phase equilibria pseudosections in combination could provide the most precise estimates.

Alternatively, a second (or third) migmatitic aluminous gneiss sample, from a different location than HS10-32, with minimal melt loss and well preserved M1 mineral assemblages, could be analyzed for pseudosection construction. Compiling pseudosection results from samples with only slightly differing bulk compositions can produce a *P-T* path representative of the unit, rather than just a sample.

### Geochronology

The growth and breakdown of garnet in the migmatitic aluminous gneiss samples can probably be linked with the monazite growth events. mapping Y zoning in garnet porphyroblasts in samples used for monazite dating could test this possibility. This has been done in many studies involving EMPA monazite dating (e.g. *Terry et al. 2000b; Williams and Jercinovic 2002*), and is extremely useful for establishing the textural context of monazite growth events.

During EMPA monazite dating, abundant zircon was observed in the matrix and as inclusions in porphyroblast phases in the aluminous gneiss samples. To constrain the timing

of initial partial melting and peak pressure metamorphism in the *Blåhø Nappe*, isotopic U/Pb zircon dating could be conducted on migmatitic aluminous gneiss leucosomes. U/Pb zircon or monazite dating on samples from the FMSZ could determine the age of leucosome between the *Blåhø Nappe* and UHP basement rocks, as well as a minimum age of juxtaposition based on melt crystallization ages.

### **Other**

A curious feature that was not specifically addressed by this study is the scapolite-bearing felsic dyke that cross-cuts the garnet amphibolite-orthogneiss contact on the southern coast of Finnøya. Scapolite is also present throughout basement orthogneisses on Harøya, so it is unclear whether the scapolite in this late dyke was derived from fluid percolation through the basement, or from the overlying marble layer in the garnet amphibolite unit. A thorough study including isotopic analysis of carbon might reveal the source of the scapolite-bearing fluid.

Finally, the sliver of orthogneiss basement below the scapolite-bearing felsic dyke on Finnøya should be investigated more closely. It is unclear whether this orthogneiss was juxtaposed with the overlying garnet amphibolite, or if it can be considered as the base of then *Blåhø Nappe*. The age, petrology, and metamorphic history of this unit could be determined and compared to the history of the *Blåhø Nappe* from this study.

# APPENDIX A

## FIELD PHOTOGRAPH LOCATIONS

Figure	UTM mE	UTM mN	Description
<b>2.2</b>			<b>Dioritic Orthogneiss</b>
a	371938	6965140	Blåhø Nappe dioritic orthogneiss-garnet amphibolite contact
b	371963	6965139	Delta clast in mylonitic zone
<b>2.3</b>			<b>Garnet Amphibolites</b>
a	369797	6964139	5 cm wide garnet porphyroblast
b	369020	6963032	Foliated garnet amphibolite
c	371848	6965445	Laterally continuous garnet-bearing quartzofeldspathic gneiss
d	372810	6965371	Coarse garnets in quartzofeldspathic gneiss
e	369020	6963032	Calcite in garnet amphibolite
f	373051	6965887	Impure marble layer in garnet amphibolite unit
<b>2.4</b>			<b>Migmatitic Pelitic Gneiss</b>
a	372984	6965721	Sharp contact between pelitic gneiss and garnet amphibolite
b	369484	6963677	Leucosome and mesosome layers
c	372981	6965721	Kyanite in the mesosome
d	369583	6963767	Kyanite in the leucosome
e	369555	6963906	Crenulated gneissosity
f	369555	6963906	Homogeneous at the outcrop-scale
<b>2.6</b>			<b>Deformation Features</b>
a	371690	6965358	Blåhø Nappe dioritic orthogneiss-pelitic gneiss
b	371690	6965358	Mylonitic pelitic gneiss
c	371671	6965347	Partial melting around amphibolite boudins
d	371671	6965347	Amphibolite boudins and foliated felsic partial melt.

Table A.1: Field photograph locations. Images have been briefly described and referenced to the figure in which they appear.

## APPENDIX B

# GEOTHERMOBAROMETRY AND THERMOCALC PSEUDOSECTION DATA

### **B.1 SEM Scans and Initial Mineral Mode Outputs**

The following figures display SEM scans, complemented by BSE images and full thin section photographs, for the samples used in AveragePT calculations (Chapter 3). Analyzed mineral compositions from these samples are highlighted in each figure, and referenced by the data tables in the following section. A detailed legend for all SEM scans with associated mineral modes as output by the SEM is in Figure B.1.

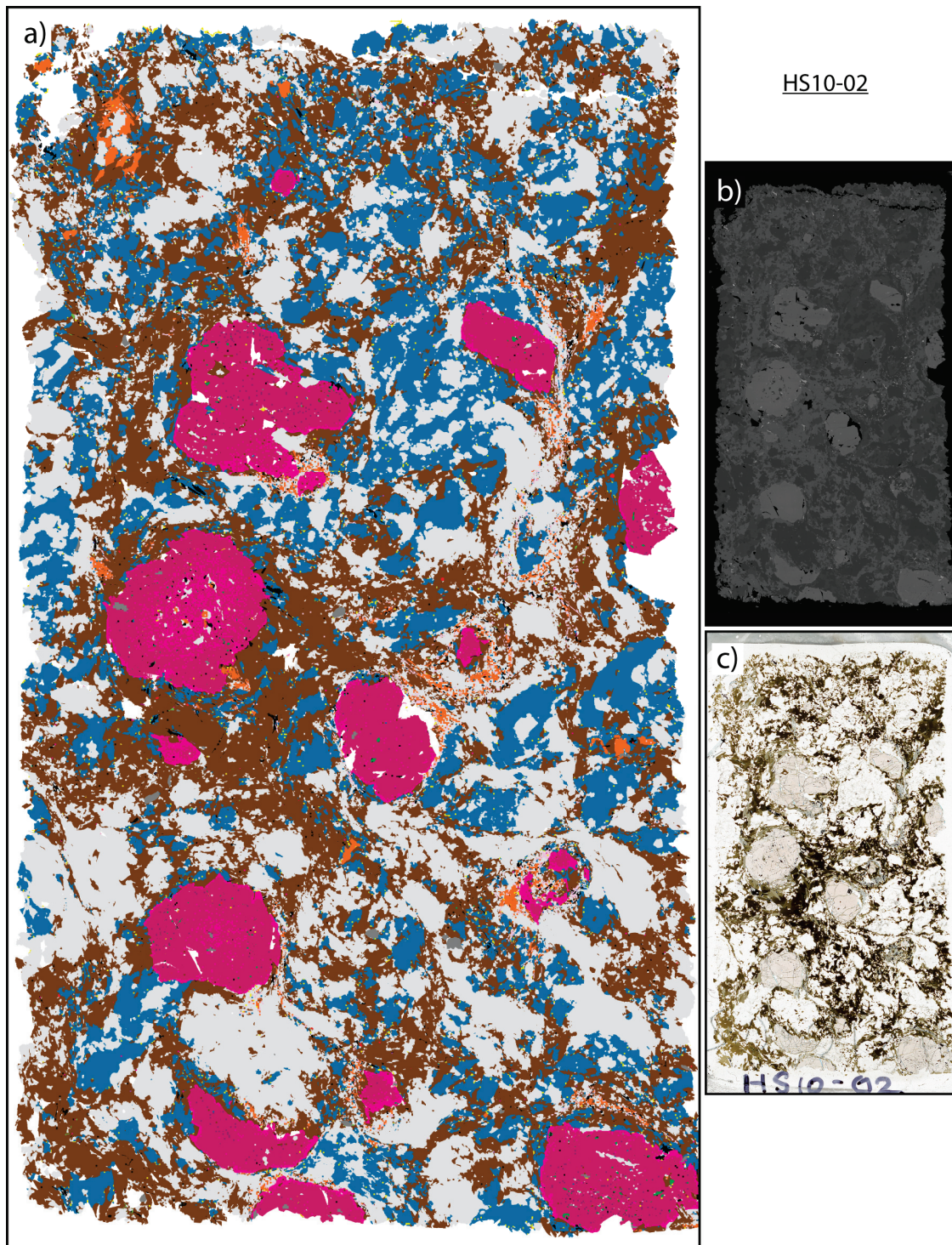


Figure B.1: SEM scan (a), BSE image (b), and photograph (c) of HS10-02 polished thin section. Mineral analysis locations are indicated on the SEM scan, and labels refer to the data tables in the following section.

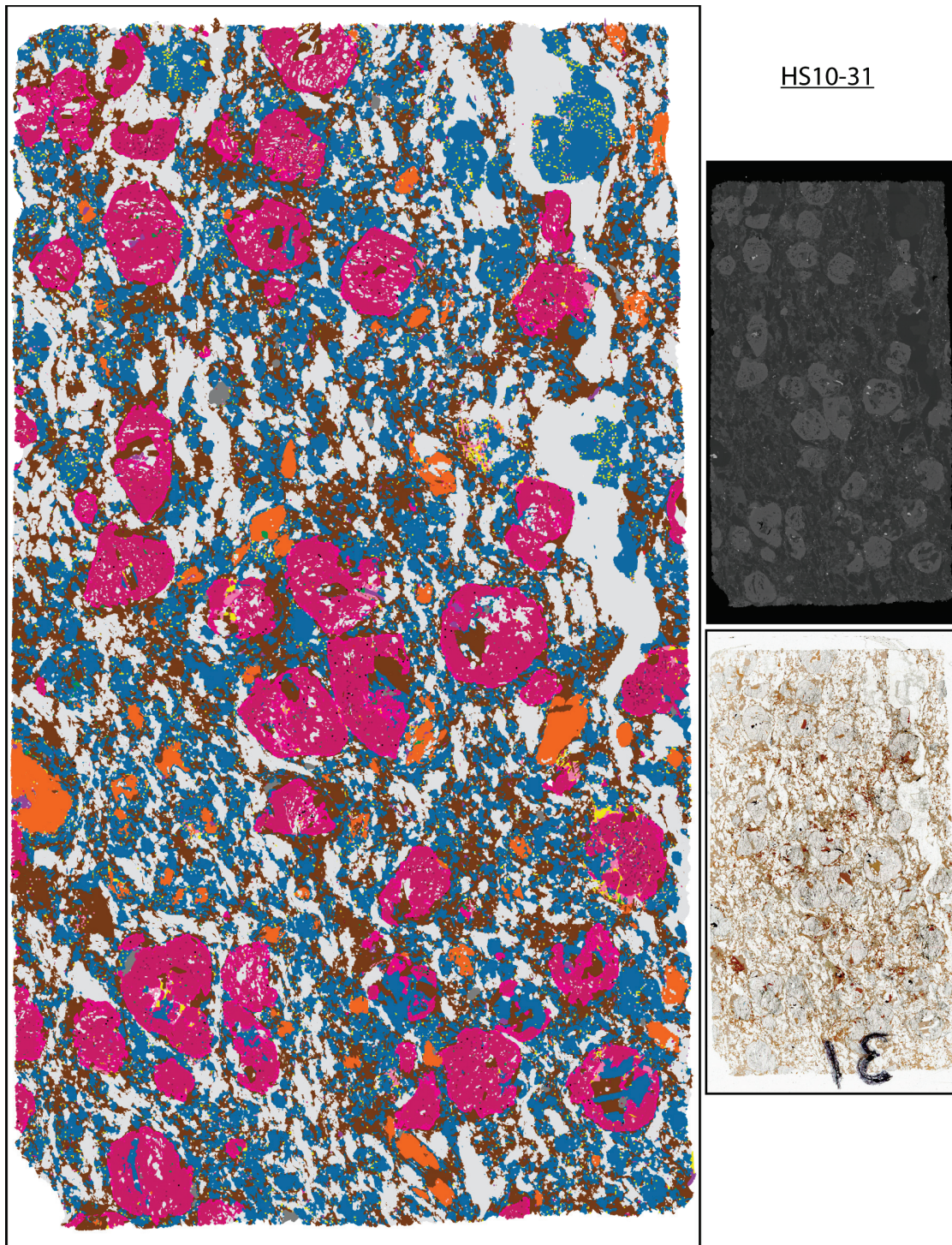


Figure B.2: SEM scan (a), BSE image (b), and photograph (c) of HS10-31 polished thin section. Mineral analysis locations are indicated on the SEM scan, and labels refer to the data tables in the following section.

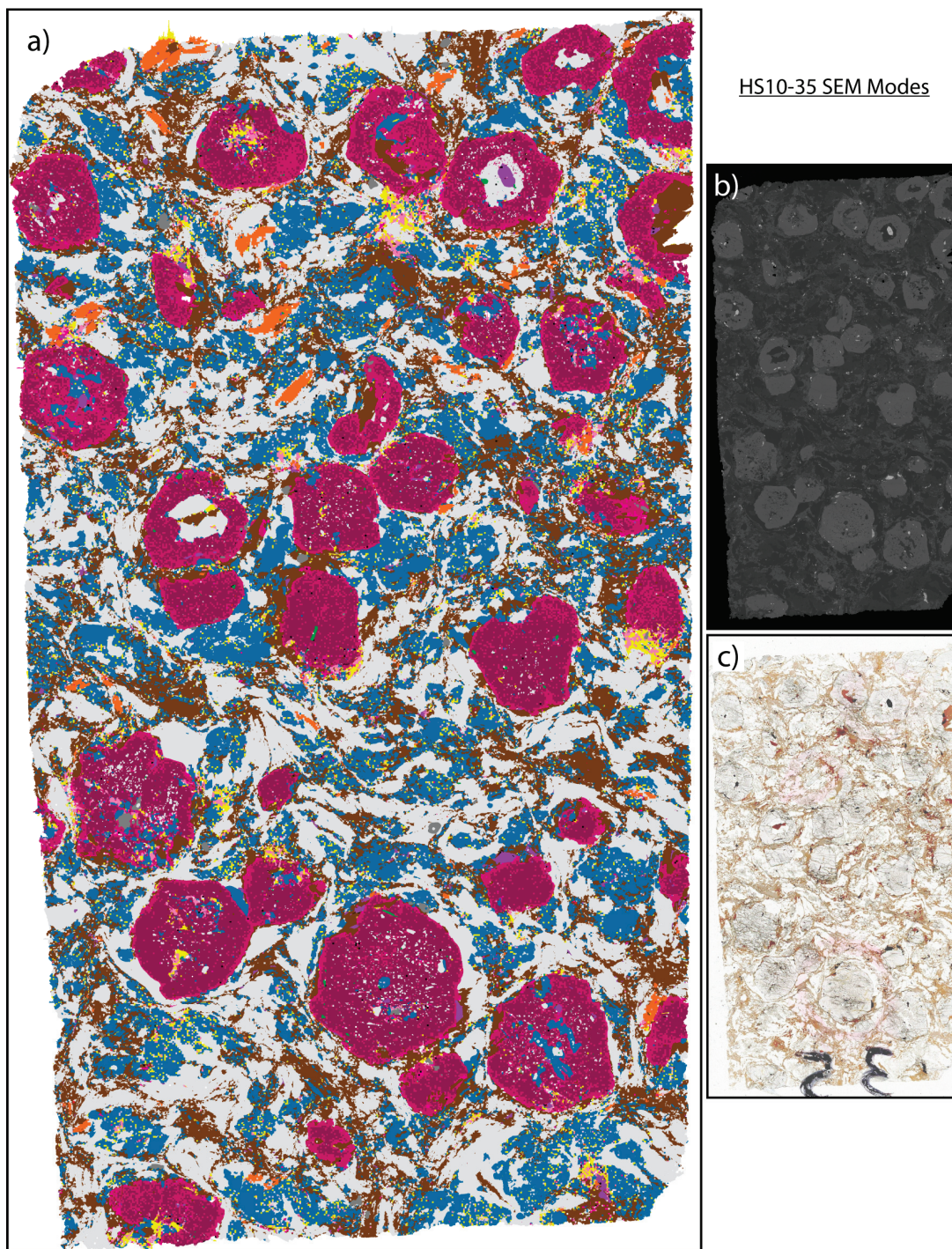


Figure B.3: SEM scan (a), BSE image (b), and photograph (c) of HS10-35 polished thin section. Mineral analysis locations are indicated on the SEM scan, and labels refer to the data tables in the following section.


















Sample	HS10-02			HS10-31			HS10-32			HS10-35		
	XRF Bulk (wt%)	Normalized Bulk (mol%)	Corrected Bulk with H2O (mol%)	XRF Bulk (wt%)	Normalized Bulk (mol%)	Corrected Bulk with H2O (mol%)	XRF Bulk (mol%)	Normalized Bulk (mol%)	Corrected Bulk with H2O (mol%)	XRF Bulk (mol%)	Normalized Bulk (mol%)	Corrected Bulk with H2O (mol%)
Oxide												
SiO2	61.15	67.73	65.08	59.39	65.34	63.56	59.70	67.02	64.55	57.82	63.24	61.76
TiO2	1.04	0.87	0.83	0.83	0.68	0.67	0.89	0.75	0.72	0.90	0.74	0.72
Al2O3	16.57	10.82	10.39	17.10	11.09	10.79	17.25	11.41	10.99	15.93	10.27	10.03
Fe2O3	10.13	--	--	11.12	--	--	8.09	--	--	11.52	--	--
FeO	--	8.45	8.12	--	9.22	8.97	--	6.84	6.59	--	9.49	9.27
MnO	0.20	--	--	0.35	--	--	0.09	--	--	0.37	--	--
MgO	4.32	7.13	6.86	4.10	6.73	6.54	4.58	7.67	7.38	5.64	9.20	8.98
CaO	2.10	2.49	2.39	3.01	3.55	3.45	1.85	2.23	2.14	3.23	3.79	3.70
Na2O	1.00	1.07	1.03	2.19	2.34	2.27	1.91	2.08	2.00	1.75	1.86	1.81
K2O	2.03	1.43	1.38	1.51	1.06	1.03	2.80	2.01	1.93	2.04	1.42	1.39
P2O5	0.26	--	--	0.21	--	--	0.18	--	--	0.14	--	--
LOI	0.40	--	--	0.00	--	--	0.90	--	--	0.30	--	--
H2O	--	--	3.91	--	--	2.72	--	--	3.68	--	--	2.34
Total	99.20	100.00	100.00	99.81	100.00	100.00	98.24	100.00	100.00	99.63	100.00	100.00
SEM Legend	Mineral Phase	SEM Mode (vol%)	Normalized Mode (vol%)	SEM Mode (vol%)	Normalized Mode (vol%)	SEM Mode (vol%)	Normalized Mode (vol%)	SEM Mode (vol%)	Normalized Mode (vol%)	SEM Mode (vol%)	Normalized Mode (vol%)	
	Quartz	32.01	33.11	27.48	28.54	30.08	31.57	29.85	31.63	29.85	31.63	
	Plagioclase	22.23	23.00	27.52	28.23	24.13	25.35	22.19	23.51	22.19	23.51	
	Biotite	30.88	32.19	22.70	23.50	28.75	30.14	19.54	20.69	19.54	20.69	
	Garnet (C-R)	11.40	10.55	16.09	16.73	7.96	8.36	21.56	22.83	21.56	22.83	
	Al2SiO5	1.03	1.07	2.74	2.85	4.27	4.48	1.17	1.24	1.17	1.24	
	Muscovite	0.53	--	1.36	--	1.00	--	2.55	--	2.55	--	
	Kaolinite	0.62	--	0.29	--	2.97	--	0.50	--	0.50	--	
	Carbonate	0.01	--	0.52	--	0.01	--	1.06	--	1.06	--	
	Apatite	0.21	--	0.37	--	0.35	--	0.32	--	0.32	--	
	Rutile	0.07	0.07	0.14	0.15	0.03	0.10	0.09	0.09	0.09	0.09	
	Ilmenite	0.57	--	0.05	--	0.07	--	0.07	--	0.07	--	
	Magnetite	0.01	--	0.00	--	0.01	--	0.01	--	0.01	--	
	Sulphides	0.01	--	0.38	--	0.10	--	0.62	--	0.62	--	
	Zircon	0.03	--	0.02	--	0.02	--	0.02	--	0.02	--	
	Monazite	0.02	--	0.01	--	0.01	--	0.01	--	0.01	--	
	Unknown*	0.37	--	0.33	--	0.24	--	0.44	--	0.44	--	
	Total	100.00	99.99	100.00	100.00	100.00	100.00	100.00	100.00	100.00	100.00	

Table B.1: SEM legend and data table. Mineral phases in the previous SEM scans are colour coded according to this legend, and the table includes the raw bulk chemistry data and SEM mineral modes for each sample. The mineral phases in peak and retrograde equilibrium assemblages, and bulk chemistry oxides required in the NCKFMASHTO system were normalized. The oxides were stoichiometrically corrected based on average mineral compositions from microprobe analyses to determine the amount of water present in each sample. The data shaded in grey were used in pseudosection modeling attempts.



## B.2 Pseudosection Isomodes and Isopleths

In each of the following figures isomodes for individual phases are plotted across the entire HS10-32 pseudosection range and overlain by the M1 and M2 assemblage areas and the three possible retrograde metamorphic paths discussed in Chapter 3. Isopleths of  $x(\text{bi})$ ,  $x(\text{g})$ , and  $z(\text{g})$  are plotted in three additional figures, also with overlying M1 and M2 assemblage polygons and retrograde metamorphic paths. Both the isomodes and isopleths are plotted in 1% increments.

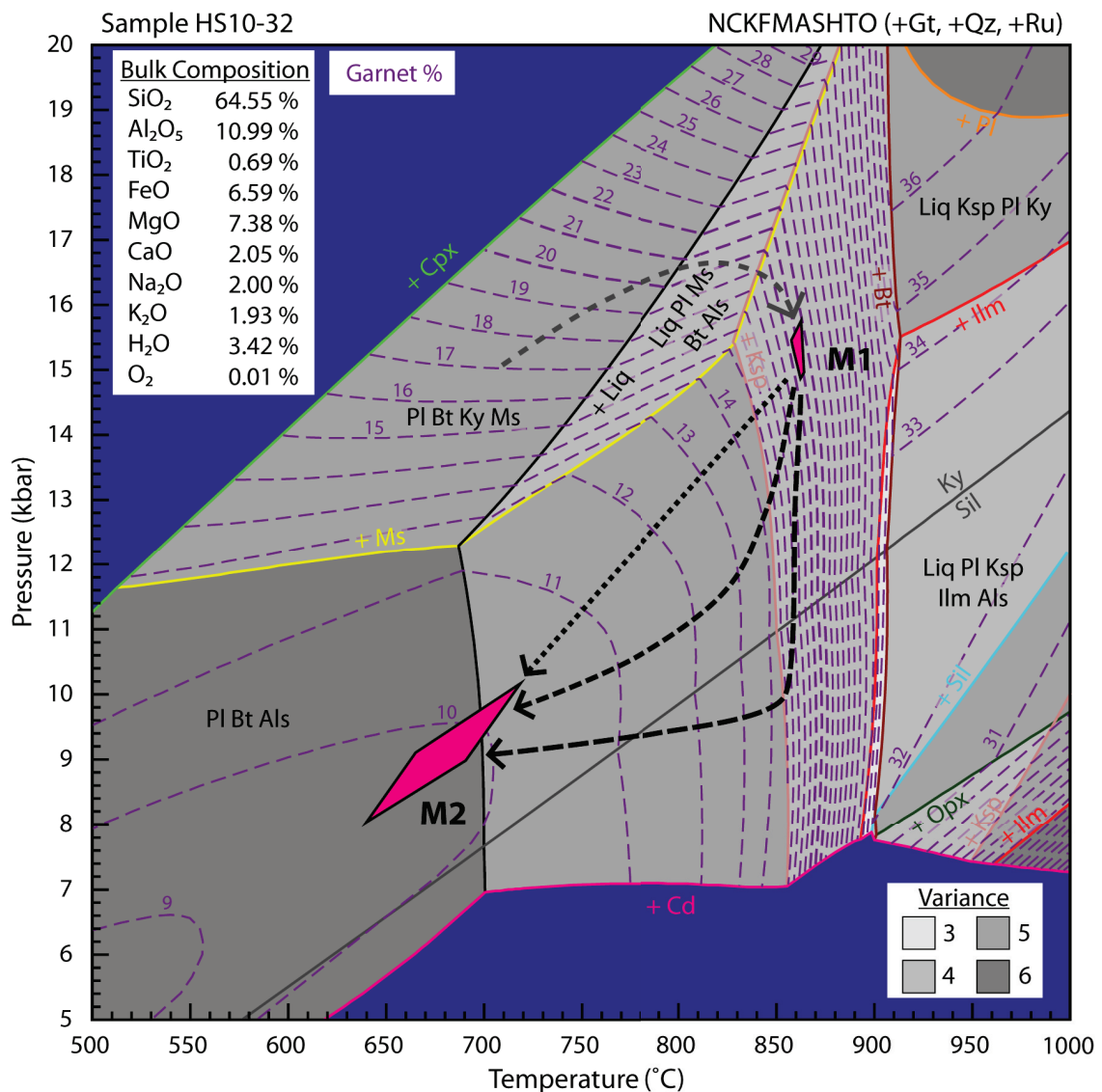


Figure B.4: Pseudosection calculated for the model bulk composition of HS10-32 contoured for garnet proportions. Lines are spaced in 1% intervals.

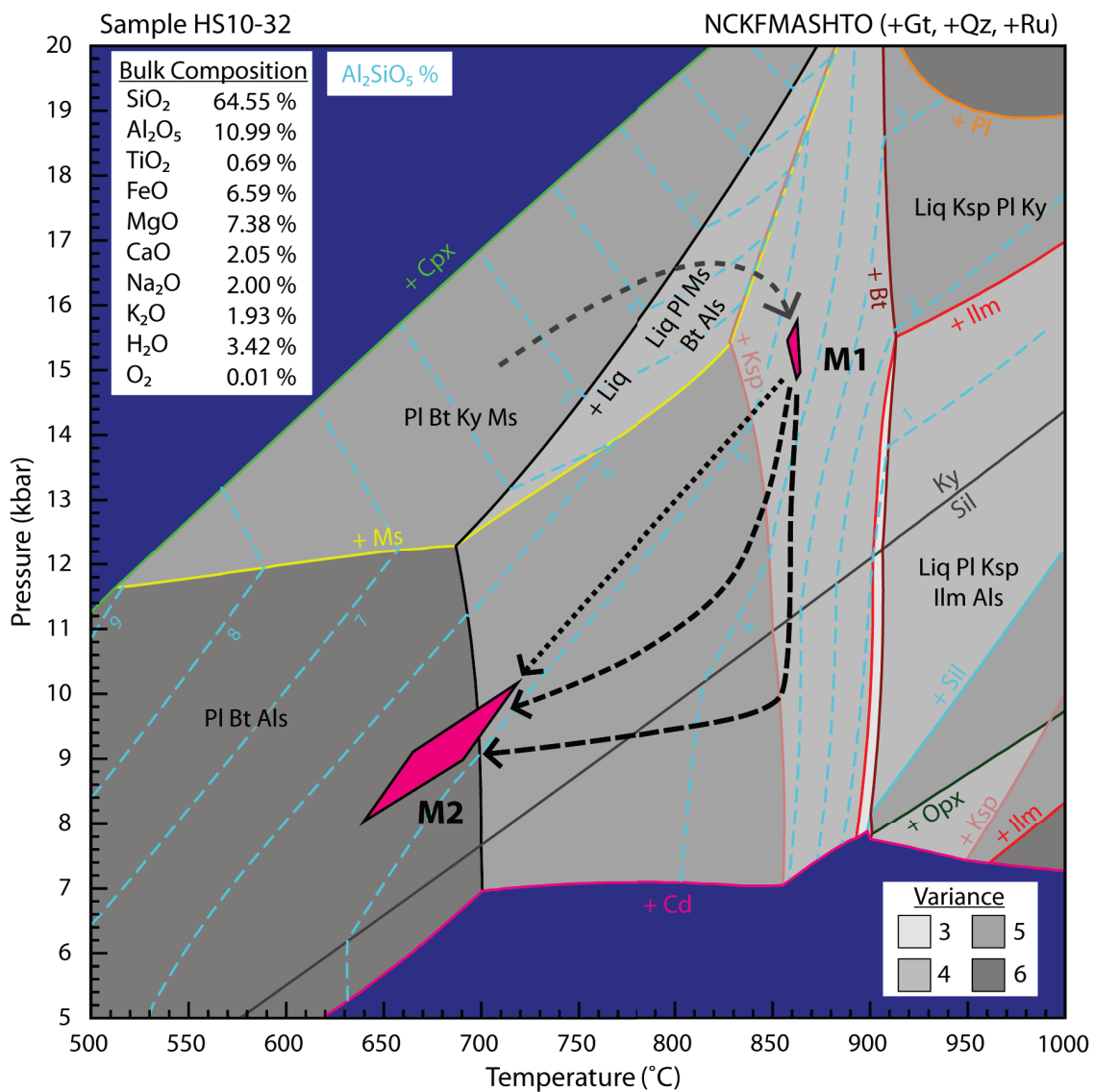


Figure B.5: Pseudosection calculated for the model bulk composition of HS10-32 contoured for Al<sub>2</sub>SiO<sub>5</sub> proportions. Lines are spaced in 1% intervals.

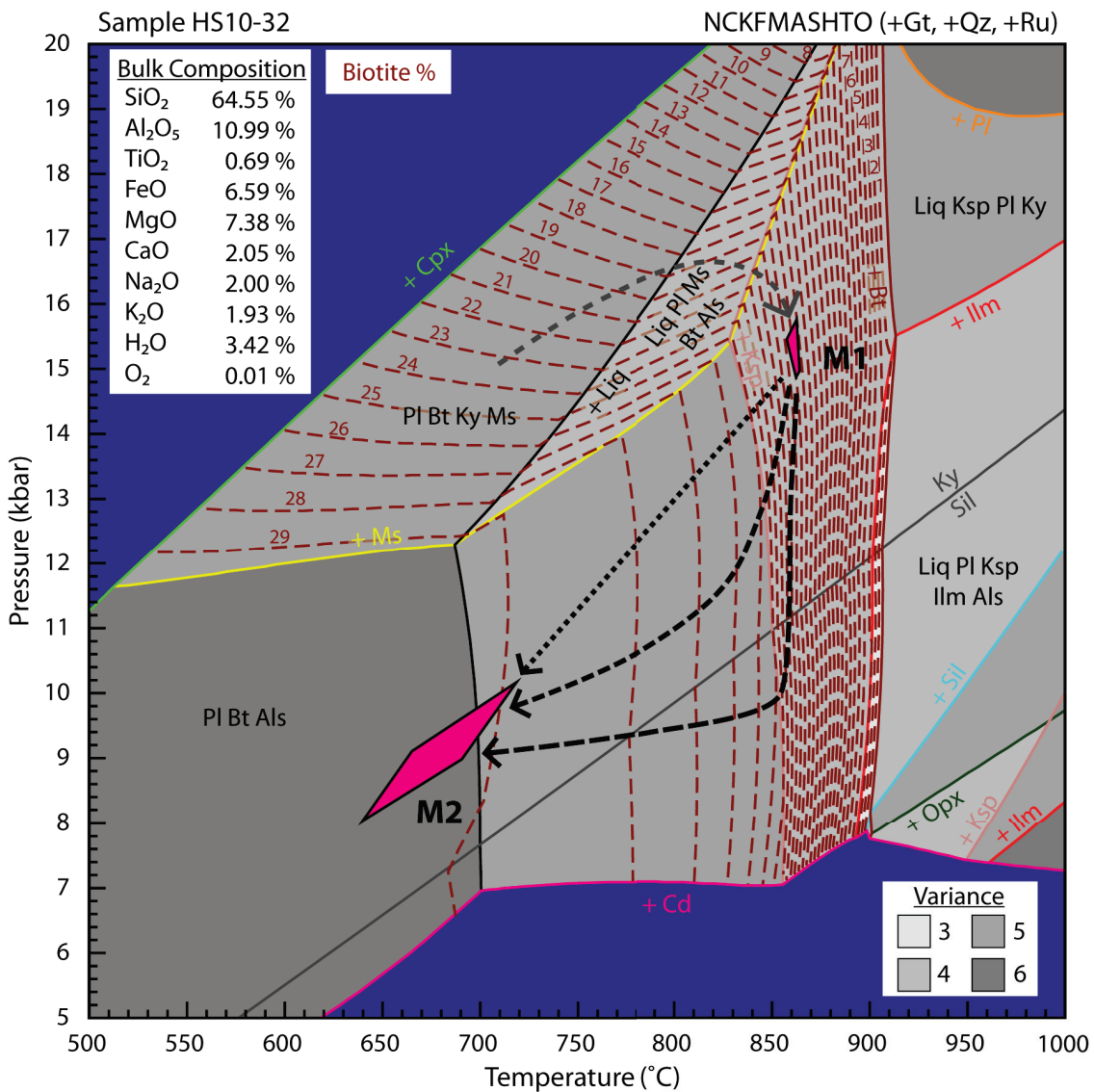


Figure B.6: Pseudosection calculated for the model bulk composition of HS10-32 contoured for biotite proportions. Lines are spaced in 1% intervals.

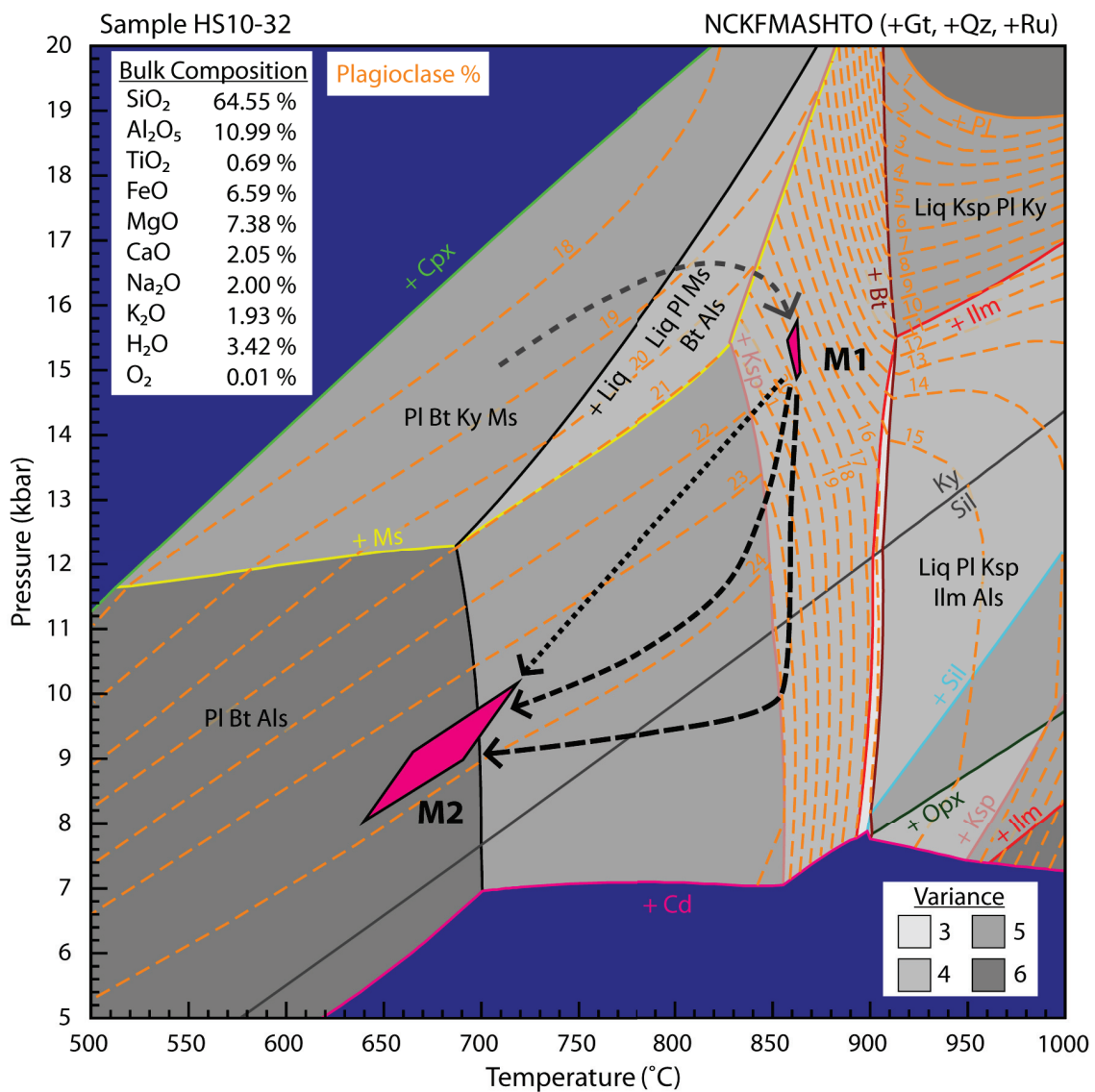


Figure B.7: Pseudosection calculated for the model bulk composition of HS10-32 contoured for plagioclase proportions. Lines are spaced in 1% intervals.

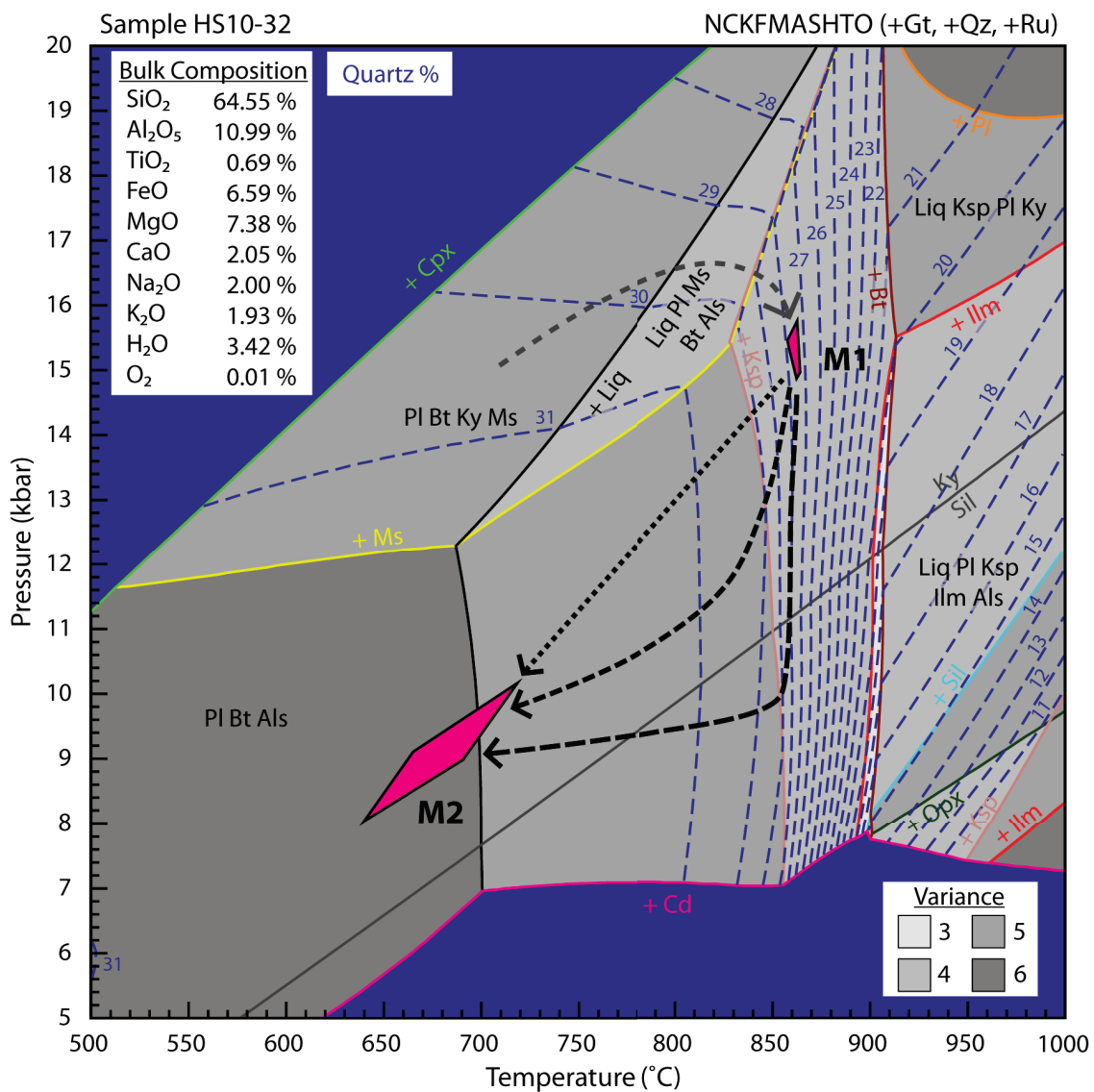


Figure B.8: Pseudosection calculated for the model bulk composition of HS10-32 contoured for quartz proportions. Lines are spaced in 1% intervals.

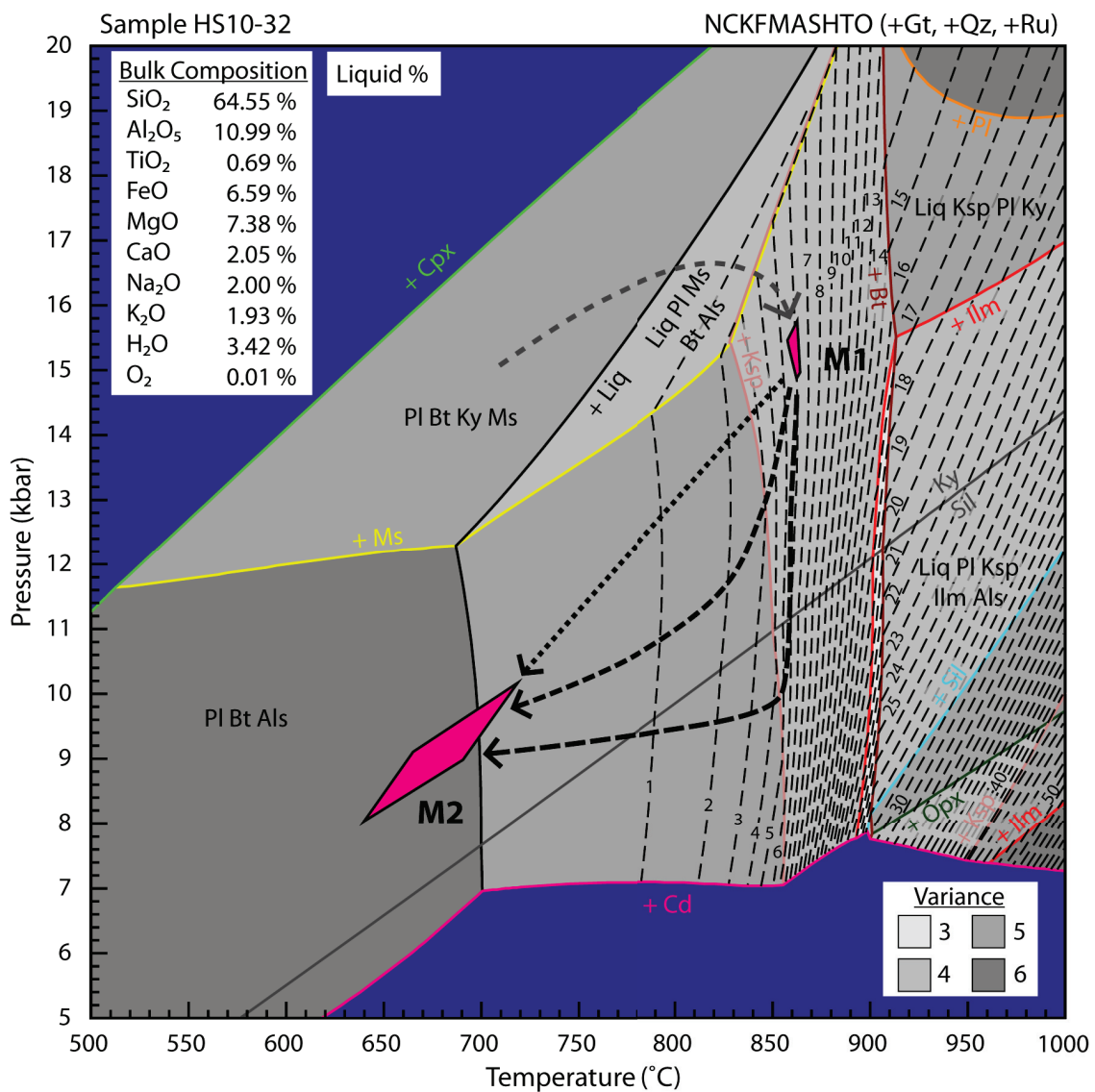


Figure B.9: Pseudosection calculated for the model bulk composition of HS10-32 contoured for melt proportions. Lines are spaced in 1% intervals.

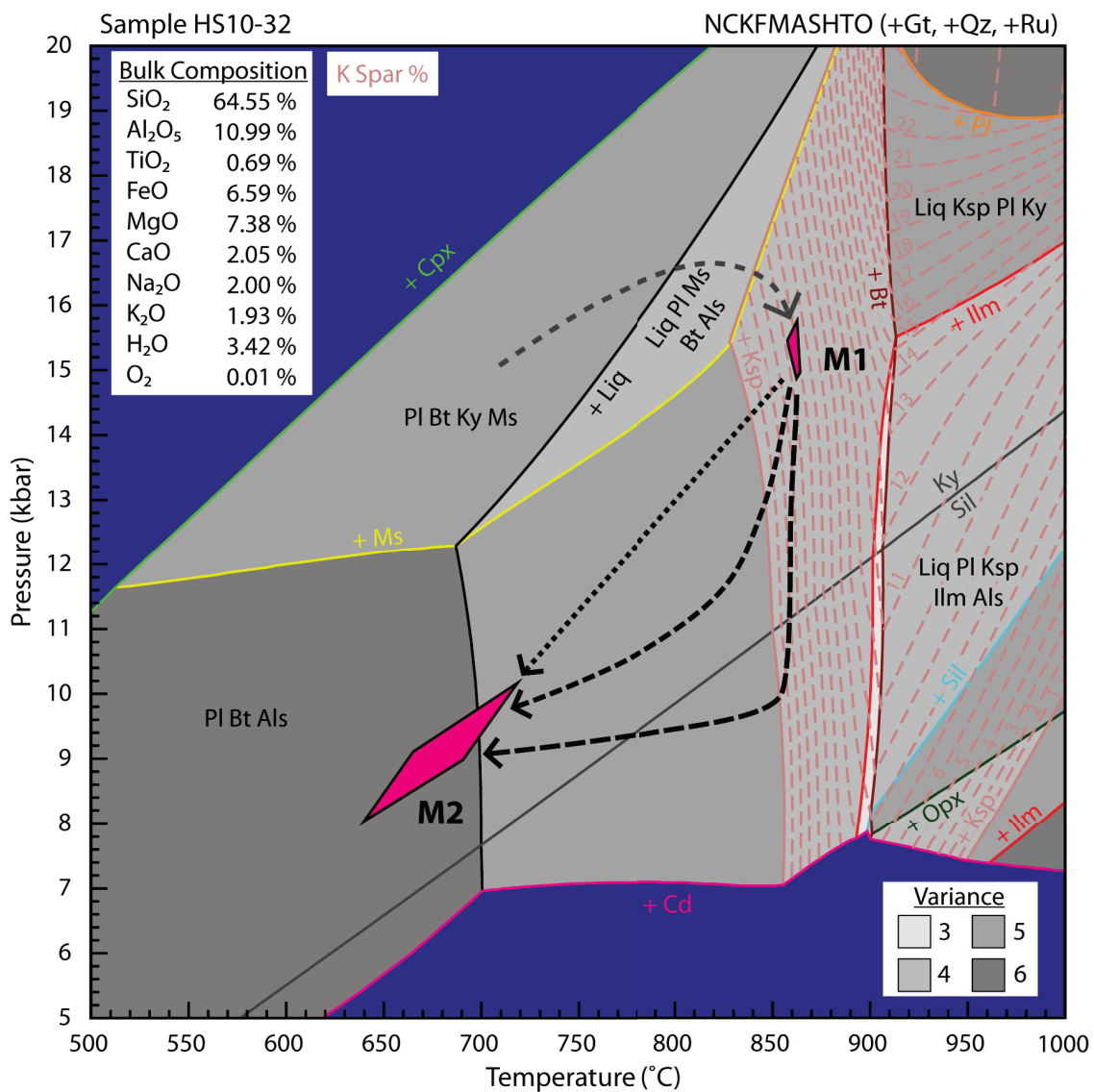


Figure B.10: Pseudosection calculated for the model bulk composition of HS10-32 contoured for potassium feldspar proportions. Contour lines are spaced in 1% intervals.

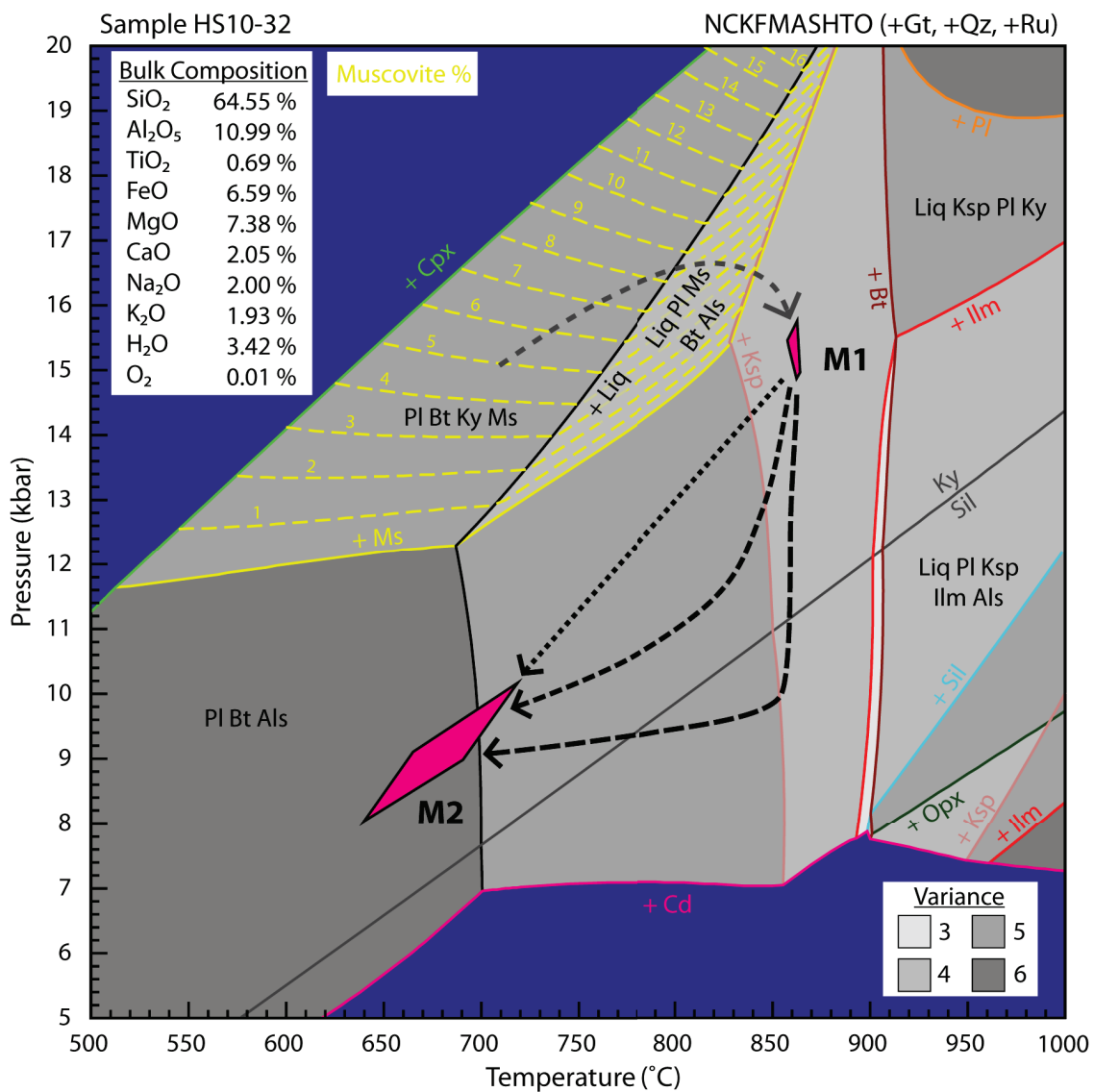


Figure B.11: Pseudosection calculated for the model bulk composition of HS10-32 contoured for muscovite proportions. Contour lines are spaced in 1% intervals.



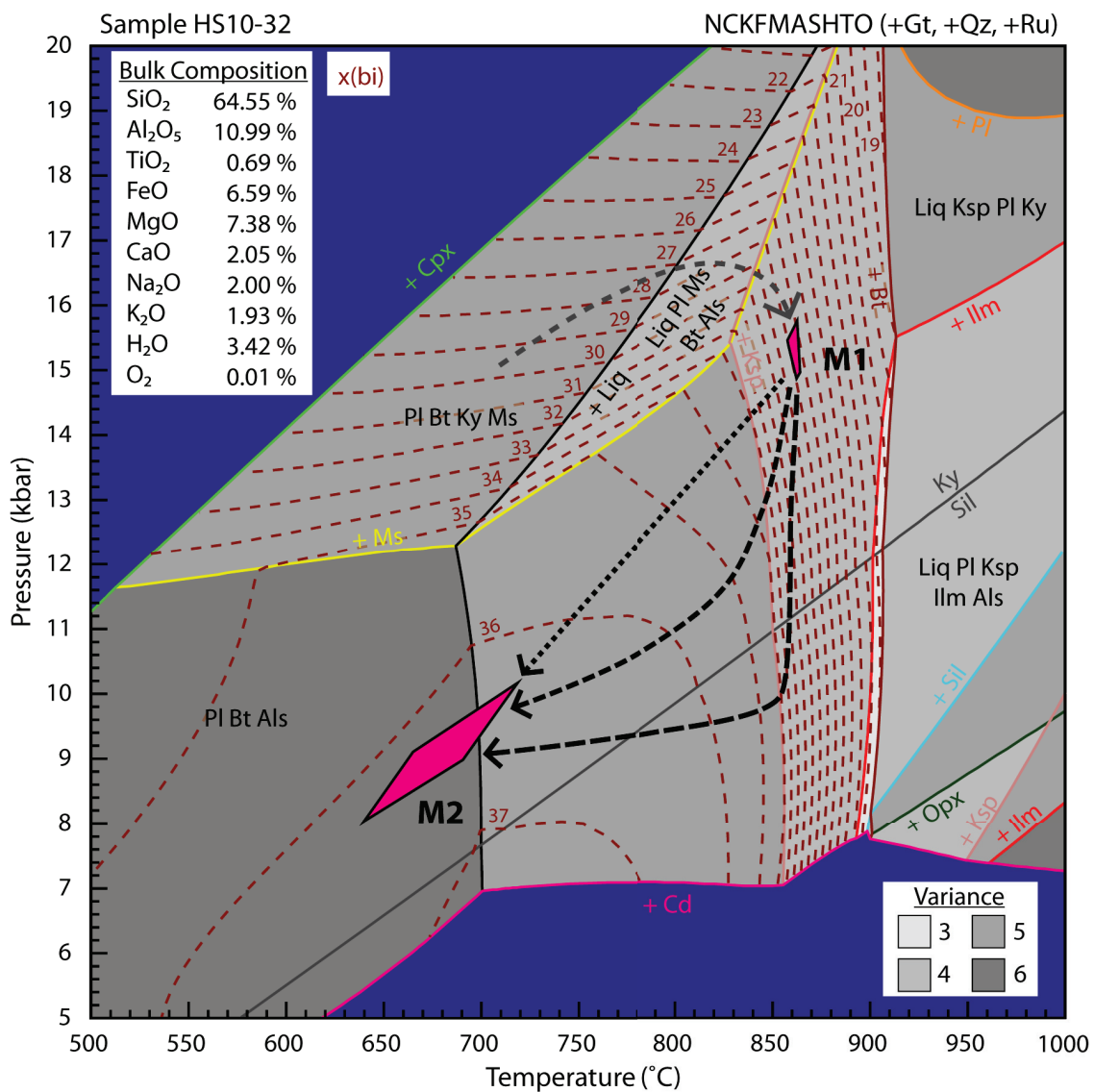


Figure B.12: Pseudosection calculated for the model bulk composition of HS10-32 contoured for  $x(\text{bi})$ . Contour lines are spaced in 1% intervals.

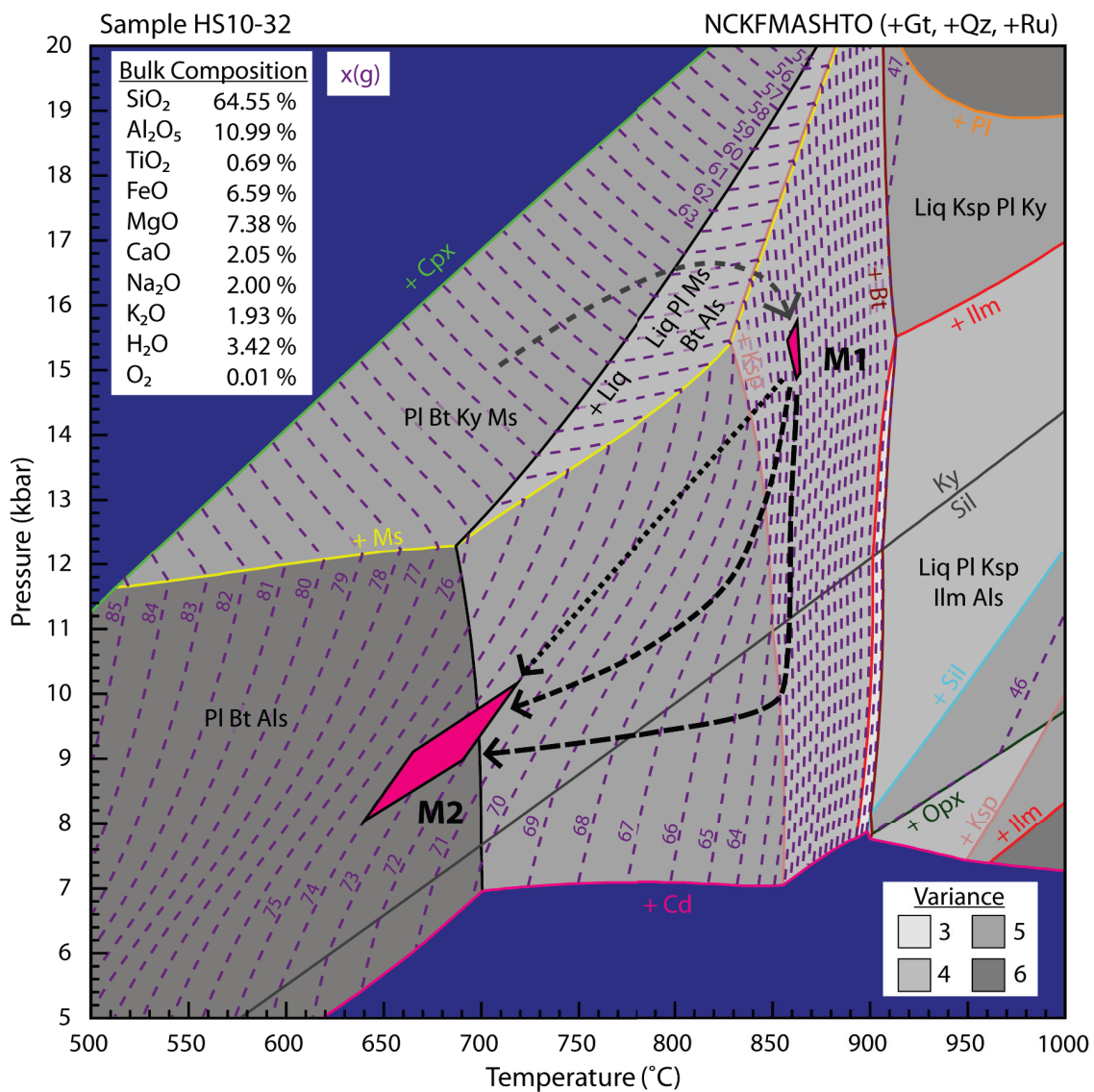


Figure B.13: Pseudosection calculated for the model bulk composition of HS10-32 contoured for  $x(g)$ . Contour lines are spaced in 1% intervals.

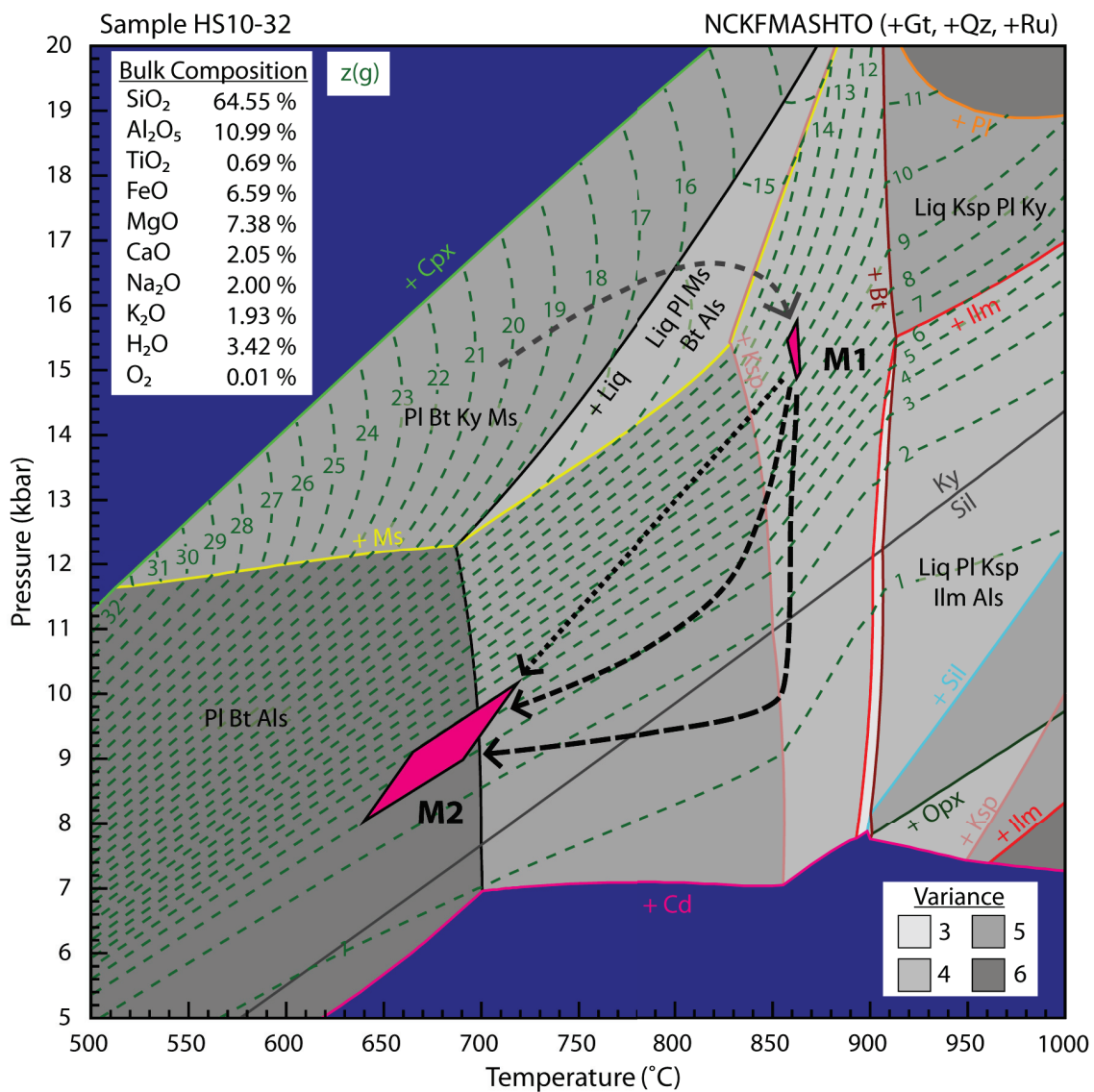


Figure B.14: Pseudosection calculated for the model bulk composition of HS10-32 contoured for z(g). Contour lines are spaced in 1% intervals.

## APPENDIX C

# MONAZITE PETROGRAPHY AND MICROPROBE DATA

### C.1 Textural Context, Analysis Locations, and Trace Element Maps

For every monazite grain that yielded analytical data used in calculating chemical domain ages, the following figures in this section show:

- The location of each monazite grain within the respective thin section (Figure C.1)
- The textural context of the monazite grain location with respect to other mineral phases in a 200x BSE image.
- A grain scale BSE image (absolute scale varies) with major element, trace element, and background scan analysis locations. Each major element location is marked with a blue circle, background scan locations with a green circle, and trace element locations with a red circle. All markers have been scaled appropriately and given a reference name that is linked to the major element data (section C.2), background scans (section C.3), and trace element data (section C.4), also found in this appendix.
- Grain scale Th, U, Pb, and Y qualitative chemical maps. Note: Relatively high concentrations of U observed *outside* of monazite are attributed to K in biotite, which has a  $K\alpha$  peak overlap with U's  $M\beta$  peak.

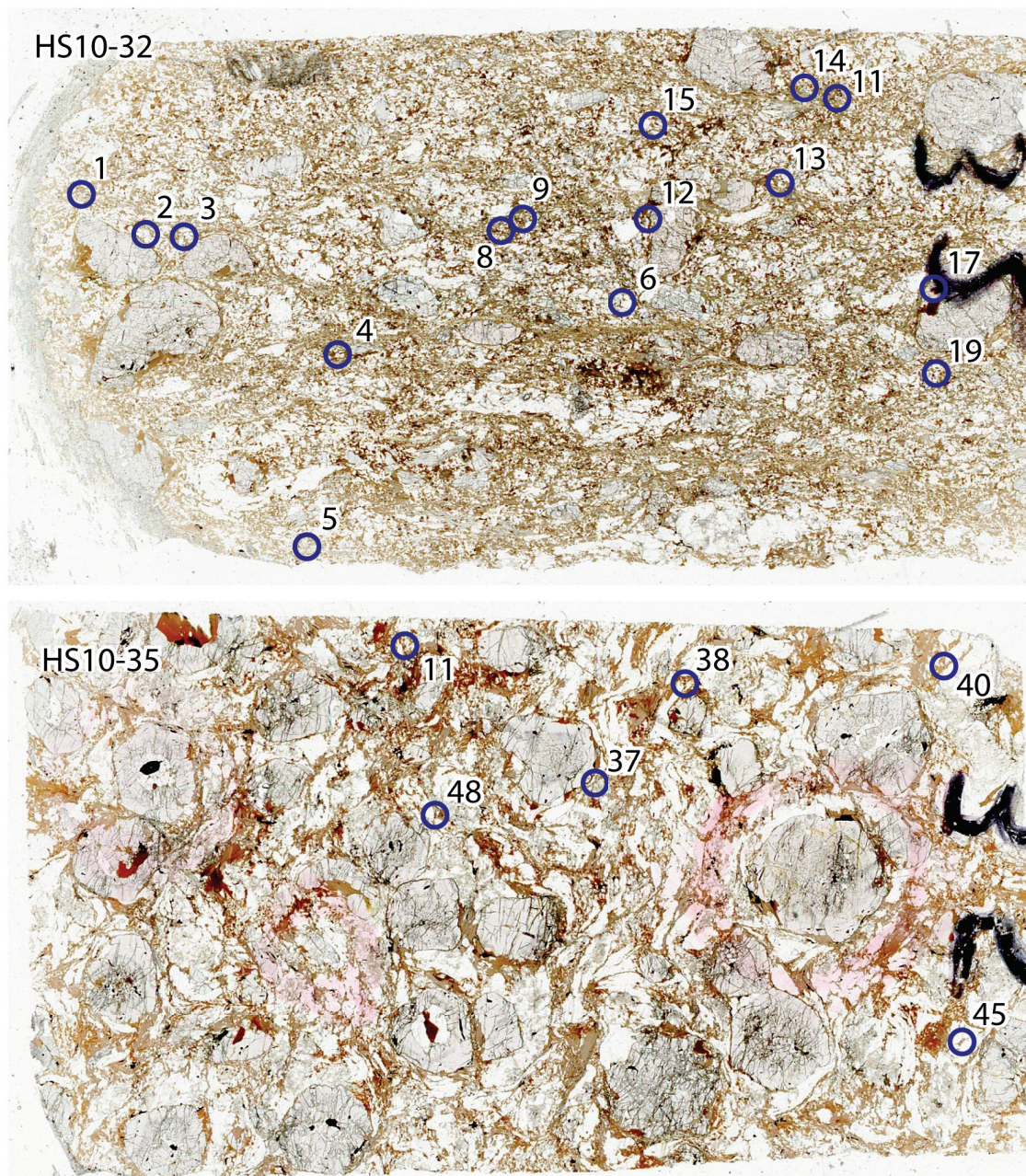


Figure C.1: HS10-32 and HS10-35 polished thin section scans. The locations of all monazite grains dated in this study are indicated and labelled.

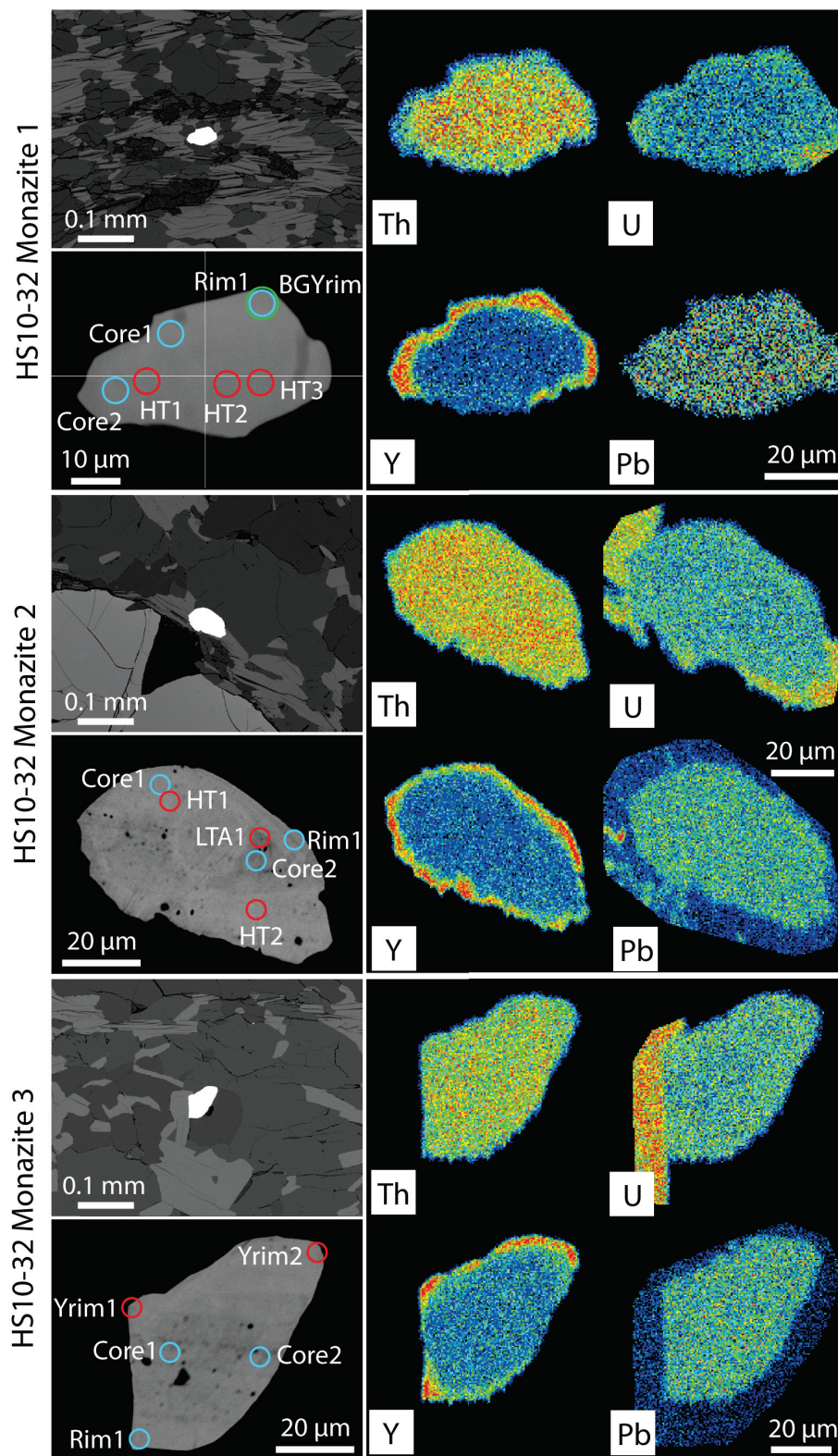


Figure C.2: Textural context, analysis locations, and chemical maps of HS10-32 monazites 1, 2, and 3.

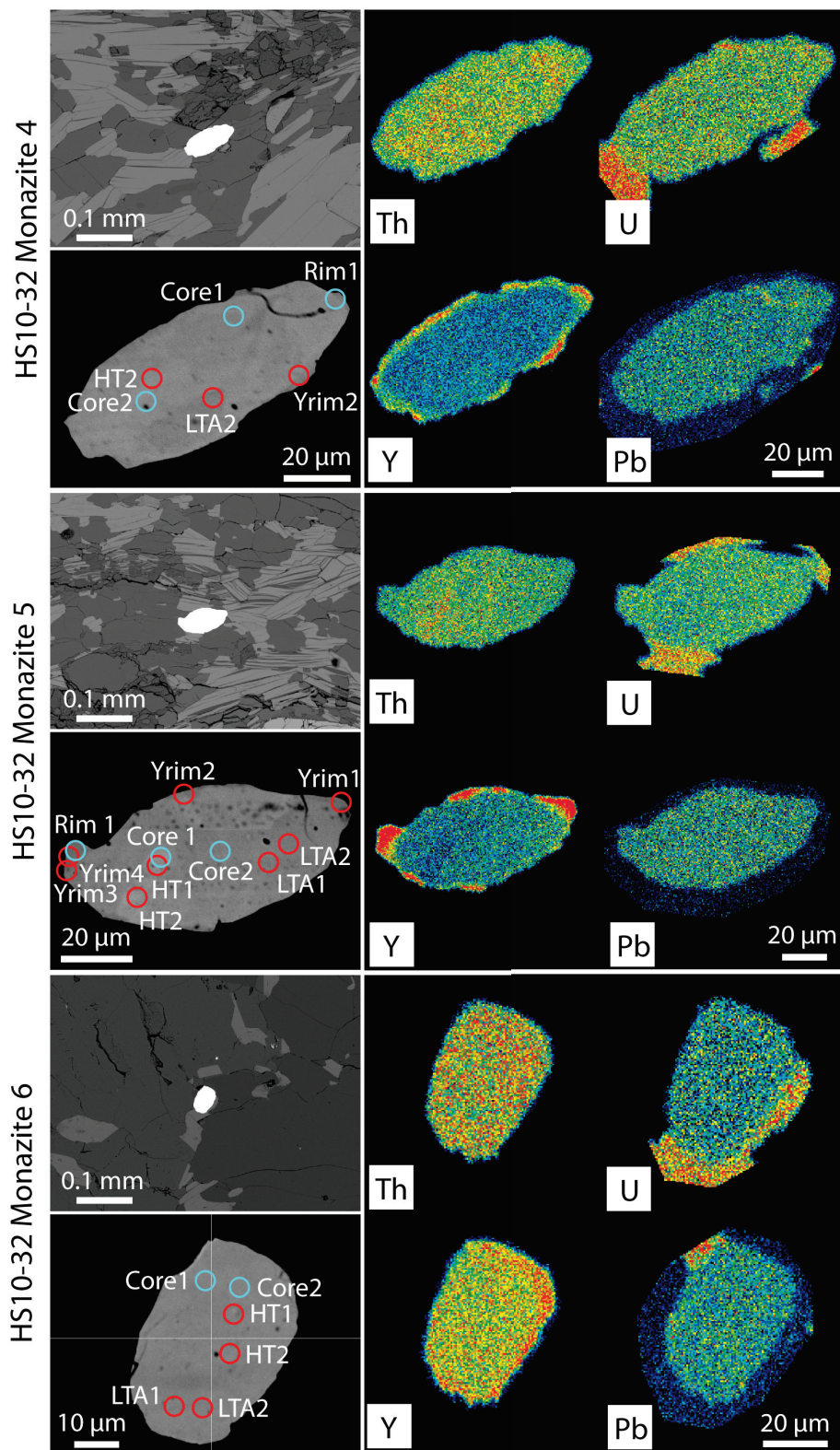


Figure C.3: Textural context, analysis locations, and chemical maps of HS10-32 monazites 4, 5, and 6.

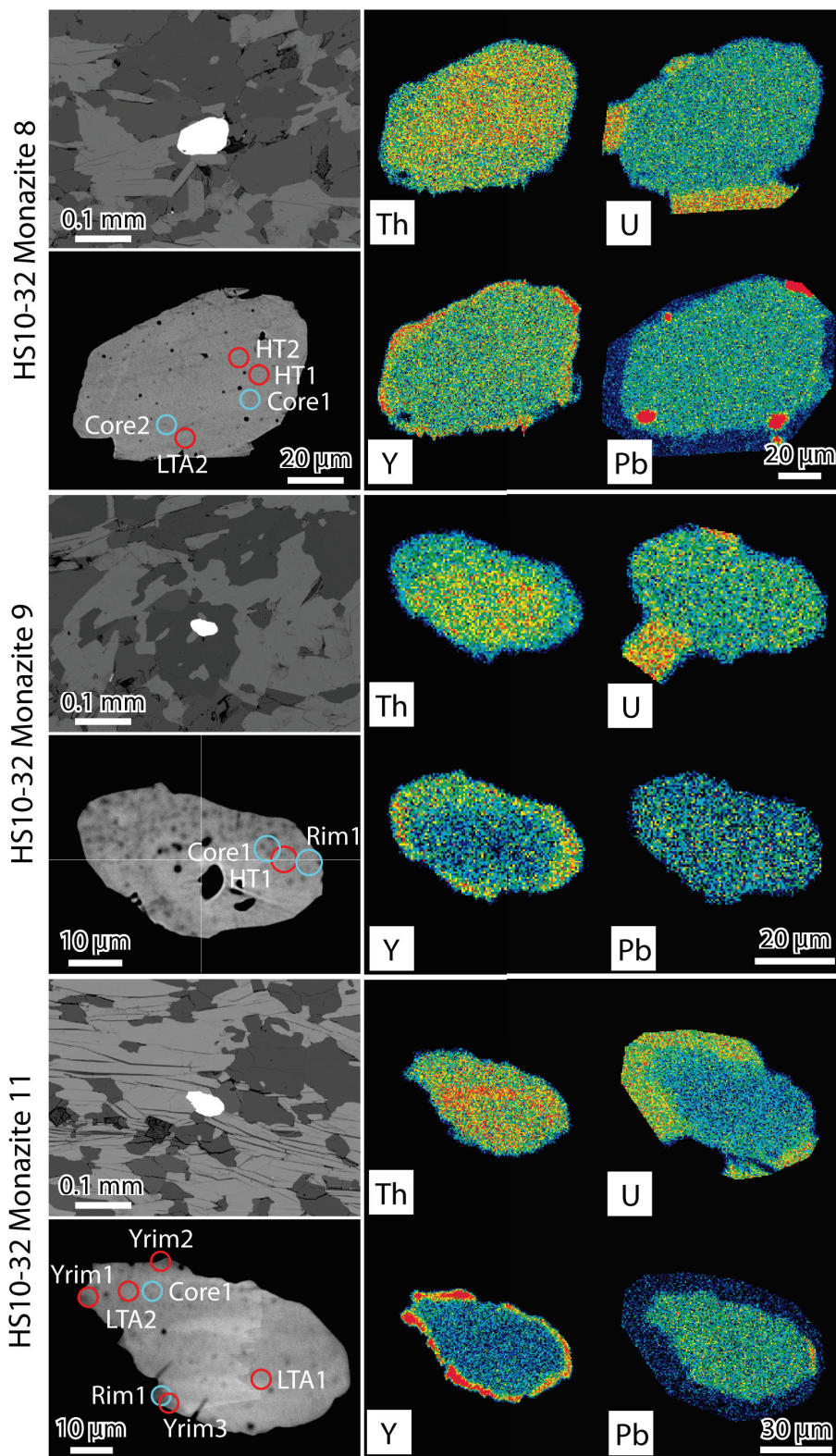


Figure C.4: HS10-32 monazites 8, 9, and 11 textural context, analysis locations, and chemical maps



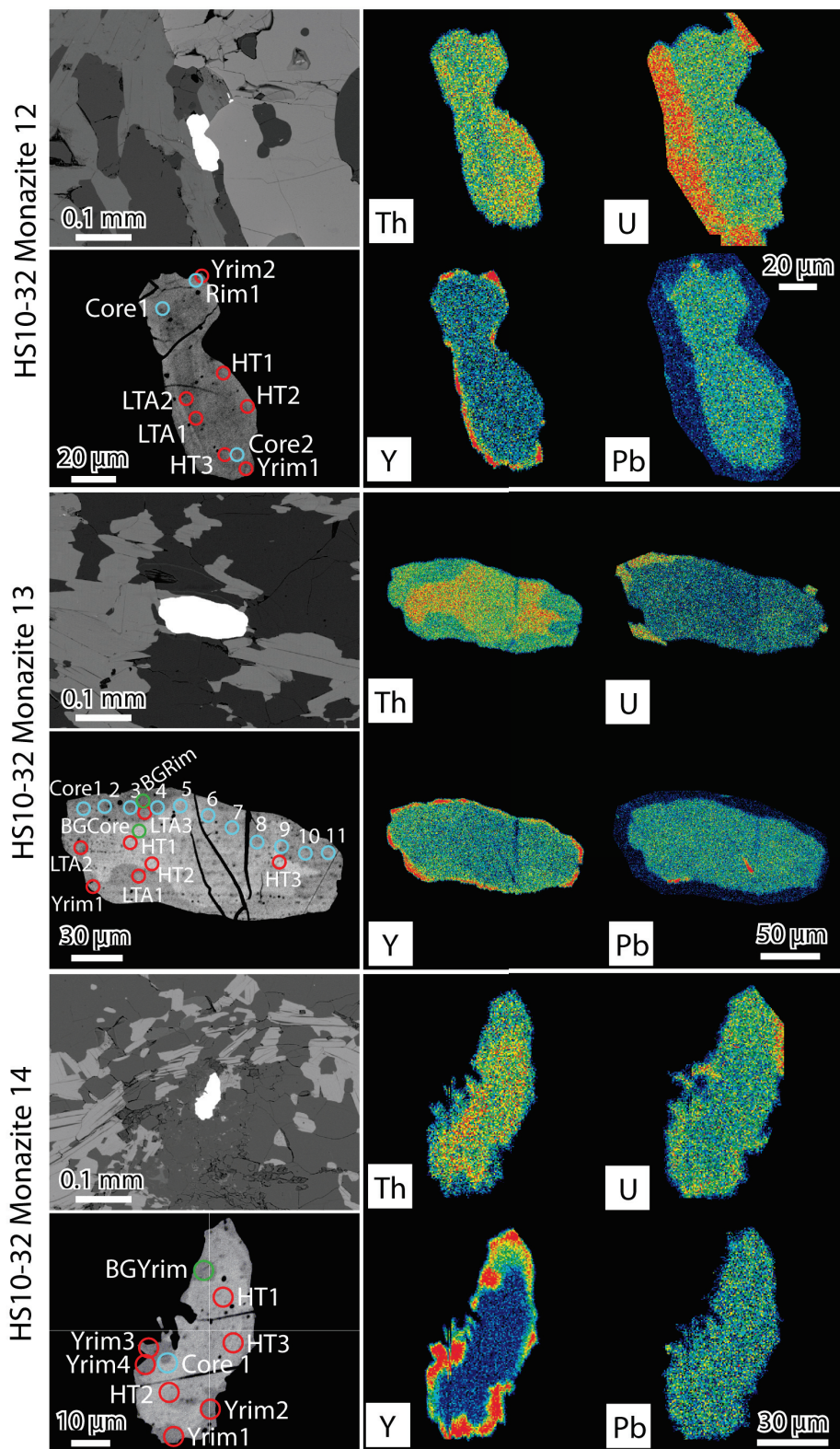


Figure C.5: Textural context, analysis locations, and chemical maps of HS10-32 monazites 12, 13, and 14.

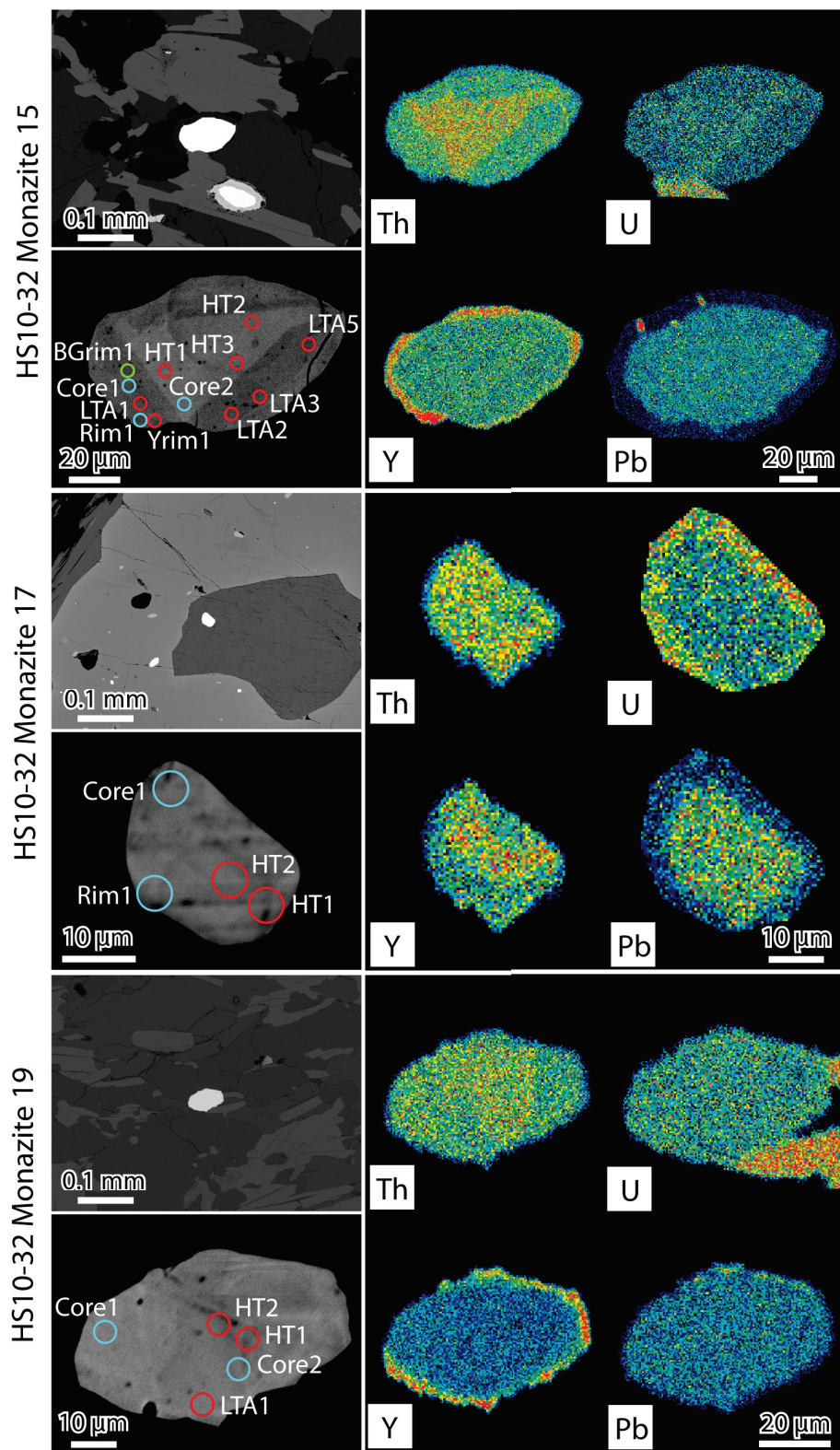


Figure C.6: Textural context, analysis locations, and chemical maps of HS10-32 monazites 15, 17, and 19.

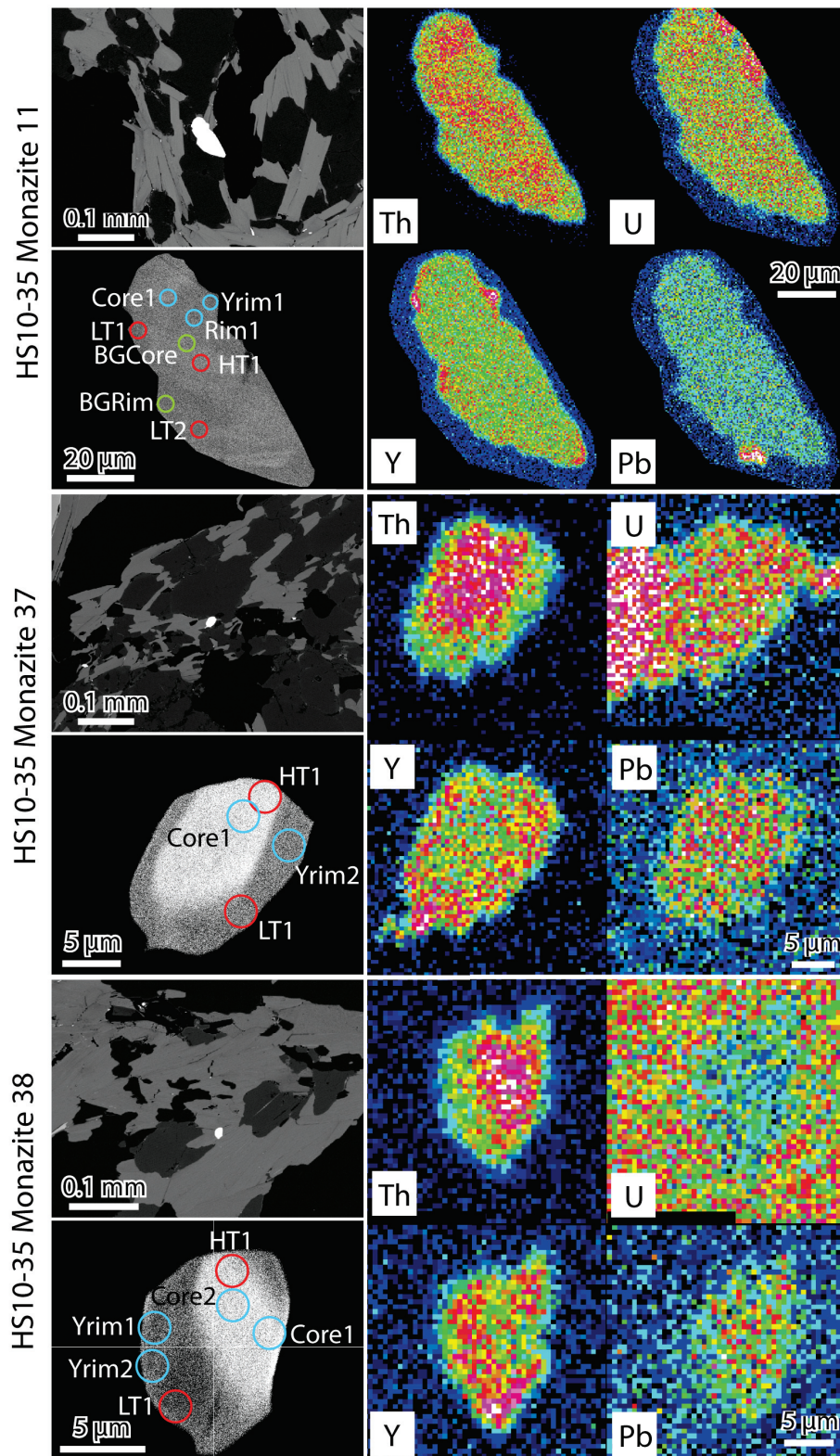


Figure C.7: Textural context, analysis locations, and chemical maps of HS10-35 monazites 11, 37, and 38.

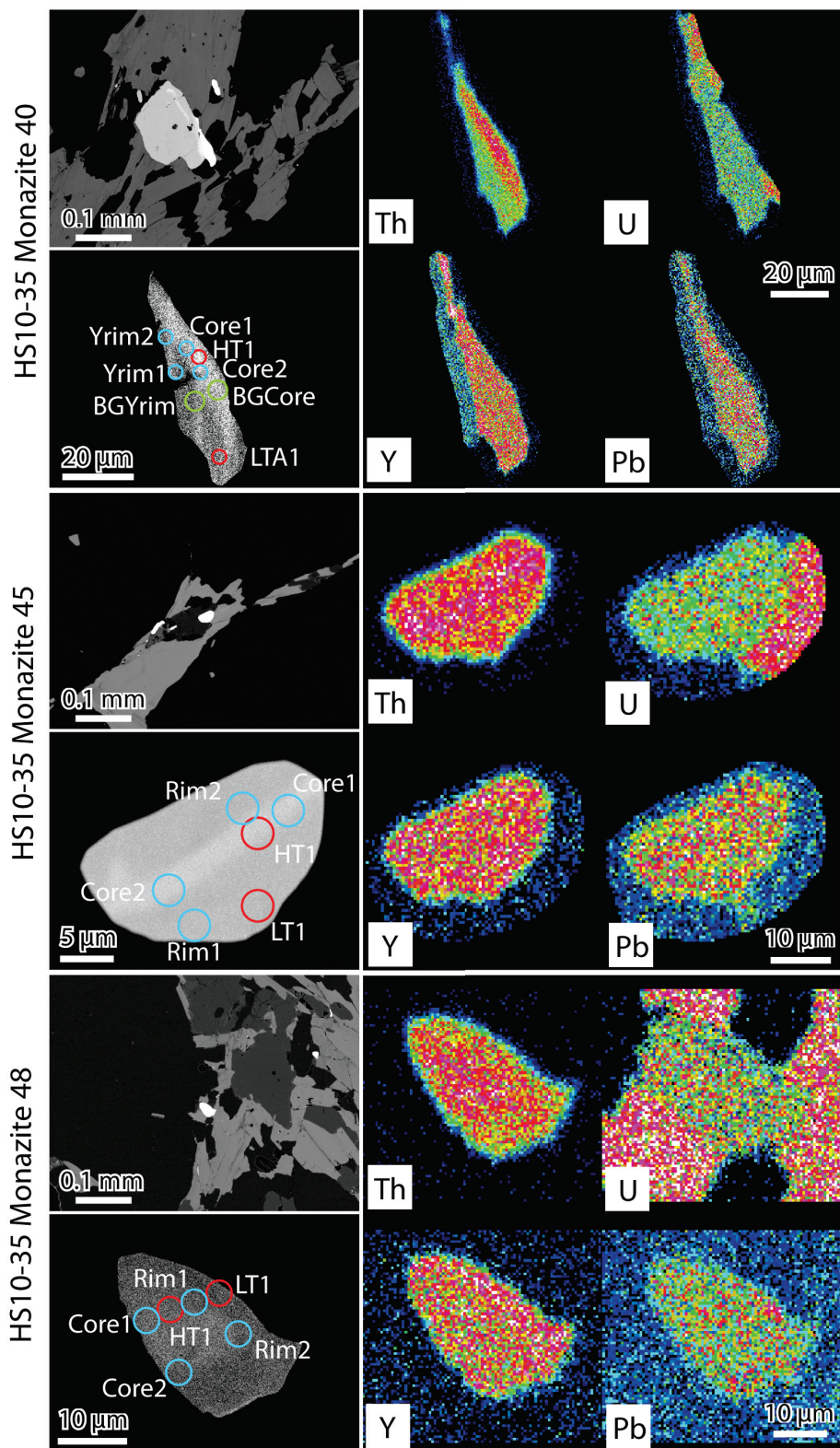


Figure C.8: Textural context, analysis locations, and chemical maps of HS10-35 monazites 40, 45, and 48.

## C.2 Quantitative Analyses of Monazite Major Elements

HS10-32 and HS10-35 major element quantitative analyses data for monazite grains with cation totals between 1.975 and 2.025 (cations per 4 oxygen) are presented in the following tables.

HS10-32 D1	Monazite 1		Monazite 2	Monazite 4	Monazite 5	Monazite 6	Monazite 8
Analysis	Core 1	Core 2	Core 1	Core 2	Core 1	Core 2	Core 1
<i>Oxides</i>							
SiO <sub>2</sub>	0.52	0.52	0.33	0.28	0.29	0.33	0.34
P <sub>2</sub> O <sub>5</sub>	28.56	28.83	28.05	29.28	28.26	28.47	28.48
SO <sub>3</sub>	1.29	0.16	1.27	1.16	1.20	1.19	1.42
CaO	0.26	1.28	0.16	0.15	0.08	0.12	0.40
Y <sub>2</sub> O <sub>3</sub>	0.08	0.03	0.23	0.19	0.19	0.23	0.19
La <sub>2</sub> O <sub>3</sub>	14.38	14.38	14.04	14.03	14.12	13.91	13.89
Ce <sub>2</sub> O <sub>3</sub>	27.88	27.71	28.08	28.08	27.12	27.47	26.95
Pr <sub>2</sub> O <sub>3</sub>	3.05	2.94	2.87	2.96	2.91	2.87	2.84
Nd <sub>2</sub> O <sub>3</sub>	12.21	11.92	12.20	12.17	11.95	12.27	11.80
Sm <sub>2</sub> O <sub>3</sub>	1.41	1.48	1.61	1.48	1.63	1.70	1.75
Eu <sub>2</sub> O <sub>3</sub>	0.83	0.91	0.92	0.95	0.93	1.02	0.97
Gd <sub>2</sub> O <sub>3</sub>	0.65	0.59	0.98	0.53	0.69	0.75	0.67
Dy <sub>2</sub> O <sub>3</sub>	0.01	0.03	0.05	0.05	0.09	0.08	0.11
ThO <sub>2</sub>	5.66	5.62	4.91	4.87	4.88	4.85	5.28
UO <sub>2</sub>	0.27	0.25	0.38	0.29	0.30	0.45	0.64
TOTAL	97.05	96.64	96.09	96.46	94.64	95.70	95.72
<i>Cations</i>							
Si	0.021	0.021	0.014	0.011	0.014	0.014	0.014
P	0.975	0.984	0.975	0.997	0.991	0.986	0.981
S	0.008	0.005	0.005	0.004	0.004	0.004	0.012
Ca	0.056	0.056	0.056	0.050	0.051	0.052	0.062
Y	0.002	0.000	0.005	0.004	0.003	0.005	0.004
La	0.214	0.214	0.213	0.208	0.212	0.210	0.208
Ce	0.412	0.409	0.422	0.414	0.413	0.411	0.401
Pr	0.045	0.043	0.043	0.044	0.042	0.043	0.042
Nd	0.176	0.172	0.179	0.175	0.174	0.179	0.172
Sm	0.020	0.020	0.023	0.020	0.022	0.024	0.024
Eu	0.012	0.012	0.013	0.013	0.013	0.014	0.014
Gd	0.009	0.008	0.013	0.007	0.008	0.010	0.009
Dy	0.000	0.000	0.001	0.001	0.000	0.001	0.002
Th	0.052	0.052	0.046	0.044	0.047	0.045	0.049
U	0.002	0.002	0.004	0.002	0.004	0.004	0.006
TOTAL	2.003	2.000	2.010	1.995	1.997	2.003	1.999

Table C.1: Core domain (D1) major element analyses for HS10-32 monazite grains.

HS10-32 D1	Monazite 9	Monazite 12	Monazite 13				
Analysis	Core 1	Core 2	Core 2	Core 5	Core 6	Core 7	Core 8
<i>Oxides</i>							
SiO <sub>2</sub>	0.35	0.33	0.34	0.51	0.49	0.44	0.49
P <sub>2</sub> O <sub>5</sub>	29.05	28.36	28.46	28.42	28.03	27.80	28.73
SO <sub>3</sub>	1.25	1.44	1.23	1.21	1.06	1.09	1.34
CaO	0.11	0.47	0.21	0.24	0.21	0.31	0.26
Y <sub>2</sub> O <sub>3</sub>	0.13	0.11	0.13	0.01	0.00	0.00	0.00
La <sub>2</sub> O <sub>3</sub>	13.89	14.13	14.02	14.17	14.48	13.98	14.45
Ce <sub>2</sub> O <sub>3</sub>	27.15	27.37	27.21	27.05	28.15	27.36	27.21
Pr <sub>2</sub> O <sub>3</sub>	2.90	2.76	2.89	2.66	2.88	2.77	2.70
Nd <sub>2</sub> O <sub>3</sub>	12.01	12.05	11.74	11.52	11.84	11.93	11.29
Sm <sub>2</sub> O <sub>3</sub>	1.50	1.71	1.45	1.38	1.27	1.43	1.30
Eu <sub>2</sub> O <sub>3</sub>	0.86	0.92	1.00	0.86	0.78	0.83	0.91
Gd <sub>2</sub> O <sub>3</sub>	0.68	0.77	0.76	0.45	0.26	0.51	0.50
Dy <sub>2</sub> O <sub>3</sub>	0.00	0.12	0.05	0.00	0.00	0.17	0.01
ThO <sub>2</sub>	5.20	5.10	5.14	5.72	5.16	5.32	5.84
UO <sub>2</sub>	0.34	0.27	0.30	0.29	0.33	0.33	0.48
TOTAL	95.38	95.89	94.92	94.49	94.93	94.26	95.51
<i>Cations</i>							
Si	0.014	0.013	0.014	0.021	0.020	0.018	0.020
P	0.998	0.976	0.988	0.988	0.979	0.978	0.988
S	0.003	0.014	0.006	0.007	0.006	0.010	0.008
Ca	0.054	0.062	0.054	0.053	0.047	0.048	0.058
Y	0.003	0.002	0.003	0.000	0.000	0.000	0.000
La	0.208	0.212	0.212	0.215	0.220	0.214	0.216
Ce	0.404	0.407	0.409	0.406	0.425	0.416	0.404
Pr	0.043	0.041	0.043	0.040	0.043	0.042	0.040
Nd	0.174	0.175	0.172	0.169	0.174	0.177	0.164
Sm	0.021	0.024	0.020	0.020	0.018	0.020	0.018
Eu	0.012	0.013	0.014	0.012	0.011	0.012	0.013
Gd	0.009	0.010	0.010	0.006	0.004	0.007	0.007
Dy	0.000	0.002	0.001	0.000	0.000	0.002	0.000
Th	0.048	0.047	0.048	0.054	0.048	0.050	0.054
U	0.003	0.002	0.003	0.003	0.003	0.003	0.004
TOTAL	1.994	2.002	1.998	1.993	1.999	1.998	1.994

Table C.1: *Continued.* Core domain (D1) major element analyses for HS10-32 monazite grains.

HS10-32 D1	Monazite 13	Monazite 14	Monazite 15	Monazite 17		Monazite 19
Analysis	Core 9	Core 1	Core 2	Core 1	Core 2	Core 2
<i>Oxides</i>						
SiO <sub>2</sub>	0.48	0.30	0.34	0.47	0.52	0.38
P <sub>2</sub> O <sub>5</sub>	28.34	28.75	28.43	28.35	28.60	28.77
SO <sub>3</sub>	1.47	1.16	1.42	1.65	1.37	1.65
CaO	0.26	0.15	0.27	0.05	0.08	0.59
Y <sub>2</sub> O <sub>3</sub>	0.03	0.16	0.13	0.47	0.18	0.12
La <sub>2</sub> O <sub>3</sub>	14.44	14.12	14.30	13.14	13.66	13.57
Ce <sub>2</sub> O <sub>3</sub>	26.54	27.19	26.64	25.65	26.43	26.98
Pr <sub>2</sub> O <sub>3</sub>	2.74	2.92	2.90	2.66	2.81	2.84
Nd <sub>2</sub> O <sub>3</sub>	10.90	11.98	11.26	11.29	11.80	11.95
Sm <sub>2</sub> O <sub>3</sub>	1.29	1.66	1.67	1.63	1.54	1.75
Eu <sub>2</sub> O <sub>3</sub>	0.90	0.98	0.93	0.94	0.92	1.06
Gd <sub>2</sub> O <sub>3</sub>	0.54	0.76	0.76	0.89	0.69	0.84
Dy <sub>2</sub> O <sub>3</sub>	0.09	0.00	0.00	0.21	0.05	0.12
ThO <sub>2</sub>	6.11	4.85	5.56	7.86	6.53	5.73
UO <sub>2</sub>	0.51	0.50	0.69	0.66	0.41	0.44
TOTAL	94.63	95.47	95.29	95.91	95.59	96.76
<i>Cations</i>						
Si	0.020	0.012	0.014	0.019	0.021	0.015
P	0.985	0.993	0.984	0.982	0.988	0.976
S	0.008	0.004	0.008	0.002	0.002	0.018
Ca	0.064	0.051	0.062	0.072	0.060	0.071
Y	0.001	0.003	0.003	0.010	0.004	0.002
La	0.218	0.212	0.216	0.198	0.206	0.200
Ce	0.399	0.406	0.399	0.384	0.395	0.396
Pr	0.041	0.043	0.043	0.040	0.042	0.042
Nd	0.160	0.174	0.164	0.165	0.172	0.171
Sm	0.018	0.023	0.024	0.023	0.022	0.024
Eu	0.013	0.014	0.013	0.013	0.013	0.014
Gd	0.007	0.010	0.010	0.012	0.009	0.011
Dy	0.001	0.000	0.000	0.003	0.001	0.002
Th	0.057	0.045	0.052	0.073	0.060	0.052
U	0.005	0.004	0.006	0.006	0.004	0.004
TOTAL	1.997	1.996	1.999	2.002	1.998	1.999

Table C.1: *Continued.* Core domain (D1) major element analyses for HS10-32 monazite grains.

HS10-32 D2	Monazite 2	Monazite 3		Monazite 4	Monazite 5	Monazite 6	Monazite 8
Analysis	Core 2	Core 1	Core 2	Core 1	Core 2	Core 1	Core 2
Oxides							
SiO <sub>2</sub>	0.39	0.33	0.32	0.33	0.34	0.32	0.33
P <sub>2</sub> O <sub>5</sub>	27.60	28.54	27.91	28.64	28.65	28.21	28.96
SO <sub>3</sub>	1.22	1.29	1.25	1.11	1.17	1.15	1.13
CaO	0.50	0.43	0.38	0.21	0.13	0.20	0.24
Y <sub>2</sub> O <sub>3</sub>	0.16	0.17	0.23	0.11	0.14	0.20	0.16
La <sub>2</sub> O <sub>3</sub>	14.07	14.46	13.60	14.33	14.03	14.04	14.27
Ce <sub>2</sub> O <sub>3</sub>	27.88	27.56	27.86	27.77	27.58	27.17	27.35
Pr <sub>2</sub> O <sub>3</sub>	2.93	3.01	2.97	3.03	2.81	2.91	3.03
Nd <sub>2</sub> O <sub>3</sub>	12.27	12.11	12.10	12.13	11.96	11.93	11.95
Sm <sub>2</sub> O <sub>3</sub>	1.62	1.72	1.73	1.64	1.56	1.66	1.65
Eu <sub>2</sub> O <sub>3</sub>	1.02	0.99	0.99	1.01	0.93	0.94	0.96
Gd <sub>2</sub> O <sub>3</sub>	0.77	0.74	0.85	0.70	0.57	0.72	0.67
Dy <sub>2</sub> O <sub>3</sub>	0.03	0.07	0.06	0.13	0.04	0.22	0.00
ThO <sub>2</sub>	4.45	4.55	4.55	4.55	5.09	4.41	4.82
UO <sub>2</sub>	0.32	0.53	0.63	0.34	0.38	0.47	0.49
TOTAL	95.22	96.48	95.43	96.03	95.36	94.52	96.00
Cations							
Si	0.016	0.013	0.013	0.013	0.012	0.013	0.013
P	0.964	0.977	0.972	0.986	0.989	0.986	0.992
S	0.016	0.013	0.012	0.006	0.003	0.006	0.007
Ca	0.054	0.056	0.055	0.048	0.053	0.051	0.049
Y	0.004	0.004	0.005	0.002	0.004	0.004	0.003
La	0.214	0.216	0.206	0.215	0.215	0.214	0.213
Ce	0.421	0.408	0.420	0.414	0.410	0.411	0.405
Pr	0.044	0.044	0.044	0.045	0.044	0.044	0.044
Nd	0.181	0.175	0.178	0.176	0.176	0.176	0.173
Sm	0.023	0.024	0.024	0.023	0.023	0.024	0.023
Eu	0.014	0.014	0.014	0.014	0.013	0.013	0.013
Gd	0.010	0.010	0.012	0.010	0.010	0.010	0.009
Dy	0.000	0.001	0.001	0.002	0.001	0.003	0.000
Th	0.042	0.042	0.042	0.042	0.046	0.041	0.044
U	0.003	0.005	0.006	0.003	0.003	0.004	0.004
TOTAL	2.006	2.001	2.004	1.999	2.003	2.001	1.994

Table C.2: Inner rim domain (D2) major element analyses for HS10-32 monazite grains.



HS10-32 D2	Monazite 9	Monazite 11	Monazite 12		Monazite 13		
Analysis	Rim 1	Core 1	Rim1	Core 1	Core 1	Core 3	Core 4
<i>Oxides</i>							
SiO <sub>2</sub>	0.30	0.24	0.25	0.24	0.27	0.25	0.28
P <sub>2</sub> O <sub>5</sub>	28.50	29.39	29.32	28.55	28.11	28.53	28.61
SO <sub>3</sub>	1.11	1.04	0.03	1.13	1.11	1.09	1.07
CaO	0.07	0.01	1.12	0.20	0.09	0.22	0.23
Y <sub>2</sub> O <sub>3</sub>	0.29	0.13	0.18	0.17	0.21	0.13	0.10
La <sub>2</sub> O <sub>3</sub>	14.16	14.05	13.90	13.91	13.99	14.11	14.17
Ce <sub>2</sub> O <sub>3</sub>	27.49	27.62	28.10	27.64	27.43	27.78	27.64
Pr <sub>2</sub> O <sub>3</sub>	2.93	2.92	2.91	2.87	2.84	2.97	2.86
Nd <sub>2</sub> O <sub>3</sub>	12.64	12.01	12.13	11.91	12.10	12.03	11.98
Sm <sub>2</sub> O <sub>3</sub>	1.69	1.57	1.67	1.76	1.65	1.60	1.51
Eu <sub>2</sub> O <sub>3</sub>	1.10	0.86	0.90	0.97	0.96	0.98	0.89
Gd <sub>2</sub> O <sub>3</sub>	1.00	0.73	0.76	0.86	0.81	0.68	0.68
Dy <sub>2</sub> O <sub>3</sub>	0.15	0.00	0.04	0.10	0.04	0.10	0.07
ThO <sub>2</sub>	4.48	4.38	4.64	4.69	4.68	4.16	3.97
UO <sub>2</sub>	0.42	0.50	0.46	0.39	0.47	0.42	0.33
TOTAL	96.32	95.42	96.40	95.37	94.75	95.04	94.38
<i>Cations</i>							
Si	0.012	0.010	0.010	0.010	0.011	0.014	0.010
P	0.984	1.008	1.001	0.990	0.986	0.988	0.990
S	0.002	0.000	0.001	0.006	0.003	0.006	0.007
Ca	0.049	0.045	0.048	0.050	0.049	0.054	0.048
Y	0.006	0.003	0.004	0.004	0.005	0.003	0.003
La	0.213	0.210	0.207	0.210	0.214	0.212	0.213
Ce	0.410	0.410	0.415	0.414	0.416	0.409	0.417
Pr	0.044	0.043	0.043	0.043	0.043	0.043	0.044
Nd	0.184	0.174	0.175	0.174	0.179	0.172	0.176
Sm	0.024	0.022	0.023	0.025	0.024	0.020	0.023
Eu	0.015	0.012	0.012	0.014	0.014	0.014	0.014
Gd	0.014	0.010	0.010	0.012	0.011	0.010	0.009
Dy	0.002	0.000	0.000	0.001	0.000	0.001	0.001
Th	0.042	0.040	0.042	0.044	0.044	0.048	0.039
U	0.004	0.004	0.004	0.004	0.004	0.003	0.004
TOTAL	2.006	1.991	1.995	1.998	2.003	1.998	1.998

Table C.2: *Continued.* Inner rim domain (D2) major element analyses for HS10-32 monazite grains.

HS10-32 D2	Monazite 13		Monazite 15	Monazite 18	Monazite 19	Monazite 20
Analysis	Core 10	Core 11	Core 1	Core 1	Core 1	Core 1
<i>Oxides</i>						
SiO <sub>2</sub>	0.29	0.33	0.30	0.28	0.38	0.32
P <sub>2</sub> O <sub>5</sub>	29.10	28.63	28.66	27.37	29.66	28.76
SO <sub>3</sub>	1.03	0.16	0.17	0.13	0.15	0.10
CaO	0.20	1.11	1.11	1.23	1.15	1.08
Y <sub>2</sub> O <sub>3</sub>	0.07	0.05	0.18	0.21	0.16	0.16
La <sub>2</sub> O <sub>3</sub>	13.82	14.07	14.33	13.32	13.63	13.92
Ce <sub>2</sub> O <sub>3</sub>	27.77	27.53	27.51	27.22	27.34	27.08
Pr <sub>2</sub> O <sub>3</sub>	2.79	2.86	2.93	2.66	2.84	2.70
Nd <sub>2</sub> O <sub>3</sub>	12.15	11.93	12.18	11.74	12.09	12.11
Sm <sub>2</sub> O <sub>3</sub>	1.43	1.49	1.67	1.68	1.67	1.69
Eu <sub>2</sub> O <sub>3</sub>	0.95	0.94	0.98	1.05	0.96	0.94
Gd <sub>2</sub> O <sub>3</sub>	0.77	0.61	0.76	0.86	0.68	0.79
Dy <sub>2</sub> O <sub>3</sub>	0.00	0.07	0.00	0.08	0.24	0.10
ThO <sub>2</sub>	4.21	4.48	4.41	4.98	4.92	4.76
UO <sub>2</sub>	0.40	0.39	0.50	0.39	0.44	0.50
TOTAL	94.99	94.65	95.65	93.17	96.30	94.99
<i>Cations</i>						
Si	0.012	0.014	0.012	0.012	0.015	0.050
P	1.001	0.994	0.990	0.980	1.004	0.941
S	0.006	0.005	0.005	0.004	0.005	0.004
Ca	0.045	0.049	0.048	0.056	0.049	0.026
Y	0.002	0.001	0.004	0.005	0.003	0.011
La	0.207	0.213	0.216	0.208	0.201	0.208
Ce	0.413	0.414	0.411	0.421	0.400	0.419
Pr	0.041	0.043	0.044	0.041	0.042	0.045
Nd	0.176	0.175	0.178	0.177	0.173	0.166
Sm	0.020	0.021	0.024	0.024	0.023	0.034
Eu	0.013	0.013	0.014	0.015	0.013	0.012
Gd	0.010	0.008	0.010	0.012	0.009	0.015
Dy	0.000	0.001	0.000	0.001	0.003	0.004
Th	0.039	0.042	0.041	0.048	0.045	0.065
U	0.004	0.004	0.004	0.004	0.004	0.003
TOTAL	1.990	1.996	2.000	2.007	1.989	2.004

Table C.2: *Continued.* Inner rim domain (D2) major element analyses for HS10-32 monazite grains.

HS10-32 D3	Monazite 1	Monazite 2	Monazite 3	Monazite 4	Monazite 5	Monazite 12
Analysis	Rim 1	Rim 1	Rim 1	Rim 1	Rim 1	Rim 1
<i>Oxides</i>						
SiO <sub>2</sub>	0.22	0.23	0.22	0.21	0.26	0.25
P <sub>2</sub> O <sub>5</sub>	29.57	28.33	28.95	28.51	29.32	29.32
SO <sub>3</sub>	0.91	1.16	1.24	1.04	1.07	1.12
CaO	0.02	0.00	0.06	0.07	0.00	0.03
Y <sub>2</sub> O <sub>3</sub>	1.79	1.16	1.27	0.68	1.67	0.18
La <sub>2</sub> O <sub>3</sub>	12.41	13.32	12.63	13.12	12.66	13.90
Ce <sub>2</sub> O <sub>3</sub>	26.27	26.02	25.98	27.16	25.83	28.10
Pr <sub>2</sub> O <sub>3</sub>	2.98	3.04	2.83	2.95	3.01	2.91
Nd <sub>2</sub> O <sub>3</sub>	12.89	12.69	13.05	12.83	12.69	12.13
Sm <sub>2</sub> O <sub>3</sub>	2.36	2.06	2.33	2.11	2.11	1.67
Eu <sub>2</sub> O <sub>3</sub>	1.05	0.98	0.99	0.96	0.98	0.90
Gd <sub>2</sub> O <sub>3</sub>	1.70	1.26	1.44	1.21	1.47	0.76
Dy <sub>2</sub> O <sub>3</sub>	0.50	0.32	0.26	0.17	0.56	0.04
ThO <sub>2</sub>	3.11	4.48	4.69	4.13	4.28	4.64
UO <sub>2</sub>	0.64	0.52	0.66	0.69	0.47	0.46
TOTAL	96.41	95.56	96.59	95.83	96.37	96.40
<i>Cations</i>						
Si	0.009	0.009	0.009	0.008	0.010	0.010
P	1.003	0.986	0.991	0.988	0.999	1.001
S	0.000	0.000	0.002	0.002	0.000	0.001
Ca	0.039	0.051	0.054	0.046	0.046	0.048
Y	0.038	0.025	0.027	0.015	0.036	0.004
La	0.183	0.202	0.188	0.198	0.188	0.207
Ce	0.385	0.392	0.384	0.407	0.380	0.415
Pr	0.044	0.046	0.042	0.044	0.044	0.043
Nd	0.184	0.186	0.188	0.188	0.182	0.175
Sm	0.033	0.029	0.032	0.030	0.029	0.023
Eu	0.014	0.014	0.014	0.013	0.014	0.012
Gd	0.023	0.017	0.019	0.016	0.020	0.010
Dy	0.006	0.004	0.003	0.002	0.007	0.000
Th	0.028	0.042	0.043	0.038	0.039	0.042
U	0.006	0.005	0.006	0.006	0.004	0.004
TOTAL	1.996	2.008	2.003	2.002	1.999	1.995

Table C.3: Y-rim domain (D3) major element analyses for HS10-32 monazite grains.

HS10-35 D1	Monazite 12	Monazite 15
Analysis	Core 2	Rim 1
<i>Oxides</i>		
SiO <sub>2</sub>	0.17	0.16
P <sub>2</sub> O <sub>5</sub>	28.38	29.20
SO <sub>3</sub>	1.01	0.94
CaO	0.00	0.02
Y <sub>2</sub> O <sub>3</sub>	2.46	0.95
La <sub>2</sub> O <sub>3</sub>	12.12	13.28
Ce <sub>2</sub> O <sub>3</sub>	25.28	26.89
Pr <sub>2</sub> O <sub>3</sub>	2.73	3.18
Nd <sub>2</sub> O <sub>3</sub>	12.20	12.48
Sm <sub>2</sub> O <sub>3</sub>	2.04	2.10
Eu <sub>2</sub> O <sub>3</sub>	0.89	1.02
Gd <sub>2</sub> O <sub>3</sub>	1.88	1.39
Dy <sub>2</sub> O <sub>3</sub>	0.68	0.18
ThO <sub>2</sub>	3.62	3.49
UO <sub>2</sub>	0.79	0.70
TOTAL	94.25	95.98
<i>Cations</i>		
Si	0.012	0.006
P	0.993	1.002
S	0.004	0.000
Ca	0.051	0.041
Y	0.003	0.020
La	0.212	0.198
Ce	0.406	0.399
Pr	0.043	0.047
Nd	0.174	0.180
Sm	0.023	0.029
Eu	0.014	0.014
Gd	0.010	0.019
Dy	0.000	0.002
Th	0.045	0.032
U	0.004	0.006
TOTAL	1.996	1.997

Table C.3: *Continued.* Y-rim domain (D3) major element analyses for HS10-32 monazite grains.

HS10-35 D1	Monazite 11	Monazite 37	Monazite 38		Monazite 40		Monazite 45
Analysis	Core 1	Core 1	Core 1	Core 2	Core 1	Core 2	Core 1
<i>Oxides</i>							
SiO <sub>2</sub>	0.38	0.65	0.63	0.60	0.39	0.41	0.57
P <sub>2</sub> O <sub>5</sub>	28.62	28.49	28.80	29.17	29.17	29.36	29.20
SO <sub>3</sub>	0.02	0.00	0.00	0.00	0.00	0.00	0.01
CaO	1.21	1.08	1.23	1.15	1.43	1.42	1.29
Y <sub>2</sub> O <sub>3</sub>	0.00	0.00	0.00	0.00	0.00	0.00	0.00
La <sub>2</sub> O <sub>3</sub>	13.64	13.67	12.81	12.59	14.76	14.86	14.01
Ce <sub>2</sub> O <sub>3</sub>	28.44	29.32	27.75	27.95	29.43	28.76	28.46
Pr <sub>2</sub> O <sub>3</sub>	2.83	2.91	2.96	2.85	2.84	2.93	2.79
Nd <sub>2</sub> O <sub>3</sub>	12.48	13.62	13.65	13.48	12.14	12.02	12.30
Sm <sub>2</sub> O <sub>3</sub>	1.74	2.12	2.00	2.04	1.66	1.56	1.63
Eu <sub>2</sub> O <sub>3</sub>	0.86	0.94	0.94	0.85	0.93	0.87	0.96
Gd <sub>2</sub> O <sub>3</sub>	0.59	0.60	0.60	0.67	0.50	0.46	0.44
Dy <sub>2</sub> O <sub>3</sub>	0.03	0.00	0.09	0.05	0.00	0.05	0.02
ThO <sub>2</sub>	5.32	6.11	6.80	6.55	5.33	5.97	6.80
UO <sub>2</sub>	0.99	0.78	0.54	0.55	0.65	0.62	0.51
TOTAL	97.15	100.31	98.81	98.50	99.21	99.29	98.98
<i>Cations</i>							
Si	0.015	0.026	0.025	0.024	0.015	0.016	0.023
P	0.983	0.962	0.975	0.984	0.981	0.984	0.982
S	0.000	0.000	0.000	0.000	0.000	0.000	0.000
Ca	0.052	0.046	0.052	0.049	0.061	0.060	0.055
Y	0.000	0.000	0.000	0.000	0.000	0.000	0.000
La	0.204	0.201	0.189	0.185	0.216	0.217	0.205
Ce	0.422	0.428	0.406	0.408	0.428	0.417	0.414
Pr	0.042	0.042	0.043	0.042	0.041	0.042	0.040
Nd	0.181	0.194	0.195	0.192	0.172	0.170	0.174
Sm	0.024	0.029	0.028	0.028	0.023	0.021	0.022
Eu	0.012	0.013	0.013	0.012	0.012	0.012	0.013
Gd	0.008	0.008	0.008	0.009	0.006	0.006	0.006
Dy	0.000	0.000	0.001	0.001	0.000	0.001	0.000
Th	0.049	0.056	0.062	0.060	0.048	0.054	0.062
U	0.009	0.007	0.005	0.005	0.006	0.006	0.004
TOTAL	2.003	2.012	2.003	1.998	2.010	2.006	2.002

Table C.4: Core domain (D1) major element analyses for HS10-35 monazite grains.

HS10-35 D3	Monazite 45	Monazite 48	
Analysis	Core 2	Core 1	Core 2
Oxides			
SiO <sub>2</sub>	0.44	0.45	0.32
P <sub>2</sub> O <sub>5</sub>	29.11	28.93	28.88
SO <sub>3</sub>	0.03	0.00	0.00
CaO	1.32	1.11	1.01
Y <sub>2</sub> O <sub>3</sub>	0.00	0.00	0.00
La <sub>2</sub> O <sub>3</sub>	13.79	14.03	13.79
Ce <sub>2</sub> O <sub>3</sub>	28.23	28.19	27.96
Pr <sub>2</sub> O <sub>3</sub>	2.94	2.94	2.90
Nd <sub>2</sub> O <sub>3</sub>	12.47	12.53	13.08
Sm <sub>2</sub> O <sub>3</sub>	1.82	1.71	1.98
Eu <sub>2</sub> O <sub>3</sub>	0.92	0.87	0.89
Gd <sub>2</sub> O <sub>3</sub>	0.54	0.57	0.61
Dy <sub>2</sub> O <sub>3</sub>	0.05	0.00	0.00
ThO <sub>2</sub>	6.52	5.34	4.52
UO <sub>2</sub>	0.54	0.93	0.73
TOTAL	98.71	97.60	96.65
Cations			
Si	0.017	0.018	0.013
P	0.983	0.986	0.992
S	0.001	0.000	0.000
Ca	0.056	0.048	0.044
Y	0.000	0.000	0.000
La	0.203	0.208	0.206
Ce	0.412	0.416	0.415
Pr	0.043	0.043	0.043
Nd	0.178	0.180	0.190
Sm	0.025	0.024	0.028
Eu	0.012	0.012	0.012
Gd	0.007	0.008	0.008
Dy	0.001	0.000	0.000
Th	0.059	0.049	0.042
U	0.005	0.008	0.006
TOTAL	2.002	2.000	1.999

Table C.4: *Continued.* Core domain (D1) major element analyses for HS10-35 monazite grains.

HS10-35 D3	Monazite 11		Monazite 37	Monazite 38	Monazite 40		Monazite 45
Analysis	Yrim 1	Rim 1	Yrim 2	Yrim 1	Yrim 1	Yrim 2	Yrim 1
Oxides							
SiO <sub>2</sub>	0.31	0.29	0.24	1.81	0.13	0.10	0.42
P <sub>2</sub> O <sub>5</sub>	29.19	29.18	29.67	28.77	30.91	30.59	29.26
SO <sub>3</sub>	0.00	0.03	0.00	0.04	0.02	0.00	0.02
CaO	0.95	0.91	0.96	0.79	2.67	2.33	1.35
Y <sub>2</sub> O <sub>3</sub>	0.05	0.00	0.06	0.20	0.00	0.03	0.00
La <sub>2</sub> O <sub>3</sub>	13.78	14.34	12.89	12.56	12.84	13.17	13.56
Ce <sub>2</sub> O <sub>3</sub>	28.43	29.15	28.91	28.31	28.67	29.09	28.24
Pr <sub>2</sub> O <sub>3</sub>	2.81	2.87	2.97	2.92	2.91	3.04	2.87
Nd <sub>2</sub> O <sub>3</sub>	12.90	12.73	13.80	13.51	13.64	13.81	12.74
Sm <sub>2</sub> O <sub>3</sub>	1.84	1.89	2.30	2.39	2.43	2.17	1.74
Eu <sub>2</sub> O <sub>3</sub>	0.84	0.87	0.97	1.03	1.04	1.00	0.92
Gd <sub>2</sub> O <sub>3</sub>	0.64	0.59	0.99	0.92	0.75	0.73	0.66
Dy <sub>2</sub> O <sub>3</sub>	0.00	0.00	0.17	0.13	0.09	0.03	0.00
ThO <sub>2</sub>	4.32	4.19	3.26	3.00	2.68	2.74	5.91
UO <sub>2</sub>	0.79	0.71	1.01	1.01	0.82	0.77	0.65
TOTAL	96.85	97.75	98.20	97.38	99.61	99.58	98.32
Cations							
Si	0.012	0.012	0.010	0.072	0.220	0.005	0.017
P	0.997	0.992	0.999	0.964	0.892	1.005	0.988
S	0.000	0.001	0.000	0.001	0.001	0.000	0.000
Ca	0.041	0.039	0.041	0.034	0.033	0.110	0.058
Y	0.001	0.000	0.001	0.004	0.003	0.000	0.000
La	0.205	0.212	0.189	0.183	0.170	0.182	0.200
Ce	0.420	0.428	0.421	0.410	0.374	0.403	0.412
Pr	0.041	0.042	0.043	0.042	0.038	0.041	0.042
Nd	0.186	0.182	0.196	0.191	0.174	0.187	0.181
Sm	0.026	0.026	0.032	0.032	0.031	0.032	0.024
Eu	0.012	0.012	0.013	0.014	0.012	0.014	0.012
Gd	0.009	0.008	0.013	0.012	0.015	0.010	0.009
Dy	0.000	0.000	0.002	0.002	0.002	0.001	0.000
Th	0.040	0.038	0.030	0.027	0.022	0.024	0.054
U	0.007	0.006	0.009	0.009	0.011	0.007	0.006
TOTAL	1.996	1.999	1.999	1.998	1.998	2.021	2.002

Table C.5: Y-rim domain (D3) major element analyses for HS10-35 monazite grains.

HS10-35 D3	Monazite 45	Monazite 48	
Analysis	Yrim 2	Yrim 1	Yrim 2
Oxides			
SiO <sub>2</sub>	0.49	0.34	0.41
P <sub>2</sub> O <sub>5</sub>	29.28	28.91	29.05
SO <sub>3</sub>	0.00	0.00	0.03
CaO	1.32	1.01	1.10
Y <sub>2</sub> O <sub>3</sub>	0.00	0.00	0.00
La <sub>2</sub> O <sub>3</sub>	14.08	13.39	14.06
Ce <sub>2</sub> O <sub>3</sub>	28.27	29.16	28.09
Pr <sub>2</sub> O <sub>3</sub>	2.90	3.05	2.91
Nd <sub>2</sub> O <sub>3</sub>	12.40	13.06	12.38
Sm <sub>2</sub> O <sub>3</sub>	1.68	1.95	1.76
Eu <sub>2</sub> O <sub>3</sub>	0.88	0.96	0.84
Gd <sub>2</sub> O <sub>3</sub>	0.37	0.60	0.60
Dy <sub>2</sub> O <sub>3</sub>	0.04	0.04	0.00
ThO <sub>2</sub>	6.18	4.56	5.16
UO <sub>2</sub>	0.66	0.75	0.70
TOTAL	98.56	97.77	97.10
Cations			
Si	0.019	0.014	0.016
P	0.986	0.986	0.991
S	0.000	0.000	0.001
Ca	0.056	0.044	0.048
Y	0.000	0.000	0.000
La	0.207	0.199	0.209
Ce	0.412	0.430	0.414
Pr	0.042	0.045	0.043
Nd	0.176	0.188	0.178
Sm	0.023	0.027	0.024
Eu	0.012	0.013	0.012
Gd	0.005	0.008	0.008
Dy	0.000	0.000	0.000
Th	0.056	0.042	0.047
U	0.006	0.007	0.006
TOTAL	2.001	2.004	1.998

Table C.5: *Continued.* Y-rim domain (D3) major element analyses for HS10-35 monazite grains.



### C.3 Background Scans for U, Th, Pb, and Y Trace Elements in Monazite Domains

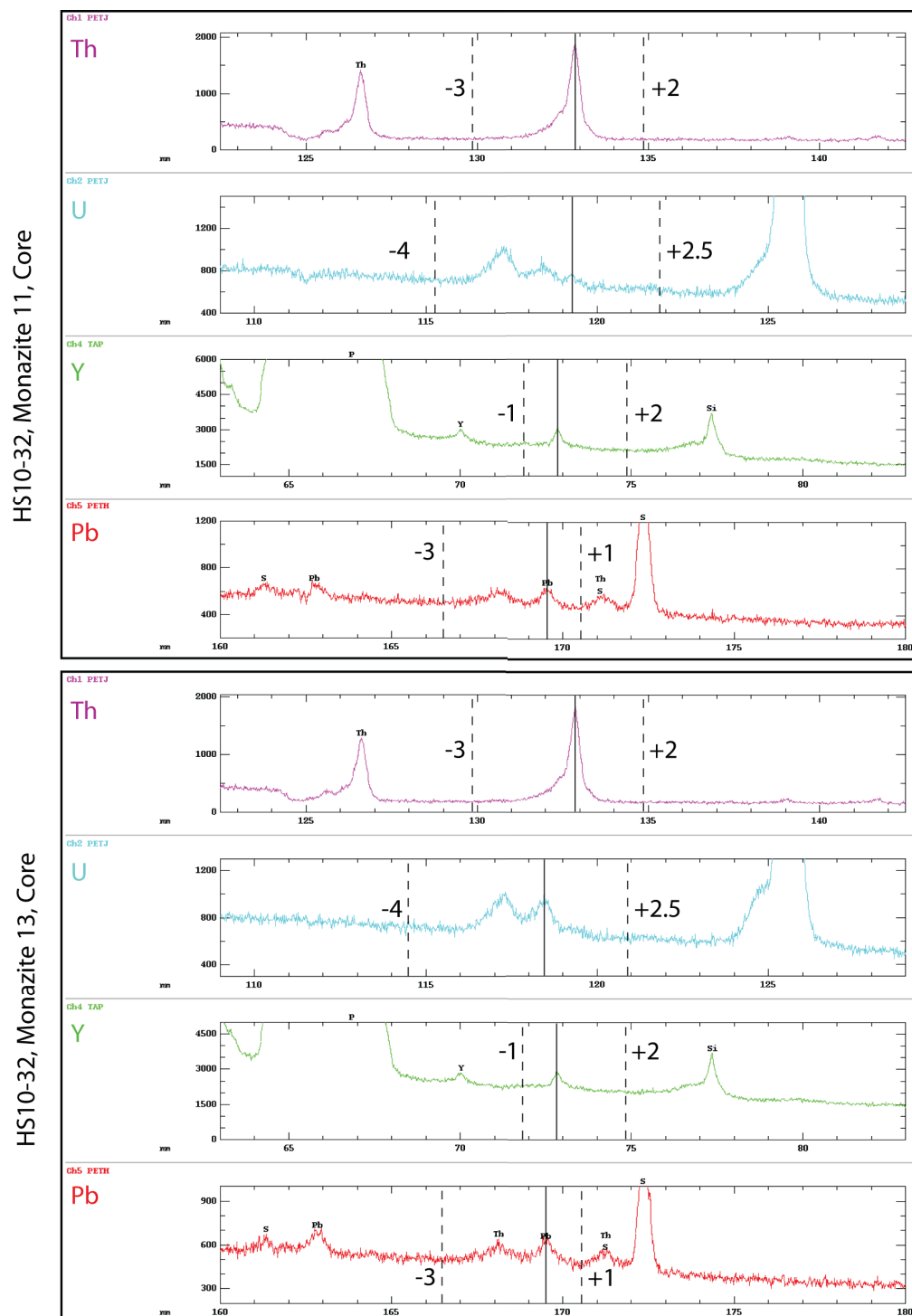
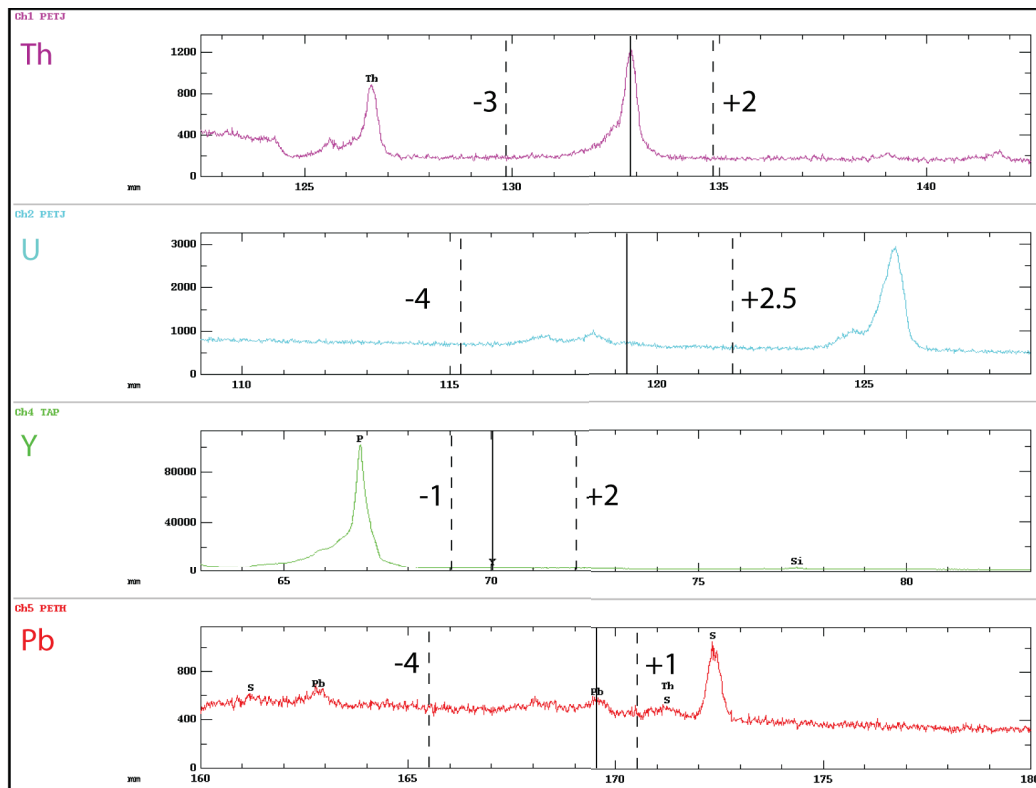


Figure C.9: HS10-32 core domain background scans.

HS10-32, Monazite 13, Rim



HS10-32, Monazite 15, Rim

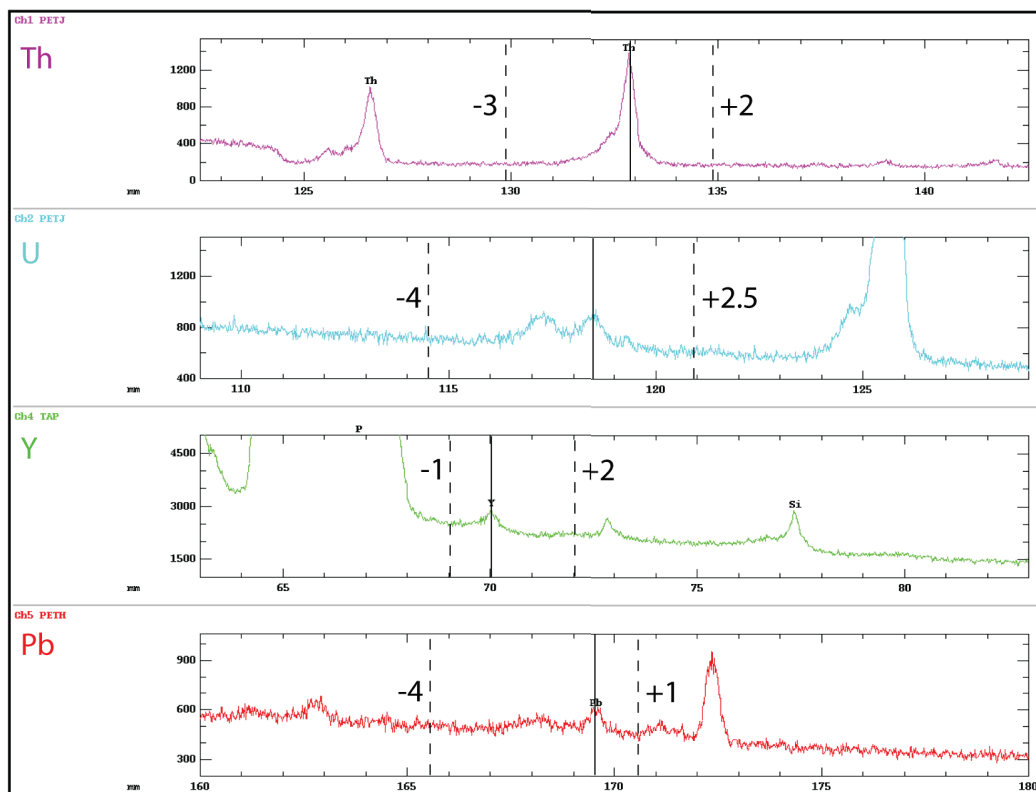
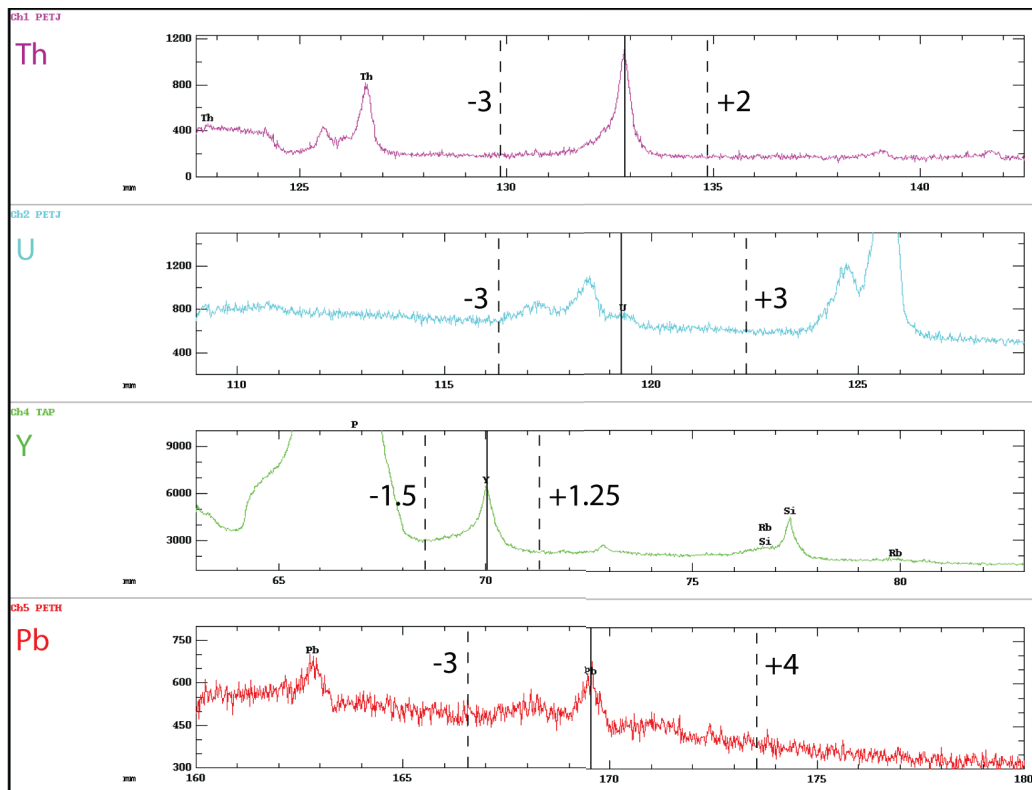


Figure C.10: HS10-32 low-Th rim domain background scans.

HS10-32, Monazite 01, Y-Rim



HS10-32, Monazite 14, Y-Rim

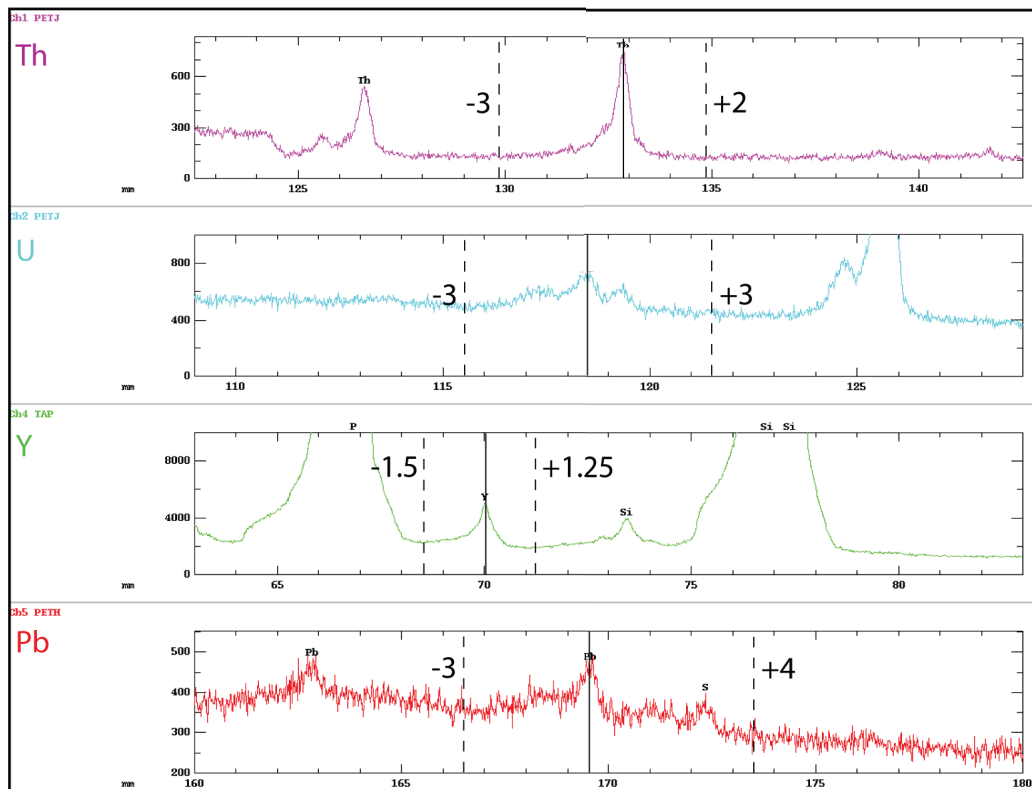
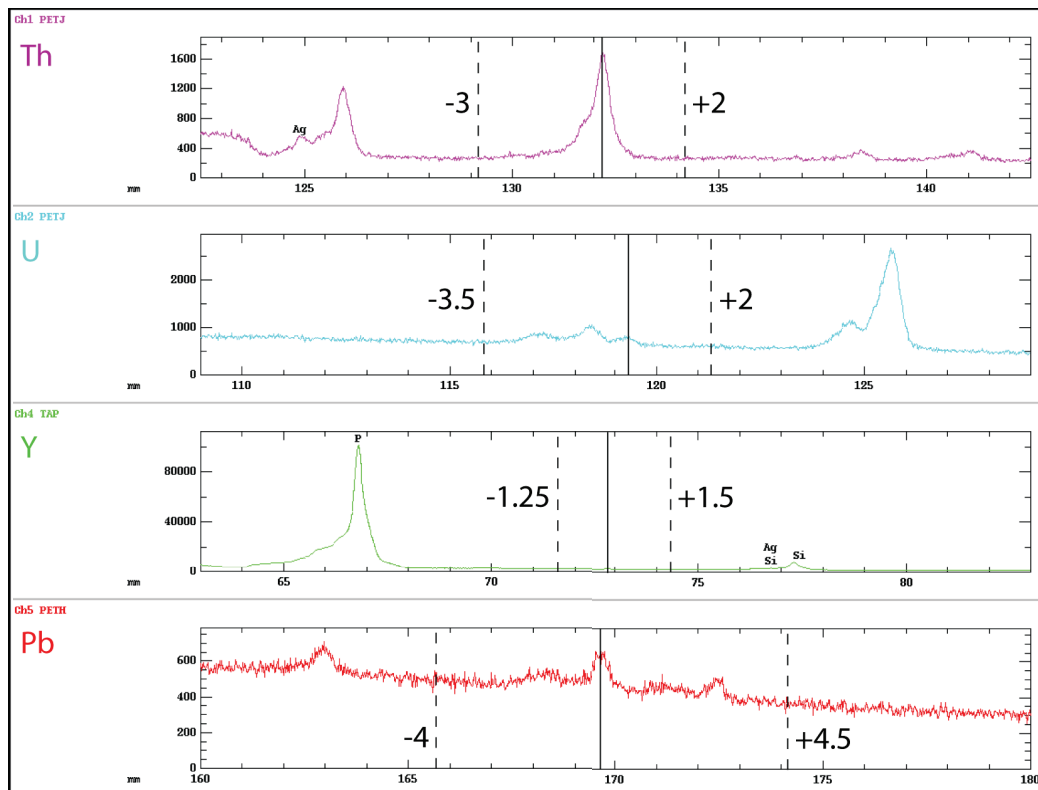


Figure C.11: HS10-32 high-Y rim domain background scans.

HS10-35, Monazite 11, Core



HS10-35, Monazite 40, Core

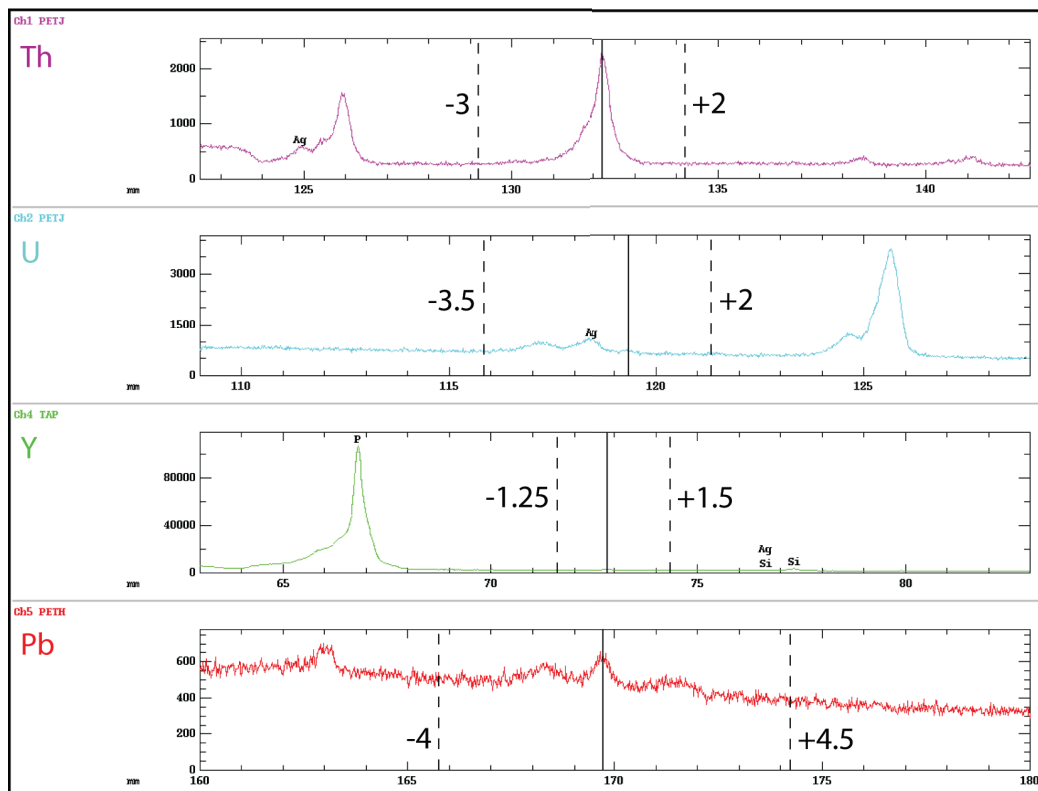
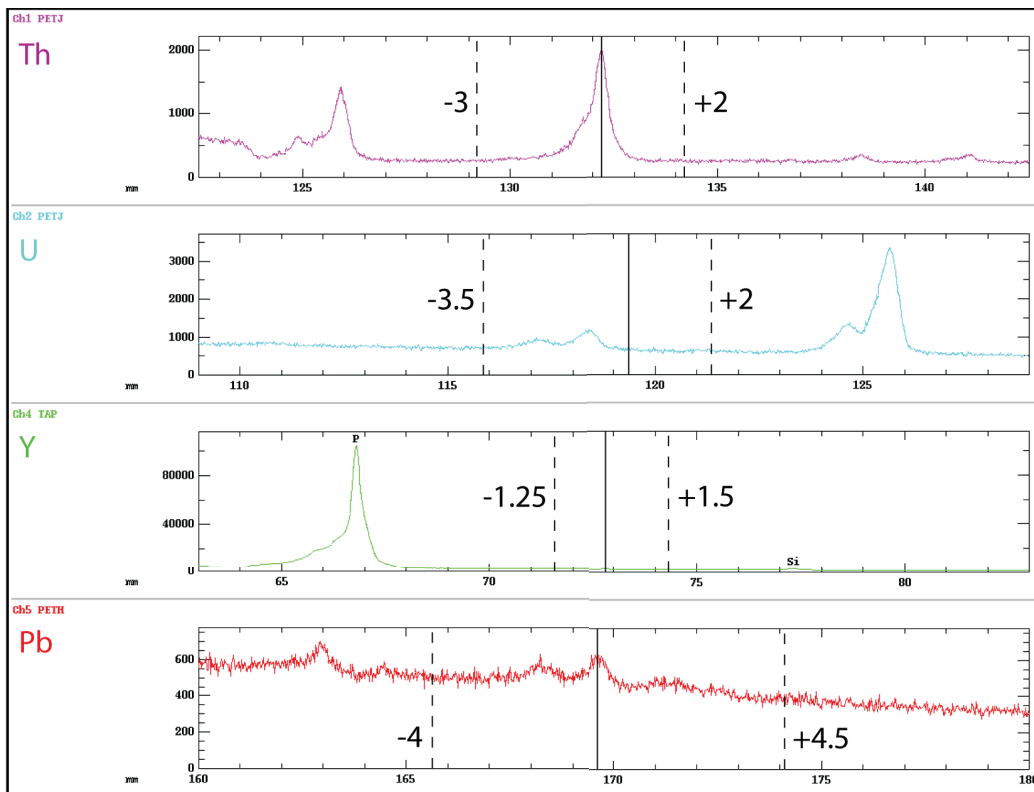


Figure C.12: HS10-35 core domain background scans.

HS10-35, Monazite 11, High-Y Rim



HS10-35, Monazite 40, High-Y Rim

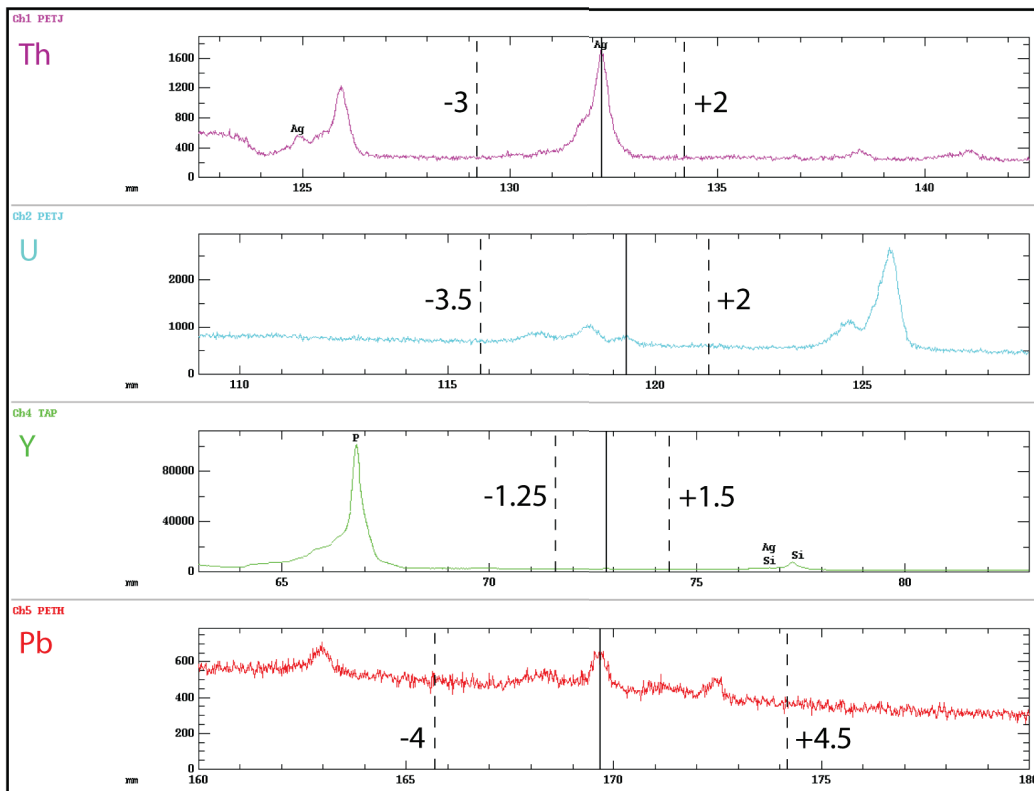


Figure C.13: HS10-35 low-Th, high-Y rim domain background scans.

## C.4 Quantitative Analyses of Monazite Trace Elements and Calculated Ages

The following data sets incorporate analyses from both HS10-32 and HS10-35 monazites, organized into three data tables according to geochemically defined domains (core, inner rim, and outer rim). The data are colour coded to represent the operating conditions set at the time of their collection. Data with a purple or red background were collected from HS10-32, with major element concentrations held constant based on previously analyzed high-Th core or low-Th rim domain geochemistry, respectively. Likewise, data with a green or orange background were collected from HS10-35, with major element concentrations held constant based on the high-Th core or low-Th rim domain geochemistry, respectively. Each table includes:

- Minor element (U, Th, Y, and Pb) concentrations (in ppm) that were directly converted from raw microprobe output (wt%) by the equation:

$$MicroprobeElementwt\% \times 10,000 = ElementConcentration(ppm) \quad (C.1)$$

- Calculated dates of individual analyses and associated uncertainties following the procedure of Gagnè (2004).
- Statistical calculations of the mean dates, standard deviations (Std Dev), weighted mean dates (WMA), error weighted mean uncertainties (EWMU),  $2\sigma$  confidence intervals, and standard deviations of the mean (SDOM), following Gagnè (2004) and Williams (2006).
- The reported WMA of each domain and associated EWMU.

Although minor element analyses were attempted on the outermost Y-rim domain, they are unfortunately contaminated by adjacent silicate phases, and are therefore useless for age determination. These data have not been presented.

Core Domain	Y (ppm)	$\sigma$ (ppm)	Th (ppm)	$\sigma$ (ppm)	U (ppm)	$\sigma$ (ppm)	Pb (ppm)	$\sigma$ (ppm)	DATE (Ma)	$2\sigma$ (Ma)
Mon01-HT1	1700	5	47190	56	3200	11	950	5	424	5.8
Mon01-HT2	3670	7	63510	59	4000	14	1310	6	419	4.9
Mon01-HT3	1330	4	48950	57	3730	19	1050	6	428	7.0
Mon04-HT2	1110	4	46790	55	2870	14	970	6	435	6.9
Mon05-HT1	2110	6	40840	50	4250	16	950	5	435	5.9
Mon05-HT2	1730	6	41410	45	2390	10	860	5	431	6.2
Mon06-HT2	1180	5	52110	56	4310	16	1160	6	435	5.8
Mon14-HT1	1370	6	49800	54	2360	13	1080	6	435	6.7
Mon14-HT2	1470	7	34650	36	3210	11	850	4	418	5.1
Mon14-HT3	1170	2	47300	46	2280	11	1040	4	421	5.5
Mon19-HT1	1730	3	36270	36	3670	17	940	4	425	5.4
Simple Mean	1688	5	46256	50	3297	14	1015	5	428	5.9
Standard Deviation	724.4	1.5	8007.9	8.3	754.3	3.0	134.7	0.8	6.7	0.7
Mon38-HT1	770	24	48680	112	5320	56	1230	21	416	16.9
Mon40-HT1	250	23	51220	114	5840	57	1280	21	427	16.5
Mon45-HT1	360	23	45270	109	7130	59	1220	21	424	16.4
Simple Mean	460	23	48390	112	6097	58	1243	21	422	16.6
Standard Deviation	274.0	0.3	2985.6	2.7	931.9	1.5	32.1	0.1	5.4	0.2
Mon11-LT3	830	24	34520	98	6380	59	1030	21	416	18.7
Mon40-LT1	1490	24	28430	92	7100	60	910	20	424	20.6
Mon45-LT1	1750	24	38680	103	5030	57	990	21	422	20.2
Simple mean	1357	24	33877	98	6170	59	977	21	421	20
Std Dev	474	0.4	5155	5.4	1051	1.8	61	0.2	4.0	1.0
<b>Domain Mean</b>	<b>1168</b>	<b>17</b>	<b>42841</b>	<b>87</b>	<b>5188</b>	<b>43</b>	<b>1078</b>	<b>15.6</b>	<b>425.6</b>	<b>14.1</b>
<b>Domain Std Dev</b>	<b>767</b>		<b>8404</b>		<b>1598</b>		<b>144</b>		<b>6.6</b>	<b>6.2</b>
<b>Domain Weighted Mean</b>	<b>782</b>		<b>44887</b>		<b>4824</b>		<b>1178</b>		<b>426.5</b>	<b>1.7</b>
<b>95% Confidence</b>		<b>4.4</b>		<b>21.6</b>		<b>10.8</b>		<b>3.9</b>		<b>3.5</b>
<b>SDOM</b>	<b>186</b>		<b>2038</b>		<b>388</b>		<b>35</b>			
<b>Core Domain Date (WMA <math>\pm</math> EWMU)</b>										<b>426.5 <math>\pm</math> 1.7 Ma</b>

Table C.6: Core domain minor elements and calculated ages. Compiled monazite minor element concentrations from samples HS10-32 and HS10-35 for the core domain were used to calculate individual analysis ages, and statistical analyses, following Gagné (unpublished M.Sc. thesis, Dalhousie University, Halifax, N.S., 2004) and Williams *et al.* (2006), was conducted to determine the domain age.

Inner Rim Domain	Y (ppm)	$\sigma$ (ppm)	Th (ppm)	$\sigma$ (ppm)	U (ppm)	$\sigma$ (ppm)	Pb (ppm)	$\sigma$ (ppm)	DATE (Ma)	$2\sigma$ (Ma)
Mon02-HT1	1700	6	40740	46	2660	14	850	5	404	6.5
Mon02-HT2	1620	6	43330	49	2380	11	880	5	407	5.9
Mon06-HT1	1640	5	36440	43	2980	13	910	5	413	6.0
Mon09-HT1	1430	5	44730	50	3190	14	980	5	414	5.9
Mon08-HT1	3100	11	64260	71	3740	11	1350	7	402	4.9
Mon08-HT2	1650	7	46830	59	5160	20	1130	6	389	5.5
Mon15-HT1	1560	6	44590	50	3250	14	1050	5	397	5.5
Mon15-HT2	1280	5	50410	54	2150	11	1100	5	400	6.0
Mon15-HT3	2060	7	38440	45	4100	17	1000	5	386	5.4
Mon17-HT1	1870	6	38380	48	2880	13	930	5	395	6.0
Mon19-HT2	2180	6	38640	47	3870	14	1000	5	397	5.3
Simple Mean	1826	6	44254	51	3305	14	1016	5	400.2	5.7
Standard Deviation	495	2	7869	7.7	865	2.6	141	0.5	9.0	0.4
Mon02-LTA1	2000	6	40940	48	2680	13	890	5	400	6.5
Mon06-LTA1	2350	6	37220	46	3970	14	880	5	392	5.9
Mon12-LTA1	1810	6	36820	46	3160	13	850	5	403	6.5
Mon13-LTA4	1540	6	37340	46	4250	15	920	6	402	5.9
Simple Mean	1925	6	38080	47	3515	14	885	5.4	399.4	6.2
Standard Deviation	340	0	1920	1.1	724	0.8	29	0.1	4.8	0.3
Mon38-LT1	2540	25	24720	88	7320	61	890	20	410	20.2
Mon48-LT1	110	23	52490	116	5470	57	1330	21	402	3.84
Simple Mean	1325	24	38605	102	6395	59	1110	21	405.9	12
Standard Deviation	1718	1	19636	20	1308	2.9	311	0.7	5.6	12
Mon11-HT1	480	24	43590	108	7530	60	1240	21	407	15.5
Mon37-HT1	130	23	50200	114	5640	57	1310	21	407	15.7
Simple Mean	305	23	46895	111	6585	59	1275	21	407.1	16
Standard Deviation	247	1	4674	4.2	1336	2.4	49	0.1	0.2	0.2
<b>Domain Mean</b>	<b>1634</b>	<b>10</b>	<b>42637</b>	<b>62</b>	<b>4020</b>	<b>23</b>	<b>1026</b>	<b>8.7</b>	<b>401.4</b>	<b>7.5</b>
<b>Domain Std Dev</b>	<b>756</b>		<b>8227</b>		<b>1557</b>		<b>170</b>		<b>7.6</b>	<b>1.4</b>
<b>Domain Weighted Mean</b>	<b>1004</b>		<b>39582</b>		<b>4226</b>		<b>986</b>		<b>400.1</b>	<b>1.4</b>
<b>95% Confidence</b>		<b>3</b>		<b>17</b>		<b>6.2</b>		<b>2.3</b>		<b>2.0</b>
<b>SDOM</b>	<b>195</b>		<b>2124</b>		<b>402</b>		<b>44</b>		<b>2.0</b>	
<b>Inner Rim Date (WMA <math>\pm</math> EWMU)</b>										<b>400.1 <math>\pm</math> 1.4 Ma</b>

Table C.7: Inner rim domain minor elements and calculated ages. Compiled monazite minor element concentrations from samples HS10-32 and HS10-35 for the inner rim domain were used to calculate individual analysis ages, and statistical analyses, following Gagné (unpublished M.Sc. thesis, Dalhousie University, Halifax, N.S., 2004) and Williams *et al.* (2006), was conducted to determine the domain age.



Outer Rim Domain	Y (ppm)	$\sigma$ (ppm)	Th (ppm)	$\sigma$ (ppm)	U (ppm)	$\sigma$ (ppm)	Pb (ppm)	$\sigma$ (ppm)	DATE (Ma)	$2\sigma$ (Ma)
Mon12-HT1	2200	4	41290	41	4390	20	1000	4	385	5.0
Mon12-HT2	2190	9	44650	47	3610	20	1020	5	391	6.0
Mon12-HT3	2100	6	40640	46	3200	12	930	5	385	5.2
Mon13-HT1	2170	6	39880	48	3860	14	970	5	384	5.3
Mon13-HT2	1670	5	43970	51	2910	10	990	5	386	5.1
Mon13-HT3	1780	9	38800	43	4320	20	990	5	392	5.8
Mon17-HT2	1770	5	40600	49	3290	15	1000	6	383	5.7
Simple Mean	1983	6	41404	46	3654	16	986	5.1	387	5.4
Standard Deviation	232	2	2140	3.6	566	4.2	29	0.5	3.5	0.4
Mon04-LTA2	2220	6	39740	48	3230	14	870	5	387	6.1
Mon05-LTA1	2240	6	43900	50	4220	14	1000	6	388	5.4
Mon05-LTA2	2700	6	40090	48	4520	15	950	5	388	5.5
Mon06-LTA2	2230	6	41280	49	3550	14	890	5	377	5.7
Mon08-LTA2	2030	6	40950	48	3440	14	870	5	373	5.8
Mon11-LTA1	1580	6	38740	47	2860	13	820	5	382	6.4
Mon11-LTA2	2190	6	38560	47	4380	15	890	5	377	5.6
Mon12-LTA2	2080	6	41220	49	4490	15	930	5	373	5.3
Mon13-LTA1	1700	6	36490	46	3870	14	840	5	383	6.0
Mon13-LTA3	1710	6	36860	46	3720	14	870	5	397	6.1
Mon15-LTA1	2050	6	38890	47	3900	14	860	5	373	5.7
Mon15-LTA2	1500	6	37130	46	3850	14	840	5	378	5.9
Mon15-LTA3	1820	6	35890	45	4010	14	860	5	393	6.0
Mon15-LTA5	1540	6	37040	46	3720	14	840	5	382	6.0
Mon19-LTA1	1710	6	39510	48	3080	13	860	5	388	6.2
Simple Mean	1953	6	39086	47	3789	14	879	5.4	383	5.8
Standard Deviation	337	0	2204	1.3	500	0.5	48	0.1	7.5	0.3
<b>Domain Mean</b>	<b>1963</b>	<b>6</b>	<b>39824</b>	<b>47</b>	<b>3746</b>	<b>15</b>	<b>913</b>	<b>5.3</b>	<b>383.8</b>	<b>5.7</b>
<b>Domain Std Dev</b>	<b>302</b>		<b>2401</b>		<b>512</b>		<b>66</b>		<b>6.7</b>	
<b>Domain Weighted Mean</b>	<b>1973</b>		<b>40279</b>		<b>3730</b>		<b>957</b>		<b>383.7</b>	<b>1.2</b>
<b>95% Confidence</b>		<b>1.3</b>		<b>10</b>		<b>3.2</b>		<b>1.2</b>		<b>1.2</b>
<b>SDOM</b>	<b>64</b>		<b>512</b>		<b>109</b>		<b>14</b>		<b>1.4</b>	
<b>Outer Rim Date (WMA <math>\pm</math> EWMU)</b>										<b>383.7 <math>\pm</math> 1.2 Ma</b>

Table C.8: Outer rim domain minor elements and calculated ages. Compiled monazite minor element concentrations from HS10-32 outer rim domain were used to calculate individual analysis ages, and statistical analyses, following Gagné (unpublished M.Sc. thesis, Dalhousie University, Halifax, N.S., 2004) and Williams *et al.* (2006), was conducted to determine the domain age.

## C.5 Quantitative Analyses of Consistency Standards

A consistency standard was analysed before, during, and after each round of monazite major and minor element analyses. For HS10-35 and HS10-32 analyses, Monazite 53 and GSC Monazite 8153 were used as standards, respectively. Monazite 53 is an internal laboratory standard that has not been dated using isotopic methods. GSC Monazite 8153 has an accepted age of  $498 \pm 8$  Ma (*Williams et al. 2006*), however B. Davis (*personal communication*) states that this standard is somewhat heterogeneous with respect to composition and age, and that it has a homogeneous Th/Pb age of 507 Ma.

Minor element analyses were conducted with average major element concentrations for each domain held constant. This means that the constant major element concentrations reflect the chemistry of the unknown samples, rather than the monazite standards. Therefore, the minor element concentrations of the standards have been normalized according to the chemistry of the unknown, and the calculated standard ages are not necessarily the true age of the standard. However, the minor element concentrations and calculated ages from the standards were used to estimate analytical reproducibility throughout the data collection. The precision on these standard ages is poor, but the accuracy on 8153 is acceptable when all the data is averaged.

Standard	GSC 8153							
Analysis	Std 1	Std 2	Std 3	Std 4	Std 5	Std 6	Std 7	Std. Dev.
<i>Oxides</i>								
SiO <sub>2</sub>	1.14	1.19	1.15	1.20	1.23	1.24	1.19	0.04
P <sub>2</sub> O <sub>5</sub>	28.31	27.68	27.34	27.73	27.81	27.39	27.83	0.45
SO <sub>3</sub>	0.57	0.57	0.58	0.62	0.60	0.59	0.60	0.02
CaO	0.05	0.05	0.06	0.13	0.10	0.14	0.11	0.04
Y <sub>2</sub> O <sub>3</sub>	0.43	0.46	0.44	0.42	0.49	0.53	0.46	0.04
La <sub>2</sub> O <sub>3</sub>	14.42	13.75	13.79	13.88	14.33	13.90	13.83	0.28
Ce <sub>2</sub> O <sub>3</sub>	28.38	28.12	28.07	28.17	28.47	28.23	28.07	0.15
Pr <sub>2</sub> O <sub>3</sub>	3.11	2.97	3.19	3.20	3.22	3.07	3.24	0.09
Nd <sub>2</sub> O <sub>3</sub>	11.56	11.12	11.32	11.19	11.46	11.43	11.49	0.15
Sm <sub>2</sub> O <sub>3</sub>	2.48	2.46	2.37	2.61	2.62	2.46	2.43	0.11
Eu <sub>2</sub> O <sub>3</sub>	0.81	0.75	0.75	0.76	0.89	0.87	0.76	0.06
Gd <sub>2</sub> O <sub>3</sub>	0.94	1.19	1.17	1.10	1.27	1.10	1.12	0.10
Dy <sub>2</sub> O <sub>3</sub>	0.30	0.36	0.25	0.36	0.20	0.29	0.40	0.07
ThO <sub>2</sub>	6.92	7.10	7.05	6.79	6.84	7.02	7.07	0.16
UO <sub>2</sub>	0.34	0.31	0.35	0.30	0.46	0.36	0.25	0.06
TOTAL	99.77	98.08	97.86	98.45	99.98	98.60	98.81	0.79
<i>Cations</i>								
Si	0.045	0.048	0.047	0.048	0.049	0.050	0.048	
P	0.956	0.952	0.947	0.949	0.943	0.941	0.950	
S	0.002	0.002	0.002	0.004	0.003	0.004	0.003	
Ca	0.024	0.025	0.025	0.027	0.026	0.026	0.026	
Y	0.009	0.010	0.010	0.009	0.010	0.011	0.010	
La	0.212	0.206	0.208	0.207	0.212	0.208	0.206	
Ce	0.414	0.418	0.420	0.417	0.417	0.419	0.414	
Pr	0.045	0.044	0.048	0.047	0.047	0.045	0.048	
Nd	0.165	0.161	0.166	0.162	0.164	0.166	0.165	
Sm	0.034	0.034	0.033	0.036	0.036	0.034	0.034	
Eu	0.011	0.010	0.010	0.010	0.012	0.012	0.010	
Gd	0.012	0.016	0.016	0.015	0.017	0.015	0.015	
Dy	0.004	0.005	0.003	0.005	0.002	0.004	0.005	
Th	0.063	0.066	0.066	0.062	0.062	0.065	0.065	
U	0.003	0.003	0.003	0.003	0.004	0.003	0.002	
TOTAL	2.000	2.000	2.004	2.001	2.004	2.004	2.001	

Table C.9: GSC 8153 major element analyses. This consistency standard was analyzed before, during, and after each round of major element analyses on monazite grains from sample HS10-32. Std Dev. = standard deviation of all standard analyses.

<b>Standard</b>	<b>Monazite 53</b>			
Analysis	Std 1	Std 2	Std 3	Std Dev
SiO2	2.124	2.037	2.037	0.05
P2O5	26.98	27.33	26.48	0.43
SO3	0.02	0.00	0.02	0.01
CaO	0.72	0.75	0.71	0.02
Y2O3	0.65	0.66	0.68	0.02
La2O3	10.15	10.18	10.40	0.14
Ce2O3	24.40	24.91	25.05	0.34
Pr2O3	2.78	2.63	2.77	0.09
Nd2O3	11.61	11.49	11.58	0.06
Sm2O3	3.86	3.91	3.89	0.02
Eu2O3	0.74	0.85	0.79	0.06
Gd2O3	2.66	2.64	2.58	0.04
Dy2O3	1.65	1.38	1.51	0.14
ThO2	11.14	10.74	10.62	0.27
UO2	0.56	0.42	0.49	0.07
TOTAL	100.04	99.90	99.60	0.22
<i>Cations</i>				
Si	0.086	0.082	0.083	
P	0.921	0.929	0.913	
S	0.000	0.000	0.001	
Ca	0.031	0.032	0.031	
Y	0.014	0.014	0.015	
La	0.151	0.151	0.156	
Ce	0.360	0.366	0.374	
Pr	0.041	0.038	0.041	
Nd	0.167	0.165	0.168	
Sm	0.054	0.054	0.055	
Eu	0.010	0.012	0.011	
Gd	0.036	0.035	0.035	
Dy	0.022	0.018	0.020	
Th	0.102	0.098	0.098	
U	0.005	0.004	0.004	
TOTAL	1.999	1.998	2.006	

Table C.10: Monazite 53 major element analyses. This consistency standard was analyzed before, during, and after major element analyses on monazite grains from sample HS10-35. Std Dev. = standard deviation of all standard analyses.

Zone	Y (ppm)	1 $\sigma$ (ppm)	Th (ppm)	1 $\sigma$ (ppm)	U (ppm)	1 $\sigma$ (ppm)	Pb (ppm)	1 $\sigma$ (ppm)	Age (Ma)	2 $\sigma$ (Ma)
<b>Core Domain</b>										
Ctrl 1	3710	13.4	57980	65.4	2620	8.1	1390	6.9	465.7	5.8
Ctrl 2	3570	12.1	55710	61.3	2750	8.2	1390	7.0	478.8	5.9
Ctrl 3	3940	8.3	57240	53.4	2730	10.2	1430	6.1	481.6	5.7
Ctrl 4	3670	6.8	57960	57.0	2590	12.6	1490	5.9	499.5	6.5
Ctrl 5	3700	6.9	58220	57.1	2650	12.7	1430	5.8	476.5	6.3
<b>SIMPLE MEAN</b>	<b>3718</b>	<b>9.5</b>	<b>57422</b>	<b>58.8</b>	<b>2668</b>	<b>10.4</b>	<b>1426</b>	<b>6.3</b>	<b>480.4</b>	<b>6.0</b>
<b>STANDARD DEV</b>	<b>136</b>		<b>1025</b>		<b>69</b>		<b>41</b>		<b>12</b>	
<b>95% Confidence</b>	<b>4.8</b>		<b>29.4</b>			<b>5.2</b>		<b>3.2</b>		<b>3.0</b>
<b>SDOM</b>	<b>61</b>		<b>458</b>		<b>31</b>		<b>18</b>		<b>5</b>	
<b>Rim Domain</b>										
Ctrl 18LT	3810	6.9	61050	58.3	2500	11.8	1390	5.9	448.0	6.0
Ctrl 16LT	3740	6.7	61820	59.6	2650	12.4	1420	6.2	449.4	6.1
Ctrl 17LT	3850	7.0	60830	58.5	2680	13.2	1380	6.0	442.5	6.1
Ctrl 19LT	3730	6.9	61400	58.9	2630	12.5	1390	6.0	443.1	6.0
<b>SIMPLE MEAN</b>	<b>3783</b>	<b>6.9</b>	<b>61275</b>	<b>58.8</b>	<b>2615</b>	<b>12.5</b>	<b>1395</b>	<b>6.0</b>	<b>445.7</b>	<b>6.1</b>
<b>STANDARD DEV</b>	<b>57</b>		<b>433</b>		<b>79</b>		<b>17</b>		<b>3</b>	
<b>95% Confidence</b>	<b>4.0</b>		<b>34.0</b>			<b>7.2</b>		<b>3.5</b>		<b>3.5</b>
<b>SDOM</b>	<b>29</b>		<b>216</b>		<b>40</b>		<b>9</b>		<b>2</b>	
<b>Y-Rim Domain</b>										
Ctrl 7Yrim	3970	7.0	59190	57.6	2560	12.4	1590	5.9	523.7	5.3
Ctrl 8Yrim	3970	7.0	59200	57.7	2640	12.6	1690	6.0	553.8	5.5
Ctrl 9Yrim	3880	6.9	59360	57.7	2640	12.6	1610	5.9	526.9	5.6
Ctrl 10Yrim	3890	6.9	59740	57.9	2490	12.4	1630	5.9	534.1	5.6
<b>SIMPLE MEAN</b>	<b>3928</b>	<b>7.0</b>	<b>59373</b>	<b>57.7</b>	<b>2583</b>	<b>12.5</b>	<b>1630</b>	<b>5.9</b>	<b>534.6</b>	<b>5.5</b>
<b>STANDARD DEV</b>	<b>49</b>		<b>257</b>		<b>72</b>		<b>43</b>		<b>14</b>	
<b>95% Confidence</b>	<b>4.0</b>		<b>33.3</b>			<b>7.2</b>		<b>3.4</b>		<b>3.2</b>
<b>SDOM</b>	<b>25</b>		<b>129</b>		<b>36</b>		<b>22</b>		<b>7</b>	

Table C.11: GSC 8153 minor element analyses and ages. This consistency standard was analyzed before, during, and after minor element analyses on monazite core, rim, and Y-rim domains from HS10-32.

Analysis	Y (ppm)	1 $\sigma$ (ppm)	Th (ppm)	1 $\sigma$ (ppm)	U (ppm)	1 $\sigma$ (ppm)	Pb (ppm)	1 $\sigma$ (ppm)	Age (Ma)	2 $\sigma$ (Ma)
Ctrl53 - 1	5020	26.9	27190	90.8	370	34.1	2230	22.4	1689.1	313.7
Ctrl53 - 2	5330	26.6	27500	91.2	190	25.4	2360	22.8	1803.7	483.2
Ctrl53 - 3	5530	26.4	27920	91.4	210	26.2	2390	22.7	1795.6	449.9
<b>SIMPLE MEAN</b>	<b>5293</b>	<b>26.6</b>	<b>27537</b>	<b>91.1</b>	<b>257</b>	<b>28.6</b>	<b>2327</b>	<b>22.6</b>	<b>1762.8</b>	<b>415.6</b>
<b>STANDARD DEV</b>	<b>257</b>		<b>366</b>		<b>99</b>		<b>85</b>		<b>64</b>	
<b>95% Confidence</b>		<b>18.8</b>		<b>64.4</b>		<b>20.2</b>		<b>16.0</b>		<b>293.9</b>
<b>SDOM</b>	<b>148</b>		<b>212</b>		<b>57</b>		<b>49</b>		<b>37</b>	

Table C.12: Monazite 53 minor element analyses and ages. This consistency standard was analyzed before, during, and after minor element analyses of HS10-35 monazite.

# REFERENCES

- Aldrich, L. T., and A. O. Nier, Argon 40 in potassium minerals, *Physical Review*, 74, 1948.
- Andersen, T. B., Extensional tectonics in the Caledonides of southern Norway, an overview, *Tectonophysics*, 285, 333–351, 1998.
- Arnaud, N. O., and S. P. Kelley, Evidence for excess argon during high pressure metamorphism in the Dora Maira Massif (western Alps, Italy), using an ultra-violet laser ablation microprobe  $^{40}\text{Ar}/^{39}\text{Ar}$  technique, *Contributions to Mineralogy and Petrology*, 121, 1–11, 1995.
- Beaumont, C., R. A. Jamieson, J. P. Butler, and C. J. Warren, Crustal structure: A key constraint on the mechanism of ultra-high-pressure rock exhumation, *Earth and Planetary Science Letters*, 287, 116–129, 2009.
- Berman, R. G., Internally-consistent thermodynamic data for minerals in the system  $\text{Na}_2\text{O}-\text{K}_2\text{O}-\text{CaO}-\text{MgO}-\text{FeO}-\text{Fe}_2\text{O}_3-\text{Al}_2\text{O}_3-\text{SiO}_2-\text{TiO}_2-\text{H}_2\text{O}-\text{CO}_2$ , *Journal of Petrology*, 29, 445–522, 1988.
- Brueckner, H., D. Carswell, W. Griffin, L. Medaris Jr, H. Van Roermund, and S. Cuthbert, The mantle and crustal evolution of two garnet peridotite suites from the Western Gneiss Region, Norwegian Caledonides: An isotopic investigation, *Lithos*, 117, 1–19, 2010.
- Bruton, D. L., and D. A. T. Harper, Arenig-Llandovery stratigraphy and faunas across the Scandinavian Caledonides, *Geological Society, London, Special Publications*, 38, 247–268, 1988.
- Bryhni, I., and B. A. Sturt, Caledonides of southwestern Norway, in *The Caledonide Orogen - Scandinavia and Related Areas*, edited by D. G. Gee and B. A. Sturt, pp. 89–108, Wiley, 1985.
- Butler, J. P., R. A. Jamieson, H. M. Steenkamp, and P. Robinson, Discovery of coesite–eclogite from the Nordøyane UHP domain, Western Gneiss Region, Norway: field relations, metamorphic history, and tectonic significance, *Journal of Metamorphic Geology*, doi: 10.1111/jmg.12004, in press, 2012.
- Carlson, W. D., Rates of Fe, Mg, Mn, and Ca diffusion in garnet, *American Mineralogist*, 91, 1–11, 2006.
- Carswell, D. A., H. K. Brueckner, S. J. Cuthbert, K. Mehta, and P. J. O'Brien, The timing of stabilisation and the exhumation rate for ultra-high pressure rocks in the Western Gneiss Region of Norway, *Journal of Metamorphic Geology*, 21, 601–612, 2003.
- Carswell, D. A., H. L. M. Van Roermund, and D. F. Wiggers de Vries, Scandian ultrahigh-pressure metamorphism of Proterozoic basement rocks on Fjørtoft and Otrøy, Western Gneiss Region, Norway, *International Geology Review*, 48, 957–977, 2006.

- Cesare, B. E., G. Cruciani, and U. Russo, Hydrogen deficiency in Ti-rich biotite from anatectic metapelites (El Joyazo, SE Spain): Crystal-chemical aspects and implications for high-temperature petrogenesis, *American*, 88, 583–595, 2003.
- Cherniak, D. J., E. B. Watson, M. Grove, and T. M. Harrison, Pb diffusion in monazite: a combined RBS/SIMS study, *Geochimica et Cosmochimica Acta*, 68, 829–840, 2004.
- Coggon, R., and T. J. B. Holland, Mixing properties of phengitic micas and revised garnet-phengite thermobarometers, *Journal of Metamorphic Geology*, 20, 683–696, 2002.
- Connolly, J., Multivariable phase diagrams; an algorithm based on generalized thermodynamics, *American Journal of Science*, 290, 666–718, 1990.
- Corfu, F., U-Pb and Rb-Sr systematics in a polyorogenic segment of the Precambrian shield, central southern Norway, *Lithos*, 13, 305–323, 1980.
- Cuthbert, S. J., D. A. Carswell, E. J. Krogh-Ravna, and A. Wain, Eclogites and eclogites in the Western Gneiss Region, Norwegian Caledonides, *Lithos*, 52, 165–195, 2000.
- de Capitani, C., and T. Brown, The computation of chemical equilibrium in complex systems containing non-ideal solutions, *Geochimica et Cosmochimica Acta*, 51, 2639–2652, 1987.
- de Capitani, C., and K. Petrakakis, The computation of equilibrium assemblage diagrams with Theriak/Domino software, *American Mineralogist*, 95, 1006–1016, 2010.
- Deer, W., R. Howie, and J. Zussman, *An Introduction to the Rock-Forming Minerals*, Longman Scientific and Technical, 1992.
- Dickin, A., *Radiogenic Isotope Geology*, Cambridge University Press, Cambridge UK, 2005.
- Dobrzhinetskaya, L. F., E. A. Eide, R. B. Larsen, B. A. Sturt, R. G. Trønnes, C. Smith, W. R. Taylor, and T. V. Posukhova, Microdiamond in high-grade metamorphic rocks of the Western Gneiss region, Norway, *Geology*, 23, 597–600, 1995.
- Dodson, M. H., Closure Temperature in Cooling Geochronological and Petrological Systems, *Contributions to Mineralogy and Petrology*, 40, 259–274, 1973.
- Ferry, J. M., and F. S. Spear, Experimental calibration of the partitioning of Fe and Mg between biotite and garnet, *Contributions to Mineralogy and Petrology*, 66, 113–117, 1978.
- Fick, D., On liquid diffusion, *The London, Edinburgh, and Dublin Philosophical Magazine and Journal of Science*, 10, 30–39, 1855.
- Gagnè, S., Textural, Chemical and Age Variation in Monazites of the Paleoproterozoic Longstaff Bluff Formation, Central Baffin Island, Nunavut, unpublished M.Sc. thesis, Dalhousie University, Halifax, N.S., 2004.



- Gagné, S., R. A. Jamieson, and R. MacKay, Texture, composition, and age variations in monazite from the lower amphibolite to the granulite facies, Longstaff Bluff Formation, Baffin Island, Canada, *The Canadian Mineralogist*, 47, 847–869, 2009.
- Garner, E. L., L. A. Machlan, and I. L. Barnes, The isotopic composition of lithium, potassium, and rubidium in some apollo 11, 12, 14, 15, and 16 samples, in *Lunar and Planetary Science Conference Proceedings*, vol. 6, pp. 1845–1855, 1975.
- Gee, D. G., J. C. Guezou, D. Roberts, and F. C. Wolff, The central-southern part of the Scandinavian Caledonides, in *The Caledonide Orogen - Scandinavia and Related Areas*, edited by D. G. Gee and B. A. Sturt, pp. 109–134, Wiley, 1985.
- Gee, D. G., H. Fossen, N. Henriksen, and A. K. Higgins, From the Early Paleozoic Platforms of Baltica and Laurentia to the Caledonide Orogen of Scandinavia and Greenland, *Episodes*, 31, 44–51, 2008.
- Gee, D. G., C. Juhlin, C. Pascal, and P. Robinson, Collisional Orogeny in the Scandinavian Caledonides (COSC), *Geologiska Foreningens i Stockholm Forhandlingar*, 132, 37–41, 2010.
- Gromet, L. P., H. Sjöström, S. Bergman, S. Claesson, R. M. Essex, P. G. Andreasson, and L. Albrecht, Constrasting ages of metamorphism in the Seve nappes: U-Pb results from the central and northern Swedish Caledonides, in *Geologiska Foreningens i Stockholm Forhandlingar*, pp. A36–A37, 1996.
- Grove, M., and T. M. Harrison,  $^{40}\text{Ar}^*$  diffusion in Fe-rich biotite, *American Mineralogist*, 81, 940–951, 1996.
- Guilmette, C., a. Indares, and R. Hébert, High-pressure anatectic paragneisses from the Namche Barwa, Eastern Himalayan Syntaxis: Textural evidence for partial melting, phase equilibria modeling and tectonic implications, *Lithos*, 124, 66–81, 2011.
- Hacker, B., and Q. Wang, Ar/Ar geochronology of ultrahigh-pressure metamorphism in central China, *Tectonics*, 14, 994–1006, 1995.
- Hacker, B. R., and P. B. Gans, Continental collisions and the creation of ultrahigh-pressure terranes: Petrology and thermochronology of nappes in the central Scandinavian Caledonides, *Geological Society of America Bulletin*, 117, 117–134, 2005.
- Hacker, B. R., T. B. Andersen, S. Johnston, A. R. Kylander-Clark, E. M. Peterman, E. O. Walsh, and D. Young, High-temperature deformation during continental-margin subduction & exhumation: The ultrahigh-pressure Western Gneiss Region of Norway, *Tectonophysics*, 480, 149–171, 2010.
- Handke, M. J., An introduction to the structure of the Scandinavian Caledonides, in *The Caledonide Orogen - Scandinavia and Related Areas*, edited by D. G. Gee and B. A. Sturt, pp. 55–68, Wiley, 1985.

- Harrison, M. T., Diffusion of  $^{40}\text{Ar}$  in hornblende, *Contributions to Mineralogy and Petrology*, 78, 324–331, 1981.
- Harrison, T. M., J. C  lerier, A. B. Aikman, J. Hermann, and M. T. Heizler, Diffusion of  $^{40}\text{Ar}$  in muscovite, *Geochimica et Cosmochimica Acta*, 73, 1039–1051, 2009.
- Henry, D. J., and C. V. Guidotti, Titanium in biotite from metapelitic rocks: Temperature effects, crystal-chemical controls, and petrologic applications, *American Mineralogist*, 87, 375–382, 2002.
- Holdaway, M. J., Recalibration of the GASP geobarometer in light of recent garnet and plagioclase activity models and versions of the garnet-biotite geothermometer, *American Mineralogist*, 86, 1117–1129, 2001.
- Holland, T. J. B., and R. Powell, An internally consistent thermodynamic data set for phases of petrological interest, *Journal of Metamorphic Geology*, 16, 309–343, 1998.
- Holness, M. B., and E. W. Sawyer, On the pseudomorphing of melt-filled pores during the crystallization of migmatites, *Journal of Petrology*, 49, 1343–1363, 2008.
- Hossack, J., A cross-section through the Scandinavian Caledonides constructed with the aid of branch-line maps, *Journal of Structural Geology*, 5, 103–111, 1983.
- Indares, A., R. W. White, and R. Powell, Phase equilibria modelling of kyanite-bearing anatectic paragneisses from the central Grenville Province, *Journal of Metamorphic Geology*, 26, 815–836, 2008.
- Johnston, S. M., B. R. Hacker, and T. B. Andersen, Exhuming Norwegian ultrahigh-pressure rocks: Overprinting extensional structures and the role of the Nordfjord-Sogn Detachment Zone, *Tectonics*, 26, 1–12, 2007a.
- Johnston, S. M., B. R. Hacker, and M. N. Ducea, Exhumation of ultrahigh-pressure rocks beneath the Hornelen segment of the Nordfjord-Sogn Detachment Zone, western Norway, *Geological Society of America Bulletin*, 119, 1232–1248, 2007b.
- Kelley, S., K-Ar and Ar-Ar dating, *Reviews in Mineralogy and Geochemistry*, 47, 785–818, 2002.
- Kelsey, D. E., C. Clark, and M. Hand, Thermobarometric modelling of zircon and monazite growth in melt-bearing systems: examples using model metapelitic and metapsammitic granulites, *Journal of Metamorphic Geology*, 26, 199–212, 2008.
- Kohn, M. J., Geochemical zoning in metamorphic minerals, *Treatise on Geochemistry, The Crust*, 3, 229–261, 2003.
- Kossert, K., and E. G  nther, LSC measurements of the half-life of  $^{40}\text{K}$ , *Applied Radiation and Isotopes*, 60, 459–464, 2004.

- Koziol, A. M., and R. C. Newton, Redetermination of the anorthite breakdown reaction and improvement of the geobarometer, *American Mineralogist*, *73*, 216–223, 1988.
- Krabbendam, M., and J. F. Dewey, Exhumation of UHP rocks by transtension in the Western Gneiss Region, Scandinavian Caledonides, *Geological Society, London, Special Publications*, *135*, 159–181, 1998.
- Krogh, T. E., S. L. Kamo, P. Robinson, M. P. Terry, and K. Kwok, U-Pb zircon geochronology of eclogites from the Scandian Orogen, northern Western Gneiss Region, Norway: 14–20 million years between eclogite crystallization and return to amphibolite-facies conditions, *Canadian Journal of Earth Sciences*, *48*, 441–472, 2011.
- Kullerud, K., M. B. Stephens, and E. Zachrisson, Pillow lavas as protoliths for eclogites: evidence from a late Precambrian-Cambrian continental margin, Seve Nappes, Scandinavian Caledonides, *Contributions to Mineralogy and Petrology*, *105*, 1–10, 1990.
- Kylander-Clark, A. R., B. R. Hacker, and C. G. Mattinson, Size and exhumation rate of ultrahigh-pressure terranes linked to orogenic stage, *Earth and Planetary Science Letters*, *321–322*, 115–120, 2012.
- Labrousse, L., L. Jolivet, P. Agard, R. Hebert, and T. B. Andersen, Crustal-scale boudinage and migmatization of gneiss during their exhumation in the UHP Province of Western Norway, *Terra Nova*, *14*, 263–270, 2002.
- Lee, J. K. W., Multipath diffusion in geochronology, *Contributions to Mineralogy and Petrology*, *120i*, 60–82, 1995.
- McDougall, I. A., and M. T. Harrison, *Geochronology and Thermochronology by the  $^{40}\text{Ar}/^{39}\text{Ar}$  Method*, Oxford University Press, 1999.
- McKerrow, W. S., C. Mac Niocaill, and J. F. Dewey, The Caledonian Orogeny redefined, *Journal of the Geological Society*, *157*, 1149–1154, 2000.
- Merrihue, C., and G. Turner, Potassium-argon dating by activation with fast neutrons, *71*, 2852–2857, 1966.
- Merrihue, C. M., Trace-element determinations and potassium-argon dating by mass spectroscopy of neutron-irradiated samples, *Transactions, American Geophysical Union*, *46*, 125, 1965.
- Montel, J.-M., S. Foret, M. Veshambre, C. Nicollet, and A. Provost, Electron microprobe dating of monazite, *Chemical geology*, *131*, 37–53, 1996.
- Montel, J. M., B. Glorieux, A. M. Seydoux-Guillaume, and R. Wirth, Synthesis and sintering of a monazite-brabantite solid solution ceramic for nuclear waste storage, *Journal of Physics and Chemistry of Solids*, *67*, 2489–2500, 2006.
- Powell, R., Geothermometry and geobarometry: a discussion, *Journal of the Geological Society*, *142*, 29–38, 1985.

- Powell, R., and T. J. B. Holland, An internally consistent dataset with uncertainties and correlations: 3. Applications to geobarometry, worked examples and a computer program, *Journal of Metamorphic Geology*, 6, 173–204, 1988.
- Powell, R., and T. J. B. Holland, On thermobarometry, *Journal of Metamorphic Geology*, 26, 155–179, 2008.
- Pyle, J. M., and F. S. Spear, Four generations of accessory-phase growth in low-pressure migmatites from SW New Hampshire, *American Mineralogist*, 88, 338–351, 2003.
- Pyle, J. M., F. S. Spear, R. L. Rudnick, and W. F. McDonough, Monazite-xenotime-garnet equilibrium in metapelites and a new monazite-garnet thermometer, *Journal of Petrology*, 42, 2083–2107, 2001.
- Roberts, D., The Scandinavian Caledonides: event chronology, paleogeographic settings and likely modern analogues, *Tectonophysics*, 365, 283–299, 2003.
- Roberts, D., and D. G. Gee, An introduction to the structure of the Scandinavian Caledonides, in *The Caledonide Orogen - Scandinavia and Related Areas*, edited by D. G. Gee and B. A. Sturt, pp. 55–68, Wiley, 1985.
- Robinson, P., M. P. Terry, T. Carswell, H. van Roermund, T. E. Krogh, R. D. Tucker, and A. Solli, Tectono-stratigraphic setting, structure and petrology of HP and UHP metamorphic rocks and garnet peridotites in the Western Gneiss Region, Møre and Romsdal, Norway, *Geological Survey of Norway Report*, pp. 1–13, 2003.
- Root, D. B., B. R. Hacker, P. B. Gans, M. N. Ducea, E. A. Eide, and J. L. Mosenfelder, Discrete ultrahigh-pressure domains in the Western Gneiss Region, Norway: Implications for formation and exhumation, *Journal of Metamorphic Geology*, 23, 45–61, 2005.
- Rosenberg, C. L., and M. R. Handy, Experimental deformation of partially melted granite revisited: Implications for the continental crust, *Journal of Metamorphic Geology*, 23, 19–28, 2005.
- Slagstad, T., Geochemistry of trondhjemites and mafic rocks in the Bymarka ophiolite fragment, Trondheim, Norway: Petrogenesis and tectonic implications, *Norwegian Journal of Geology*, 83, 167–185, 2003.
- Smith, D. C., Coesite in clinopyroxene in the Caledonides and its implications for geodynamics, *Nature*, 310, 641–643, 1984.
- Spear, F. S., *Metamorphic Phase Equilibria and Pressure-Temperature-Time Paths*, 1993.
- Spear, F. S., and J. M. Pyle, Theoretical modeling of monazite growth in a low-Ca metapelite, *Chemical Geology*, 273, 111–119, 2010.
- Spear, F. S., M. J. Kohn, and J. T. Cheney, P-T paths from anatectic pelites, *Contributions to Mineralogy and Petrology*, 134, 17–32, 1999.

- Steel, R., A. Siedlecka, and D. Roberts, The Old Red Sandstone basins of Norway and their deformation: a review, in *The Caledonide Orogen - Scandinavia and Related Areas*, edited by D. G. Gee and B. A. Sturt, pp. 293–316, Wiley, 1985.
- Suzuki, K., and M. Adachi, The chemical Th-U-total Pb isochron ages of zircon and monazite from the gray granite of the Hida Terrane, Japan, *Journal of Earth Sciences at Nagoya University*, 38, 11–38, 1991.
- Terry, M. P., Structural and thermal evolution of Baltica basement and infolded cover nappes on Nordøyane and their bearing on mechanisms for production and exhumation of high-pressure rocks, Western Gneiss Region, Norway, unpublished Ph.D. thesis, University of Massachusetts, Amherst, MA, 2000.
- Terry, M. P., and P. Robinson, Evolution of amphibolite-facies structural features and boundary conditions for deformation during exhumation of high- and ultrahigh-pressure rocks, Nordøyane, Western Gneiss Region, Norway, *Tectonics*, 22, 1–23, 2003.
- Terry, M. P., and P. Robinson, Geometry of eclogite-facies structural features: Implications for production and exhumation of ultrahigh-pressure and high-pressure rocks, Western Gneiss Region, Norway, *Tectonics*, 23, 1–23, 2004.
- Terry, M. P., P. Robinson, M. A. Hamilton, and M. J. Jercinovic, Monazite geochronology of UHP and HP metamorphism, deformation, and exhumation, Nordøyane, Western Gneiss Region, Norway, *American Mineralogist*, 85, 1651–1664, 2000a.
- Terry, M. P., P. Robinson, and E. J. Krogh Ravn, Kyanite eclogite thermobarometry and evidence for thrusting of UHP over HP metamorphic rocks, Nordøyane, Western Gneiss Region, Norway, *American Mineralogist*, 85, 1637–1650, 2000b.
- Thompson, A. B., Dehydration melting of pelitic rocks and the generation of H<sub>2</sub>O-undersaturated granitic liquids, *American Journal of Science*, 282, 1567–1595, 1982.
- Tindle, A., and P. Webb, PROBE-AMPH: A spreadsheet program to classify microprobe-derived amphibole analyses, *Computers & Geosciences*, 20, 1201–1228, 1994.
- Torsvik, T., Palaeozoic palaeogeography: a North Atlantic viewpoint, *Geologiska Föreningen i Stockholm Förhandlingar*, 120, 109–118, 1998.
- Tucker, R., T. Krogh, and A. Råheim, Proterozoic evolution and age-province boundaries in the central part of the Western Gneiss Region, Norway: Results of U-Pb dating of accessory minerals from Trondheimsfjord to Geiranger, in *Middle Proterozoic Geology of the Southern Margin of Proto Laurentia-Baltica*, edited by C. F. Gower, B. Ryan, and T. Rivers, pp. 149–173, Geological Association of Canada Special Paper 38, 1990.
- Tucker, R. D., P. Robinson, A. Solli, D. G. Gee, T. Thorsnes, T. E. Krogh, Ø. Nordgulen, and M. E. Bickford, Thrusting and extension in the Scandian hinterland, Norway: New U-Pb ages and tectonostratigraphic evidence, *American Journal of Science*, 304, 477–532, 2004.

- Turner, G., Argon-40/Argon-39 dating of lunar rock samples, *Science*, *167*, 466–468, 1970.
- van Roermund, H., Recent progress in Scandian ultrahigh-pressure metamorphism in the northernmost domain of the Western Gneiss Complex, SW Norway: continental subduction down to 180-200 km depth, *Journal of the Geological Society, London*, *166*, 739–751, 2009.
- Vrijmoed, J. C., H. L. M. van Roermund, and G. R. Davies, Evidence for diamond-grade ultra-high pressure metamorphism and fluid interaction in the Svartberget Fe-Ti garnet peridotite-websterite body, Western Gneiss Region, Norway, *Mineralogy and Petrology*, *88*, 381–405, 2006.
- Vrijmoed, J. C., D. C. Smith, and H. L. M. van Roermund, Raman confirmation of microdiamond in the Svartberget Fe-Ti type garnet peridotite, Western Gneiss Region, Western Norway, *Terra Nova*, *20*, 295–301, 2008.
- Wain, A., New evidence for coesite in eclogite and gneisses: Defining an ultrahigh-pressure province in the Western Gneiss Region of Norway, *Geology*, *25*, 927, 1997.
- Walsh, E. O., B. R. Hacker, P. B. Gans, M. Grove, and G. Gehrels, Protolith ages and exhumation histories of (ultra)high-pressure rocks across the Western Gneiss Region, Norway, *Geological Society of America Bulletin*, *119*, 289–301, 2007.
- Warren, C., C. Beaumont, and R. Jamieson, Modelling tectonic styles and ultra-high pressure (UHP) rock exhumation during the transition from oceanic subduction to continental collision, *Earth and Planetary Science Letters*, *267*, 129–145, 2008.
- Warren, C. J., F. Hanke, and S. P. Kelley, When can muscovite  $^{40}\text{Ar}/^{39}\text{Ar}$  dating constrain the timing of metamorphic exhumation?, *Chemical Geology*, *291*, 79–86, 2012.
- White, R. W., and R. Powell, Melt loss and the preservation of granulite facies mineral assemblages, *Journal of Metamorphic Geology*, *20*, 621–632, 2002.
- White, R. W., R. Powell, and T. J. B. Holland, Progress relating to calculation of partial melting equilibria for metapelites, *Journal of Metamorphic Geology*, *25*, 511–527, 2007.
- Williams, M. L., and M. J. Jercinovic, Microprobe monazite geochronology: putting absolute time into microstructural analysis, *Journal of Structural Geology*, *24*, 1013–1028, 2002.
- Williams, M. L., M. J. Jercinovic, P. Goncalves, and K. Mahan, Format and philosophy for collecting, compiling, and reporting microprobe monazite ages, *Chemical Geology*, *225*, 1–15, 2006.
- Williams, M. L., M. J. Jercinovic, and C. J. Hetherington, Microprobe monazite geochronology: Understanding geologic processes by integrating composition and chronology, *Annual Review of Earth and Planetary Sciences*, *35*, 137–175, 2007.

- Young, D. J., B. R. Hacker, T. B. Andersen, and F. Corfu, Prograde amphibolite facies to ultrahigh-pressure transition along Nordfjord, western Norway: Implications for exhumation tectonics, *Tectonics*, 26, 1–15, 2007.
- Zen, E., Construction of pressure-temperature diagrams for multicomponent systems after the method of Schreinemakers: A geometric approach, *US Geological Survey Bulletin*, 1225, 1–56, 1966.
- Ziegler, P. A., Late Caledonian framework of western and central Europe, in *The Caledonide Orogen - Scandinavia and Related Areas*, edited by D. G. Gee and B. A. Sturt, pp. 3–18, Wiley, 1985.